TECHNISCHE UNIVERSITÄT MÜNCHEN

Professur für Mechanik auf Höchstleistungsrechnern

In-Silico Endovascular Repair of Abdominal Aortic Aneurysms

André Hemmler

Vollständiger Abdruck der von der Fakultät für Maschinenwesen der Technischen Universität München zur Erlangung des akademischen Grades eines

Doktor-Ingenieurs (Dr.-Ing.)

genehmigten Dissertation.

Vorsitzender:	Prof. Dr. rer. nat. Tim C. Lüth
Prüfer der Dissertation:	
	1. Prof. Dr.-Ing. Michael W. Gee
	2. Prof. Dr. Stéphane Avril

Die Dissertation wurde am 05.11.2019 bei der Technischen Universität München eingereicht und durch die Fakultät für Maschinenwesen am 03.03.2020 angenommen.

Abstract

In recent years, endovascular aneurysm repair (EVAR) has established itself as the treatment of choice for abdominal aortic aneurysms. However, non-negligible postinterventional complication rates, as well as a complex and partially experience-based preinterventional planning process remain great challenges of EVAR. Since the long-term success of EVAR depends largely on the preinterventional planning, clinicians are striving for suitable predictive tools. Patient-specific in-silico (computational) models are perhaps one of the most promising approaches to improve this preinterventional planning process. Toward the use of such in-silico models in clinical practice, three major objectives are addressed in this thesis: (i) model development, (ii) validation and (iii) application of an in-silico EVAR model which predicts the postinterventional state of stent-graft (SG) and abdominal aortic aneurysm (AAA).

In the first part of this thesis, a novel in-silico EVAR model is developed. The entire formulation of the model is geometrically nonlinear. Therefore, it allows for the simulation of large deformations and can accurately reproduce kinking and buckling processes. To this end, an elastically deformable, patient-specific vessel model is presented, which incorporates several different vessel constituents such as the vessel wall, intraluminal thrombus and calcifications. To the best of the author's knowledge, this vessel model is one of the most realistic among the available in-silico EVAR studies. Further, a fully resolved, realistic and elastically deformable SG model of bifurcated, commercial SG devices is used. It includes a newly developed stent predeformation methodology to account for residual strains and stresses that arise from the real-world SG manufacturing process. A novel in-silico SG placement and deployment methodology is proposed, which utilizes a centerline-based morphing algorithm to apply suitable deformation constraints to the SG model during the in-silico SG placement. A SG parameter continuation approach is suggested for the first time as a valuable SG sizing tool in which different SG sizes can be investigated within a single EVAR simulation. It is based on a continuous change of the SG size via alteration of the stress-free reference configuration of the SG. In this way, very efficient parameter and sensitivity studies of important design variables, such as the SG oversizing, are possible. Furthermore, based on a large literature study, several mechanical and geometrical parameters are defined to evaluate the quality of the in-silico EVAR outcome from an engineering perspective. This represents an essential postprocessing step that provides the link between in-silico EVAR models and the assessment of the predicted postinterventional configuration with respect to EVAR related complication likelihoods.

In the second part of this thesis, the in-silico EVAR model is validated against real-world patient-specific postinterventional measurements. The qualitative and quantitative comparison between predicted stent configurations by the simulation and stent configurations extracted from postinterventional CT data showed very good agreement. As a first step toward a patient-specific, predictive tool in the preinterventional planning process, various potential applications of the validated in-silico EVAR model are suggested. Four patient-specific cases of AAAs and bifurcated SGs are used in illustrative examples, including the patient-specific prediction of EVAR related complication likelihoods. Moreover, the impact of certain AAA and SG parameters on the successful application of EVAR is highlighted in a large parameter study of fully parameterized AAA and SG models. Finally, in a numerical proof of concept the advantage of highly customized SGs is demonstrated for patients with challenging vessel morphologies. These customized SGs have the same morphology as the luminal vessel surface.

In conclusion, this thesis contains significant steps toward the use of in-silico EVAR models in clinical practice. The good predictive quality makes the in-silico EVAR model very promising for future use with potentially a multitude of possible applications.

Zusammenfassung

Die endovaskuläre Aneurysmenreparatur (EVAR) hat sich in den letzten Jahren als bevorzugte Behandlungsmethode von abdominalen Aortenaneurysmen etabliert. Nicht zu vernachlässigende methodenassoziierte Komplikationsraten sowie ein komplexer und teilweise erfahrungsbasierter präoperativer Planungsprozess bleiben jedoch große Herausforderungen der EVAR. Da der langfristige Erfolg von EVAR wesentlich von der präoperativen Planung abhängt, suchen Ärzte nach geeigneten Prognosewerkzeugen. Patientenspezifische in-silico Modelle (Simulationsmodelle) sind wohl eine der vielversprechendsten Ansätze zur Verbesserung dieses präoperativen Planungsprozesses. Im Hinblick auf die Verwendung solcher in-silico Modelle in der klinischen Praxis werden in dieser Arbeit drei Hauptziele behandelt: (i) Die Modellentwicklung, (ii) die Validierung und (iii) die Anwendung eines in-silico EVAR Modells, das die postoperative Konfiguration von Stentgraft (SG) und abdominalem Aortenaneurysma (AAA) vorhersagt.

Im ersten Teil dieser Arbeit wird ein neues in-silico EVAR Modell entwickelt. Die gesamte Formulierung des Modells ist geometrisch nichtlinear. Daher können große Verformungen simuliert und Knick- und Beulvorgänge präzise reproduziert werden. Zu diesem Zweck wird ein elastisches, patientenspezifisches Arterienmodell vorgestellt, das zahlreiche unterschiedliche Arterienbestandteile wie die Arterienwand, intraluminaler Thrombus und Kalkablagerungen berücksichtigt. Dieses Arterienmodell ist nach Kenntnis des Autors eines der realistischsten unter den verfügbaren Studien zu in-silico EVAR. Ferner wird ein detailgetreues und elastisch verformbares Modell kommerzieller SGs mit Bifurkation präsentiert. Dieses verwendet eine neu entwickelte Methode um Eigenspannungen und -dehnungen zu berücksichtigen, die sich aus dem realen Herstellungsprozess von SGs ergeben. Außerdem wird eine neuartige in-silico SG-Platzierungs- und SG-Deploymentmethodik vorgeschlagen. Diese verwendet einen mittelachsenbasierten Morphing-Algorithmus um geeignete Deformationsbedingungen auf das SG-Modell während der in-silico SG-Platzierung aufzubringen. Weiterhin wird ein in-silico Ansatz vorgestellt, welcher es erlaubt mehrere unterschiedliche SG-Größen in einer EVAR Simulation zu untersuchen. Der Ansatz basiert auf einer kontinuierlichen Änderung der SG-Größe durch Änderung der spannungsfreien Referenzkonfiguration des SG. Auf diese Weise sind sehr effiziente Parameter- und Sensitivitätsstudien wichtiger Designvariablen, wie z.B. dem SG-Oversizing, möglich. Darüber hinaus werden auf Grundlage einer umfangreichen Literaturrecherche verschiedene mechanische und geometrische Parameter definiert, um die Qualität des in-silico EVAR Ergebnisses aus technischer Sicht zu bewerten. Dies ist ein wesentlicher Postprocessingschritt, der das Bindeglied zwischen in-silico EVAR Modellen und der Bewertung der vorhergesagten postoperativen Konfiguration in Bezug auf EVAR Komplikationswahrscheinlichkeiten darstellt.

Im zweiten Teil dieser Arbeit wird das in-silico EVAR Modell unter Verwendung von patientenspezifischen postoperativen Messungen validiert. Der qualitative und quantitative Vergleich zwischen berechneten Stentkonfigurationen durch das in-silico EVAR Modell und aus postoperativen CT-Daten extrahierten Stentkonfigurationen zeigt eine sehr gute Übereinstimmung. Als erste Schritte auf dem Weg zu einem patientenspezifischen, prädiktiven Werkzeug des präoperativen Planungsprozesses, werden mögliche Anwendungen des in-silico EVAR Modells vorgeschlagen. In anschaulichen Beispielen, wie der patientenspezifischen Vorhersage von methodenassoziierten Komplikationswahrscheinlichkeiten, werden vier patientenspezifische Fälle betrachtet. Des Weiteren wird in einer umfangreichen Parameterstudie mit

vollständig parametrisierten AAA- und SG-Modellen der Einfluss bestimmter AAA- und SG-Parameter auf die erfolgreiche Anwendung von EVAR aufgezeigt. Abschließend wird in einem numerischen Konzeptnachweis der Vorteil hochgradig individualisierter SGs in Patienten mit anspruchsvollen Aortenmorphologien demonstriert. Diese individualisierten SGs besitzen dieselbe Morphologie wie die luminale Oberfläche der Aorta.

In Summe enthält diese Arbeit wichtige Schritte auf dem Weg zur Verwendung von in-silico EVAR Modellen im klinischen Alltag. Die gute Vorhersagequalität macht das in-silico EVAR Modell sehr vielversprechend für die zukünftige Verwendung mit möglicherweise einer Vielzahl von Anwendungsmöglichkeiten.

Danksagung

An erster Stelle danke ich meinem Doktorvater, Prof. Dr. Michael Gee, für das mir entgegengebrachte Vertrauen sowie den mir gewährten Freiraum in der Themenwahl und deren Umsetzung. Vielen Dank für die vielen fachlichen Impulse, die interessanten Diskussionen und die motivierenden Worte, auch in scheinbar ausweglosen Situationen an dem Promotionsthema festzuhalten. Weiterhin danke ich Prof. Dr. Stéphane Avril für die Übernahme des Mitberichts und die inspirierenden fachlichen Diskussionen sowie Prof. Dr. Tim Lüth für die Übernahme des Vorsitzes der Prüfungskommission.

Ein großer Dank gebührt außerdem meinen klinischen Kooperationspartnern Prof. Dr. Christian Reeps und Dr. Brigitta Lutz vom Universitätsklinikum Carl Gustav Carus Dresden. Vielen Dank für euren wertvollen Beitrag als Bindeglied zwischen wissenschaftlichen Spielereien und praktischer Relevanz im klinischen Alltag. Außerdem möchte ich Prof. Dr. Thomas Franz, Prof. Dr. Deon Bezuidenhout und Andrew Lin für die wissenschaftliche Kooperation und für einen wunderschönen Forschungsaufenthalt an der University of Cape Town danken. John Nchejane und Dodzi Motchon danke ich für die herzliche Aufnahme in die Arbeitsgruppe des Mechanobiology Labs und die zahlreichen außeruniversitären Unternehmungen, welche die Monate in Kapstadt zu einer unvergesslichen Zeit machten.

Meinen ehemaligen Kolleginnen und Kollegen am Fachgebiet Mechanik auf Höchstleistungsrechnern danke ich für die stets angenehme Arbeitsatmosphäre mit fachlichem Austausch und spannenden außerfachlichen Diskussionen. Insbesondere bedanke ich mich bei Marina Bassilious, Dr. Moritz Thon und Dr. Marc Hirschvogel für die entstandene Freundschaft sowie die gemeinsamen Ausflüge und Urlaube während unserer Promotionszeit. Ebenso danke ich meinem MTU-Kollegen Dr. Christian Roth für die wertvollen Anregungen zur Ausarbeitung meiner Dissertation.

Schließlich gebührt meinen Eltern sowie meiner Frau Lisa ein riesen Dank, da sie mir jederzeit Rückhalt gegeben haben und mich von ganzem Herzen während Studium und Promotion unterstützt haben.

München, im Juni 2020 André Hemmler

Contents

1. Introduction **1**
1.1. Medical background . . . 1
1.1.1. Abdominal aortic aneurysm . . . 1
1.1.2. Endovascular aneurysm repair (EVAR) . . . 4
1.1.2.1. Procedure of EVAR . . . 5
1.1.2.2. Stent-grafts . . . 6
1.1.2.3. Instructions for use and stent-graft sizing guidelines . . . 8
1.1.2.4. Stent-graft related complications after EVAR . . . 10
1.2. Medical challenges and motivation of in-silico EVAR . . . 12
1.3. Existing in-silico and experimental studies related to EVAR . . . 14
1.3.1. Vessel modeling . . . 15
1.3.2. Stent-graft modeling . . . 16
1.3.3. In-silico SG P&D methodologies . . . 18
1.3.4. Applications of in-silico EVAR models . . . 20
1.4. Objectives . . . 22
1.5. Outline . . . 23

I. In-silico EVAR modeling **25**

2. Fundamentals of computational solid mechanics **27**
2.1. Nonlinear solid mechanics . . . 27
2.1.1. Kinematics . . . 27
2.1.2. Kinetics and constitutive relations . . . 29
2.1.3. Balance of linear momentum . . . 30
2.1.4. Boundary value problem of nonlinear elastostatics . . . 30
2.1.5. Frictional contact mechanics . . . 31
2.2. Numerical approximation . . . 32

3. Computational tools for in-silico EVAR **37**
3.1. Definition of the boundary value problem of in-silico EVAR . . . 38
3.2. Morphing algorithms for in-silico EVAR . . . 40
3.2.1. Morphing algorithms of existing in-silico SG P&D methodologies . . . 41
3.2.2. 3D morphing algorithm based on control curves . . . 43
3.2.2.1. Mapping between morphing object and control curve . . . 44
3.2.2.2. Point correspondence and path interpolation . . . 48
3.2.2.3. Numerical example of a straight tube demonstrator . . . 50
3.2.2.4. Toward the application to in-silico EVAR . . . 52

3.3. Vessel modeling . . . 54
3.3.1. Patient-specific vessel segmentation, model construction and discretization 54
3.3.2. Constitutive modeling . . . 57
3.3.2.1. Vessel wall . . . 58
3.3.2.2. Intraluminal thrombus . . . 60
3.3.2.3. Calcifications . . . 61
3.3.3. Vessel prestressing . . . 62
3.4. Stent-graft modeling . . . 63
3.4.1. Stent-graft model construction and discretization . . . 63
3.4.2. Constitutive modeling . . . 68
3.4.2.1. Stent . . . 68
3.4.2.2. Graft . . . 68
3.4.3. Stent predeformation . . . 70
3.5. In-silico EVAR and stent-graft parameter continuation . . . 73
3.5.1. In-silico EVAR with tube stent-grafts . . . 75
3.5.1.1. Vessel and stent-graft preconditioning . . . 75
3.5.1.2. Stent-graft placement . . . 76
3.5.1.3. Stent-graft deployment . . . 78
3.5.2. In-silico EVAR with bifurcated stent-grafts . . . 79
3.5.3. Stent-graft parameter continuation . . . 82
3.6. Postprocessing of the in-silico EVAR outcome . . . 84
3.6.1. Shape of the deployed stent-graft configuration . . . 85
3.6.2. EVAR quality parameters . . . 87
3.6.2.1. Vessel and stent-graft stresses and tractions . . . 88
3.6.2.2. Drag and fixation forces . . . 91
3.6.2.3. Quality of seal . . . 91
3.6.2.4. Geometrical parameters of the deployed stent-graft . . . 92
3.6.2.5. Parameters depending on the pulsatile blood pressure . . . 94
3.6.2.6. Summary of the EVAR quality parameters . . . 95
3.7. Summary of assumptions . . . 95
3.8. Summary . . . 98

II. In-silico EVAR application and validation 101

4. Validation of the in-silico EVAR model 103
4.1. Validation methodology using postinterventional CT data . . . 104
4.2. Results . . . 107
4.2.1. Qualitative validation . . . 107
4.2.2. Quantitative validation . . . 109
4.3. Discussion . . . 112
4.4. Limitations . . . 113
4.5. Conclusions . . . 114

5. Application to patient-specific cases: toward a predictive tool 115
5.1. Methods . . . 116

5.2. Illustrative applications and selected results . . . 117
5.2.1. Assessment of EVAR complication likelihoods . . . 117
5.2.1.1. Postinterventional configuration of stent-graft and vessel . . . 117
5.2.1.2. Tissue overstress after EVAR . . . 119
5.2.1.3. A focus on the landing zone . . . 120
5.2.2. Assistance in stent-graft device selection . . . 122
5.2.3. Assessment of stent-graft misplacement . . . 123
5.3. Discussion . . . 126
5.4. Limitations . . . 127
5.5. Conclusions . . . 127

6. In-silico EVAR study of parameterized vessel and stent-graft models 129
6.1. Methods . . . 130
6.1.1. Vessel parameterization . . . 130
6.1.2. Stent-graft parameterization . . . 132
6.1.3. Framework of the parameter study . . . 133
6.2. Results . . . 137
6.2.1. Overall impact of vessel and stent-graft parameters . . . 137
6.2.2. Influence of the degree of stent-graft oversizing . . . 139
6.2.3. Influence of vessel parameters . . . 141
6.2.4. Influence of stent-graft parameters . . . 145
6.2.5. Influence of the arterial blood pressure . . . 147
6.3. Summary of the results and discussion . . . 148
6.4. Limitations . . . 151
6.5. Conclusions . . . 151

7. Customized stent-grafts for EVAR with challenging necks: a numerical proof of concept 153
7.1. Methods . . . 155
7.1.1. Morphology of second level customized stent-grafts . . . 155
7.1.2. Basic manufacturing idea of second level customized stent-grafts . . . 157
7.1.3. Framework of the study . . . 157
7.2. Results . . . 159
7.2.1. Reference solution of a straight, cylindrical vessel . . . 159
7.2.2. Straight, conical vessel . . . 160
7.2.3. Straight, elliptical vessel . . . 162
7.2.4. Straight, barrel shaped vessel . . . 162
7.2.5. Straight, hourglass shaped vessel . . . 162
7.2.6. Straight, irregularly shaped vessels . . . 162
7.2.7. Curved, cylindrical vessel . . . 165
7.3. Discussion . . . 168
7.4. Limitations . . . 170
7.5. Conclusions . . . 170

8. Summary and outlook **171**
8.1. Overall summary 171
8.2. Outlook on future work 172

A. Appendix **175**
A.1. Summary of clinical data 175
A.2. In-silico study of stent predeformation 176
A.3. Mesh convergence study 177
A.4. Study of path-dependency of the stent-graft parameter continuation approach . 178
A.5. Calculation of percentiles 179
A.6. Filtering of postinterventional CT data 179
A.7. Quality estimation of segmented data from postinterventional CT scans 179
A.8. Auxiliary plane for visualization of the results 181
A.9. Detailed overview of the parameter study 181

Bibliography **189**

Nomenclature

Abbreviations

AAA	Abdominal aortic aneurysm
ACE	French: “Anévrysme de l’aorte abdominale: Chirurgie versus Endoprothèse”
ANS	Assumed natural strain
BVP	Boundary value problem
CFD	Computational fluid dynamics
CHEVAR	Chimney endovascular aneurysm repair
CT	Computed tomography
CZ-SG	SG model imitating Cook Zenith Flex/Spiral-Z® SGs
DREAM	Dutch randomised endovascular aneurysm management
DOFs	Degrees of freedom
EAS	Enhanced assumed strain
ePTFE	Expanded polytetrafluoroethylene
EVAR	Endovascular aneurysm repair, endovascular aortic repair
FEM	Finite element method
FEVAR	Fenestrated endovascular aneurysm repair
FF	Frenet frame
FSI	Fluid-structure-interaction
GMRES	Generalized minimal residual method
HU	Hounsfield unit
hex8-fbar	8-node trilinear displacement-based hexahedral finite element with F-bar element technology
IFU	Instructions for use
ILT	Intraluminal thrombus
KKT	Karush-Kuhn-Tucker
ME-SG	SG model imitating Medtronic Endurant™ II SGs
MULF	Modified updated Lagrangian formulation
OR	Open repair
OVER	Open versus endovascular repair
P&D	Placement and deployment
PET	Polyethylene terephthalate
pyramid5	5-node linear displacement-based pyramid finite element
RMF	Rotation minimizing frame
SEF	Strain energy function
SG	Stent-graft
TEVAR	Thoracic endovascular aortic repair
tet4	4-node linear displacement-based tetrahedral finite element

Operators and symbols

$(\bullet)^{-1}$	Inverse of $(\bullet)$
$(\bullet)^{\mathrm{T}}$	Transpose of $(\bullet)$
$(\bullet)^{-\mathrm{T}}$	Transpose of inverse of $(\bullet)$
$\frac{\partial}{\partial(\bullet)}$	Partial differentiation with respect to $(\bullet)$
$\nabla_0(\bullet)$	Material gradient of $(\bullet)$
$\nabla(\bullet)$	Spatial gradient of $(\bullet)$
$\nabla_0 \cdot (\bullet)$	Material divergence of $(\bullet)$
$\nabla \cdot (\bullet)$	Spatial divergence of $(\bullet)$
$\lvert(\bullet)\rvert$	Absolute value of $(\bullet)$
$\lvert\lvert(\bullet)\rvert\rvert$	2-norm of $(\bullet)$
$(\bullet)\lvert_{\xi}$	At pseudo-time ξ
$(\tilde{\bullet})$	Geometrical operation or problem
$(\breve{\bullet})$	Quantity related to auxiliary plane for visualization
$\cup$	Union of sets
$\cap$	Intersection of sets
$\emptyset$	Empty set
$\otimes$	Dyadic product
$\mathbf{1}$	Identity tensor
$\mathrm{d}(\bullet)$	Infinitesimal quantity of $(\bullet)$
$\delta(\bullet)$	Virtual quantity of $(\bullet)$
$\det(\bullet)$	Determinant of $(\bullet)$
$\mathrm{tr}(\bullet)$	Trace of $(\bullet)$
$\ln(\bullet)$	Natural logarithm of $(\bullet)$
$I_{(\bullet)>0}$	Indicator function
$\min(\bullet)$, $\max(\bullet)$	Minimum and maximum value of $(\bullet)$
$\mathrm{argmin}(\bullet)$, $\mathrm{argmax}(\bullet)$	Arguments of minima and maxima of $(\bullet)$

Main notations

$\hat{\boldsymbol{b}}_0$, $\hat{\boldsymbol{b}}$	External (prescribed) body force in reference and current configuration
$\boldsymbol{C}$, $\boldsymbol{b}$	Right and left Cauchy-Green deformation tensor
$\bar{\boldsymbol{C}}$	Modified right Cauchy-Green deformation tensor
$\mathrm{d}\boldsymbol{A}$, $\mathrm{d}\boldsymbol{a}$	Infinitesimal surface element in reference and current configuration
$\mathrm{d}\boldsymbol{f}$	Infinitesimal force resultant vector
$\mathrm{d}\boldsymbol{V}$, $\mathrm{d}\boldsymbol{v}$	Infinitesimal volume element in reference and current configuration
$\mathrm{d}\boldsymbol{X}$, $\mathrm{d}\boldsymbol{x}$	Infinitesimal line element in reference and current configuration

$\delta\mathcal{W}$	Virtual work
E, ν	Young's modulus and Poisson's ratio
$\boldsymbol{E}$, $\boldsymbol{e}$	Green-Lagrange strain tensor and Euler-Almansi strain tensor
$\boldsymbol{e}_X$, $\boldsymbol{e}_Y$, $\boldsymbol{e}_Z$	Basis vectors of Cartesian coordinate system
$\boldsymbol{F}$	Deformation gradient
I_i	i-th principal invariant of right (left) Cauchy-Green deformation tensor
$\bar{I}_i$	i-th modified invariant of right (left) Cauchy-Green deformation tensor
J	Determinant of $\boldsymbol{F}$
$\boldsymbol{N}$, $\boldsymbol{n}$	Unit normal vector in reference and current configuration
$\boldsymbol{P}$	First Piola-Kirchhoff stress tensor
p	Pressure
$\mathbb{R}$	Space of real numbers
$\boldsymbol{S}$	Second Piola-Kirchhoff stress tensor
s	Arc length of curve
$\boldsymbol{\sigma}$	Cauchy stress tensor
$\boldsymbol{t}$	Cauchy traction vector
$\boldsymbol{t}_0$	First Piola-Kirchhoff traction vector
$\hat{\boldsymbol{t}}_0$, $\hat{\boldsymbol{t}}$	External (prescribed) traction load in reference and current configuration
$\hat{\boldsymbol{u}}$	Prescribed displacement
$\boldsymbol{\Phi}$	Mapping between reference and current configuration
$\boldsymbol{u}$	Displacement
$\boldsymbol{X}$, $\boldsymbol{x}$	Position in reference and current configuration
Ψ	Strain energy function
Ψ_{iso}, Ψ_{vol}	Isochoric and volumetric part of strain energy function

Superscripts and Subscripts

$(\bullet)_1$, $(\bullet)_{99}$	1-percentile and 99-percentile
$(\bullet)^{(1)}$	Slave
$(\bullet)^{(2)}$	Master
$(\bullet)^{\text{Ao}}$	Vessel
$(\bullet)^{\text{bif}}$	Bifurcated SGs
$(\bullet)_{\text{C}}$	Control curve
$(\bullet)_{\text{De}}$	In-silico SG deployment
$(\bullet)^{\text{diast}}$	Diastolic blood pressure state
$(\bullet)_{\text{dist}}$	Distal landing zone
$(\bullet)^{(e)}$	Element
$(\bullet)_{\text{f}}$	Filtered
$(\bullet)_{\text{FF}}$	Frenet frame
$(\bullet)^{\text{G}}$	Graft
$(\bullet)_{\text{h}}$	Discretized in space with the FEM
$(\bullet)_{\text{I}}$	Initial state

$(\bullet)_{\mathrm{lz}}$	Landing zone (proximal or distal)
$(\bullet)^{(\Lambda)}$	Quantity related to blood pressure state $\Lambda \in \{\mathrm{diast}, \mathrm{sys}\}$, i.e., diastolic (diast) and systolic (sys)
$(\bullet)_{\mathrm{PC}}$	SG parameter continuation
$(\bullet)_{\mathrm{Pl}}$	In-silico SG placement
$(\bullet)_{\mathrm{postIV}}$	Postinterventional CT data (real-world)
$(\bullet)_{\mathrm{Pre}}$	Stent predeformation
$(\bullet)_{\mathrm{prox}}$	Proximal landing zone
$(\bullet)^{(\Pi)}$	Quantity related to body $\Pi \in \{\mathrm{Ao}, \mathrm{G}, \mathrm{S}\}$, i.e., vessel (Ao), graft (G) and stent (S)
$(\bullet)_{\mathrm{RM}}$	Ring-shaped stent limb with M-profile
$(\bullet)_{\mathrm{RZ}}$	Ring-shaped stent limb with Z-profile
$(\bullet)^{\mathrm{S}}$	Stent
$(\bullet)^{\mathrm{SG}}$	Stent-graft
$(\bullet)_{\mathrm{sim}}$	Simulation (in-silico)
$(\bullet)^{\mathrm{sys}}$	Systolic blood pressure state
$(\bullet)_{\mathrm{SZ}}$	Spiral-shaped stent limb with Z-profile
$(\bullet)_{\mathrm{T}}$	Target state
$(\bullet)^{(\Theta)}$	Quantity related to SG part $\Theta \in \{\mathrm{P}, \mathrm{L}, \mathrm{R}\}$, i.e., proximal part (P), left iliac part (L) and right iliac part (R)
$(\bullet)_{(\Upsilon)}$	Quantity related to state $\Upsilon \in \{\mathrm{I}, \mathrm{Pre}, \mathrm{Pl}, \mathrm{De}, \mathrm{PC}\}$, i.e., initial state (I), stent predeformation (Pre), in-silico SG placement (Pl), in-silico SG deployment (De) and SG parameter continuation (PC)
$(\bullet)^{\mathrm{wall}}$	Vessel wall

Domains and boundaries

Γ, γ	Boundary in reference and current configuration
Γ_σ, γ_σ	Neumann boundary in reference and current configuration
Γ_{u}, γ_{u}	Dirichlet boundary in reference and current configuration
Γ_{c}, γ_{c}	Potential contact boundary in reference and current configuration
Γ_{m}	Mesh tying boundary in reference configuration
$\Gamma_{\mathrm{l}}^{\mathrm{Ao}}$, $\gamma_{\mathrm{l}}^{\mathrm{Ao}}$	Luminal boundary of the vessel in reference and current configuration
$\Gamma_{\mathrm{ex}}^{\mathrm{Ao}}$, $\gamma_{\mathrm{ex}}^{\mathrm{Ao}}$	Exterior boundary of the vessel in reference and current configuration
$\Gamma_{\mathrm{io}}^{\mathrm{Ao}}$, $\gamma_{\mathrm{io}}^{\mathrm{Ao}}$	Inlet/outlet boundary of the vessel in reference and current configuration
$\Gamma_{\mathrm{l}}^{\mathrm{G}}$, $\gamma_{\mathrm{l}}^{\mathrm{G}}$	Luminal boundary of the graft in reference and current configuration
$\Gamma_{\mathrm{ex}}^{\mathrm{G}}$, $\gamma_{\mathrm{ex}}^{\mathrm{G}}$	Exterior boundary of the graft in reference and current configuration
$\Gamma_{\mathrm{ex}}^{\mathrm{S}}$, $\gamma_{\mathrm{ex}}^{\mathrm{S}}$	Exterior boundary of the stent in reference and current configuration
Ω_0, Ω	Reference (material) domain and current (spatial) domain
Ω_0^{Ao}, Ω^{Ao}	Reference domain and current domain of the vessel
Ω_0^{G}, Ω^{G}	Reference domain and current domain of the graft
Ω_0^{S}, Ω^{S}	Reference domain and current domain of the stent

Contact mechanics

$\mathfrak{F}$	Friction coefficient
$\boldsymbol{g}$, g_{n}	Gap vector and its normal projection
$\boldsymbol{n}_{\mathrm{c}}$	Current unit normal vector at contact interface
p_{n}	Normal contact traction (pressure) in current configuration
$\boldsymbol{v}_{\tau,\mathrm{rel}}$	Relative tangential velocity vector
$\boldsymbol{t}_{\mathrm{c}}$	Contact traction vector in current configuration
$\boldsymbol{t}_{\tau}$	Tangential contact traction vector in current configuration

Discretization and solution

$\mathbf{C}$	Global discrete (Rayleigh) damping matrix
c_{M}, c_{K}	Mass and stiffness Rayleigh damping coefficients
$\mathbf{f}_{\mathrm{ext}}$	Global discrete external force vector
$\mathbf{f}_{\mathrm{int}}$	Global discrete internal force vector
$H^1(\bullet)$	Sobolev space of functions with square integrable values and first derivatives on domain $(\bullet)$
$\mathbf{K}_0$	Reference tangent system matrix
$\mathbf{M}$	Global discrete mass matrix
N^i	Finite element shape function of node i
n_{node}	Number of nodes
$\boldsymbol{u}^i$	Nodal displacements of node i
$\mathbf{u}$, $\dot{\mathbf{u}}$, $\ddot{\mathbf{u}}$	Global vector of nodal displacements, velocities and accelerations
$\mathcal{U}$	Solution space for displacements
$\mathcal{V}$	Weighting space for displacements
$\boldsymbol{\xi}$	Finite element parameter space
$\boldsymbol{X}^i$	Nodal reference coordinates of node i
$\boldsymbol{x}^i$	Nodal current coordinates of node i

Morphing specific

A	Total set of morphed nodes
A^j	Subset of morphed nodes assigned to point j
$\mathbb{B}^j$	Bounding box around point j
$\boldsymbol{b}^j$, $\boldsymbol{b}'^j$	Unit binormal vector and its first spatial derivative at point j
$\mathcal{C}(t)$	Control curve at pseudo-time t

$\boldsymbol{\mathcal{C}}'^j$, $\boldsymbol{\mathcal{C}}''^j$	First and second spatial derivative of control curve at point j
$\mathcal{C}_\mathrm{I}$, $\mathcal{C}(t_\mathrm{I})$	Control curve in initial configuration
$\mathcal{C}_\mathrm{T}$, $\mathcal{C}(t_\mathrm{T})$	Control curve in target configuration
Δr	Radius change
Δs^j	Mean edge length of two adjacent edges of point j
Δt	Pseudo-time step size
$(\boldsymbol{e}_r \boldsymbol{e}_\theta \boldsymbol{e}_{\hat{z}})^{i,j}$	Local cylindrical coordinate system of node i assigned to point j
ϵ_r	Tolerance of non-penetration condition
f_r^j	Non-penetration condition at point j
$\bar{\theta}^i$	Mean angular distance of node i
l_a, l_b	Longitudinal overlap and transverse distance between control curves
$\tilde{\boldsymbol{M}}$, $\tilde{\boldsymbol{m}}$	Morphing map applied to reference and current configuration
$\tilde{\boldsymbol{m}}_\mathrm{De}$	Mapping between current configuration after in-silico SG placement and current configuration after in-silico SG deployment
$\tilde{\boldsymbol{M}}_\mathrm{PC}$	Mapping between reference configuration after SG parameter continuation and reference configuration after stent predeformation
$\tilde{\boldsymbol{m}}_\mathrm{Pl}$	Mapping between current configuration of initial state and current configuration after in-silico SG placement
$\tilde{\boldsymbol{M}}_\mathrm{Pre}$	Mapping between reference configuration after stent predeformation and reference configuration of initial state
$n^\mathrm{B}_\mathrm{node}$	Number of nodes of morphing object
n_C	Number of points of control curve
n^j_node	Number of nodes in set A^j
$\boldsymbol{n}^j$	Unit normal vector at point j
r^i, $\hat{z}^i$, θ^i	Local cylindrical coordinates of node i
r^j_κ	Radius of curvature of control curve at point j
T	Accumulated torsion of control curve
t	Pseudo-time of path interpolation
$\boldsymbol{t}^j$	Unit tangent vector at point j
τ^j	Torsion at point j
t_I, t_T	Pseudo-time at initial and target state
$\mathcal{T}$	Interval of pseudo-time t
$\boldsymbol{\varphi}$	Mapping between morphing object and control curve
$\boldsymbol{\psi}$	Mapping between initial and target configuration of control curve
$\tilde{\Omega}^\mathrm{B}(t)$	Morphing object at pseudo-time t
$\tilde{\Omega}^\mathrm{B}_\mathrm{I}$, $\tilde{\Omega}^\mathrm{B}(t_\mathrm{I})$	Morphing object in initial configuration
$\tilde{\Omega}^\mathrm{B}_\mathrm{T}$, $\tilde{\Omega}^\mathrm{B}(t_\mathrm{T})$	Morphing object in target configuration
$\tilde{\boldsymbol{x}}^i(t)$	Position of node i of morphing object at pseudo-time t
$\tilde{\boldsymbol{x}}^i(t_\mathrm{I})$, $\tilde{\boldsymbol{x}}^i_\mathrm{I}$	Position of node i of morphing object in initial configuration
$\tilde{\boldsymbol{x}}^i(t_\mathrm{T})$, $\tilde{\boldsymbol{x}}^i_\mathrm{T}$	Position of node i of morphing object in target configuration
$\tilde{\boldsymbol{x}}^j_\mathrm{C}(t)$	Position of point j of control curve at pseudo-time t
$\tilde{\boldsymbol{x}}^j_\mathrm{C}(t_\mathrm{I})$, $\tilde{\boldsymbol{x}}^j_\mathrm{C,I}$	Position of point j of control curve in initial configuration
$\tilde{\boldsymbol{x}}^j_\mathrm{C}(t_\mathrm{T})$, $\tilde{\boldsymbol{x}}^j_\mathrm{C,T}$	Position of point j of control curve in target configuration
ξ	Pseudo-time of progress of morphing map

Stent-graft specific

a_i, b_i	i-th Fourier coefficients of stents with M-profile
$\mathcal{C}_{\mathrm{De}}$	Centerline of SG in deployed state
D^{G}	Outer diameter of graft
D^{S}	Outer diameter of stent
$D^{\mathrm{S}}_{\mathrm{I}}$	Initial outer diameter of stent
$D^{\mathrm{S}}_{\mathrm{Pre}}$	Stress-free outer diameter of unassembled stent
D^{SG}	Nominal diameter of the SG
d^{S}	Stent wire thickness
$\hat{d}^{\mathrm{S}}$	Adapted stent wire thickness of quadratic cross section
$\overline{d^{\mathrm{S}}}$	Mean stent limb diameter
$\mathcal{G}^{\mathrm{SG}}$	Set of parameters of parameterized SG model
g^{SG}	Parameter of parameterized SG model
h^{S}	Height of stent limb
L^{SG}	Length of SG
$l^{\mathrm{S}}_{\mathrm{SZ}}$	Lead of spiral-shaped stent limb
n^{S}	Number of stent limbs of parameterized SG model
$n^{\mathrm{S}}_{\mathrm{SZ}}$	Number of turns of spiral-shaped stent limb
n^{SG}	Number of SG parameter realizations of parameterized vessel model
$n^{\mathrm{SG}}_{\mathrm{node}}$	Number of nodes of discretized SG model
o	(Nominal) degree of SG oversizing
p^{S}	Number of sinusoidal periods of stent limb
s_{De}	Arc length of SG centerline in deployed state
t^{G}	Graft thickness
ω	Degree of stent predeformation
$\boldsymbol{x}^{j}_{\mathrm{C,De}}$	Position of point j of SG centerline in deployed state

Vessel specific

$\boldsymbol{A}_i$	Mean fiber direction of fiber i
a, b	Stiffness parameters of AAA wall
α_{p}, α_{d}	Proximal and distal neck angle of parameterized vessel model
$\mathcal{C}^{\mathrm{Ao}}$	Centerline of parameterized vessel model
$\hat{\mathcal{C}}^{\mathrm{Ao}}$	Luminal centerline of parameterized vessel model
c^{AA}	Stiffness of aortic ground material
c^{calc}	Stiffness of calcified tissue
$\hat{c}^{\mathrm{calc}}$	Stiffness of pure calcifications
$c^{\mathrm{ILT}}_{\mathrm{lum}}$, $c^{\mathrm{ILT}}_{\mathrm{med}}$, $c^{\mathrm{ILT}}_{\mathrm{abl}}$	ILT stiffness of luminal, medial and abluminal layer

$\bar{c}^{\mathrm{Ao}}_{\mathrm{prox}}$	Percentage circumferential proximal neck calcification of parameterized vessel model
γ	Scaling parameter of vessel wall stiffness of parameterized vessel model
D^{Ao}	Preinterventional vessel diameter (inner wall to inner wall)
d_{AAA}	Aneurysm diameter of parameterized vessel model
e_{l}	Luminal eccentricity of parameterized vessel model
e_{p}, e_{d}	Proximal and distal eccentricity of parameterized vessel model
$\mathcal{G}^{\mathrm{Ao}}$	Set of parameters of parameterized vessel model
g^{Ao}	Parameter of parameterized vessel model
h	Local HU value
θ_i	Orientation angle of i-th fiber
K	Volumetric bulk modulus
k_1	Fiber stiffness
k_2	Exponential parameter of fibers
$\hat{k}_{\mathrm{ex}}$, $\hat{k}_{\mathrm{io}}$	Spring stiffness at exterior and inlet/outlet boundaries of the vessel
κ	Dispersion parameter
l_{AAA}	Aneurysm length of parameterized vessel model
l_{p}, l_{d}	Proximal and distal neck length of parameterized vessel model
l_{sp}, l_{sd}	Proximal and distal shoulder length of parameterized vessel model
λ	Blend parameter to blend between "healthy" and "aneurysmatic" vessel wall
n^{Ao}	Number of vessel parameter realizations of parameterized vessel model
p^{diast}, p^{sys}	Blood pressure at diastolic and systolic state
r	Local radius of vessel
r^{AA}	Subrenal radius of the preinterventional vessel
t_{ILT}	Maximum ILT thickness of parameterized vessel model
t_{w}	Vessel wall thickness of parameterized vessel model
$\Psi^{\mathrm{AA}}_{\mathrm{fi}}$	Anisotropic part of vessel wall strain energy function

In-silico EVAR specific

D_{Pl}	Minimum SG diameter during in-silico SG placement
$\mathcal{G}$	Set of parameters of parameterized vessel and SG model
g	Parameter of parameterized vessel and SG model
$\hat{g}$	Basic parameter of parameterized vessel and SG model
$\mathbf{\Phi}_{\mathrm{I}}$	Mapping between reference and current configuration at initial state
$\mathbf{\Phi}_{\mathrm{PC}}$	Mapping between reference and current configuration after SG parameter continuation
$\mathbf{\Phi}_{\mathrm{Pre}}$	Mapping between reference and current configuration after stent predeformation
$\Omega^{\{\mathrm{S,G}\}}_{0,\mathrm{I}}$, $\Omega^{\{\mathrm{S,G}\}}_{\mathrm{I}}$	Reference/current domain of stent and graft in initial state
$\Omega^{\{\mathrm{S,G}\}}_{0,\mathrm{De}}$, $\Omega^{\{\mathrm{S,G}\}}_{\mathrm{De}}$	Reference/current domain of stent and graft after in-silico SG deployment
$\Omega^{\{\mathrm{S,G}\}}_{0,\mathrm{PC}}$, $\Omega^{\{\mathrm{S,G}\}}_{\mathrm{PC}}$	Reference/current domain of stent and graft after SG parameter continuation

$\Omega_{0,\mathrm{Pl}}^{\{\mathrm{S,G}\}}$, $\Omega_{\mathrm{Pl}}^{\{\mathrm{S,G}\}}$	Reference/current domain of stent and graft after in-silico SG placement
$\Omega_{0,\mathrm{Pre}}^{\{\mathrm{S,G}\}}$, $\Omega_{\mathrm{Pre}}^{\{\mathrm{S,G}\}}$	Reference/current domain of stent and graft after stent predeformation
$\boldsymbol{X}_{\mathrm{I}}^{\{\mathrm{S,G}\}}$, $\boldsymbol{x}_{\mathrm{I}}^{\{\mathrm{S,G}\}}$	Position of stent and graft in reference/current configuration at initial state
$\boldsymbol{X}_{\mathrm{De}}^{\{\mathrm{S,G}\}}$, $\boldsymbol{x}_{\mathrm{De}}^{\{\mathrm{S,G}\}}$	Position of stent and graft in reference/current configuration after in-silico SG deployment
$\boldsymbol{X}_{\mathrm{PC}}^{\{\mathrm{S,G}\}}$, $\boldsymbol{x}_{\mathrm{PC}}^{\{\mathrm{S,G}\}}$	Position of stent and graft in reference/current configuration after SG parameter continuation
$\boldsymbol{X}_{\mathrm{Pl}}^{\{\mathrm{S,G}\}}$, $\boldsymbol{x}_{\mathrm{Pl}}^{\{\mathrm{S,G}\}}$	Position of stent and graft in reference/current configuration after in-silico SG placement
$\boldsymbol{X}_{\mathrm{Pre}}^{\{\mathrm{S,G}\}}$, $\boldsymbol{x}_{\mathrm{Pre}}^{\{\mathrm{S,G}\}}$	Position of stent and graft in reference/current configuration after stent predeformation
x_{mis}	SG misplacement

Validation specific

$\bar{\Delta s}_{\mathrm{De}}$	Mean edge length of SG centerline in deployed state
Δz_{CT}	Slice thickness of CT data
ε	Local mean relative error (mean between different blood pressure states)
$\varepsilon^{(\Lambda)}$	Relative error at blood pressure state $\Lambda \in \{\mathrm{diast}, \mathrm{sys}\}$
ε_f	Relative difference between measured and filter data
l_{span}	Span of moving average filter
μ_ε	Spatial mean relative error
μ_f	Mean value of relative difference between measured and filter data
σ_ε	Spatial standard deviation of relative error
σ_f	Standard deviation of relative difference between measured and filter data

EVAR quality parameters

A_{lz}, a_{lz}	Area of landing zone (proximal or distal) in preinterventional and postinterventional state
$a_{\mathrm{lz}}^{\mathrm{seal}}$	Fixation area in landing zone (proximal or distal)
C	Compliance
$\bar{C}$	Mean diametric graft compliance
$\mathrm{CV}q$	Coefficient of variation of EVAR quality parameter q
c_i^{S}	Degree of conical stent shape of stent limb i
$\gamma_\perp^{\mathrm{SG}}$	Orthogonal slice through SG
$\bar{d}$	Average diameter
Δq	Relative change of EVAR quality parameter q
e^{S}	Degree of stent expansion

$\boldsymbol{F}_{\mathrm{drag}}$	SG drag force
$\hat{F}_{\mathrm{lz}}$	Passive SG fixation force in landing zone (proximal or distal)
L_{lz}	Length of landing zone (proximal or distal)
μ_q	Mean value of EVAR quality parameter q
o^{eff}	Effective degree of SG oversizing
$\bar{o}_{\mathrm{lz}}^{\mathrm{eff}}$	Mean effective degree of SG oversizing in landing zone (proximal or distal)
$\mathcal{Q}$	Set of EVAR quality parameters
q	EVAR quality parameter
$\breve{R}$	Auxiliary radius of virtual cylinder for visualization
$r_{\min}, r_{\max}$	Minimum and maximum radius
$r_{q,o}$	Pearson product-moment correlation coefficient between EVAR quality parameter q and SG oversizing o
$r_{\hat{q},\breve{q}}$	Pearson product-moment correlation coefficient between two EVAR quality parameters
σ_{pre}	Preinterventional von Mises Cauchy stress
σ_q	Standard deviation of EVAR quality parameter q
$\bar{\sigma}$	Von Mises Cauchy overstress
$\bar{\sigma}^{\lambda}$	Aneurysmatic von Mises Cauchy overstress
$\boldsymbol{u}^{\mathrm{pul}}$	Movement (relative displacement) during change from diastolic to systolic blood pressure state
$\breve{X}, \breve{Y}, \breve{Z}$	Auxiliary coordinates for visualization
$\breve{\boldsymbol{x}}$	Closest point
y^{S}	In-plane stent asymmetry
$z_{\max}^{\mathrm{GA}}, z_{\max}^{\mathrm{SA}}$	Maximum graft-vessel gap and maximum stent-vessel gap

Definition of terms

Stent-graft (SG):	A stent-graft is the combination of a stabilizing wire mesh (stent) and an artificial blood vessel made of polymeric material (graft). SGs are used in particular to exclude aneurysms from the bloodstream.
SG component:	SGs to treat AAAs consist of multiple modular components. In standard EVAR, SGs consist of a main body component and one or two iliac leg components that are docked to the main component.
SG part:	For evaluation and validation purpose, the bifurcated SGs are separated into three parts: proximal part, left iliac part and right iliac part.
Landing zone:	The most proximal/distal part of the SG which is directly attached to the luminal vessel surface and which is responsible for a leak-proof seal and fixation of the SG. For infrarenal AAAs, the potential proximal landing zone is defined by the region from the most inferior renal artery to the beginning of the vessel dilatation of the AAA. In all patient-specific cases considered in this thesis the distal landing zones are in the common iliac arteries.
Stent predeformation:	Stents generally are produced with a diameter that is larger than the associated graft. During the assembling process of SGs, stents are radially compressed and are fixed on the graft in this compressed state. This circumstance, which results in an assembled SG with residual strains and stresses, is denoted as stent predeformation.
SG oversize:	SG oversize describes the ratio of outer nominal SG diameter to inner preinterventional vessel wall diameter in the landing zone of the SG.
SG placement:	Process of positioning the SG in the interior of the vessel.
SG deployment:	Process of removing the delivery sheath and therefore allowing the SG to freely deform in the interior of the vessel.
Vessel prestressing:	Geometry reconstruction from in-vivo medical imaging involves an initial geometric configuration that is not stress-free. Vessel prestressing is the computational approach of initializing the vessel model to this stressed configuration.
In-silico EVAR model:	Computational model to predict the postinterventional configuration of SG and vessel. The in-silico EVAR model is subject to simplifications and assumptions associated with the vessel model, the SG model and the in-silico SG P&D methodology.

In-silico SG P&D methodology:	Computational SG placement and deployment methodology.
EVAR quality parameter:	Geometrical and mechanical parameters to assess the quality of the in-silico EVAR outcome with respect to EVAR related complication likelihoods.

1. Introduction

The *abdominal aortic aneurysm* (AAA) is a pathological dilatation of the abdominal aorta exhibiting a maximum diameter larger than 3 cm. To prevent AAA rupture, which has a high mortality rate of more than 80% [69], elective AAA repair is carried out. Established techniques of elective AAA repair are the conventional *open repair* (OR) and the minimally invasive *endovascular aneurysm repair* (EVAR), where nowadays EVAR is the preferred choice of treatment and constitutes around 70% of all AAA repairs in Germany [144]. However, despite significant technical improvements of EVAR in recent decades, it is still subject to severe shortcomings including an elevated likelihood of EVAR related complications.

In-silico approaches can provide a valuable predictive tool to improve the preinterventional planning of EVAR and to reduce EVAR related complication rates. Hence, in this thesis an in-silico (computational) EVAR model is developed to predict the deployed stent-graft (SG) configuration in an AAA. Toward the application as patient-specific tool in clinical practice, several applications of this in-silico EVAR model are presented.

At the beginning of this chapter, the medical fundamentals of EVAR are provided in Section 1.1, followed by medical challenges associated with EVAR and motivations to use in-silico EVAR in Section 1.2. A comprehensive literature overview of in-silico EVAR models is given in Section 1.3. Subsequently, the objectives and the outline of this thesis are presented in Section 1.4 and 1.5.

The content of this thesis is largely based on work previously published by the author, namely [106–110]. This chapter is partly taken from [106, 107, 109] with permission.

1.1. Medical background

The aneurysm is one of the most frequent diseases of the aorta [71] with the aortic aneurysm being located primarily in the abdominal region. The underlying medical background of AAA especially concerning the treatment with EVAR is provided in the following sections.

1.1.1. Abdominal aortic aneurysm

An abdominal aortic aneurysm is a local dilatation of the abdominal aorta which is exposed to the immanent risk of rupture. Among persons over the age of 65, the prevalence of an AAA with a maximum diameter of 3 cm or larger lies between 4% and 8% in men and between 0.5% and 1.5% in women [69]. Risk factors for AAA development are: male sex, high age, smoking, familial predisposition, obesity and hypertension [92, 144]. However, the exact pathogenesis of AAAs has not yet been fully understood. Among other factors, the mechanism of AAA development is thought to be associated with a decreased elastin content and structural degeneration

of the AAA wall [37]. Most AAAs are asymptomatic and the diagnosis mostly is an incidental finding, although ultrasound screening programs are becoming increasingly common among people above 65 years [69]. Dependent on the AAA location relative to the branch-offs into the renal arteries, AAAs are classified according to:

- *Infrarenal AAA*: Complete AAA is located distal to the branch-offs into the renal arteries (more than 90% of all AAAs [105]).
- *Juxtarenal AAA*: AAA starts proximal and ends distal to the branch-offs into the renal arteries.
- *Suprarenal AAA*: Complete AAA is located proximal to the branch-offs into the renal arteries.

When to intervene

Since only some AAAs rupture while others remain stable for the remaining lifetime of the patient, the question of the best time of elective repair of non-ruptured AAAs arises. Based on the law of Laplace, in clinical practice the question of *when to intervene* is most commonly answered using the *maximum diameter criterion*. This criterion states that above a certain threshold of the AAA diameter (typically $5.0 - 5.5\,\mathrm{cm}$) the AAA should be treated by elective repair. Indices other than the maximum diameter criterion, such as AAA wall stress-strength based [163, 208] and AAA morphology based [77, 137] rupture risk assessment, are current area of research.

How to intervene

Once the patient is selected for elective AAA repair, the clinician must decide between a conventional *OR* and an *EVAR*. OR is a highly invasive technique in which transabdominal access is used to reach the AAA. Subsequently, the AAA is replaced by a vascular graft, that is sutured to the "healthy" part of the aorta. In contrast, in the minimally invasive intervention of EVAR, AAA rupture prevention is achieved by the deployment of a SG inside the AAA to exclude the aneurysm sac from the main blood flow and remove the load of the pulsatile blood pressure from the aneurysm wall.

Similar to the first question of *when to intervene*, the second question of *how to intervene* is subject of discussions. Several clinical trials comparing EVAR to OR for elective AAA repair have been performed since the launch of EVAR. *EVAR trial 1* was the first and largest clinical trial for which 1252 patients, who were physically fit enough to undergo either EVAR or OR, were randomly assigned to either EVAR or OR between 1999 and 2004 at 37 hospitals in the United Kingdom. The results of EVAR trial 1 were published as 30-day postinterventional results [95], mid-term results [96], long-term follow-up results over 8 years [98] and late follow-up results of up to 15 years [200]. Other, large clinical trials are the Dutch *DREAM* trial [54, 213], the *OVER* trial in the USA [150, 151] and the *ACE* trial in France [19]. A meta-analysis combining these trials is provided in the work of Patel et al. [201].

Among all these clinical trials the following advantages and drawbacks of EVAR compared to OR could be identified. Since EVAR is less invasive, it enables AAA repair of patients who are physically ineligible for OR. The sister trial of the EVAR trial 1, the *EVAR trial 2* [125],

compares the aneurysm-related mortality rate between EVAR and no intervention of patients with AAA of diameter ≥ 5.5 cm that are ineligible for OR. According to EVAR trial 2, the 8 year cumulative aneurysm-related mortality is significantly lower for patients who underwent EVAR (14%) than for patients who had no intervention at all (36%).

The avoidance of cross-clamping of the aorta in EVAR removes the risk of cardiac decompensation during and briefly after the intervention. Therefore, the 30-day operative mortality rate is significantly lower for EVAR (approximately 1.8%, EVAR trial 1) compared to OR (approximately 4.4%, EVAR trial 1) [98].

Apart from these positive characteristics, EVAR is also subject to several drawbacks. It is not applicable to all patients. Especially in case of an unfavorable vessel anatomy, EVAR might fail or require secondary interventions. Hence, device manufacturers formulate the limits of applicability of EVAR in their instructions for use (IFU), which state, for instance, that the aortic neck should not exceed a certain angle and that the neck requires a certain minimum length for the fixation of the SG.

Further, EVAR might not have the same longevity as OR. After OR, the vascular graft usually serves the patient's remaining lifetime, while SG related complications and reinterventions are higher with EVAR [54, 98] (cf. Figure 1.1).

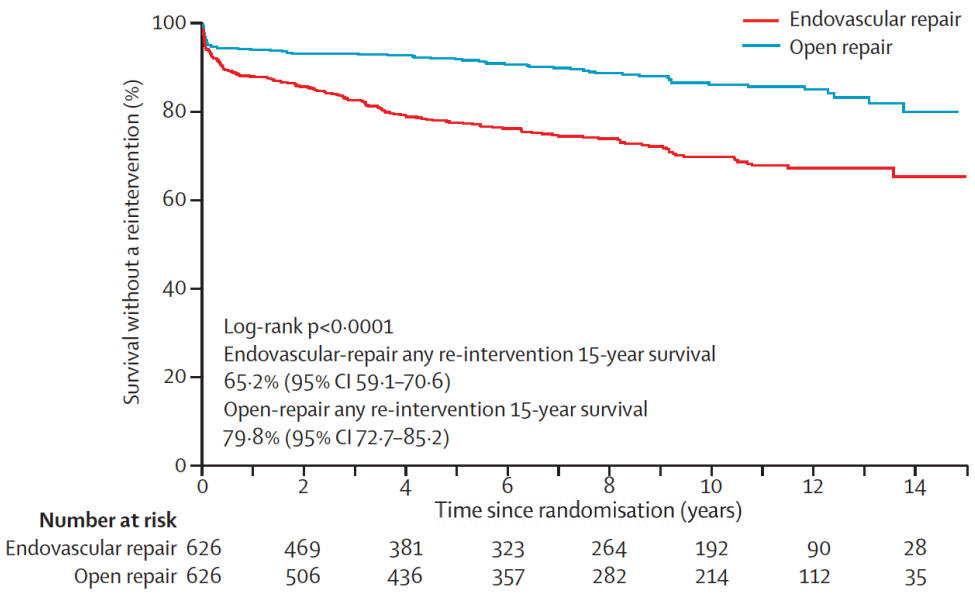

Figure 1.1 Kaplan-Meier estimates of time to first reintervention in the EVAR and OR groups during 15 years of follow-up (EVAR trial 1). Reproduced with permission from [200], copyright Elsevier Ltd.

OR allows an in-situ assessment of the anatomical conditions and potential adaptions of the preinterventional plan during surgery. In contrast, EVAR has to rely on impeccable preinterventional planning based on computed tomography (CT) data and imaging software. Besides reliable preinterventional EVAR planning tools this also requires an experienced clinician. Numerous studies point out the correlation between the clinician's experience and the successful application of EVAR (e.g., [78, 170, 252]). Related to the required experience, the preinterventional planning of EVAR is strongly affected by the subjective choices of the clinician.

Due to relatively high SG related long-term complication rates, regular follow-up checks are needed. Follow-up recommendations advocate screening (mostly CT) in regular intervals (mostly at 1, 6, and 12 months after the intervention, and annually thereafter [44, 176]). Although CT screening can be partly replaced by less harmful control methods, such as duplex ultrasound, the large amount of cumulative radiation exposure during EVAR and in follow-up checks remains a problem [179, 199].

1.1.2. Endovascular aneurysm repair

Minimally invasive endovascular aneurysm repair, also known as *endovascular aortic repair*, was first performed in 1990 by the vascular surgeon Juan Parodi in Buenos Aires, Argentina [198]. This AAA treatment method was initially designed for patients who are physically ineligible for treatment with OR. Over the last decades both the EVAR procedure as well as the SG prosthesis have been further developed and the outcomes of EVAR could be drastically improved [262]. Nowadays, EVAR is the treatment of choice for the majority of AAA patients [246]. Also patients that are physically eligible for OR are frequently treated by EVAR. But only around 70% of patients with AAA have suitable AAA anatomies for standard EVAR [134, 272].

In the minimally invasive treatment of infrarenal AAAs by EVAR, a bifurcated SG prosthesis with two iliac legs is deployed inside the AAA to exclude the aneurysm sac from the main blood flow, remove the load of the pulsatile blood pressure from the aneurysm wall, stop the aneurysm from ongoing aneurysm growth and consequently prevent the aneurysm from rupture. After a successful EVAR, thrombosis of the aneurysm sac as well as shrinkage of the AAA sac can be observed in follow-up studies [70, 97]. Standard EVAR is applicable to infrarenal AAAs when certain anatomical requirements are fulfilled as described in Section 1.1.2.3. Among other requirements, an adequate length of the potential *landing zone* is required. The proximal landing zone describes the most proximal part of the SG and the distal landing zones describe the most distal parts of the SG which are directly attached to the luminal vessel surface in the deployed state. These landing zones have a crucial impact on the success of EVAR since they are responsible for the leak-proof seal and the fixation of the SG. For infrarenal AAAs, the proximal landing zone of the vessel is defined by the region from the most inferior renal artery to the beginning of the vessel dilatation of the AAA. This region is also denoted as *proximal neck* of the AAA. In all patient-specific cases considered in this thesis the distal landing zones are in the common iliac arteries.

Complex aneurysm geometries such as juxtarenal AAAs preclude standard EVAR as feasible treatment option. In these cases, *fenestrated endovascular aneurysm repair* (FEVAR) [261] and *chimney endovascular aneurysm repair* (CHEVAR) [31] are alternatives to OR. In FEVAR, a semi-customized SG is deployed such that it covers the branch-offs into the renal arteries. Fenestrations in the SG at the location of the renal arteries allow for blood flow through the SG into the renal arteries. Instead of fenestrations, the CHEVAR uses additional tubular SGs that are deployed inside the renal arteries. The proximal parts of these additional tubular SGs must extend above the proximal ends of the main SG such that blood flow from the aorta into the renal arteries is possible.

Although EVAR is also used for the treatment of ruptured AAAs [218], in this thesis it is only considered as treatment option of elective AAA repair. A similar procedure is also used for thoracic aortic aneurysms. In this case, the endovascular procedure is denoted as *thoracic*

endovascular aortic repair (TEVAR). However, in this thesis focus lies on infrarenal AAAs and EVAR.

1.1.2.1. Procedure of EVAR

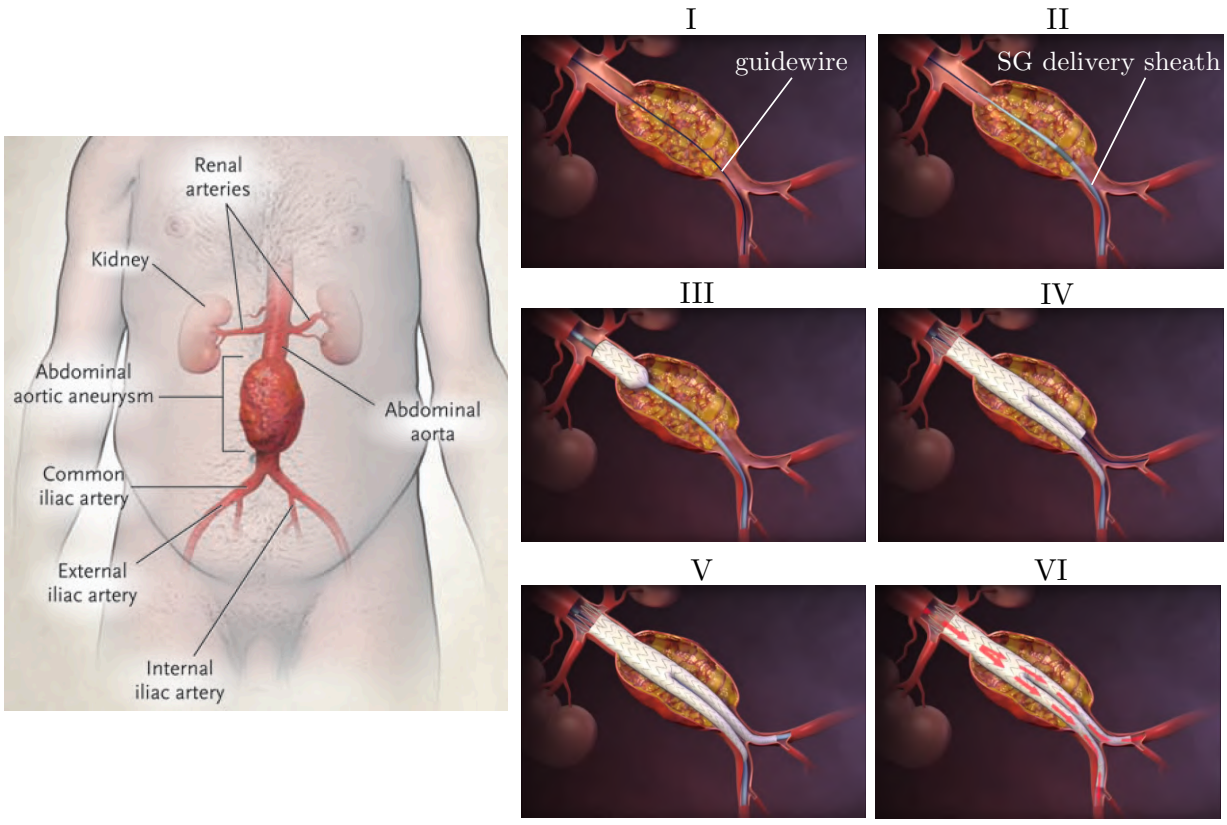

Figure 1.2 Illustration of an AAA and the procedure of EVAR described by the steps I-VI. Modified figure reproduced with permission from [97], copyright Massachusetts Medical Society.

Depending on the SG device and the SG manufacturer, the EVAR procedure slightly differs. In this section, an overview over the procedure of standard EVAR with a modular SG combination of a main body SG and one iliac leg SG is given without mimicking the procedure of one specific SG device. EVAR is a minimal invasive procedure which is performed under continuous blood flow. It only requires either small incisions in the groins or can even be performed just using percutaneous access. EVAR is carried out under intrainterventional use of fluoroscopy imaging to be able to precisely position the SG in the AAA. It can be performed under general or even local anesthesia. As visualized in Figure 1.2, the standard EVAR procedure consists of the following steps:

I. Insertion of a stiff guidewire into the abdominal aorta through the access of one femoral artery. The purpose of the guidewire is to straighten the occasionally very tortuous iliac arteries and to provide guidance for the introduction of further medical devices [87].

II. The SG delivery sheath, which contains the main body SG in a strongly crimped state, is pushed along the guidewire and positioned using fluoroscopy imaging.

III. Having reached the correct position slightly distal to the renal arteries, the SG delivery sheath is successively withdrawn and the self-expandable SG is deployed starting from the proximal end.

IV. A second guidewire is introduced through the contralateral iliac artery into the short limb of the main body SG.

V. A second delivery sheath containing the iliac leg SG component is pushed along the second guidewire and deployed inside the short limb of the main body SG with an overlap length to guarantee seal and fixation between the two modular SG components.

VI. After the deployment of the total iliac leg SG component, all devices other than the SG are removed.

All considered SG devices in this thesis are self-expandable SGs, i.e., the SGs expand on their own after the removal of the delivery sheath. Nevertheless, a molding balloon is used to improve the expansion of the SG and improve the SG-vessel attachment in the SG landing zones. After having established a leak-proof seal between SG and vessel at the proximal and distal landing zones, blood flows only through the SG (cf. Figure 1.2VI). As a consequence, the pulsatile load of blood flow and pressure is removed from the aneurysm wall.

1.1.2.2. Stent-grafts

Since the first EVAR in 1990, SG design has drastically improved over the last decades with the goal of decreasing SG related complication rates and the number of required secondary interventions. Nowadays, many different commercial SG devices exist. Most SGs are composed of a wire mesh (stent) which is attached to a polymeric fabric (graft) as shown in Figure 1.3.

Remark. *In the medical context, often the total prosthesis is denoted as "stent" or as "graft". In this thesis, the total prosthesis is denoted as "stent-graft" and the terms "stent" and "graft" only denote the single components of the SG.*

The graft serves as a conduit for the blood flow and excludes the arterial blood pressure from the aneurysm sac. The stent provides radial compression stiffness while not reducing the bending flexibility of the SG which is required in tortuous vessels [58]. Woven polyethylene terephthalate (PET) and expanded polytetrafluoroethylene (ePTFE) are common materials of grafts of commercial SG devices, whereas stent material is either stainless steel or nitinol which is a nickel-titanium alloy. Depending on whether the stent is attached on the outer graft surface or at the inner graft surface, the stent is denoted as exterior and interior, respectively. To be able to better determine the orientation of the SG on fluoroscopy images during EVAR and for better positioning of the SG, radiopaque markers are attached on the graft.

The stress-free stent diameters of many commercial SG devices are larger than the associated stress-free graft diameter. During the assembling process of SGs, stents are radially compressed and are fixed on the graft in this compressed state which leads to residual strains and stresses in the assembled SG. This predeformation has a positive effect on the buckling and kinking behavior of the SG. In the technical and computational context, this effect is named *stent predeformation* [106] or *stent preload* [228].

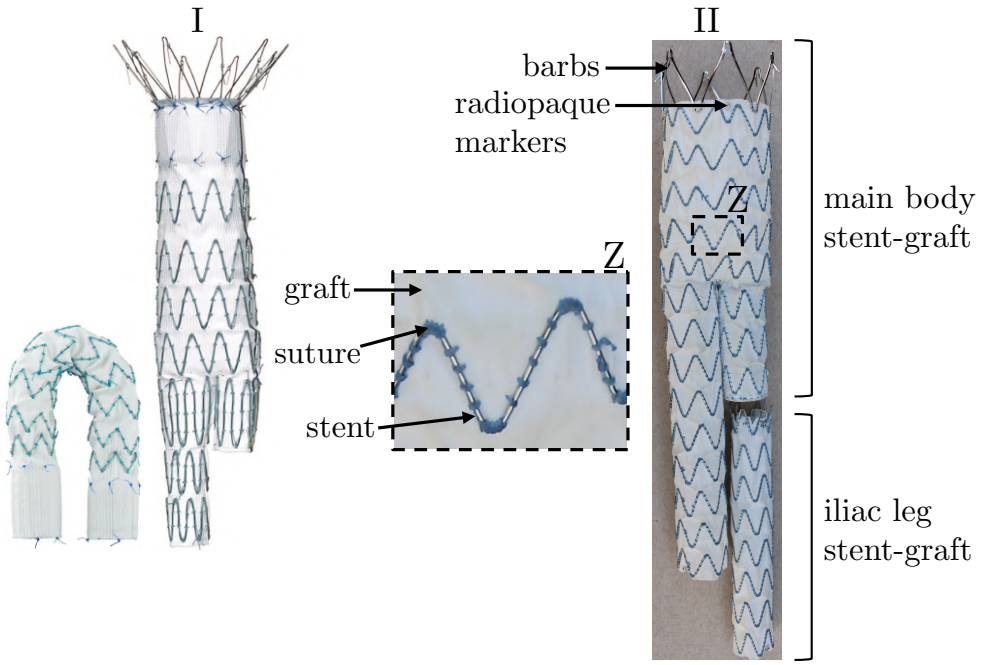

Figure 1.3 Commercial SG devices for treatment of AAAs: (I) Cook Zenith Flex/Spiral-Z® SG, figure reproduced with permission from [107]; (II) Medtronic Endurant™ II SG.

Standard SGs for EVAR are bifurcated, modular off-the-shelf SGs consisting of a main body SG that includes the bifurcation into the iliac limbs. Depending on the SG manufacturer, i.e., depending on the SG device, either one or two iliac leg SGs are used as iliac extension to the main body SG. All SG components, i.e., main body SG and iliac leg SGs, are mainly tubular shaped and SG manufacturers provide these products as off-the-shelf products in various different sizes. This modularity of commercial SGs allows to combine many different SG components to a semi-personalized product and even aortoiliac aneurysms can be treated by extension of the standard SG components by a branched iliac SG component [67].

In addition to the *passive fixation* of the SG by SG oversizing with respect to the vessel diameter, most commercial SG devices use *active fixation* by barbs. Depending on the location of barbs, one distinguishes between suprarenal and infrarenal active SG fixation [178]. In case of suprarenal fixation, the most proximal stent limb including barbs is not covered by a graft. Hence, this stent limb can be positioned at the branch-offs into the renal arteries without cutting off the renal arteries from blood supply.

The selection of the ideal SG is governed by patient-specific needs such as anatomic properties of the AAA and the proximal neck. This leads to the fact that there is no general “best” commercial SG. In the following only two of the most used commercial SG devices are briefly described. A more detailed overview of commercial SG devices is given for instance in [22, 49, 60, 68].

Cook Zenith Flex/Spiral-Z®

This modular Cook SG system (Cook Medical, Bloomington, Indiana, USA), cf. Figure 1.3I, is a combination of a bifurcated main body SG of type Cook Zenith Flex® and two iliac leg SG components of type Cook Zenith Spiral-Z®. The graft of Cook Zenith Flex® and Cook Zenith

Spiral-Z® SGs is made of woven PET. The Cook Zenith Flex® SG consists of several stainless steel stent rings, whereas the Cook Zenith Spiral-Z® SG consists of two stainless steel stent rings and one intermediate nitinol spiral shaped stent limb. The stent limbs are sutured to the fabric graft in a combination of interior and exterior stents. The most proximal stent ring of the Cook Zenith Flex® SG is not covered by the graft and includes barbs for suprarenal active fixation of the SG.

Medtronic Endurant™ II

The Medtronic Endurant™ II SG system (Medtronic Cardiovascular, Santa Rosa, California, USA), cf. Figure 1.3II, is a modular combination of one bifurcated main body SG and one docking iliac leg SG. Several nitinol stent rings are sutured on the outer graft surface of the woven PET graft. The most proximal stent ring of the main body SG is a bare stent ring, i.e., is not covered by the graft, and includes barbs for suprarenal active fixation.

1.1.2.3. Instructions for use and stent-graft sizing guidelines

Suitable anatomic properties of the aneurysm, the proximal neck and the iliac arteries are a prerequisite for successful application of EVAR. A *hostile neck*, i.e., a proximal neck with poor anatomic properties, is often associated with an increased likelihood of EVAR related complications. Short, angulated and conical proximal necks are frequently mentioned characteristics of a hostile neck [2, 8, 129, 134]. Moreover, the degree of proximal neck calcification and the degree of proximal neck thrombus are sometimes related to hostile necks [3, 194, 231, 275].

SG manufacturers express the limits of applicability of EVAR in corresponding IFU, which state anatomic limits for instance with respect to the aortic neck angle and neck length. The patient-specific anatomic properties are evaluated based on preinterventional CT data. Although the IFU are formulated in terms of hard, quantitative limits (e.g., a neck angle smaller than $60°$), the evaluation of the applicability of EVAR is strongly affected by subjective interpretations of the clinician. Even intentional treatment outside of the IFU is performed by many clinicians with reported positive outcomes (e.g., [40, 124, 152, 238, 268]). Hence, the question whether the formulation of the IFU should be weakened is an ongoing debate [124, 152, 268].

Correct sizing of SGs is one of the most challenging preinterventional tasks that requires an experienced clinician. The clinician has to determine the correct length and diameter of the modular SG components based on measurements using the preinterventional patient-specific CT data. Exceedingly long SGs might erroneously cover aortic side branches such as the internal iliac artery, whereas too short SGs might not be able to seal the aneurysm such that it is leak-proof.

To achieve a proper fixation of the SG and a leak-proof seal between SG and vessel in the landing zones, the SG is oversized with respect to the vessel diameter. The degree of SG oversizing o is defined by

$$o = \frac{D^{\mathrm{SG}}}{D^{\mathrm{Ao}}} - 1, \tag{1.1}$$

where D^{SG} is the diameter of the SG and D^{Ao} is the preinterventional diameter of the vessel at the location of the potential landing zone. The definition of the degree of SG oversizing is

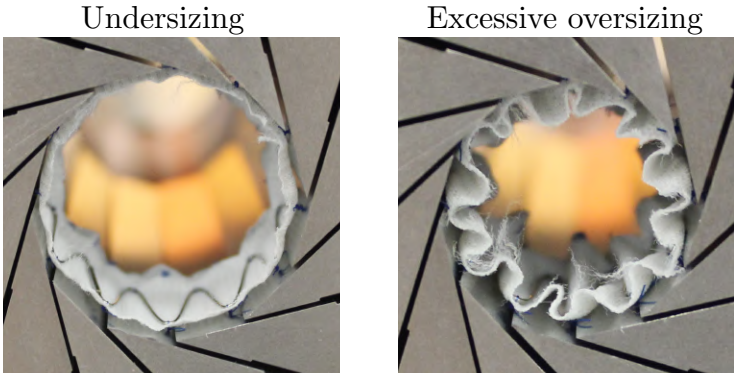

Figure 1.4 Visualization of the effects of SG undersizing and excessive SG oversizing for a SG segment of a Cook Zenith Flex® SG.

not unique in literature [257]. For instance, the IFU of Cook Zenith Flex/Spiral-Z® SGs request the measurement of the vessel diameter outer wall to outer wall, whereas the IFU of Medtronic Endurant™ II SGs demand an inner wall to inner wall measurement of the vessel diameter. Further, since the resolution of the preinterventional CT data is generally in the range of the vessel wall thickness, a clear distinction between inner wall to inner wall measurements and outer wall to outer wall measurements is not possible in clinical practice. Bearing in mind that the thickness of abdominal aortic walls and iliac artery walls is approximately $1-2\,\mathrm{mm}$ [219], this inconsistency can have a major impact on the degree of SG oversizing and therefore should be considered in any study related to the degree of SG oversizing [257]. Deterministic in-silico models have an unambiguous vessel wall thickness, i.e., outer wall to outer wall or inner wall to inner wall diameters can be measured precisely. Therefore, to be consistent, in this thesis the inner wall to inner wall diameter is used, i.e., D^{Ao} in Equation (1.1) denotes the preinterventional inner vessel wall diameter.

Contact pressure between the oversized SG and the aorta in combination with friction results in *passive fixation* of the SG. Some oversizing of the SG with respect to the vessel diameter is necessary to obtain an adequate seal and fixation of the SG in the proximal and distal landing zones [245, 257]. However, excessive SG oversizing might also lead to negative results such as excessive graft buckling and incomplete SG expansion [122, 136, 159] with poor sealing properties. Moreover, high stresses in the surrounding tissue associated with long-term complications of EVAR [197, 241] as described in detail in Section 1.1.2.4 are frequently mentioned negative results. Figure 1.4 visualizes the effects of a SG with insufficient SG oversizing (undersizing) and excessive SG oversizing with severe graft buckling. Consequently, the degree of SG oversizing is a major design variable of SGs that essentially contributes to the likelihood of EVAR related complications. The IFU of commercial SGs generally suggest an oversizing of $10-20\%$. However, there is no consensus with regard to the optimal degree of SG oversizing and even SG oversizing above 30% is practically used [182, 245, 257]. While Mohan et al. [182] report a significant decrease in EVAR related complications with increasing degree of SG oversizing, Sternbergh et al. [245] state that SG oversizing above 30% is associated with poor long-term SG fixation. Sincos et al. [241] strengthen these findings by studying histologic changes in the aortic wall of experimental porcine models after SG deployment of several SGs with different degree of SG oversizing. The study revealed structural disarrangements of the aortic wall as well

as a reduction of the supporting force by the aortic wall which was more pronounced for a large degree of SG oversizing.

1.1.2.4. Stent-graft related complications after EVAR

In this thesis, only SG device related complications are considered. These complications can be seen as of mechanical origin. They are the consequence of the complex mechanical interaction between vessel, SG, blood flow and pressure. Other procedure related complications are beyond the scope of this thesis.

The total likelihood of EVAR related complications is reported to be 46% after 8 years (EVAR trial 1, [30]). Only few of them are imminently life-threatening. Thus, not every SG related complication requires immediate reintervention. Most of them are related to the failure of proper AAA protection by the SG, which generally goes hand in hand with the reenlargement of the AAA, ongoing aneurysm growth and the reemergence of the AAA rupture risk. Depending on the complication type, EVAR related complications are treated by endovascular techniques, conversion to open repair or other techniques. In the following the most frequently reported EVAR related complications are briefly described.

Endoleak

An endoleak is the most frequently mentioned reason for secondary interventions after EVAR. In general, an endoleak is defined as the persistent perfusion of the aneurysm sac after EVAR. General discussions on endoleaks and their treatment are provided for instance in [71, 93, 97, 111]. According to the location and type of leakage, endoleaks have been classified into four different endoleak types:

- *Type I endoleak* [194, 231]: Type I endoleaks occur when a gap between SG and vessel in the proximal landing zone (type Ia) or the distal landing zone (type Ib) allows blood to flow into the aneurysm sac. Type I endoleaks can have many reasons. Among others, frequently stated reasons are unsuitable vessel geometry, migration of the SG, SG infolding or a change of the sealing zone due to growth and remodeling of the vessel.

- *Type II endoleak* [171, 239]: Type II endoleaks correspond to perfusion of the AAA sac by retrograde blood flow from small arterial side branches within the aneurysm such as in most cases the lumbar arteries or inferior mesenteric arteries, but also in rare cases the sacral, gonadal or accessory renal artery. There is only poor understanding of predictive factors of the formation of type II endoleaks [171]. It is the most common endoleak type [239], but it only requires intervention, when associated with aneurysm sac growth.

- *Type III endoleak* [29, 169]: Type III endoleaks describe the leakage between modular SG components or through defects of fractured SGs.

- *Type IV endoleak* [48]: A type IV endoleak is a leakage through the graft due to graft porosity. Type IV endoleaks were primarily seen in first-generation SGs. In modern SGs with enhanced graft material, type IV endoleaks are extremely rare.

In addition to the four endoleak types, continued AAA expansion without identifiable leakage sometimes is denoted as *type V endoleak* or *endotension*. Type I and III endoleaks are the most dangerous ones, because they are expected to apply a high pressure on the aneurysm sac and hence enlarge the rupture risk tremendously, whereas Type II endoleaks have only a small impact on the aneurysm sac [269].

Stent-graft migration

Pulsatile blood flow and pressure exerts a permanent displacement force onto the deployed SG. In combination with poor fixation of the SG, this may lead to movement of the SG called SG migration [47, 215, 251, 277]. By introduction of fixation barbs in modern SG devices, the risk of SG migration has been strongly reduced [33].

Aortic neck dilatation

Aortic neck dilatation defines the enlargement of the aorta in the proximal landing zone after EVAR. Dilatation of the aortic neck affects the SG fixation and the sealing between SG and aorta and therefore can trigger SG migration or an endoleak type Ia. Two phenomena must be differentiated: (i) immediate postimplant dilatation [232], which is an instant enlargement of the aortic neck due to the radial force exerted by the oversized SG and (ii) aortic neck enlargement due to long-term changes of the aortic neck such as growth and remodeling. In the context of this thesis, the term *aortic neck dilatation* is referred to the long-term enlargement of the aortic neck which is explained by two different phenomena. First, Palombo et al. [197] and Simon-Kupilik et al. [240] concluded that aortic neck dilatation is the result of a growth and remodeling process of the originally "healthy" abdominal aortic wall which is driven by changes of the aortic tissue in the SG landing zone such as increased wall stresses. Second, other researchers claim that aortic neck dilatation is the result of the continuation of the aneurysm disease process [62, 234]. Both, phenomena are widely discussed in the literature but without full agreement regarding the major source of aortic neck dilatation [47, 142, 256, 257].

Stent-graft fracture

Both stent fracture [127, 246] and fabric tear [38, 127] have been widely reported as SG defects associated with subsequent SG migration or type III endoleak. Mostly, the SG fracture is the result of fatigue loading due to pulsatile blood flow and pressure in combination with high strains and stresses in the SG due to the large deformation of the SG in the deployed state [47].

Stent-graft kinking

Insufficient flexibility of the SG can lead to SG kinking [43, 167, 168] especially within tortuous iliac arteries which in turn may cause limb occlusion associated with ischemic complications. Moreover, SG kinking induces irregular blood flow and can induce local thrombosis formation [47].

Ischemic complications

Occlusion of aortic side branches after EVAR can include colonic, renal, and pelvic ischemia [168]. Renal ischemia mostly arises immediately after EVAR or even during the intervention as a result of SG misplacement leading to coverage of one or both renal arteries [26, 104]. Pelvic ischemia immediately after EVAR mostly is associated with wrong sizing of the length of a iliac SG limb and/or SG misplacement of the iliac SG limb such that the SG covers the bifurcation of the common iliac artery into the external and internal iliac arteries [168]. Several years after EVAR, ischemic complications can arise as a result of SG kinking and graft thrombosis formation or as a result of SG migration and subsequent coverage of aortic side branches [43, 167].

Aortic compliance mismatch

Arterial compliance is defined as the ratio of change in arterial blood volume to change in arterial blood pressure. It is well known that the insertion of a SG reduces the local compliance in the region of the SG generally denoted as aortic compliance mismatch. This may have negative effects such as increased pressure wave reflection, decreased distal perfusion and increased pulsatile stresses and vessel distension of the vessel at the interface between the native, compliant vessel and the SG with reduced compliance [64, 240, 242, 255]. The latter effect of increased pulsatile vessel stresses and vessel distension is mentioned as main initiator of aortic neck dilatation by some studies [64, 240]. Although the effect of aortic compliance mismatch on the cardiovascular system may be much smaller in case of EVAR than in case of TEVAR, aortic compliance mismatch induced by abdominal aortic SGs is also a current area of research [130, 248, 255].

The likelihood of the single complications slightly varies between the clinical trials such as the EVAR trial 1 and the DREAM trial (cf. Section 1.1.1). According to the EVAR trial 1 [30], eight years after the intervention the most frequent complication was type II endoleak (25% of all EVAR patients), followed by type I endoleak (9.9%). Further, it has to be noted that in clinical practice the reason of reintervention often is a combination of many of the above listed EVAR related complications. For example, severe SG migration goes mostly hand in hand with a type I endoleak.

1.2. Medical challenges and motivation of in-silico EVAR

The complication-free use of EVAR requires an individual adaptation of the preinterventional planning to the patient-specific needs such as the selection of a SG device that perfectly suits the vessel geometry. The currently available preinterventional planning tools are limited to the IFU of SG manufacturers as well as measuring tools of medical imaging software. The use of patient-specific computational models or 3D-printed ex-vivo models is still the exception in clinical practice. To improve the patient-specific, preinterventional planning phase on the way toward a more personalized medicine, in-silico EVAR can be applied as objective, predictive tool in five respects:

- **Assessment of EVAR complication likelihoods**
  The prediction of the complication likelihood based solely on currently available preinterventional planning tools is very challenging. In-silico EVAR can predict the postinterventional state of SG and patient-specific vessel under physiological conditions. It provides mechanical insight into the deployed configuration, such as vessel and SG stresses as well as contact tractions between SG and vessel. Thus, it can number the potential likelihood of SG related complications and assist the clinician in the decision whether EVAR is suitable or not.

- **Assistance in SG device selection**
  The risk of SG related complications is affected by the device choice [206, 251, 264] as not all commercial SGs fit to a specific vessel geometry to the same extent. In-silico EVAR models can be used to predict the outcome for several different commercial SG devices for the same patient, allowing a comparison of predicted outcomes. Hence, in-silico EVAR models could assist the clinician in the choice of the SG from a large portfolio of commercially available SG devices from different SG manufacturers.

- **Assistance in SG sizing**
  Correct sizing of the SG (length and diameter) is a challenging preinterventional task. Since the "ideal" amount of SG oversizing for a patient-specific case depends on various factors, such as the shape of the vessel and the degree of vessel calcification, it is difficult to estimate only from information obtained from preinterventional CT data. In-silico EVAR models can provide a predictive comparison of different SG sizes for the same patient and compare the quality of the outcome. Thus, the use of in-silico EVAR can improve the SG sizing process in the preinterventional planning phase, both with respect to SG length as well as SG diameter.

- **What-if predictions**
  The medical EVAR intervention is subject to certain intrainterventional uncertainties such as the accuracy of SG positioning due to limited resolution of intrainterventional medical imaging and pulsatile forces acting on the SG resulting from the blood flow. Already in the preinterventional planning phase, in-silico EVAR could be used to assess the outcome if such an adverse event like SG misplacement occurs during EVAR.

- **Predictive comparison of specific types of EVAR**
  Especially in complex vessel geometries, predictive in-silico EVAR can be used to compare different types of EVAR, such as FEVAR and CHEVAR, with respect to their feasibility and long-term performance.

Besides the main objective of minimizing the complication likelihood by patient-specific in-silico predictions, in-silico EVAR models can further contribute to the advancement of EVAR as a tool for education [180, 259, 260]. Furthermore, the additional mechanical information of SG and vessel obtained by in-silico EVAR can help to clarify the occurrence of some complications after EVAR that are not yet fully understood, such as aortic neck dilatation. An ongoing area of research is the permanent improvement of SGs. In-silico EVAR can be a valuable tool in the development of optimized SG designs that are able to reduce the complication likelihood after

EVAR and that are able to expand the applicability of EVAR to patients with very challenging anatomy of the abdominal aorta.

1.3. Existing in-silico and experimental studies related to EVAR

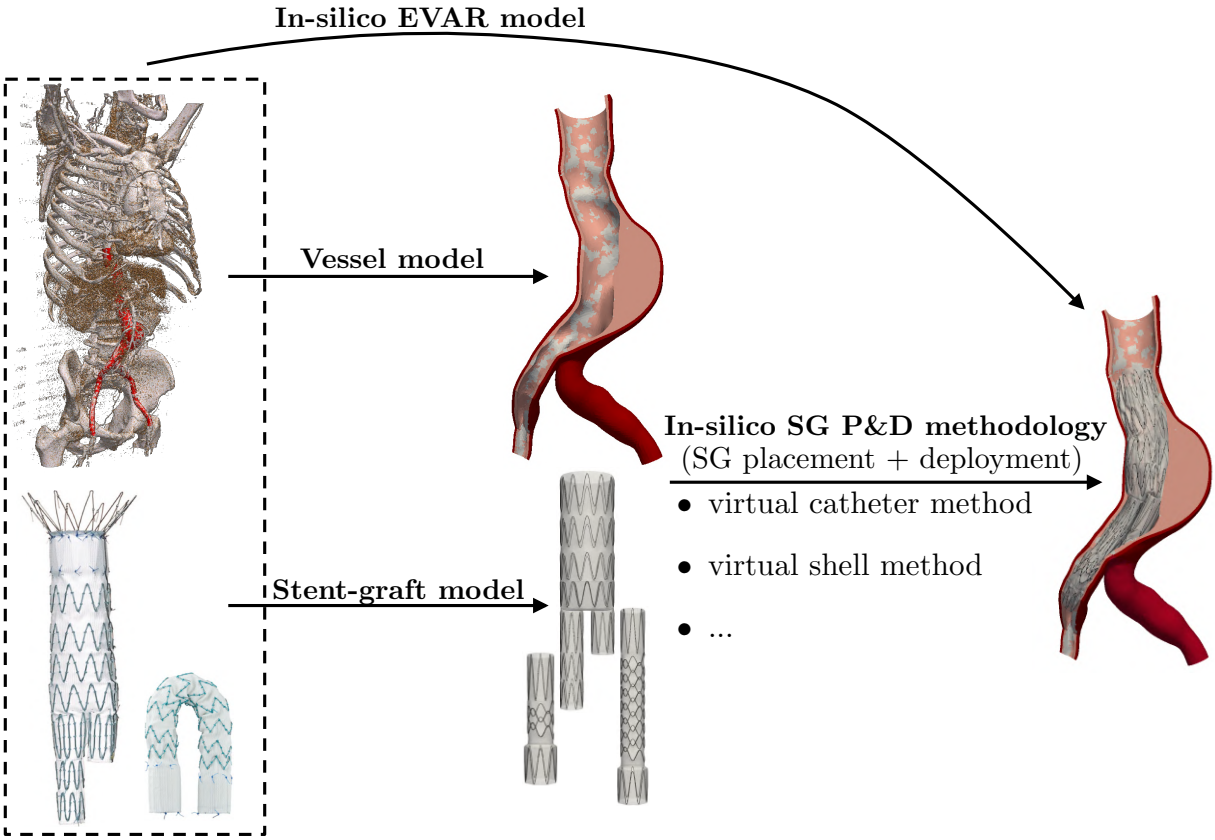

Figure 1.5 Visualization of the three modeling aspects of in-silico EVAR models: vessel model, SG model and in-silico SG P&D methodology. Portions of the figure are taken with permission from [107].

In this thesis, the *in-silico EVAR model* is defined as computational model to predict the postinterventional configuration (cf. *Definition of terms* on page xxi). It is not designed to extensively reproduce all steps of the EVAR procedure as stated in Section 1.1.2.1, but only the results of the postinterventional configuration are of elevated interest. Therefore, the considered in-silico EVAR models cannot be applied to obtain intrainterventional results.

The in-silico EVAR model incorporates three different modeling aspects (cf. Figure 1.5): (i) the *vessel model*, (ii) the *SG model* and (iii) the *in-silico SG placement and deployment (P&D) methodology* which defines all virtual steps from a given SG model and a given vessel model to the final postinterventional configuration. Hence, the in-silico EVAR model is subject to simplifications and assumptions associated with the vessel model, the SG model and the in-silico SG P&D methodology.

The vessel model defines the abstraction of a patient-specific computational model from preinterventional CT data. In the context of this thesis, the term *vessel* is used as collective term, which includes parts of the "healthy" abdominal aorta, the "aneurysmatic" dilated part of the abdominal aorta, intraluminal thrombus (ILT) and calcifications. The SG model is a computational model to approximate the mechanical behavior of different commercial SG devices.

The virtual steps of the in-silico SG P&D methodology classically include the steps *in-silico SG placement* and *in-silico SG deployment*. In-silico SG placement defines the virtual step of positioning the SG within the vessel. In-silico SG deployment defines all virtual steps subsequent to the in-silico SG placement, i.e., the processes that let the SG freely deform within the vessel.

The following literature overview is subdivided into the three modeling aspects as visualized in Figure 1.5. In Section 1.3.1, an overview of existing vessel models of infrarenal AAAs is given. Section 1.3.2 provides an overview of existing experimental and in-silico studies on SG mechanics. Existing in-silico SG P&D methodologies are reviewed in Section 1.3.3. Finally, in Section 1.3.4, applications of in-silico EVAR models are stated and their results are summarized. An overview of all three modeling aspects and applications of in-silico EVAR models can also be found in the review by Roy et al. [227] as well as in the theses by Perrin [204] and De Bock [49].

1.3.1. Vessel modeling

Several studies have already been conducted in the field of patient-specific AAA modeling to assess the rupture risk based on AAA wall stress and strength. Since the first finite element based studies of AAA rupture risk assessment [76, 126, 217], model complexity has drastically increased. In more recent studies, calcifications and ILT had been included into the AAA model and a significant impact on AAA wall stresses could be shown [17, 162, 208, 221]. Vessel prestressing methodologies (e.g., [83, 160]) that reconstruct non-stress-free vessel configurations of patient-specific in-vivo medical imaging further improved the rupture risk assessment of AAAs.

The vessel models for AAA rupture risk assessment mainly focus on the mechanical behavior of the AAA. The "healthy" vessel parts, i.e., the proximal neck and the iliac arteries, are either not part of the model [154, 217] or are modeled by the same material model and model parameters for the vessel wall as the AAA wall [76, 162]. In the context of in-silico EVAR, besides sophisticated modeling of the AAA, also realistic modeling of the "healthy" vessel parts is of major importance since many EVAR related complications are associated with these parts of the vessel. Using one equivalent material model for the "healthy" and the "aneurysmatic" vessel wall leads to wrong estimations of the vessel deformation and vessel wall stresses since substantial differences in the material behavior of "healthy" aortic walls and AAA walls can be identified [192].

However, to reduce complexity most in-silico EVAR studies use either rigid wall assumptions [9, 224, 225] or use simplified linearized material models [53, 205, 207]. None of the available in-silico EVAR studies uses vessel wall models that incorporate state of the art models of the "healthy" vessel wall [80, 102, 118] and state of the art models of the AAA wall [192, 219]. Furthermore, calcifications, ILT, vessel prestressing and the application of physiological blood pressure states are mainly neglected.

Remark. *The location of interest includes "aneurysmatic" parts as well as "healthy" parts of the blood vessels. Hence, throughout this thesis, it is distinguished between the terms "AAA (model)" and "vessel (model)". The term "AAA (model)" only refers to the "aneurysmatic", dilated part of the abdominal aorta whereas the term "vessel (model)" defines all parts of the blood vessel in the location of interest, i.e., "aneurysmatic" and "healthy" parts of the blood vessel as well as ILT and calcifications.*

The in-silico EVAR study with the most elaborated vessel model was presented in the thesis by De Bock [49]. Similar to recent studies investigating the AAA rupture risk, ILT and calcifications were considered in addition to the vessel wall. This pioneering study highlighted the mechanical impact of stiff calcifications on the deployment of the SG. However, this study was limited to only one patient-specific case. Disregard of vessel prestressing and the blood pressure state are further limitations of this study, which make reasonable stress measurements in the vessel tissue impossible.

Constitutive modeling of vessel constituents has made enormous progress during the last decades. Present constitutive models of the "healthy" aortic wall are the so-called two-fiber [80, 116, 118] and four-fiber models [74, 222], which consider the hyperelastic and anisotropic mechanical behavior. In AAA walls, anisotropy is less pronounced and isotropy is a widely used model assumption [87, 163, 217]. Several experimental and numerical studies on the mechanical behavior of ILT and vessel calcifications were published. Mostly, hyperelastic and isotropic mechanical behavior of ILT is assumed in the constitutive models [81, 258, 270]. Isotropic and almost linear material behavior mostly is stated for vessel calcifications (e.g., [162, 172]). For a detailed summary of the state of the art modeling approaches of AAAs in the context of rupture risk assessment and an extensive overview on constitutive models of vessel constituents of AAAs, the interested reader is referred to the thesis by Maier [164].

1.3.2. Stent-graft modeling

For the sake of simplicity, *homogenous SG models* (e.g., [75, 120, 156, 187, 189]) were used as a first approach in a large number of in-silico studies. These homogenous SG models do not differentiate between stent and graft, but rather model the SG as simple tubular structure with one identical material. Since the metallic stent and the membranous graft are geometrically and mechanically very different components, these homogenous SG models cannot reproduce the realistic mechanical behavior of SGs [60].

The first study on realistic *multi-material SG models*, which considered stent and graft as separate components, was performed by Kleinstreuer et al. [139]. Kleinstreuer et al. investigated stent stresses of a SG with a diamond shaped nitinol stent under cyclic loading. This pioneering study was limited by the fact that only straight SG configurations subjected to internal pressure loading were investigated and that the used SG models did not mimic specific commercial devices. The first large in-silico studies of several commercial SG devices were provided by Demanget et al. [57–60]. Demanget et al. used elaborated multi-material SG models to compare the bending behavior of eight different commercial SGs. They were the first who performed extensive experimental and numerical testings on graft samples of commercial abdominal SGs and proposed an in-plane orthotropic elastic model for woven PET grafts. More recently, Roy et al. [228] experimentally and numerically investigated the behavior of Cook Zenith Flex® SGs and fitted the

graft material behavior of this specific SG device to the same constitutive model. Despite the inherent anisotropic material behavior of woven PET, isotropic material models are frequently applied with reasonable results [9, 139, 225]. A frequently used material model of nitinol in stent models, that considers the phase transformation between the austenitic and the martensitic phase associated with this type of alloy, is provided by Auricchio et al. in a series of publications [10–12]. This model was applied to a large number of SG models (e.g., [9, 139, 205]). For a more extensive review of the mechanical properties of nitinol as a shape memory alloy and its modeling approaches, the reader is referred to the book of Lagoudas [146]. Recently, Perrin et al. [204, 207] stated that nitinol remains in its austenitic phase during SG deployment simulations which do not model the full crimping process of the SG inside its delivery sheath. Hence, to reduce complexity, the constitutive behavior of nitinol was modeled by a purely elastic model without phase transformation. The fixation of the stent on the graft (mostly by suture) generally is modeled by tie constraints [58, 228], which neglect the slight slippage that mostly is possible between stent and graft. Since multi-material SG models can be computationally very expensive, reduced SG models that are still able to reproduce realistic mechanical behavior of the SG, are the focus of current research [4].

In early stages of multi-material SG models, stent predeformation was rarely considered. In recent years, some computational approaches to consider stent predeformation were proposed. In a SG assembly simulation, Demanget et al. [59] applied an artificial pressure on the internal graft surface to increase the graft diameter to the larger diameter of the stent rings. A contact constraint between stent and graft prevented penetration of those two components. Once stent and graft were in contact, a tie constraint was applied between stent and graft and the artificial pressure was removed. Drawback of this very practical approach to stent predeformation is that this approach requires an additional assembly simulation prior to the actual EVAR simulation. In another study [60], Demanget et al. developed a mechanically sophisticated SG assembling strategy for Anaconda$^{\text{TM}}$ SGs (Vascutek, Inchinnan, UK) which considered the predeformed stent configuration of this specific type of commercial SG. Roy et al. [228] developed a rule of thumb for the consideration of stent predeformation of Cook Zenith Flex® SGs. In their study, the Young's modulus of the stent was augmented by a factor of 2 to consider the effect of stent predeformation. This rule of thumb required mechanical tests for calibration and was based on the assumption of a linear relationship between radial force and diameter reduction of stents. More recently, an assembly simulation of stent and graft was used to consider stent predeformation in a customized SG of the aortic arch [61]. In this SG assembly simulation, the oversized stent rings were radially compressed by a rigid cylinder until they are in contact with the graft. In this configuration, tied contact was assigned between stent and graft. Afterwards, static mechanical equilibrium of the assembled SG model was sought.

Besides in-silico studies, mechanics of SGs have been investigated in numerous experimental studies with very different objectives. The radial force of thoracic [173] and abdominal aortic SGs [52] during SG compression was measured using radial force testing machines. Other experimental studies investigated the pull-out force of SGs [82, 143, 177], i.e., the axial force that is required to dislocate the SG from the landing zone. For instance, Kratzberg et al. [143] concluded that SG oversizing above 30% leads to a reduced pull-out force due to an increased likelihood of stent collapse[1]. This means that SG oversizing above 30% is associated with worse SG fixation

[1] In the medical context, stent collapse often is denoted as *SG infolding* [135, 247].

according to their experimental study. The SG drag force, i.e., the force that is exerted onto the SG by the blood flow and pressure and which tends to dislocate the SG, was experimentally studied for a bifurcated SG by Corbett et al. [45]. In [226], Roos et al. experimentally analyzed the SG drag force under pulsatile blood flow. They concluded that the SG drag force increases with rising blood pressure and rising SG angulation. Using imaging and mechanical testing, Lin et al. [159] investigated the folding behavior of abdominal aortic SGs with respect to the degree of SG oversizing and the shape of the proximal barbs. Lin et al. concluded that excessive SG oversizing of more than 30% is very likely associated with adverse results such as SG infolding and a reduced seal quality.

1.3.3. In-silico SG P&D methodologies

Since the results of intrainterventional steps are not of interest for the considered type of in-silico EVAR studies, the intrainterventional steps can be simplified as long as the final postinterventional configuration of SG and vessel is not substantially influenced by these simplifications. Consequently, the following in-silico SG P&D methodologies do not aim at representing the real-world intrainterventional steps of EVAR. Instead, in-silico SG P&D methodologies are computational approaches to efficiently place and deploy the SG model in the vessel model. As a further simplification, these in-silico SG P&D methodologies neglect blood flow, but treat the EVAR procedure as purely solid mechanical problem. The existing in-silico SG P&D methodologies can be roughly subdivided into two different methodologies, which in the context of this thesis are denoted as the *virtual catheter method* and the *virtual shell method*.

Virtual catheter method

Several in-silico deployment studies of self-expandable pure stents (i.e., without graft) have been published within the last decade (e.g., [13, 50, 117, 121, 122, 188, 191]). These can be seen as pioneering work for in-silico SG P&D methodologies. The computational consideration of SG deployment is much more complex than the deployment of a pure stent mainly due to the challenging modeling of the membranous graft that is subjected to severe buckling during the SG placement and deployment. Nevertheless, since the medical procedures of pure stent deployment and EVAR are very similar, many in-silico EVAR studies [9, 51, 53, 206, 225] have adopted the in-silico SG P&D methodology from pure stent deployment simulations. This methodology was first applied to SGs for aneurysm repair by Auricchio et al. [9]. It is denoted as *virtual catheter method* in the context of this thesis and is visualized in Figure 1.6 for the treatment of an ascending aortic pseudoaneurysm by an endovascular SG. In addition to the vessel model and the SG model, this in-silico SG P&D methodology requires modeling of a cylindrical delivery catheter (white sheath in Figure 1.6), which is mostly modeled by 2D surface elements and whose deformation is fully prescribed. The virtual catheter is used to radially crimp and position the SG onto the preinterventional vessel centerline. During this SG placement step, contact constraints between the virtual catheter and the SG force the SG to remain inside the virtual catheter. Afterwards, additional contact constraints between SG and luminal vessel surface are activated. The diameter of the virtual catheter is gradually enlarged until the SG is not in contact with the virtual catheter anymore but solely in contact with the vessel (see SG deployment in Figure 1.6).

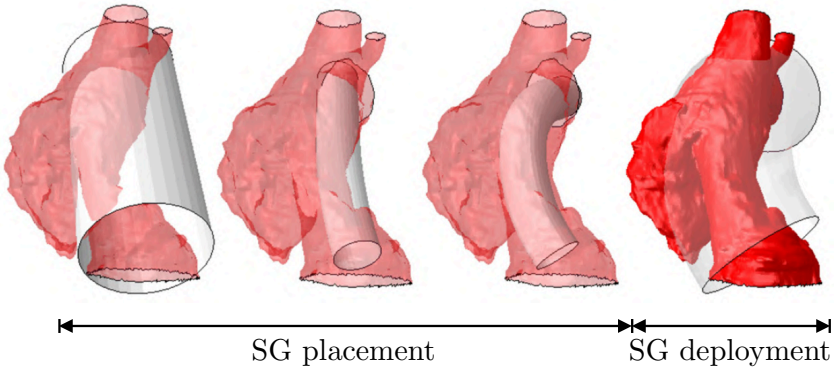

Figure 1.6 In-silico EVAR based on the virtual catheter method applied to a patient-specific ascending aortic pseudoaneurysm. Virtual catheter (white) and pseudoaneurysm (red). The SG is not visible in this figure. Reproduced with permission from [9], copyright Elsevier.

In [49] and [224], the virtual catheter method was extended by consideration of the deployment direction of the SG, i.e., the enlargement of the virtual catheter is started at the proximal side and ends at the distal side. In addition, in the thesis by De Bock [49], the virtual catheter method was extended for a bifurcated AAA SG, necessitating multiple virtual catheters.

A major challenge of the virtual catheter method is the numerical complexity arising from the high degree of SG buckling during radial crimping in the SG placement process, i.e., during a process whose results are not of interest for the considered in-silico EVAR studies. The numerical complexity of radial crimping is less pronounced for pure stents, for which the methodology was initially intended, since in these simulations no complex graft buckling exists. Hence, the virtual catheter method has proven itself as a robust and efficient methodology for the placement and deployment of pure stents. However, when applied to EVAR it may not be the most elegant method.

Virtual shell method

Perrin et al. [204, 205] developed a different in-silico SG P&D methodology in which a clear separation between SG placement and deployment is difficult. The in-silico SG P&D methodology is denoted as *virtual shell method* in the context of this thesis and is visualized in Figure 1.7. In this methodology, a virtual tubular shell, whose diameter is slightly larger than the diameter of the SG, is placed around the SG. Using proper prescribed displacement constraints on the nodes of the virtual shell, it is mapped onto the luminal vessel wall surface of the patient's preinterventional vessel geometry. Frictional contact constraints force the SG to remain inside the virtual shell during this deformation process of the virtual shell and gradually deform the SG. Until this step, the virtual shell does not represent any mechanical behavior, but is solely used as a prescribed geometrical constraint. Afterwards, vessel wall material properties are assigned to the virtual shell, which from this step on acts as vessel wall, allowing the vessel wall to deform elastically until static mechanical equilibrium is reached. The virtual shell method requires a robust morphing algorithm [94, 204] that governs the deformation of the virtual shell. This morphing algorithm will be reviewed in Section 3.2.1. The virtual shell method has been successfully applied to bifurcated SGs to treat AAAs [205, 207]. Recently, this in-silico SG P&D

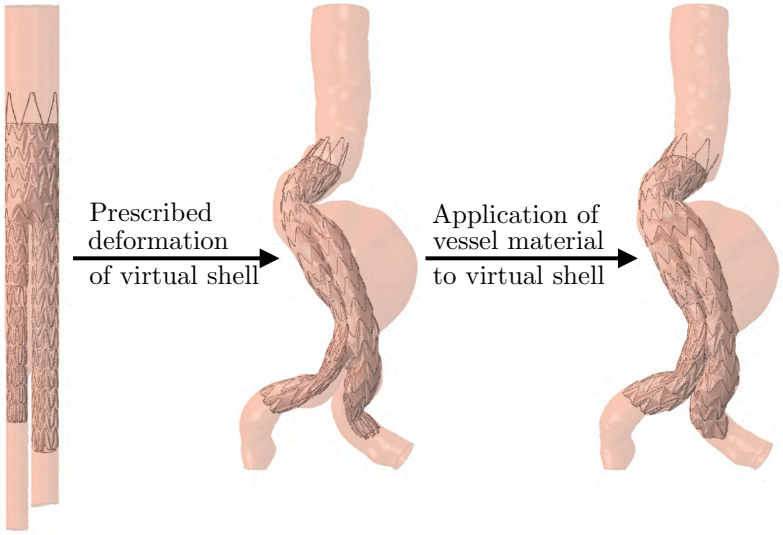

Figure 1.7 In-silico EVAR based on the virtual shell method applied to a patient-specific AAA. The virtual shell (red) is smoothly morphed from the cylindrical shape to the shape of the patient-specific preinterventional vessel. Modified figure reproduced with permission from [205], copyright Elsevier.

methodology was extended to the deployment of a double branched SG for the treatment of an aortic arch aneurysm [61].

Although the virtual shell method circumvents the numerical complexity arising from the radial crimping process of the SG, during the deformation of the virtual shell the SG still undergoes a complex deformation process with severe buckling and complex contact interaction between SG and vessel.

Other in-silico SG P&D methodologies

The only in-silico SG P&D methodology that avoids the high degree of complexity encountered during crimping and placement of the SG was published by Prasad et al. [212]. In this in-silico SG P&D methodology, first the SG model is moved to the vessel centerline without deforming the straight SG model. Afterwards, the vessel is inflated by an unphysiological pressure increase to make room for the SG. As soon as the SG is fully inside the vessel, contact constraints between vessel and SG are activated and the artificial pressure is removed again. This computationally very simple approach is however restricted to simple vessel geometries and not applicable to patient-specific cases with diverse geometric characteristics.

1.3.4. Applications of in-silico EVAR models

Many studies have already been published using in-silico EVAR models to approximate the final deployed SG configuration in idealized vessel geometries (e.g., [51, 53, 206, 212]). However, only few patient-specific in-silico EVAR studies exist [9, 61, 205, 207, 224, 225] most of which are restricted to strong simplifications with respect to the vessel model (cf. Section 1.3.1). In

the following, different applications of in-silico EVAR models in idealized and patient-specific vessel geometries are reviewed.

In [9, 61, 205, 207], patient-specific cases were considered and the comparison between simulation results and real-world postinterventional CT data was used as validation of the computational models. In a simple but pioneering study, Auricchio et al. [9] were the first who validated an in-silico EVAR model by postinterventional CT data. The most comprehensive validation study was performed by Perrin et al. for three patient-specific cases of Medtronic Endurant™ II SGs [205] and three Anaconda™ SGs [207]. A complex model of the SG, but a relatively simple model of the patient-specific vessel led to good agreement between simulation results and real-world postinterventional CT data in these studies. A more detailed review of validation methodologies and validation studies of in-silico EVAR models will be provided in Chapter 4.

In [206], Perrin et al. studied the mechanical performance of five commercial iliac leg SG components in idealized vessel geometries. Their numerical study highlighted the difference in the outcomes among the five commercial devices. While for some commercial devices large gaps between SG and vessel wall in the landing zone could be identified, other SG devices showed good SG-vessel attachment even for highly angulated vessels.

Altnji et al. [6, 7] performed a small parameter study in a thoracic aneurysm geometry with respect to the likelihood of SG migration. They concluded that the neck angle, the length of the landing zone and the degree of SG oversizing have the most crucial impact on SG migration. However, rather strong simplifications were used in the studies by Altnji et al. [6, 7], such as neglecting the graft.

De Bock et al. [53] performed a parameter study, where they varied vessel parameters, SG position and the degree of SG oversizing in an idealized tube-shaped vessel geometry. Assessment of the deployed SG configuration confirmed the impact of the vessel stiffness on the SG expansion. In stiffer vessels (e.g., due to vessel calcifications) the deployed SG lead to less diameter increase under the radial forces of the stent, which implies that the effective degree of SG oversizing in the deployed state is larger when considering the deformed vessel diameter. Further results of this comprehensive parameter study are the increased risk of SG kinking and the beneficial effect of high SG oversizing in highly angulated vessel geometries. This finding is in accordance with the study by Prasad et al. [212], where a combined framework of purely solid mechanical SG deployment and computational fluid dynamics (CFD) to consider realistic in-vivo loading conditions was used. Prasad et al. [212] showed that an increase in the degree of SG oversizing can improve the positional stability of the SG. Senf et al. [237] numerically investigated the impact of the degree of SG oversizing on the fixation force between SG and vessel under consideration of different blood pressures as well as different material properties of vessel, plaque and stent. This parameter study was performed considering the deployment of one stent ring of an Anaconda™ SG without modeling of the graft in a straight hyperelastic vessel. Despite this very simplified numerical setting, Senf et al. [237] could show that besides the degree of SG oversizing, the vessel material properties as well as the presence of plaque have an influence on the fixation force between stent and vessel. A difference of 29% in the fixation force was obtained when opposing a hyperelastic and a linear elastic vessel model. Furthermore, the study by Senf et al. [237] showed that the fixation force increases when raising the degree of SG oversizing. The maximum fixation force for the Anaconda™ stent ring was obtained for a SG oversizing in the range $20\% - 24\%$.

One step further toward the application of in-silico EVAR models in clinical practice was presented by von Sachsen et al. [264]. They proposed a medical visualization and planning tool to assess the SG fixation force. However, von Sachsen et al. [264] rather focused on developing an interface that is easily understandable by clinicians than on precise modeling of the mechanics of SG and vessel as well as their interaction. Despite of strong model assumptions, such as negligence of the graft and the use of a rigid vessel wall, this study showed how a clinical software could be designed to assist clinicians in the preinterventional planning of EVAR.

Recently, Romarowski et al. [224] demonstrated how in-silico EVAR models can improve the SG device selection in clinical practice. To this end, they qualitatively compared the in-silico EVAR outcome of two commercial tube SGs and one customized tube SG deployed in a patient-specific ascending aortic pseudoaneurysm. Further, by comparison of the commercial off-the-shelf SGs to the customized SG device, this study encourages the development of customized SG devices for challenging vessel geometries where off-the-shelf SG devices cannot be used.

For the sake of completeness, other objectives of in-silico approaches in the field of EVAR than predicting the postinterventional state are mentioned in the following. Another area of research related to EVAR where in-silico approaches are used, is the determination of vessel deformations due to the insertion of stiff guidewires prior to the SG deployment [66, 87, 88, 131, 181]. The investigation of changes in postinterventional blood flow is another area of research that is worth mentioning. These studies utilize CFD simulations [14, 75, 120, 190, 225] or fluid-structure-interaction (FSI) simulations [79, 128, 148, 157, 187] to simulate postinterventional blood flow through the AAA with SG. Apart from investigations of the blood flow, these studies mostly come to the conclusion that blood pressure related tractions are magnitudes larger than blood flow related tractions [120, 157]. Therefore, purely solid approaches, which neglect the blood flow, but consider the blood pressure, may be sufficient for the majority of investigations.

1.4. Objectives

This thesis provides essential steps toward the use of in-silico EVAR models to assist clinicians in clinical practice. In particular, based on medical needs stated in Section 1.2 and available studies reviewed in Section 1.3, this thesis focuses on the following three major objectives:

- **Development of a predictive, patient-specific in-silico EVAR model**
  In-silico EVAR models, as defined in the context of this thesis, aim at predicting the final postinterventional configuration of SG and vessel rather than accurately reproducing all steps of the EVAR procedure. These models can improve the preinterventional planning of EVAR for patient-specific cases and serve as valuable tool in clinical research and clinical education. However, most of the available in-silico EVAR models are restricted to severe simplifications especially with respect to the vessel model that limit the scope of application.

  A major objective of this thesis is to improve available in-silico EVAR models with respect to the vessel model. To this end, a patient-specific vessel model is proposed, which incorporates nonlinear state of the art material models of ILT, calcifications, “healthy” aortic wall and AAA wall. Further, the proposed model takes vessel prestressing and physiologically meaningful blood pressure states into account. Moreover, a newly developed stent

predeformation methodology is used for fully resolved SG models of bifurcated, commercial SG devices. This methodology accounts for residual strains and stresses that arise from the SG assembly process and which exist in most commercial SG devices. A novel in-silico SG P&D methodology is proposed, that is applicable to bifurcated, patient-specific SG and vessel models. It is based on the consistent reduction in computational complexity of modeling the intrainterventional steps of EVAR without substantially changing the results of the final deployed configuration. The proposed in-silico EVAR model incorporates only preinterventional data such that it can be used as predictive tool. Further, focus lies on the development of a computationally efficient in-silico SG sizing tool that can be used to evaluate several different SG sizes within a single EVAR simulation.

- **Validation of the in-silico EVAR model**
  In-silico EVAR models are a simplification of the real-world EVAR procedure that incorporate several assumptions. Hence, the proposed approximation of the postinterventional configuration by in-silico EVAR models requires qualitative and quantitative validation.

  A major goal of this thesis is to develop and apply a validation methodology that qualitatively and quantitatively compares the predicted patient-specific stent configuration produced by in-silico EVAR to the stent configuration extracted from postinterventional CT data for realistic clinical cases.

- **Application of the in-silico EVAR model**
  Many potential applications of in-silico EVAR models are stated in literature such as the predictive assessment of the complication likelihood. However, publications on these potential applications mostly lack specific and suitable examples. Furthermore, specific descriptions of how to assess the in-silico EVAR outcome with respect to EVAR complication likelihoods (e.g., endoleaks and SG migration) are rarely mentioned.

  To this end, a main contribution of this thesis is the definition of a set of mechanical and geometrical parameters to assess the quality of the in-silico EVAR outcome with respect to EVAR complication likelihoods from an engineering perspective. Toward the use of in-silico EVAR as predictive tool in clinical practice, a major goal of this thesis is the demonstrative application of the in-silico EVAR model to realistic patient-specific cases. Focus lies on the illustrative presentation of how the computational model can be used to optimize the preinterventional planning process. Besides patient-specific cases, fully parameterized synthetic, but realistic, SG and vessel geometries are developed. These parameterized geometries are used to investigate the influence of the SG and vessel geometry on EVAR outcomes in a statistical analysis.

1.5. Outline

The first objective, the development of a novel patient-specific in-silico EVAR model, is addressed in Part I of this thesis. The second and third objective, i.e., the validation and application of the in-silico EVAR model, are presented in Part II of this thesis.

Accordingly, the remainder of this work is organized as follows: in Chapter 2, fundamentals of computational solid mechanics are presented which include the basic governing equations

of nonlinear multibody continuum mechanics with frictional contact as well as their numerical approximation by the finite element method (FEM).

In Chapter 3, the in-silico EVAR model is developed. This includes the presentation of patient-specific vessel and SG models as well as a novel in-silico SG P&D methodology. Subsequently, a parameter continuation approach to model various different sizes of SGs within a single EVAR simulation is proposed. Finally, in this chapter, mechanical and geometrical parameters to assess the quality of the in-silico EVAR outcome are defined.

Chapter 4 focuses on the qualitative and quantitative validation of the in-silico EVAR model. The deployed SG configuration of patient-specific cases is predicted solely using preinterventional data. Subsequently, in-silico EVAR is validated by comparison of the in-silico EVAR results to postinterventional real-world CT data.

Afterwards, in Chapter 5, illustrative examples are presented how in-silico EVAR can optimize the preinterventional planning process of EVAR. Four patient-specific cases of infrarenal AAAs treated by commercial SG devices of two different manufacturers are considered. The illustrative examples include the assessment of EVAR complication likelihoods, the assistance in the SG device selection as well as the assessment of the influence of SG misplacement at patient-specific examples of infrarenal AAAs using in-silico EVAR.

In Chapter 6, fully parameterized synthetic SG and vessel geometries with AAA are developed. In-silico EVAR is applied to a large cohort of these parameterized vessel and SG geometries and the quality of the in-silico EVAR outcome is evaluated with respect to EVAR complication likelihoods. Conclusions concerning the impact on the EVAR outcome of certain SG and vessel parameters, such as the neck angle or the neck length, are drawn at the end of this chapter.

Chapter 7 provides a numerical proof of concept that the use of highly customized SGs can substantially improve EVAR outcomes with respect to reduced complication likelihoods. For this purpose, in-silico EVAR is used to compare the deployed configuration of highly customized SGs, which have the same morphology as the luminal vessel surface, to off-the-shelf SGs in several different aortic neck morphologies.

Finally, Chapter 8 provides a summary of this thesis and an outlook on potential future research.

Part I.

In-silico EVAR modeling

2. Fundamentals of computational solid mechanics

In this chapter, the basic governing equations of nonlinear continuum mechanics including frictional contact mechanics are presented in Section 2.1. Subsequently, the basic concepts to approximate the resulting nonlinear boundary value problem (BVP) using the FEM are provided in Section 2.2.

2.1. Nonlinear solid mechanics

In this section, only the very fundamental governing equations of nonlinear solid mechanics including frictional contact mechanics are stated. For a more comprehensive review on nonlinear continuum mechanics, the reader is referred for instance to Holzapfel [114]. A detailed description of frictional contact mechanics can be found in the work by Wriggers [274].

2.1.1. Kinematics

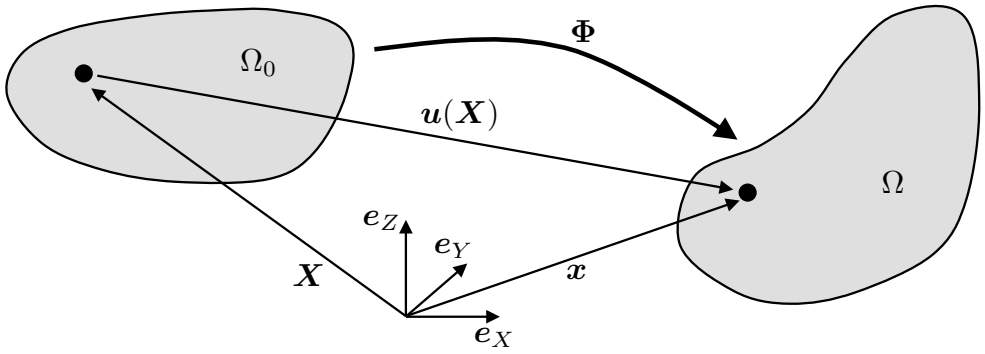

Figure 2.1 Reference configuration Ω_0 and current configuration Ω of a continuum body.

Given a continuum body (cf. Figure 2.1) in the reference configuration Ω_0 that is described by the reference coordinates $\boldsymbol{X} \in \Omega_0$, the current configuration Ω that is described by the current coordinates $\boldsymbol{x} \in \Omega$ can be tracked by the diffeomorphic mapping

$$\boldsymbol{\Phi} : \begin{cases} \Omega_0 & \to \Omega \\ \boldsymbol{X} & \mapsto \quad \boldsymbol{x} \end{cases} . \tag{2.1}$$

The definition of the diffeomorphic map allows for the notations $\boldsymbol{x} = \boldsymbol{\Phi}(\boldsymbol{X})$ and $\boldsymbol{X} = \boldsymbol{\Phi}^{-1}(\boldsymbol{x})$. Consequently, the displacement vector field $\boldsymbol{u}$ is given by

$$\boldsymbol{u}(\boldsymbol{X}) = \boldsymbol{\Phi}(\boldsymbol{X}) - \boldsymbol{X} = \boldsymbol{x} - \boldsymbol{X}. \tag{2.2}$$

The deformation gradient $\boldsymbol{F}$ defined by

$$\boldsymbol{F} = \frac{\partial \boldsymbol{x}}{\partial \boldsymbol{X}} = \boldsymbol{1} + \frac{\partial \boldsymbol{u}}{\partial \boldsymbol{X}} = \boldsymbol{1} + \nabla_0 \boldsymbol{u} \tag{2.3}$$

is a fundamental kinematic variable that is used as basis for the definition of many strain measures in the context of finite deformation solid mechanics. The deformation gradient $\boldsymbol{F}$ and its determinant

$$J = \det(\boldsymbol{F}) > 0 \tag{2.4}$$

relate an infinitesimal line element $\mathrm{d}\boldsymbol{X}$, an infinitesimal surface element $\mathrm{d}\boldsymbol{A}$ and an infinitesimal volume element $\mathrm{d}V$ in the reference configuration into their current configuration. Mathematically, the quantities of the reference configuration $\mathrm{d}\boldsymbol{X}$, $\mathrm{d}\boldsymbol{A} = \boldsymbol{N}\mathrm{d}A$ and $\mathrm{d}V$ are mapped to the quantities in the current configuration $\mathrm{d}\boldsymbol{x}$, $\mathrm{d}\boldsymbol{a} = \boldsymbol{n}\mathrm{d}a$ and $\mathrm{d}v$ by

$$\mathrm{d}\boldsymbol{x} = \boldsymbol{F}\mathrm{d}\boldsymbol{X}, \tag{2.5}$$

$$\mathrm{d}\boldsymbol{a} = J\boldsymbol{F}^{-\mathrm{T}}\mathrm{d}\boldsymbol{A}, \tag{2.6}$$

$$\mathrm{d}v = J\mathrm{d}V, \tag{2.7}$$

where $\boldsymbol{N}$ and $\boldsymbol{n}$ denote unit outward surface normal vectors of the area element in the reference and current configuration, respectively. Based on the definition of the deformation gradient the right Cauchy-Green deformation tensor

$$\boldsymbol{C} = \boldsymbol{F}^{\mathrm{T}}\boldsymbol{F} \tag{2.8}$$

and the left Cauchy-Green deformation tensor

$$\boldsymbol{b} = \boldsymbol{F}\boldsymbol{F}^{\mathrm{T}} \tag{2.9}$$

are frequently used deformation measures. Two strain measures that are relevant for the present thesis are the Green-Lagrange strain tensor

$$\boldsymbol{E} = \frac{1}{2}(\boldsymbol{F}^{\mathrm{T}}\boldsymbol{F} - \boldsymbol{1}) = \frac{1}{2}(\boldsymbol{C} - \boldsymbol{1}) \tag{2.10}$$

and the Euler-Almansi strain tensor

$$\boldsymbol{e} = \frac{1}{2}(\boldsymbol{1} - \boldsymbol{F}^{-\mathrm{T}}\boldsymbol{F}^{-1}) = \frac{1}{2}(\boldsymbol{1} - \boldsymbol{b}^{-1}). \tag{2.11}$$

Constitutive laws are frequently formulated in terms of principal invariants of the right Cauchy-Green deformation tensor $\boldsymbol{C}$ and the left Cauchy-Green deformation tensor $\boldsymbol{b}$ according to

$$I_1 = I_1(\boldsymbol{C}) = I_1(\boldsymbol{b}) = \mathrm{tr}(\boldsymbol{C}), \tag{2.12}$$

$$I_2 = I_2(\boldsymbol{C}) = I_2(\boldsymbol{b}) = \frac{1}{2}\left(\mathrm{tr}(\boldsymbol{C})^2 - \mathrm{tr}(\boldsymbol{C}^2)\right), \tag{2.13}$$

$$I_3 = I_3(\boldsymbol{C}) = I_3(\boldsymbol{b}) = \det(\boldsymbol{C}). \tag{2.14}$$

2.1.2. Kinetics and constitutive relations

Given an infinitesimal force resultant vector $\mathrm{d}\boldsymbol{f}$ acting on an infinitesimal surface element $\mathrm{d}\boldsymbol{a}$ in the current configuration with $\mathrm{d}a = ||\mathrm{d}\boldsymbol{a}||$, the traction vector $\boldsymbol{t}$ is defined by

$$\boldsymbol{t} = \frac{\mathrm{d}\boldsymbol{f}}{\mathrm{d}a}. \tag{2.15}$$

Cauchy's stress theorem relates the traction vector $\boldsymbol{t}$ in the current configuration to the second-order Cauchy stress tensor $\boldsymbol{\sigma}$ by

$$\boldsymbol{t} = \boldsymbol{\sigma}\boldsymbol{n}, \tag{2.16}$$

where $\boldsymbol{n}$ is the unit surface outward normal vector on $\mathrm{d}a$. Analogously, the traction vector can be expressed with respect to the reference configuration according to

$$\boldsymbol{t}_0 = \frac{\mathrm{d}\boldsymbol{f}}{\mathrm{d}A}, \tag{2.17}$$

where $\boldsymbol{t}_0$ denotes the so-called first Piola-Kirchhoff traction vector and where the surface element becomes $\mathrm{d}\boldsymbol{A} = \boldsymbol{N}\mathrm{d}A = J^{-1}\boldsymbol{F}^{\mathrm{T}}\mathrm{d}\boldsymbol{a}$. The first Piola-Kirchhoff stress tensor $\boldsymbol{P}$ is related to the first Piola-Kirchhoff traction vector $\boldsymbol{t}_0$ by

$$\boldsymbol{t}_0 = \boldsymbol{P}\boldsymbol{N}, \tag{2.18}$$

where $\boldsymbol{N}$ is the unit surface outward normal vector on $\mathrm{d}A$. Another frequently used stress measure that is relevant for this thesis is the second Piola-Kirchhoff stress tensor

$$\boldsymbol{S} = \boldsymbol{F}^{-1}\boldsymbol{P} = J\boldsymbol{F}^{-1}\boldsymbol{\sigma}\boldsymbol{F}^{-\mathrm{T}}. \tag{2.19}$$

Having introduced the essential kinematic and kinetic quantities of nonlinear solid mechanics, constitutive relations provide the missing link between those quantities. Elastic material behavior of solids under large deformation can be characterized in terms of an elastic energetic potential Ψ, which is called strain energy function (SEF). The SEF has to obey certain important properties, such as the requirement of objectivity, that are not further discussed in the scope of this thesis. The interested reader is referred for instance to Holzapfel [114]. Given Ψ, the stress

state can be calculated by differentiation of Ψ according to

$$\boldsymbol{S} = 2\frac{\partial \Psi}{\partial \boldsymbol{C}} = \frac{\partial \Psi}{\partial \boldsymbol{E}}. \tag{2.20}$$

2.1.3. Balance of linear momentum

The static balance of linear momentum of a body described in the current configuration reads

$$\int_{\Omega} \hat{\boldsymbol{b}} \mathrm{d}v + \int_{\gamma} \hat{\boldsymbol{t}} \mathrm{d}a = \boldsymbol{0}, \tag{2.21}$$

where $\hat{\boldsymbol{t}}$ is an external traction load on the boundary γ of the body and $\hat{\boldsymbol{b}}$ is an external body force. After incorporation of (2.16) and application of Gauss' divergence theorem, the static balance of linear momentum is given by

$$\int_{\Omega} (\nabla \cdot \boldsymbol{\sigma} + \hat{\boldsymbol{b}}) \mathrm{d}v = \boldsymbol{0}. \tag{2.22}$$

Similarly, (2.22) can be expressed with respect to the reference configuration according to

$$\int_{\Omega_0} (\nabla_0 \cdot (\boldsymbol{F}\boldsymbol{S}) + \hat{\boldsymbol{b}}_0) \mathrm{d}V = \boldsymbol{0}. \tag{2.23}$$

Under consideration that the balance of linear momentum has to hold for any infinitesimal small subregion of the body, the local forms of (2.22) and (2.23) can be stated by

$$\nabla \cdot \boldsymbol{\sigma} + \hat{\boldsymbol{b}} = \boldsymbol{0} \quad \text{in } \Omega \subset \mathbb{R}^3 \tag{2.24}$$

and

$$\nabla_0 \cdot (\boldsymbol{F}\boldsymbol{S}) + \hat{\boldsymbol{b}}_0 = \boldsymbol{0} \quad \text{in } \Omega_0 \subset \mathbb{R}^3, \tag{2.25}$$

respectively.

2.1.4. Boundary value problem of nonlinear elastostatics

After introduction of the basic equations of nonlinear continuum mechanics in Sections 2.1.1-2.1.3, the BVP of nonlinear elastostatics reads

$$\nabla_0 \cdot (\boldsymbol{F}\boldsymbol{S}) + \hat{\boldsymbol{b}}_0 = \boldsymbol{0} \qquad \text{in } \Omega_0 \subset \mathbb{R}^3, \tag{2.26}$$

$$\boldsymbol{F}\boldsymbol{S}\boldsymbol{N} = \hat{\boldsymbol{t}}_0 \qquad \text{on } \Gamma_\sigma, \tag{2.27}$$

$$\boldsymbol{u} = \hat{\boldsymbol{u}} \qquad \text{on } \Gamma_{\mathrm{u}}, \tag{2.28}$$

where (2.26) is the static balance of linear momentum in the reference configuration, (2.27) is a Neumann boundary condition and (2.28) is a Dirichlet boundary condition. At the Neumann boundary Γ_σ the first Piola-Kirchhoff traction $\hat{\boldsymbol{t}}_0$ is prescribed and at the Dirichlet boundary Γ_{u}

the displacement vector $\hat{\boldsymbol{u}}$ is given. Neumann and Dirichlet boundaries have to be disjoint sets, i.e.,

$$\Gamma = \Gamma_{\mathrm{u}} \cup \Gamma_{\sigma}, \quad \Gamma_{\mathrm{u}} \cap \Gamma_{\sigma} = \emptyset, \tag{2.29}$$

where Γ denotes the total boundary of the body in the reference configuration. Completion of the BVP is provided by the constitutive relations as introduced in Section 2.1.2. These constitutive relations will be further concretized for SGs and vessel constituents in Chapter 3.

2.1.5. Frictional contact mechanics

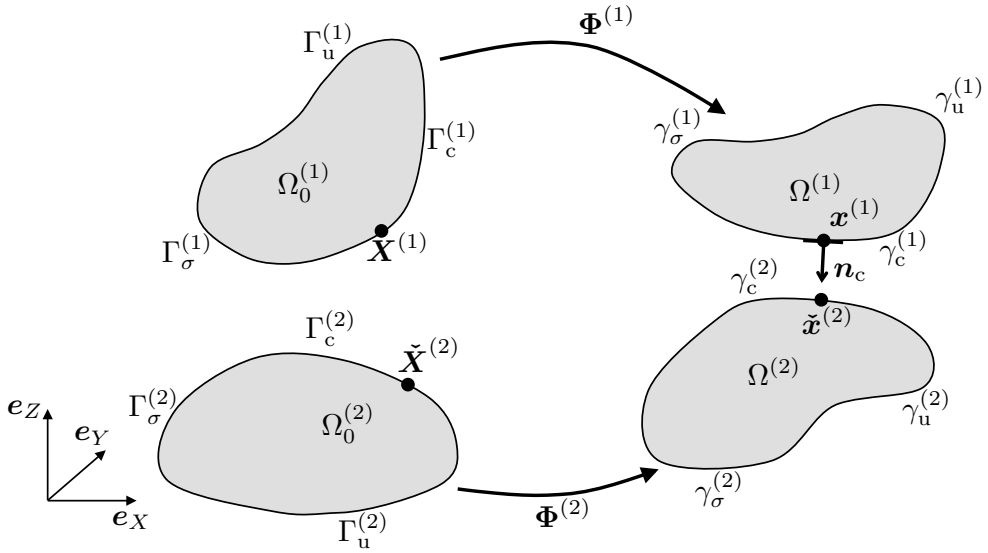

Figure 2.2 Notation for the contact description of two deformable continuum bodies.

The concepts of frictional contact mechanics and their computational realization as used in this thesis are based on the work by Popp [209] and Gitterle [89]. Figure 2.2 illustrates two deformable continuum bodies in the reference configuration $\Omega_0^{(\mathit{II})}$ and the current configuration $\Omega^{(\mathit{II})}$ with $\mathit{II} \in \{1, 2\}$ which undergo potential contact. Both bodies obey the BVP as presented in Section 2.1.4. Since contact interaction of the two bodies occurs in the current configuration at the contact boundaries $\gamma_{\mathrm{c}}^{(\mathit{II})}$, the contact boundaries $\Gamma_{\mathrm{c}}^{(\mathit{II})}$ in the reference configuration are a priori unknown. This circumstance introduces an additional source of nonlinearity to the given problem.

The fundamental quantity to describe the kinematics of the potential contact between the two bodies is given by the gap vector

$$\boldsymbol{g} = \boldsymbol{x}^{(1)} - \check{\boldsymbol{x}}^{(2)} \tag{2.30}$$

and its projection in normal direction

$$g_{\mathrm{n}} = -\boldsymbol{n}_{\mathrm{c}} \cdot \boldsymbol{g}, \tag{2.31}$$

where $\boldsymbol{n}_{\mathrm{c}}$ is the unit outward normal vector on the contact boundary $\gamma_{\mathrm{c}}^{(1)}$ at point $\boldsymbol{x}^{(1)}$. The corresponding contact point of $\boldsymbol{x}^{(1)}$ is $\check{\boldsymbol{x}}^{(2)} \in \gamma_{\mathrm{c}}^{(2)}$, which is the result of a smooth interface mapping of $\boldsymbol{x}^{(1)}$ onto $\gamma_{\mathrm{c}}^{(2)}$ along $\boldsymbol{n}_{\mathrm{c}}$ as defined in [211]. The fundamental kinematic variable for frictional sliding of the two bodies is the tangential slip rate

$$\boldsymbol{v}_{\tau,\mathrm{rel}} = (\boldsymbol{1} - \boldsymbol{n}_{\mathrm{c}} \otimes \boldsymbol{n}_{\mathrm{c}}) \cdot (\dot{\boldsymbol{x}}^{(1)} - \dot{\check{\boldsymbol{x}}}^{(2)}), \tag{2.32}$$

where $\dot{\boldsymbol{x}}^{(1)}$ and $\dot{\check{\boldsymbol{x}}}^{(2)}$ are the velocities of material point $\boldsymbol{X}^{(1)}$ and $\check{\boldsymbol{X}}^{(2)}$, respectively. It has to be pointed out that this representation of $\boldsymbol{v}_{\tau,\mathrm{rel}}$ does not consider a change of the contact point $\check{\boldsymbol{X}}^{(2)}$, i.e., it does not include a change of the projection of point $\boldsymbol{x}^{(1)}$ onto $\gamma_{\mathrm{c}}^{(2)}$. This representation of $\boldsymbol{v}_{\tau,\mathrm{rel}}$ does not fulfill the fundamental requirement of objectivity as shown for instance in [89]. In the current work, an appropriate algorithmic modification of the discretized representation of $\boldsymbol{v}_{\tau,\mathrm{rel}}$ is used to guarantee frame indifference as presented in [89].

In order to satisfy the balance of linear momentum on the contact interface,

$$\boldsymbol{t}_{\mathrm{c}}^{(1)} = -\boldsymbol{t}_{\mathrm{c}}^{(2)} \tag{2.33}$$

has to hold, where $\boldsymbol{t}_{\mathrm{c}}^{(1)}$ is the traction vector on $\gamma_{\mathrm{c}}^{(1)}$ and $\boldsymbol{t}_{\mathrm{c}}^{(2)}$ is the traction vector on $\gamma_{\mathrm{c}}^{(2)}$. The contact traction $\boldsymbol{t}_{\mathrm{c}}^{(1)}$ can be split into normal and tangential components according to

$$\boldsymbol{t}_{\mathrm{c}}^{(1)} = \boldsymbol{t}_{\mathrm{n}} + \boldsymbol{t}_{\tau} = p_{\mathrm{n}} \boldsymbol{n}_{\mathrm{c}} + \boldsymbol{t}_{\tau}, \tag{2.34}$$

where p_{n} is the normal contact traction (pressure) and $\boldsymbol{t}_{\tau}$ is the tangential traction vector.

The set of non-adhesive, frictional contact constraints is then given by

$$g_{\mathrm{n}} \geq 0, \quad p_{\mathrm{n}} \leq 0, \quad p_{\mathrm{n}} g_{\mathrm{n}} = 0, \tag{2.35}$$

$$\Lambda := ||\boldsymbol{t}_{\tau}|| - \mathfrak{F}|p_{\mathrm{n}}| \leq 0, \quad \boldsymbol{v}_{\tau,\mathrm{rel}} + \zeta \boldsymbol{t}_{\tau} = \boldsymbol{0}, \quad \zeta \geq 0, \quad \Lambda \zeta = 0, \tag{2.36}$$

where (2.35) represents normal contact constraints and (2.36) are tangential contact constraints. The normal contact constraints (2.35) are formulated as a classical set of Karush-Kuhn-Tucker (KKT) conditions, where the first KKT condition enforces non-penetration of the contact bodies, the second KKT condition entails non-adhesive contact and the third KKT condition is a complementarity condition. In this thesis, the mathematical model of friction is restricted to dry friction with the friction coefficient $\mathfrak{F}$ classically described by Coulomb's law. In the tangential contact constraints (2.36), Λ defines the slip condition and ζ is a complementarity parameter. In case of $\Lambda < 0$ (i.e., $\zeta = 0$), the second condition in (2.36) implies that no tangential slip occurs ($\boldsymbol{v}_{\tau,\mathrm{rel}} = \boldsymbol{0}$). This state is denoted as stick state. In contrast, $\Lambda = 0$ defines the slip state.

2.2. Numerical approximation

The FEM approximation of the strong form of the BVP defined in Equations (2.26)-(2.28) requires the expression of the BVP in the weak form. Using the principle of virtual work, the weak

form of the BVP reads

$$\delta\mathcal{W} = \int_{\Omega_0} \boldsymbol{S} : \delta\boldsymbol{E}\mathrm{d}V - \int_{\Omega_0} \hat{\boldsymbol{b}}_0 \cdot \delta\boldsymbol{u}\mathrm{d}V - \int_{\Gamma_\sigma} \hat{\boldsymbol{t}}_0 \cdot \delta\boldsymbol{u}\mathrm{d}A = 0, \quad \forall\delta\boldsymbol{u}, \tag{2.37}$$

where

$$\boldsymbol{u} \in \mathcal{U} = \left\{\boldsymbol{u} \in [H^1(\Omega_0)]^3 \mid \boldsymbol{u} = \hat{\boldsymbol{u}} \text{ on } \Gamma_\mathrm{u}\right\}, \tag{2.38}$$

$$\delta\boldsymbol{u} \in \mathcal{V} = \left\{\delta\boldsymbol{u} \in [H^1(\Omega_0)]^3 \mid \delta\boldsymbol{u} = \boldsymbol{0} \text{ on } \Gamma_\mathrm{u}\right\}. \tag{2.39}$$

In (2.37)-(2.39), $\delta\boldsymbol{u}$ are the virtual displacements and $\delta\boldsymbol{E} = \frac{1}{2}[(\nabla_0(\delta\boldsymbol{u}))^\mathrm{T}\boldsymbol{F} + \boldsymbol{F}^\mathrm{T}\nabla_0(\delta\boldsymbol{u})]$ is the virtual strain tensor. Further, $\mathcal{U}$ is the solution space and $\mathcal{V}$ is the weighting space for the displacements, where $H^1(\Omega_0)$ denotes the usual Sobolev space on Ω_0.

In this thesis, only the very basic idea of FEM is stated. For more detailed information on FEM, the reader is referred for instance to Zienkiewicz et al. [281]. For the FEM approximation, Ω_0 is divided into a finite number of sub-domains $\Omega_0^{(e)}$ that are called finite elements. The displacement field $\boldsymbol{u}_\mathrm{h}^{(e)}(\boldsymbol{\xi})$ on element e with the parameter space $\boldsymbol{\xi} \in \mathbb{R}^3$ is then approximated by local interpolation functions $N^{i,(e)}(\boldsymbol{\xi})$, so-called shape functions. Accordingly, the discretized displacement field of element e is given by

$$\boldsymbol{u}_\mathrm{h}^{(e)}(\boldsymbol{\xi}) = \sum_{i=1}^{n_\mathrm{node}^{(e)}} N^{i,(e)}(\boldsymbol{\xi})\boldsymbol{u}^{i,(e)}. \tag{2.40}$$

Similarly, the element geometry in the reference configuration is

$$\boldsymbol{X}_\mathrm{h}^{(e)}(\boldsymbol{\xi}) = \sum_{i=1}^{n_\mathrm{node}^{(e)}} N^{i,(e)}(\boldsymbol{\xi})\boldsymbol{X}^{i,(e)}. \tag{2.41}$$

Here, all spatially discretized quantities are indicated by $(\bullet)_\mathrm{h}$. The number of nodes that are associated with element e is $n_\mathrm{node}^{(e)}$ and $\boldsymbol{u}^{i,(e)}$ as well as $\boldsymbol{X}^{i,(e)}$ are nodal displacements and nodal reference coordinates, respectively. A Bubnov-Galerkin approach is applied where the same shape functions are used for the interpolation of the virtual displacements $\delta\boldsymbol{u}_\mathrm{h}^{(e)}$ and the displacements $\boldsymbol{u}_\mathrm{h}^{(e)}$. After inserting the approximations $\boldsymbol{u}_\mathrm{h}^{(e)}$ and $\delta\boldsymbol{u}_\mathrm{h}^{(e)}$ into (2.37), element-wise numerical integration and assembly into global vectors, the spatially discrete static balance of linear momentum reads

$$\mathbf{f}_\mathrm{int}(\mathbf{u}) - \mathbf{f}_\mathrm{ext} = \mathbf{0}. \tag{2.42}$$

In (2.42), $\mathbf{u}$ is the global vector comprising all nodal displacements, $\mathbf{f}_\mathrm{int}(\mathbf{u})$ is the nonlinear internal force vector referred to the first integral in (2.37) and $\mathbf{f}_\mathrm{ext}$ is the external force vector referred to the last two integrals in (2.37).

Remark. *In Chapter 3, a nonlinearity will also be introduced for the external force. Hence,* $\mathbf{f}_\mathrm{ext} = \mathbf{f}_\mathrm{ext}(\mathbf{u})$.

To circumvent volumetric locking of nearly incompressible vessel tissue, finite elements with F-bar technology [55] are considered. The F-bar element entails an isochoric-volumetric split of the deformation gradient, where the volumetric part of the deformation gradient is evaluated at the element's centroid to prevent the emergence of parasitic stresses associated with spurious volumetric locking phenomena. The SG undergoes severe bending and buckling during in-silico EVAR. It would be subjected to severe geometric locking phenomena, such as shear locking, if standard lower order displacement-based finite elements were used. Therefore, in this thesis, two different anti-locking technologies are utilized in the SG discretization. First, the assumed natural strain (ANS) technology which uses special collocation points to evaluate the strain state of the displacement based element. At these collocation points, spurious strains vanish which are responsible for the geometric locking phenomena. Second, the enhanced assumed strain (EAS) technology relies on the three-field variational Hu-Washizu principle and utilizes an enhanced strain field as balance to the spurious strains that are responsible for locking phenomena. The specific element formulation enables the condensation of the additional degrees of freedom related to the enhanced strain field such that no additional degrees of freedom need to be solved compared to the standard displacement-based element without EAS technology. Besides geometric locking phenomena, the EAS technology is also able to reduce volumetric locking phenomena which depending on the compressibility of the stent and the graft material can be essential. For a more detailed review of the EAS and the ANS technology, the interested reader is referred to the thesis by Koschnick [141], where an extensive overview of both anti-locking technologies is provided.

Mortar-based discretization methods [210, 211] are used in this thesis for mesh tying and contact interfaces. Mesh tying, also denoted as tied contact, is a special case of the aforementioned contact interaction (cf. Section 2.1.5), where the two bodies are "tied" together at the common interface in the reference configuration. Hence, the gap vector $\boldsymbol{g}$ as defined in Equation (2.30) has to vanish in this case, i.e., $\boldsymbol{g} = \mathbf{0}$. Mortar discretization methods provide a more precise evaluation of the contact interface compared to other contact discretization methods (e.g., the node-to-segment discretization) which often lack essential accuracy requirements. For more detailed information on mortar methods in the context of contact mechanics, the reader is referred to the theses by Popp [209], Gitterle [89] and Farah [72]. In this thesis, the enforcement of the contact constraints (2.35)-(2.36) is based on a penalty regularization which represents a good compromise between accuracy and efficiency.

For the given problems of this thesis, a dynamic relaxation technique (see e.g., [16, 193]) has proven to be a more robust solution scheme for the resulting set of nonlinear equations than other available purely static nonlinear solution schemes. In the dynamic relaxation technique, the static solution is achieved as steady-state response to a dynamic analysis. Hence, the static balance of linear momentum (2.42) is enhanced by an inertia term and an artificial damping term. Consequently, the adapted spatially discrete balance of linear momentum reads $\mathbf{M}\ddot{\mathbf{u}} + \mathbf{C}\dot{\mathbf{u}} + \mathbf{f}_{\mathrm{int}}(\mathbf{u}) - \mathbf{f}_{\mathrm{ext}} = \mathbf{0}$, where $\dot{\mathbf{u}}$ and $\ddot{\mathbf{u}}$ are the global vectors containing nodal values of the velocities and the accelerations. The global mass matrix $\mathbf{M}$ is based on the physical density of the body and the global damping matrix $\mathbf{C}$ is based on the Rayleigh model for viscous damping. The purely phenomenological Rayleigh model reads $\mathbf{C} = c_{\mathrm{M}}\mathbf{M} + c_{\mathrm{K}}\mathbf{K}_0$, where c_{M} as well as c_{K} are damping coefficients and $\mathbf{K}_0$ is the reference tangent system matrix. Since according to the dynamic relaxation technique, the transient part of the solution is not of interest, but only the steady-state response, the implicit backward Euler scheme with considerable numerical damp-

ing is used as temporal discretization scheme. The resulting set of nonlinear equations is solved using a semi-smooth Newton approach with consistent linearization [90]. In the current work, it is switched from the classical Newton method to a more stable pseudo-transient continuation scheme [86] whenever necessary. The large system of linearized equations is solved every Newton step by a parallel iterative GMRES method [229] preconditioned using algebraic multigrid [85].

3. Computational tools for in-silico EVAR

The process of SG placement and deployment is highly nonlinear mainly due to the occurrence of complex contact between SG and vessel, buckling of the very thin graft as well as nonlinear material behavior. Thus, computational modeling of these processes is challenging and the methodology how the SG is placed and deployed within the vessel is essential for the accuracy, efficiency and robustness of the approach. Stent predeformation as well as in-vivo non-stress-free vessel geometries from medical imaging require special computational techniques which have to be consistently integrated into the mechanical framework. High complexity of vessel and SG shapes and their large interpatient variability are further challenges of in-silico EVAR models [106].

As improvement of available in-silico EVAR models (cf. Section 1.3), in this chapter special attention is paid to detailed modeling of all vessel and aneurysm constituents as they can have a distinct impact on the outcome of EVAR [231, 273, 275]. This means that the vessel model differentiates between “healthy” and “aneurysmatic” vessel wall. This is essential as in general the landing zone of the SG is in the region of “healthy” vessel tissue and not in the “aneurysmatic” part [97]. Nevertheless, since the reduction of wall stresses in the “aneurysmatic” part of the vessel is a major goal of EVAR, the sophisticated modeling of this part of the vessel is also essential. Furthermore, ILT as well as calcifications are considered in the vessel model and a vessel prestressing technique [84] is incorporated to consider in-vivo non-stress-free vessel geometries extracted from in-vivo CT images.

Additionally, in this chapter a novel in-silico SG P&D methodology is developed which avoids extremely complex steps during placement of the SG but nevertheless provides a high level of accuracy of the deployed SG in the patient-specific vessel. This in-silico SG P&D methodology is related to the virtual catheter method, however avoids additional modeling of virtual catheters as well as the computationally very complex radial crimping process of the SG. Instead, during the entire in-silico SG placement, the deformation of the SG is prescribed by displacement constraints resulting from a newly developed 3D morphing algorithm. Therefore, during the entire in-silico SG placement, buckling of the SG is prevented, the degrees of freedom (DOFs) of the SG do not need to be solved and the contact interaction between SG and vessel reduces to a computationally relatively simple *Signorini contact problem* of one rigid (SG) and one elastically deformable body (vessel). Nevertheless, after the SG deployment of the presented in-silico SG P&D methodology, both SG and vessel are elastically deformable bodies that are considered at static, but physiologically meaningful blood pressure states. Investigations on the influence of the dynamics of the pulsatory blood flow are not part of this thesis.

Additionally, the novel 3D morphing algorithm is utilized in a stent predeformation methodology to consider residual strains and stresses in the SG model arising from the real-world assembling process of SGs. The stent predeformation methodology is based on the alteration of the

stress-free reference configuration of the stent after SG assembly. This methodology is flexible and is consistently integrated into the framework of nonlinear continuum mechanics.

One further advantage of direct application of the morphing algorithm to the SG, instead of the application to a virtual catheter, is used in the development of an efficient in-silico SG sizing tool. Using the morphing algorithm and parameter continuation, the SG diameter can be continuously changed via alteration of the stress-free reference configuration of the SG, which allows to evaluate several different degrees of SG oversizing within a single EVAR simulation. This approach results in a substantial saving of simulation time compared to other approaches, where different degrees of SG oversizing are investigated in separate simulations [53, 212].

All developed models are applicable to synthetic and patient-specific cases. Both will be required in Part II of this thesis, where the application of the in-silico model is demonstrated. Therefore, both patient-specific cases (with bifurcation into the iliac arteries) as well as synthetic cases (without bifurcation into the iliac arteries) are considered for the development of the models in this thesis.

The presented methods utilize the FEM and mortar-based frictional penalty contact as presented in Chapter 2. The newly developed algorithms are implemented in an in-house C++ based parallel nonlinear finite element code. High performance computing resources are provided by the Leibniz Rechenzentrum München of the Bavarian Academy of Sciences.

The outline of this chapter is as follows: first, the BVP of the in-silico EVAR model is defined in Section 3.1. Subsequently, in Section 3.2, a 3D morphing algorithm is presented, which will subsequently be used in the in-silico SG P&D methodology, the stent predeformation methodology as well as in the parameter continuation approach for SG sizing. Patient-specific vessel models and SG models are presented in Section 3.3 and 3.4. Given the vessel as well as the SG model in the preinterventional configuration, in Section 3.5, the integration of vessel prestressing and stent predeformation into the in-silico EVAR model, the in-silico SG P&D methodology as well as the parameter continuation approach as in-silico SG sizing tool are presented. In Section 3.6, so-called EVAR quality parameters are proposed to geometrically and mechanically assess the quality of the in-silico EVAR outcome with respect to EVAR related complication likelihoods. Since the in-silico EVAR model incorporates several assumptions, a detailed overview of the major assumptions is provided in Section 3.7. Finally, a short summary of this chapter is given in Section 3.8.

This chapter is primarily based on three previous publications by the author of this thesis, which are used here with permission. Sections 3.1-3.7 are partly taken from [106, 107] and Section 3.6 is taken from [107, 109].

3.1. Definition of the boundary value problem of in-silico EVAR

In this section the BVP of nonlinear elastostatics including frictional contact as presented in Chapter 2 is concretized for the in-silico EVAR problem (cf. Figure 3.1). The BVP describing the in-silico EVAR model reads

$$\nabla_0 \cdot (\boldsymbol{F}^{(\Pi)}\boldsymbol{S}^{(\Pi)}) + \hat{\boldsymbol{b}}_0^{(\Pi)} = \boldsymbol{0} \qquad \text{in } \Omega_0^{(\Pi)} \subset \mathbb{R}^3, \tag{3.1}$$

$$\boldsymbol{F}^{(\Pi)}\boldsymbol{S}^{(\Pi)}\boldsymbol{N}^{(\Pi)} = \hat{\boldsymbol{t}}_0^{(\Pi)} \qquad \text{on } \Gamma_\sigma^{(\Pi)}, \tag{3.2}$$

$$\boldsymbol{F}^{(\Pi)}\boldsymbol{S}^{(\Pi)}\boldsymbol{N}^{(\Pi)} = \boldsymbol{t}_{\mathrm{c},0}^{(\Pi)} \qquad \text{on } \Gamma_\mathrm{c}^{(\Pi)}, \tag{3.3}$$

$$\boldsymbol{u}^\mathrm{S} = \boldsymbol{u}^\mathrm{G} \qquad \text{on } \Gamma_\mathrm{m}, \tag{3.4}$$

$$\boldsymbol{F}^\mathrm{Ao}\boldsymbol{S}^\mathrm{Ao}\boldsymbol{N}^\mathrm{Ao} = -\hat{k}_\mathrm{ex}\boldsymbol{u}^\mathrm{Ao} \qquad \text{on } \Gamma_\mathrm{ex}^\mathrm{Ao}, \tag{3.5}$$

$$\boldsymbol{F}^\mathrm{Ao}\boldsymbol{S}^\mathrm{Ao}\boldsymbol{N}^\mathrm{Ao} = -\hat{k}_\mathrm{io}\boldsymbol{u}^\mathrm{Ao} \qquad \text{on } \Gamma_\mathrm{io}^\mathrm{Ao} \tag{3.6}$$

for the three bodies $\Pi \in \{\mathrm{Ao}, \mathrm{G}, \mathrm{S}\}$ and with the frictional contact constraints (cf. Section 2.1.5)

$$\begin{gathered} g_\mathrm{n} \geq 0, \quad p_\mathrm{n} \leq 0, \quad p_\mathrm{n} g_\mathrm{n} = 0, \\ \Lambda := ||\boldsymbol{t}_\tau|| - \mathfrak{F}|p_\mathrm{n}| \leq 0, \quad \boldsymbol{v}_{\tau,\mathrm{rel}} + \zeta \boldsymbol{t}_\tau = \boldsymbol{0}, \quad \zeta \geq 0, \quad \Lambda\zeta = 0 \qquad \text{on } \gamma_\mathrm{c}^{(\Pi)}. \end{gathered} \tag{3.7}$$

Equation (3.1) represents the static balance of linear momentum of the three involved bodies $\Pi \in \{\mathrm{Ao}, \mathrm{G}, \mathrm{S}\}$. Here, "Ao" denotes the vessel, "S" the stent and "G" the graft (cf. Figure 3.1). Body forces are neglected, i.e., $\hat{\boldsymbol{b}}_0^{(\Pi)} = \boldsymbol{0}$.

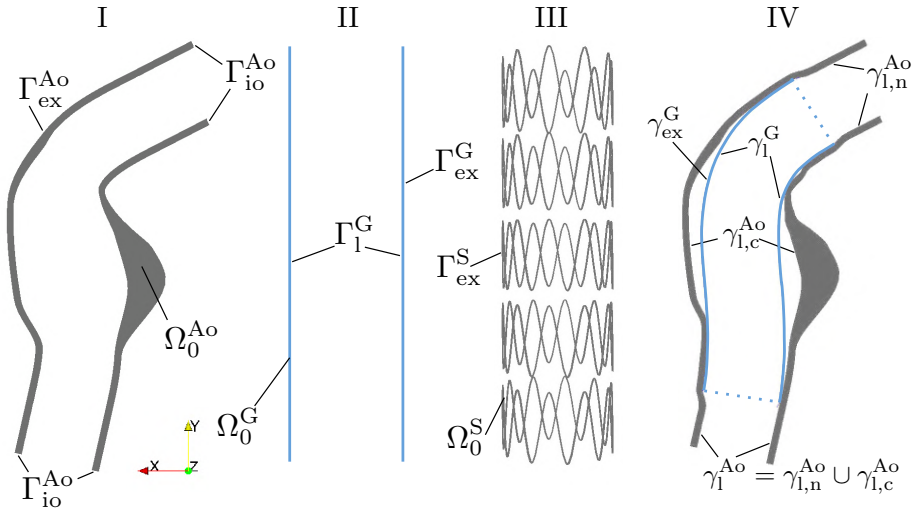

Figure 3.1 Simplified scheme of domains and boundaries of the vessel Ω_0^Ao (I), the graft Ω_0^G (II) and the stent Ω_0^S (III) in the reference configuration and in the current configuration (IV). $(\bullet)_\mathrm{ex}$ denotes the exterior boundaries of the vessel $\Gamma_\mathrm{ex}^\mathrm{Ao}$, the graft $\Gamma_\mathrm{ex}^\mathrm{G}$ and the stent $\Gamma_\mathrm{ex}^\mathrm{S}$. $(\bullet)_\mathrm{l}$ describes the luminal boundaries of the vessel covered by the graft $\gamma_\mathrm{l,c}^\mathrm{Ao}$ and not covered by the graft $\gamma_\mathrm{l,n}^\mathrm{Ao}$ as well as the luminal boundary of the graft $\gamma_\mathrm{l}^\mathrm{G}$. $\Gamma_\mathrm{io}^\mathrm{Ao}$ denotes the boundary at the in- and outlet of the vessel segment. Modified figure reproduced with permission from [107].

A nonlinear traction load $\hat{\boldsymbol{t}}^{(\Pi)}(\boldsymbol{u}^{(\Pi)}) \neq \boldsymbol{0}$ is applied on the Neumann boundaries $\gamma_\mathrm{l}^\mathrm{G} \cup \gamma_\mathrm{l,n}^\mathrm{Ao}$ in the current configuration, where $\gamma_\mathrm{l}^\mathrm{G}$ is the luminal surface of the graft and $\gamma_\mathrm{l,n}^\mathrm{Ao} = \gamma_\mathrm{l}^\mathrm{Ao} \setminus \gamma_\mathrm{l,c}^\mathrm{Ao}$ is the luminal vessel surface not covered by the SG. The nonlinear traction load $\hat{\boldsymbol{t}}^{(\Pi)}(\boldsymbol{u}^{(\Pi)})$ is a

so-called follower load. In the current configuration it is formulated by

$$\hat{\boldsymbol{t}}^{(\Pi)} = -p\boldsymbol{n}^{(\Pi)} \qquad \text{on } \gamma_{\mathrm{l}}^{\mathrm{G}} \cup \gamma_{\mathrm{l,n}}^{\mathrm{Ao}}, \tag{3.8}$$

where p is the hydrostatic blood pressure and $\boldsymbol{n}^{(\Pi)}$ is the unit outward surface normal in the current configuration. To be in accordance with the remaining equations of the BVP, the Neumann boundary condition in Equation (3.2) is formulated with respect to the reference configuration. Accordingly, the first Piola-Kirchhoff traction vector reads

$$\hat{\boldsymbol{t}}_0^{(\Pi)} = -pJ^{(\Pi)}(\boldsymbol{F}^{(\Pi)})^{-\mathrm{T}}\boldsymbol{N}^{(\Pi)} \qquad \text{on } \Gamma_{\mathrm{l}}^{\mathrm{G}} \cup \Gamma_{\mathrm{l,n}}^{\mathrm{Ao}}. \tag{3.9}$$

On the luminal vessel surface $\gamma_{\mathrm{l,c}}^{\mathrm{Ao}}$ covered by the SG, i.e., the luminal surface of the vessel between the most proximal SG attachment and the most distal SG attachment, a zero traction load ($\hat{\boldsymbol{t}}^{(\Pi)} = \boldsymbol{0}$) is assumed as the hydrostatic blood pressure is carried by the SG.

Equation (3.3) relates the contact tractions acting on the potential contact surfaces: the slave surface (the outer graft surface $\Gamma_{\mathrm{ex}}^{\mathrm{G}}$) and the master surface (the luminal vessel surface $\Gamma_{\mathrm{l}}^{\mathrm{Ao}}$). A friction coefficient of $\mathfrak{F} = 0.4$ [205, 253] between SG and vessel is assumed throughout this thesis. Fixation between stent and graft is realized by a tied contact constraint on the common boundary Γ_{m} between the luminal graft surface $\Gamma_{\mathrm{l}}^{\mathrm{G}}$ and the outer stent surface $\Gamma_{\mathrm{ex}}^{\mathrm{S}}$, i.e., $\Gamma_{\mathrm{m}} = \Gamma_{\mathrm{l}}^{\mathrm{G}} \cap \Gamma_{\mathrm{ex}}^{\mathrm{S}}$.

Remark. *SG models of this thesis are restricted to interior stent limbs. Hence, the outer stent surface is attached to the luminal (inner) graft surface.*

The spring boundary conditions of Equations (3.5) and (3.6) on the abluminal surface of the vessel $\Gamma_{\mathrm{ex}}^{\mathrm{Ao}}$ and on the in- and outlet of the vessel $\Gamma_{\mathrm{io}}^{\mathrm{Ao}}$ model the surrounding tissue of the vessel. Spring stiffnesses $\hat{k}_{\mathrm{ex}}$ and $\hat{k}_{\mathrm{io}}$ are defined per unit reference area and $\boldsymbol{N}^{\mathrm{Ao}}$ is the unit outward surface normal of the reference configuration. Throughout this thesis, $\hat{k}_{\mathrm{ex}} = 2.0\mathrm{kPa/mm}$ and $\hat{k}_{\mathrm{io}} = 2.0\mathrm{kPa/mm}$ are assumed [184].

Completion of the BVP is provided by the constitutive relations of the vessel as well as the stent and the graft. Note that this definition of the BVP defines the final deployed state of vessel and SG. However, during the in-silico SG P&D methodology, some modifications of this BVP are required. For instance, to place the SG within the vessel, the contact constraints between the outer graft surface $\gamma_{\mathrm{ex}}^{\mathrm{G}}$ and the luminal vessel surface $\gamma_{\mathrm{l}}^{\mathrm{Ao}}$ are omitted. These modifications will be stated in Section 3.5, where the in-silico SG P&D methodology is described.

3.2. Morphing algorithms for in-silico EVAR

Morphing (metamorphosis) is the process of continuously and smoothly transforming one object into another originally developed for image processing (cf. for instance [21, 149, 153]). In this section, first the morphing algorithms of existing in-silico SG P&D methodologies are reviewed in Section 3.2.1. Afterwards, in Section 3.2.2, a newly developed morphing algorithm is presented that is used for the novel in-silico SG P&D methodology.

3.2.1. Morphing algorithms of existing in-silico SG P&D methodologies

In Section 1.3.3, the most used in-silico SG P&D methodologies, the *virtual catheter method* and the *virtual shell method*, were reviewed. Both in-silico SG P&D methodologies use suitable morphing algorithms for the in-silico SG placement and deployment. In this section, the basic concepts of morphing algorithms of those two in-silico SG P&D methodologies are presented.

Morphing algorithm of the virtual catheter method

In the virtual catheter method [9], a morphing algorithm is used to prescribe the deformation of the cylindrical virtual catheter during in-silico SG placement. Algorithmic aspects that govern the deformation process of the virtual catheter are rarely described in full detail.

A possible way to describe this deformation process is by generating the initial and the target configurations of the catheter and computing the difference between those two configurations. The initial configuration is a straight cylinder and the target configuration is the tubular structure resulting from sweeping a circular cross section along the preinterventional vessel centerline. As long as the initial and the target configuration of the virtual catheter are discretized consistently, no special morphing algorithms are required to trace the deformation process of the virtual catheter during in-silico SG placement. Instead, the virtual catheter is deformed along the trajectories given by the vector differences between the nodal positions of the catheter in the initial and the target configuration. However, this deformation process based on direct node correspondence requires proper alignment of the initial straight catheter configuration with respect to the vessel and may lead to non-smooth deformations with potential self-intersections of the catheter in case of highly tortuous vessel geometries.

Morphing algorithm of the virtual shell method

The virtual shell method proposed by Perrin et al. [204, 205] requires a robust morphing algorithm that governs the deformation of the virtual shell from the initial straight configuration to the patient-specific preinterventional vessel geometry. This morphing algorithm originally described in [94, 204] is briefly reviewed in the following.

In contrast to the in-silico SG P&D methodology where the tubular shell is mapped onto the patient's preinterventional vessel geometry, the actual morphing algorithm works in reverse, i.e., the meshed preinterventional vessel geometry is first morphed to a straight tubular shell (cf. Figure 3.2). Once this morphing process from the patient's preinterventional vessel geometry to the tubular shell is established, the deformation maps are stored and can be applied in the in-silico SG P&D methodology in reverse manner to gradually transform the meshed tubular shell to the meshed preinterventional vessel geometry. This reverse approach has the benefit that the quality of the meshed preinterventional vessel geometry is not affected by the morphing algorithm. Only the mesh quality of the shell in the tubular configuration and all intermediate configurations between the tubular shell and the vessel geometry are affected by the morphing algorithm. However, in these configurations the mesh quality is not of particular importance for the in-silico SG P&D methodology.

Required inputs of the morphing algorithm are the meshed preinterventional vessel geometry, the centerline of the preinterventional vessel geometry as well as B-splines that describe the contour of the luminal vessel surface in a plane orthogonal to the vessel centerline. Each of these contour splines is described by ten points which serve as control points during mesh morphing. The mesh morphing process of the preinterventional vessel geometry onto the tubular shell consists of the following steps which are illustratively presented for a non-bifurcated vessel (cf. Figure 3.2):

1. Generation of straightened centerline and circular contour splines orthogonal to the straightened centerline.

2. Projection of the nodes of the patient's preinterventional vessel geometry onto the straight tubular shell. The projection method is based on a radial basis function regression that is constrained by the point correspondence between the control points (points of the contour splines) of the vessel geometry and the tubular shell. Each control point corresponds to the center of a radial basis function. Accordingly, the motion of each node of the mesh is governed by the motion of the control points weighted by the inverse distance between control point and node.

3. The result of step 2 does not yield the perfect tubular shape since the projection is based on a finite number of control points. Therefore, subsequent radial projection of the nodes is used to improve the recovery of the tubular shape.

4. Finally, Laplacian smoothing is used to improve element shapes of the meshed tubular shell.

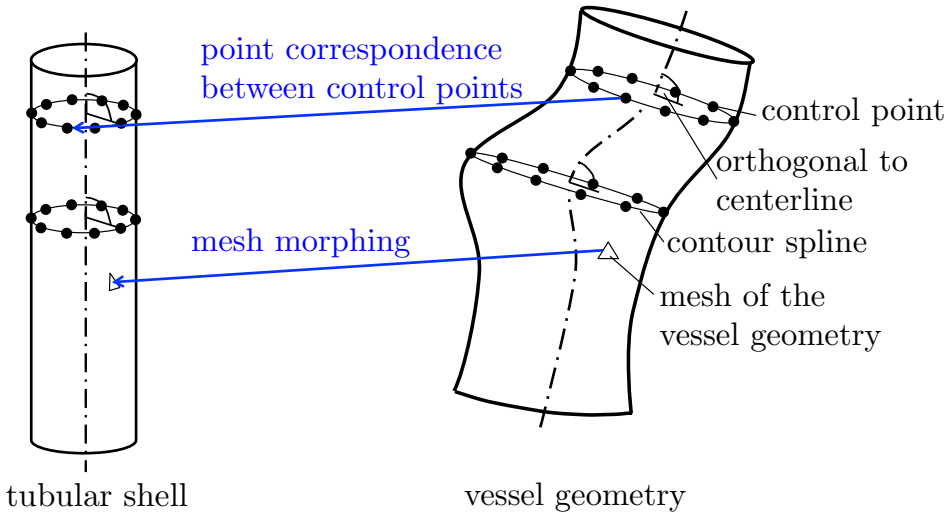

Figure 3.2 Visualization of the mesh morphing algorithm used to generate the mesh of the tubular shell of the virtual shell method. Figure is based on the work in [204].

3.2.2. 3D morphing algorithm based on control curves

The in-silico SG P&D methodology proposed in this thesis is based on a morphing algorithm that is directly applied to the SG. In contrast, existing methodologies either apply the morphing algorithm to a virtual catheter (virtual catheter method) or to the vessel model (virtual shell method). Therefore, in this section, a 3D morphing algorithm is developed to morph tubular objects like SGs. Similar to the morphing algorithms of the virtual catheter method and the virtual shell method, the centerline of the straight, undeformed SG and the centerline of the preinterventional vessel centerline play a decisive role. These centerlines serve as so-called *control curves*[2].

The newly developed morphing algorithm is based on a dimensional reduction from the 3D morphing object to 1D control curves, where the definition of rotation minimizing frames provides a unique mapping between the 1D control curves and the 3D morphing object at any stage of the morphing process. For a simplified representation, the basic theoretical aspects of the morphing algorithm are presented for one control curve which is able to morph non-bifurcated SGs. However, the extension to multiple control curves is straight forward and will be introduced when the in-silico SG P&D methodology of bifurcated SGs is presented in Section 3.5.2. In addition to the in-silico SG P&D methodology, the 3D morphing algorithm developed in this section will be utilized for the stent predeformation methodology in Section 3.4.3 and an in-silico SG sizing tool in Section 3.5.3. In this section, the theoretical aspects of the morphing algorithm first will be described in an abstract manner, i.e., independent of the underlying in-silico EVAR model. Afterwards, the morphing algorithm is concretized and applied to in-silico EVAR.

From a mechanical perspective the morphing process describes a gradual transition of a body $\tilde{\Omega}^{\mathrm{B}}(t) \subset \mathbb{R}^3$ from its initial configuration $\tilde{\Omega}^{\mathrm{B}}_{\mathrm{I}} = \tilde{\Omega}^{\mathrm{B}}(t_{\mathrm{I}}) \subset \mathbb{R}^3$ into the target configuration $\tilde{\Omega}^{\mathrm{B}}_{\mathrm{T}} = \tilde{\Omega}^{\mathrm{B}}(t_{\mathrm{T}}) \subset \mathbb{R}^3$. In the context of this thesis, the morphing algorithm is restricted to discretized bodies described by $n^{\mathrm{B}}_{\mathrm{node}}$ nodes with the coordinates $\tilde{\boldsymbol{x}}^i_{\mathrm{I}} \in \tilde{\Omega}^{\mathrm{B}}_{\mathrm{I}}$ and $\tilde{\boldsymbol{x}}^i_{\mathrm{T}} \in \tilde{\Omega}^{\mathrm{B}}_{\mathrm{T}}$, respectively, with $i = 1, 2, ..., n^{\mathrm{B}}_{\mathrm{node}}$. The objective is to find all intermediate configurations $\tilde{\Omega}^{\mathrm{B}}(t) \subset \mathbb{R}^3 \times \mathcal{T} \setminus \{t_{\mathrm{I}}, t_{\mathrm{T}}\}$ with the nodal coordinates $\tilde{\boldsymbol{x}}^i(t) \in \tilde{\Omega}^{\mathrm{B}}(t)$ and $\mathcal{T} = [t_{\mathrm{I}}, t_{\mathrm{T}}]$ satisfying the following conditions:

- **Mechanical compatibility:** Maintain the proper history of mechanical quantities with regard to the stress-free reference configuration.
- **Smoothness:** The transition from $\tilde{\Omega}^{\mathrm{B}}_{\mathrm{I}}$ to $\tilde{\Omega}^{\mathrm{B}}_{\mathrm{T}}$ has to be smooth in space and in pseudo-time t.

The notation $(\tilde{\bullet})$ is used to indicate that the morphing algorithm is a pure geometrical problem. Nevertheless, for a consistent embedding into the mechanical framework of the BVP (cf. Section 3.1), the first of the above conditions is required. To satisfy the second condition, morphing algorithms generally deal with two main issues:

- **Point correspondence:** Establishing a correspondence of each point (or node) of $\tilde{\Omega}^{\mathrm{B}}_{\mathrm{I}}$ to a point (or node) of $\tilde{\Omega}^{\mathrm{B}}_{\mathrm{T}}$.
- **Path interpolation:** Creating an interpolation along a pseudo-time t between all corresponding points.

[2] According to [21] who introduced the term "control primitives".

In particular, the point correspondence problem can be challenging in general 3D problems. Thus, a common way is to reduce the dimensionality of the problem during the morphing process to 2D [132], 1D [21] or even 0D [36]. This approach called "field morphing" or "feature-based metamorphosis" was first introduced by Beier et al. [21] for morphing problems in 2D. The presented morphing algorithm strongly follows the idea of Beier et al. [21] and Lerios et al. [153] who reduced a multidimensional morphing object to 1D curves.

The subsequent presentation of the 3D morphing algorithm is structured as follows: First, the mapping between the 3D morphing object and the 1D control curve as well as the definition of local rotation minimizing frames is given in Section 3.2.2.1. Subsequently, point correspondence and path interpolation techniques are presented in Section 3.2.2.2. Accuracy and robustness of the morphing algorithm are tested for a straight tube demonstrator in Section 3.2.2.3 and the link toward the application of the morphing algorithm to in-silico EVAR is provided in Section 3.2.2.4.

3.2.2.1. Mapping between morphing object and control curve

Given a piecewise linear approximation $\mathcal{C}(t) \subset \mathbb{R}^3 \times \mathcal{T}$ to a 1D curve described by n_C discrete points in its initial configuration $\mathcal{C}_\mathrm{I} = \mathcal{C}(t_\mathrm{I}) \subset \mathbb{R}^3, \quad \tilde{\boldsymbol{x}}^j_{\mathrm{C,I}} \in \mathcal{C}_\mathrm{I}$ and in its target configuration $\mathcal{C}_\mathrm{T} = \mathcal{C}(t_\mathrm{T}) \subset \mathbb{R}^3, \quad \tilde{\boldsymbol{x}}^j_{\mathrm{C,T}} \in \mathcal{C}_\mathrm{T}$ with $j = 1, 2, ..., n_\mathrm{C}$, it is possible to define a unique deformation path of the 3D body from $\tilde{\Omega}^\mathrm{B}_\mathrm{I}$ to $\tilde{\Omega}^\mathrm{B}_\mathrm{T}$ based on the deformation of the curve from $\mathcal{C}_\mathrm{I}$ to $\mathcal{C}_\mathrm{T}$ (cf. Figure 3.3I). In doing so, the dimensionality of the problem is reduced from general 3D morphing objects $\tilde{\Omega}^\mathrm{B}$ to 1D curves $\mathcal{C}$. Hence, the two main issues of the morphing algorithm, point correspondence and path interpolation, only have to be established for 1D curves. In contrast, to classical morphing algorithms, the target configuration of the morphing object $\tilde{\Omega}^\mathrm{B}_\mathrm{T}$ is unknown. Only the initial configuration of the morphing object $\tilde{\Omega}^\mathrm{B}_\mathrm{I}$, the initial configuration of the curve $\mathcal{C}_\mathrm{I}$ and the target configuration of the curve $\mathcal{C}_\mathrm{T}$ are given (cf. Figure 3.3).

Obviously, at any pseudo-time t a map between the 1D curve $\mathcal{C}$, in the following called *control curve*, and the 3D body $\tilde{\Omega}^\mathrm{B}$ is required. Accordingly, the map

$$\boldsymbol{\varphi} : \begin{cases} \tilde{\Omega}^\mathrm{B}(t) & \rightarrow & \mathcal{C}(t) \\ \tilde{\boldsymbol{x}}^i(t) & \mapsto & \tilde{\boldsymbol{x}}^j_\mathrm{C}(\tilde{\boldsymbol{x}}^i(t)) \end{cases} \tag{3.10}$$

and its inverse

$$\boldsymbol{\varphi}^{-1} : \begin{cases} \mathcal{C}(t) & \rightarrow & \tilde{\Omega}^\mathrm{B}(t) \\ \tilde{\boldsymbol{x}}^j_\mathrm{C}(t) & \mapsto & \tilde{\boldsymbol{x}}^i(\tilde{\boldsymbol{x}}^j_\mathrm{C}(t)) \end{cases} \tag{3.11}$$

are defined.

The mapping is based on the definition of n_C local, orthonormal coordinate frames $(\boldsymbol{tnb})^j(t)$ at each point of the control curve tangentially aligned to the curve at any pseudo-time $t \in \mathcal{T}$, where $\boldsymbol{t}^j(t)$ is the unit tangent vector, $\boldsymbol{n}^j(t)$ the unit normal vector and $\boldsymbol{b}^j(t)$ the unit binormal vector (cf. Figure 3.4).

The resulting description must be independent of the orientation of the control curve $\mathcal{C}(t)$ in $\mathbb{R}^3$. This means the local coordinate frames $(\boldsymbol{tnb})^j(t)$ have to be uniquely defined for any configuration $\mathcal{C}(t)$ of the control curve at any pseudo-time $t \in \mathcal{T}$. The base vectors $\boldsymbol{t}^j(t)$, $\boldsymbol{n}^j(t)$

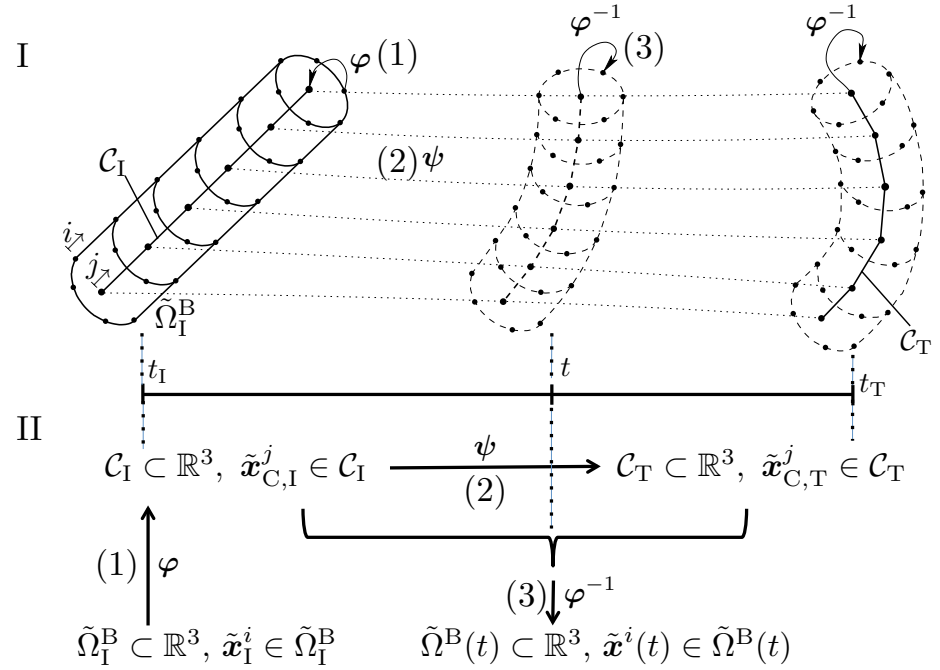

Figure 3.3 Schematic overview (I) and algorithmic overview (II) of the proposed morphing algorithm based on control curves consisting of three main steps: (1) initialization, i.e., mapping from $\tilde{\Omega}^\mathrm{B}_\mathrm{I}$ to $\mathcal{C}_\mathrm{I}$; (2) path interpolation; (3) inverse mapping from $\mathcal{C}(t)$ to $\tilde{\Omega}^\mathrm{B}(t)$. Solid lines indicate the given configurations $\tilde{\Omega}^\mathrm{B}_\mathrm{I}$, $\mathcal{C}_\mathrm{I}$ and $\mathcal{C}_\mathrm{T}$. Dashed lines refer to unknown configurations of $\tilde{\Omega}^\mathrm{B}$ and $\mathcal{C}$. Reproduced with permission from [107].

and $\boldsymbol{b}^j(t)$ change over pseudo-time t, but for reasons of clarity the pseudo-time t is not explicitly written as function parameter in the following. Unless specified differently, the variables are valid for any pseudo-time $t \in \mathcal{T}$.

Whereas the definition of the unit tangent vector $\boldsymbol{t}^j = \frac{\boldsymbol{\mathcal{C}}'^j}{||\boldsymbol{\mathcal{C}}'^j||}$ is straight forward with $\boldsymbol{\mathcal{C}}'^j$ being the first derivative of the curve at point j, the definition of $\boldsymbol{n}^j$ and $\boldsymbol{b}^j$ in general is not unique. The so-called *Frenet frame* (FF) is the most common definition of $\boldsymbol{n}^j$ and $\boldsymbol{b}^j$ since it can be analytically calculated by

$$\boldsymbol{t}^j_\mathrm{FF} = \frac{\boldsymbol{\mathcal{C}}'^j}{||\boldsymbol{\mathcal{C}}'^j||}, \quad \boldsymbol{b}^j_\mathrm{FF} = \frac{\boldsymbol{\mathcal{C}}'^j \times \boldsymbol{\mathcal{C}}''^j}{||\boldsymbol{\mathcal{C}}'^j \times \boldsymbol{\mathcal{C}}''^j||}, \quad \boldsymbol{n}^j_\mathrm{FF} = \boldsymbol{b}^j_\mathrm{FF} \times \boldsymbol{t}^j_\mathrm{FF}, \quad \forall\, j = 1, 2, ..., n_\mathrm{C}, \tag{3.12}$$

where $\boldsymbol{\mathcal{C}}'^j$ is the first derivative and $\boldsymbol{\mathcal{C}}''^j$ is the second derivative of the curve at point j. However, Frenet frames are not applicable to a wide range of general curves in 3D due to their drawback of not being defined at points where the curvature of the curve vanishes, i.e., at points where $\boldsymbol{\mathcal{C}}''^j = \boldsymbol{0}$. As a consequence, at straight sections of a curve and at inflection points, the normal vector can reverse direction leading to an inappropriate rotation of the Frenet frames around the tangent vector of the curve as extensively demonstrated for instance by Wang et al. [271]. Therefore, Frenet frames are not applied in this thesis.

A frame that does not rotate around the tangent vector when moving along the curve is called a *rotation minimizing frame* (RMF) [271]. In the present algorithm, a discrete form of a RMF def-

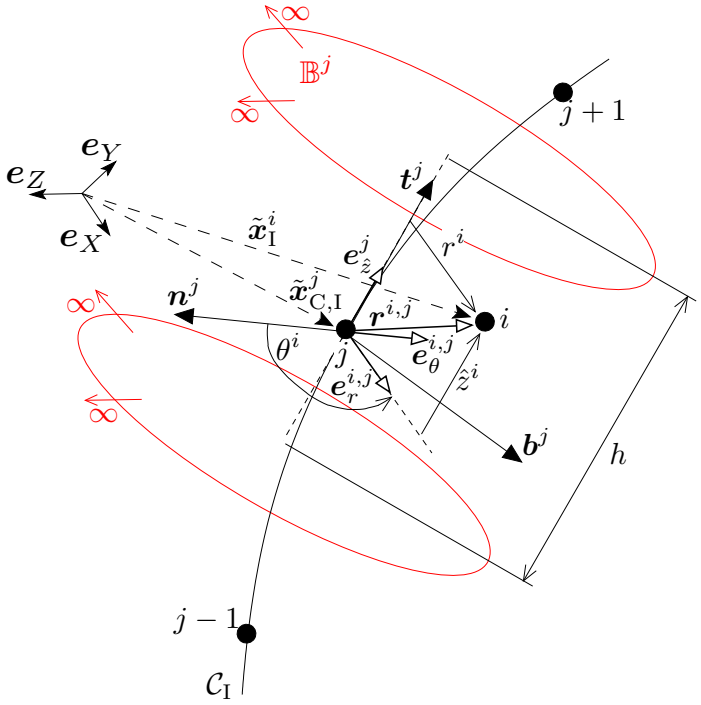

Figure 3.4 Illustration of the local cylindrical coordinate system and the bounding box (red) around point j of the control curve $\mathcal{C}_{\mathrm{I}}$. Reproduced with permission from [107].

inition [99, 140, 271] is used. Such a set of n_{C} local frames $(\boldsymbol{tnb})^j$ is called rotation minimized if

$$\boldsymbol{t}^j = \frac{\boldsymbol{\mathcal{C}}'^j}{||\boldsymbol{\mathcal{C}}'^j||} = \frac{\frac{1}{2}(\tilde{\boldsymbol{x}}^{j+1}_{\mathrm{C}} - \tilde{\boldsymbol{x}}^{j-1}_{\mathrm{C}})}{||\frac{1}{2}(\tilde{\boldsymbol{x}}^{j+1}_{\mathrm{C}} - \tilde{\boldsymbol{x}}^{j-1}_{\mathrm{C}})||}, \tag{3.13}$$

$$\boldsymbol{n}^j = \underset{\boldsymbol{n}}{\operatorname{argmin}} \left(\sum_{j=1}^{n_{\mathrm{C}}} |\tau^j| \, ||\boldsymbol{\mathcal{C}}'^j|| \right), \tag{3.14}$$

$$\boldsymbol{n}^j \cdot \boldsymbol{t}^j = 0, \tag{3.15}$$

$$\boldsymbol{b}^j = \boldsymbol{t}^j \times \boldsymbol{n}^j, \quad \forall\, j = 1, 2, ..., n_{\mathrm{C}} \tag{3.16}$$

holds. Equation (3.14) states that for RMFs the total angle of rotation of the normal vectors $\boldsymbol{n}^j$ around curve $\mathcal{C}$ has to be minimal where the torsion

$$\tau^j = -\boldsymbol{n}^j \cdot \boldsymbol{b}'^j \tag{3.17}$$

is a measure of the speed of rotation of the normal vector around the control curve at point j [73, 271] with $\boldsymbol{b}'^j$ being the first derivative of the binormal vector at point j. Equations (3.15) and (3.16) preserve the orthogonality property of the triads $(\boldsymbol{tnb})^j$. Accordingly, the triad $(\boldsymbol{tnb})^j$ at any point j is given by the solution of an initial-value problem [140], where $\boldsymbol{n}^1$ and $\boldsymbol{b}^1$ at point $j = 1$ can be chosen arbitrarily[3].

[3]Obviously the orthogonality property of the triad according to Equations (3.15) and (3.16) has to be preserved.

A number of powerful methods to approximate the given problem are available [24, 140, 271]. In this thesis, the approximation in Bloomenthal [24] is applied which allows an explicit computation of all n_C local frames starting from a given frame spanned by the unit vectors $\boldsymbol{t}^1$, $\boldsymbol{n}^1$ and $\boldsymbol{b}^1$ at point $j = 1$. Accordingly, the triad at point j is defined by

$$\boldsymbol{t}^j = \frac{\boldsymbol{\mathcal{C}}'^j}{||\boldsymbol{\mathcal{C}}'^j||} = \frac{\frac{1}{2}(\tilde{\boldsymbol{x}}_\mathrm{C}^{j+1} - \tilde{\boldsymbol{x}}_\mathrm{C}^{j-1})}{||\frac{1}{2}(\tilde{\boldsymbol{x}}_\mathrm{C}^{j+1} - \tilde{\boldsymbol{x}}_\mathrm{C}^{j-1})||}, \tag{3.18}$$

$$\boldsymbol{n}^j = \frac{\boldsymbol{b}^{j-1} \times \boldsymbol{t}^j}{||\boldsymbol{b}^{j-1} \times \boldsymbol{t}^j||}, \tag{3.19}$$

$$\boldsymbol{b}^j = \frac{\boldsymbol{t}^j \times \boldsymbol{n}^j}{||\boldsymbol{t}^j \times \boldsymbol{n}^j||}, \quad \forall\, j = 2, 3, ..., n_\mathrm{C}. \tag{3.20}$$

In Section 3.2.2.3, it is demonstrated that this is an approximation of the exact initial-value problem of RMFs, which is largely sufficient for the presented application and also represents an exact solution of the RMFs for the trivial case of straight segments of curves ($\tau^j = 0$).

As initialization of the morphing algorithm, at each point j of the control curve in the initial configuration with $\tilde{\boldsymbol{x}}_{\mathrm{C,I}}^j \in \mathcal{C}_\mathrm{I}$, a semi-infinite bounding box $\mathbb{B}^j \subset \mathbb{R}^3$ spanned by two infinite planes in the local $(\boldsymbol{nb})^j(t_\mathrm{I})$-plane with a search distance of h is used to assign the nodes i of the morphing object with $\tilde{\boldsymbol{x}}_\mathrm{I}^i \in \tilde{\Omega}_\mathrm{I}^\mathrm{B}$ to one point on the control curve $\mathcal{C}_\mathrm{I}$ (cf. Figure 3.4). Accordingly, the semi-infinite bounding box $\mathbb{B}^j$ is infinite in radial direction but finite in tangential direction. All nodes i of the morphing object $\tilde{\Omega}_\mathrm{I}^\mathrm{B}$ with $\tilde{x}_\mathrm{I}^i \in \mathbb{B}^j$ are assigned to point j of the control curve $\mathcal{C}_\mathrm{I}$ and are put into the subset $\mathsf{A}_\mathrm{I}^j \subseteq \mathsf{A}_\mathrm{I} = \{1, 2, ..., n_\mathrm{node}^\mathrm{B}\}$ where

$$\bigcup_{j=1}^{n_\mathrm{C}} \mathsf{A}_\mathrm{I}^j = \mathsf{A}_\mathrm{I}, \tag{3.21}$$

$$\mathsf{A}_\mathrm{I}^j \cap \mathsf{A}_\mathrm{I}^k = \emptyset, \quad \forall k \neq j,\ j = 1, 2, ..., n_\mathrm{C},\ k = 1, 2, ..., n_\mathrm{C} \tag{3.22}$$

holds. According to Equation (3.21), all nodes $i = 1, 2, ..., n_\mathrm{node}^\mathrm{B}$ of the morphing object $\tilde{\Omega}_\mathrm{I}^\mathrm{B}$ are assigned to a point $j = 1, 2, ..., n_\mathrm{C}$ of the control curve $\mathcal{C}_\mathrm{I}$. Further, Equation (3.22) states that all subsets A_I^j are pairwise disjoint sets, i.e., every node $i = 1, 2, ..., n_\mathrm{node}^\mathrm{B}$ of the morphing object $\tilde{\Omega}_\mathrm{I}^\mathrm{B}$ is assigned to exactly one point $j = 1, 2, ..., n_\mathrm{C}$ of the control curve $\mathcal{C}_\mathrm{I}$. Within this section, it is restricted to a generic description of the morphing algorithm in which the subsets A^j are constant during the total morphing process, i.e.,

$$\mathsf{A}^j = \mathsf{A}_\mathrm{I}^j, \quad \forall\, j = 1, 2, ..., n_\mathrm{C}. \tag{3.23}$$

However, in Section 3.2.2.4, a different definition of A^j will be used for the application of the morphing algorithm to in-silico EVAR.

The primary objective of the described morphing algorithm is to morph tube-like structures such as SGs which are rotationally symmetric about the longitudinal axis. Hence, the position vectors $\tilde{\boldsymbol{x}}^i(t)$ of the morphing object are described in local cylindrical coordinate systems $(\boldsymbol{e}_r \boldsymbol{e}_\theta \boldsymbol{e}_{\hat{z}})^{i,j}(t)$ (cf. Figure 3.4). The relation between the previously introduced local frames $(\boldsymbol{tnb})^j(t)$ and the local cylindrical coordinate systems $(\boldsymbol{e}_r \boldsymbol{e}_\theta \boldsymbol{e}_{\hat{z}})^{i,j}(t)$ with the base vec-

tors $\boldsymbol{e}_r^{i,j}(t)$, $\boldsymbol{e}_\theta^{i,j}(t)$ and $\boldsymbol{e}_{\hat{z}}^{j}(t)$ is given by

$$\boldsymbol{e}_r^{i,j}(t) = \boldsymbol{n}^j(t)\cos(\theta^i) + \boldsymbol{b}^j(t)\sin(\theta^i), \tag{3.24}$$

$$\boldsymbol{e}_\theta^{i,j}(t) = -\boldsymbol{n}^j(t)\sin(\theta^i) + \boldsymbol{b}^j(t)\cos(\theta^i), \tag{3.25}$$

$$\boldsymbol{e}_{\hat{z}}^{j}(t) = \boldsymbol{t}^j(t), \quad \theta^i \in [0, 2\pi], \quad \forall\, i \in \mathsf{A}^j, \quad j = 1, 2, ..., n_\mathrm{C}. \tag{3.26}$$

Hence, the position vectors of the object $\tilde{\Omega}^\mathrm{B}$ to be morphed can be expressed by

$$\tilde{\boldsymbol{x}}^i(t) = \tilde{\boldsymbol{x}}_\mathrm{C}^j(t) + \boldsymbol{r}^{i,j}(t) = \tilde{\boldsymbol{x}}_\mathrm{C}^j(t) + r^i\boldsymbol{e}_r^{i,j}(t) + \hat{z}^i\boldsymbol{e}_{\hat{z}}^{j}(t), \quad \forall\, i \in \mathsf{A}^j, \quad j = 1, 2, ..., n_\mathrm{C}. \tag{3.27}$$

Consequently, the position $\tilde{\boldsymbol{x}}^i$ of all nodes $i \in \mathsf{A}^j$ of the morphing object $\tilde{\Omega}^\mathrm{B}$ assigned to point j of the control curve are described in the local cylindrical coordinate systems $(\boldsymbol{e}_r\boldsymbol{e}_\theta\boldsymbol{e}_{\hat{z}})^{i,j}(t)$ according to Equations (3.24)-(3.27), cf. Figure 3.4. Within this section, it is restricted to constant local cylindrical coordinates, i.e.,

$$r^i = r_\mathrm{I}^i,\ \hat{z}^i = \hat{z}_\mathrm{I}^i,\ \theta^i = \theta_\mathrm{I}^i, \quad \forall\, i = 1, 2, ..., n_\mathrm{node}^\mathrm{B}. \tag{3.28}$$

This means during the total morphing process, the local cylindrical coordinates r^i, $\hat{z}^i$ and θ^i are equal to the local cylindrical coordinates r_I^i, $\hat{z}_\mathrm{I}^i$ and θ_I^i that correspond to the initial configuration of the morphing object $\tilde{\Omega}_\mathrm{I}^\mathrm{B}$. However, as the cylindrical base vectors $\boldsymbol{e}_r^{i,j}(t)$, $\boldsymbol{e}_\theta^{i,j}(t)$ and $\boldsymbol{e}_{\hat{z}}^{i,j}(t)$ are aligned to the control curve $\mathcal{C}$ at any pseudo-time $t \in \mathcal{T}$, the base vectors $\boldsymbol{e}_r^{i,j}(t)$, $\boldsymbol{e}_\theta^{i,j}(t)$ and $\boldsymbol{e}_{\hat{z}}^{i,j}(t)$ change during the morphing process. The change in the base vectors $\boldsymbol{e}_r^{i,j}(t)$, $\boldsymbol{e}_\theta^{i,j}(t)$ and $\boldsymbol{e}_{\hat{z}}^{i,j}(t)$ leads to a transformation of the morphing object $\tilde{\Omega}^\mathrm{B}(t)$ from $\tilde{\Omega}_\mathrm{I}^\mathrm{B}$ to $\tilde{\Omega}_\mathrm{T}^\mathrm{B}$ based on the transformation of the control curve $\mathcal{C}(t)$ from $\mathcal{C}_\mathrm{I}$ to $\mathcal{C}_\mathrm{T}$ (cf. Figure 3.3). The transformation of the control curve $\mathcal{C}(t)$ over the pseudo-time t will be further specified in Section 3.2.2.2. In Section 3.2.2.4, a different definition of Equations (3.28) will be introduced in order to change the radius of the SG during morphing operations.

3.2.2.2. Point correspondence and path interpolation

In the previous section, the dimensionality of the problem was reduced from general 3D morphing objects $\tilde{\Omega}^\mathrm{B}$ to a 1D control curve $\mathcal{C}$. Thus, point correspondence and path interpolation are only an issue of the 1D control curve. The point correspondence

$$\tilde{\boldsymbol{x}}_{\mathrm{C,I}}^j \leftrightarrow \tilde{\boldsymbol{x}}_{\mathrm{C,T}}^j, \quad \forall\, j = 1, 2, ..., n_\mathrm{C} \tag{3.29}$$

is used between the two known configurations $\mathcal{C}_\mathrm{I}$ and $\mathcal{C}_\mathrm{T}$ of the control curve, i.e., the first point of configuration $\mathcal{C}_\mathrm{I}$ corresponds to the first point of configuration $\mathcal{C}_\mathrm{T}$, the second point of configuration $\mathcal{C}_\mathrm{I}$ corresponds to the second point of configuration $\mathcal{C}_\mathrm{T}$ and so on. Addressing the path interpolation problem, a map $\boldsymbol{\psi}(t)$ is required that generates the intermediate configuration $\mathcal{C}(t)$ at any pseudo-time $t \in \mathcal{T} \setminus \{t_\mathrm{I}, t_\mathrm{T}\}$ of the two known configurations $\mathcal{C}_\mathrm{I}$ and $\mathcal{C}_\mathrm{T}$, i.e.,

$$\boldsymbol{\psi} : \begin{cases} \mathcal{C}_\mathrm{I}, \mathcal{C}_\mathrm{T} & \rightarrow \quad \mathcal{C}(t) \\ \tilde{\boldsymbol{x}}_{\mathrm{C,I}}^j, \tilde{\boldsymbol{x}}_{\mathrm{C,T}}^j & \mapsto \quad \tilde{\boldsymbol{x}}_\mathrm{C}^j(t, \tilde{\boldsymbol{x}}_{\mathrm{C,I}}^j, \tilde{\boldsymbol{x}}_{\mathrm{C,T}}^j). \end{cases} \tag{3.30}$$

In this thesis, a simple linear path interpolation is applied despite some known shortcomings of linear interpolation between the initial configuration $\mathcal{C}_\mathrm{I}$ and the target configuration $\mathcal{C}_\mathrm{T}$ as described in detail in [5, 91]. The linear path interpolation is defined by

$$\tilde{\boldsymbol{x}}_\mathrm{C}^j(t) := (1 - \frac{t - t_\mathrm{I}}{t_\mathrm{T} - t_\mathrm{I}})\tilde{\boldsymbol{x}}_\mathrm{C,I}^j + \frac{t - t_\mathrm{I}}{t_\mathrm{T} - t_\mathrm{I}}\tilde{\boldsymbol{x}}_\mathrm{C,T}^j, \quad \forall\, j = 1, 2, ..., n_\mathrm{C}, \tag{3.31}$$

To prevent the morphing object $\tilde{\Omega}^\mathrm{B}$ from spurious torsion between two different configurations $\tilde{\Omega}^\mathrm{B}(t)$ and $\tilde{\Omega}^\mathrm{B}(t + \Delta t)$, the same explicit RMF scheme of Equations (3.18)-(3.20) is applied not only in space but also in pseudo-time t. The RMF computation in pseudo-time t is done only for the local coordinate system of the first point ($j = 1$) of the control curve $\mathcal{C}$ as all other RMFs for $j > 1$ are explicitly computed by the RMF scheme in space as defined in Equations (3.18)-(3.20). Hence, from arbitrarily chosen base vectors $\boldsymbol{n}^1(t_\mathrm{I})$ and $\boldsymbol{b}^1(t_\mathrm{I})$ at point $j = 1$ of $\mathcal{C}_\mathrm{I}$, all other RMFs at point $j = 1$ of $\mathcal{C}(t)$ with $t \in \mathcal{T} \setminus \{t_\mathrm{I}\}$ can be computed explicitly according to

$$\boldsymbol{t}^1(t + \Delta t) = \frac{\boldsymbol{\mathcal{C}}(t + \Delta t)'^1}{||\boldsymbol{\mathcal{C}}(t + \Delta t)'^1||}, \tag{3.32}$$

$$\boldsymbol{n}^1(t + \Delta t) = \frac{\boldsymbol{b}^1(t) \times \boldsymbol{t}^1(t + \Delta t)}{||\boldsymbol{b}^1(t) \times \boldsymbol{t}^1(t + \Delta t)||}, \tag{3.33}$$

$$\boldsymbol{b}^1(t + \Delta t) = \frac{\boldsymbol{t}^1(t + \Delta t) \times \boldsymbol{n}^1(t + \Delta t)}{||\boldsymbol{t}^1(t + \Delta t) \times \boldsymbol{n}^1(t + \Delta t)||}, \tag{3.34}$$

where $\boldsymbol{\mathcal{C}}'^1$ is the first spatial derivative of the control curve at point $j = 1$ and Δt is the pseudo-time step size.

Morphing algorithms may induce self-intersections leading to unphysical configurations of $\tilde{\Omega}^\mathrm{B}$. In particular, local self-intersections have to be prevented. Local self-intersections arise if the radius of curvature r_κ^j of the control curve is smaller than the local radius r^i of the morphing object at this point. Hence, during the whole morphing operation

$$f_r^j(t) = \max\left(\frac{r_\kappa^j(t)}{r^i}\right) = \max\left(\frac{1}{||\boldsymbol{\mathcal{C}}''^j||\, r^i}\right) > \epsilon_r, \quad \forall\, i \in \mathsf{A}^j \tag{3.35}$$

has to be guaranteed, where $\epsilon_\mathrm{r} > 1$ is a user-defined tolerance and r_κ^j is the radius of curvature of the control curve at point j. In the limit case of a straight control curve, the radius of curvature r_κ^j of the control curve is infinity at any point $j = 1, 2, ..., n_\mathrm{C}$ and the condition of Equation (3.35) is satisfied for any radius r^i of the morphing object.

As condition (3.35) would restrict the algorithm to relatively straight control curves, local smoothing of the curve is used which locally increases the radius of curvature r_κ^j of the control curve such that condition (3.35) is satisfied. In the presented approach, local, iterative Laplacian smoothing according to

$$\tilde{\boldsymbol{x}}_\mathrm{C}^j(t) = \begin{cases} \frac{1}{2}(\tilde{\boldsymbol{x}}_\mathrm{C}^{j-1}(t) + \tilde{\boldsymbol{x}}_\mathrm{C}^{j+1}(t)), & f_r^j(t) \leq \epsilon_r \\ \tilde{\boldsymbol{x}}_\mathrm{C}^j(t), & f_r^j(t) > \epsilon_r \end{cases}, \quad \forall\, j = 1, 2, ..., n_\mathrm{C} \tag{3.36}$$

is applied at locations where condition (3.35) is violated. The number of required smoothing iterations depends on the shape of the control curve. Laplacian smoothing induced shrinkage is removed by edge length scaling of all subsequent points of point j

$$\tilde{\boldsymbol{x}}_{\mathrm{C}}^{k}(t) = \tilde{\boldsymbol{x}}_{\mathrm{C}}^{k-1}(t) + \Delta s^{j}\boldsymbol{t}^{j}, \quad \forall\, k \geq j,\ j = 1, 2, ..., n_{\mathrm{C}}, \tag{3.37}$$

where Δs^j is the mean edge length of the two adjacent edges of point j. Due to the inherent map $\boldsymbol{\varphi}^{-1}$ of Equation (3.11) any smoothing of the control curve $\mathcal{C}$ results in a smoothed morphing object $\tilde{\Omega}^{\mathrm{B}}$ as well.

In summary, the proposed morphing algorithm computes all configurations $\tilde{\Omega}^{\mathrm{B}} \subset \mathbb{R}^3 \times (t_{\mathrm{I}}, t_{\mathrm{T}}]$ of the morphing object from the given initial configuration of the morphing object $\tilde{\Omega}_{\mathrm{I}}^{\mathrm{B}}$, the initial configuration of the control curve $\mathcal{C}_{\mathrm{I}}$ and the target configuration of the control curve $\mathcal{C}_{\mathrm{T}}$ (cf. Figure 3.3). The morphing algorithm is the solution to a purely geometric problem, i.e., the BVP stated in Section 3.1 does not have to be solved to obtain the deformation of the morphing object$\tilde{\Omega}^{\mathrm{B}}$.

3.2.2.3. Numerical example of a straight tube demonstrator

In this section, an exemplary straight tube demonstrator is morphed to show the accuracy and robustness of the morphing algorithm based on control curves with RMF. The discretized tube demonstrator and its centerline (control curve $\mathcal{C}_{\mathrm{I}}$) are given at pseudo-time $t = t_{\mathrm{I}} = 0.0$. Using the proposed morphing algorithm, the straight tube demonstrator is morphed to a highly bend configuration at $t = t_{\mathrm{T}} = 1.0$ which is defined by the given control curve $\mathcal{C}_{\mathrm{T}}$ at $t = t_{\mathrm{T}} = 1.0$ (cf. Figure 3.5I+II). The control curve $\mathcal{C}_{\mathrm{T}}$ in the target configuration ($t = t_{\mathrm{T}} = 1.0$) is arbitrarily orientated in the global coordinate system to show the general applicability of the morphing algorithm in 3D. The resulting morphing process has to be smooth in pseudo-time $t \in [t_{\mathrm{I}}, t_{\mathrm{T}}] = [0.0, 1.0]$ and space $s \in [0.0, 1.0]$ where s is the arc length parameter of the control curve of constant length 1. The deformation of the tube demonstrator is fully described by morphing constraints, i.e., the given problem is a pure geometrical problem and the BVP of Section 3.1 does not have to be solved. The RMF property according to Equations (3.18)-(3.20) and (3.32)-(3.34) of the local coordinate frames aligned to the control curve is investigated in detail as this property is essential to obtain a smooth morphing process.

All intermediate configurations of the control curve $\mathcal{C}(t)$ with $t \in (t_{\mathrm{I}}, t_{\mathrm{T}})$ are determined as interpolation between the given initial configuration $\mathcal{C}(t_{\mathrm{I}}) = \mathcal{C}_{\mathrm{I}}$ and the given target configuration $\mathcal{C}(t_{\mathrm{T}}) = \mathcal{C}_{\mathrm{T}}$ according to Equation (3.31). The inherent mapping according to Equation (3.11) between 1D control curve and 3D morphing object (i.e., the tube demonstrator) is based on local RMFs defined at each point of the control curve at any time $t \in [t_{\mathrm{I}}, t_{\mathrm{T}}]$.

The RMF property in pseudo-time t is qualitatively visualized in Figure 3.5I. Red color markers on the bottom of the tube at $t = 0.0$ indicate the direction of the normal vectors of the locally defined coordinate frames. The red color markers transform smoothly in time without undesired torsion around the centerline of the tube. Without specification of the RMF in pseudo-time t, the tube would exhibit spurious rotations around its centerline when transforming in pseudo-time t.

The RMF property in space is additionally visualized in Figure 3.5II where the arrows are the normal vectors $\boldsymbol{n}^j(t)$ of the local coordinate frames aligned to the control curve at any pseudo-time t. The normal vectors $\boldsymbol{n}^j(t)$ indicate the orientation of the local coordinate frames. Due

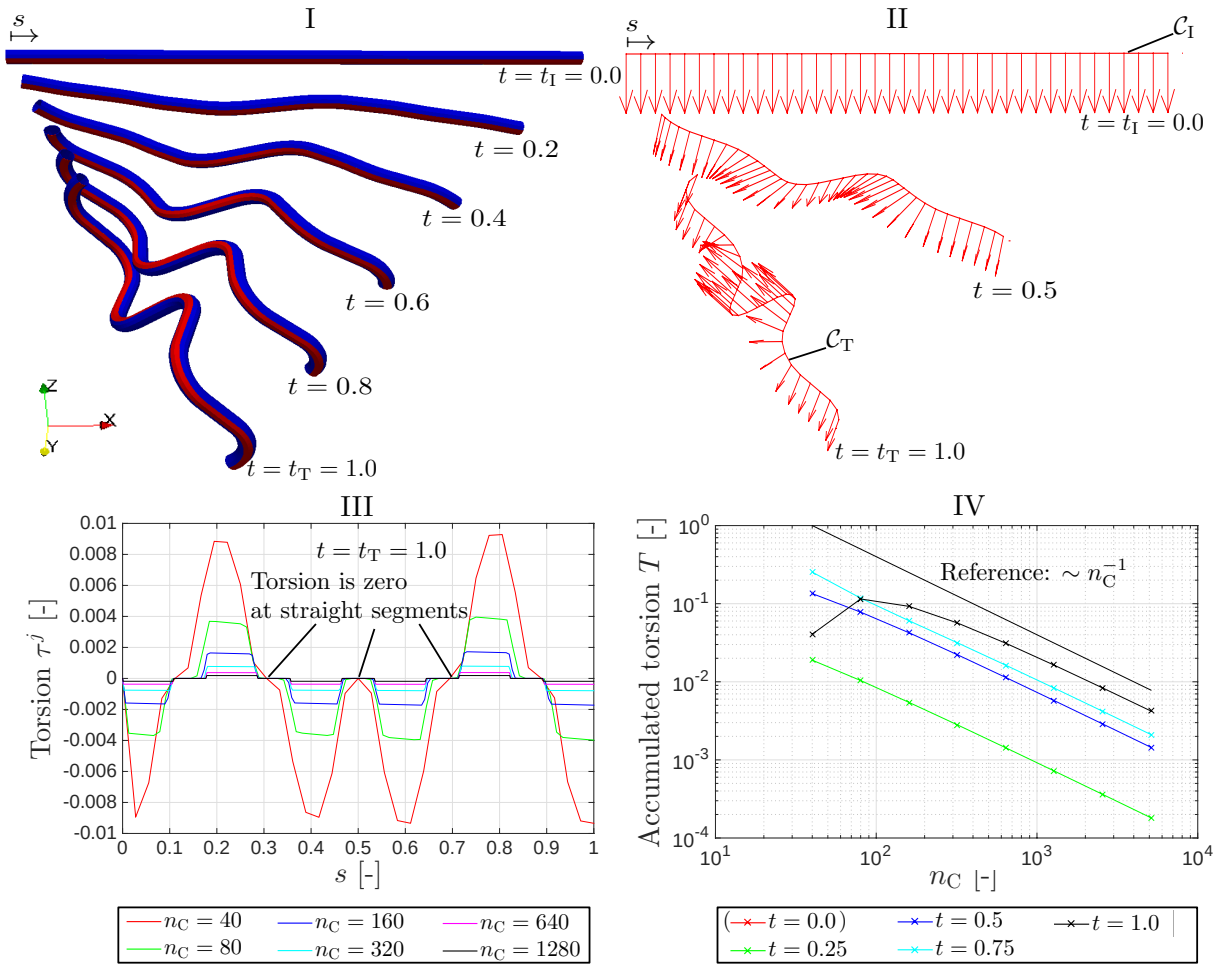

Figure 3.5 Morphing of an exemplary straight tube demonstrator to a highly bend tube. Red markers indicate the direction of normal vectors of the locally defined coordinate frames (I). Visualization of normal vectors of the locally defined coordinate frames according to the RMF definition (II). Local (III) and accumulated (IV) convergence behavior of the RMF approximation for refinement of the control curve. In (IV), the curve for $t = 0.0$ is not visible in the logarithmic scale as $T = 0$ for the perfectly straight curve. Reproduced with permission from [106].

to the RMF property in space $s \in [0.0, 1.0]$, the orientation of the normal vector $\boldsymbol{n}^j(t)$ varies smoothly along the spatial coordinate s. Any non-smooth variation of the orientation of the normal vectors along s would result in an undesirable torsion τ^j of the morphing object.

In Figure 3.5III and 3.5IV, the convergence behavior of the suggested RMF approximation according to Equations (3.18)-(3.20) is investigated for different discretizations of the control curve discretized by n_C points. By refinement of the control curve ($n_\mathrm{C} \to \infty$), the local torsion converges to $\tau^j = 0$ (cf. Figure 3.5III, plotted for $t = 1.0$). The configuration $\mathcal{C}_\mathrm{T} = \mathcal{C}(t = 1.0)$ of the control curve consists of five straight segments arbitrarily oriented in space (e.g., in the middle of the tube: $s = [0.47, 0.53]$). At these straight segments the RMF approximation scheme even leads to the exact solution of $\tau^j = 0$ independent of the discretization of the curve with exception of $n_\mathrm{C} = 40$ which discretization is too coarse to geometrically capture the straight

segments. This property is essential for morphing SGs as SGs in the undeformed configuration naturally are straight.

Figure 3.5IV illustrates the convergence behavior of the accumulated torsion

$$T = \sum_{j=1}^{n_{\mathrm{C}}} |\tau^j| \; ||\boldsymbol{\mathcal{C}}'^j|| \tag{3.38}$$

which is a measure of the total angle of rotation of the normal vectors $\boldsymbol{n}^j(t)$ around curve $\mathcal{C}$. In Equation (3.38), τ^j is the torsion at point j and $\boldsymbol{\mathcal{C}}'^j$ is the first derivative of the control curve $\mathcal{C}$ at point j. The convergence behavior is of first order independent of the considered pseudo-time step t. For $t = 1.0$ coarse discretizations are not able to capture the full geometry of the curve as was already discussed for the local convergence behavior in Figure 3.5III. The curve for $t = 0.0$ is not visible in the logarithmic scale of Figure 3.5IV as $T = 0$ for the perfectly straight curve.

3.2.2.4. Toward the application to in-silico EVAR

In this section, abstract definitions of morphing maps are introduced to provide the transition from pure geometrical morphing to the application to in-silico EVAR. In contrast to the previous sections, now the morphing operations are applied to physical bodies (e.g., stent and graft) underlying the BVP of Equations (3.1)-(3.7). Nevertheless, morphing operations, as introduced in this thesis, are purely geometric operations, i.e., by the application of a morphing operation to a physical body, the physical body will be subject to certain geometric morphing constraints. Thus, morphing maps will be expressed with $\tilde{(\bullet)}$ in this thesis. In the presented in-silico EVAR model, morphing maps will be applied to change both the current configuration Ω of a body as well as to change the reference configuration Ω_0 of a body. To clearly distinguish between a change in the *current configuration* and a change in the *reference configuration*, any morphing map that changes the *current configuration* is denoted by a small letter $\tilde{\boldsymbol{m}}$ and any morphing map that changes the *reference configuration* by a capital letter $\tilde{\boldsymbol{M}}$.

In Section 3.2.2.2, the pseudo-time $t \in [t_{\mathrm{I}}, t_{\mathrm{T}}]$ was introduced, which describes the interpolation between the two known configurations of the control curve $\mathcal{C}_{\mathrm{I}}$ and $\mathcal{C}_{\mathrm{T}}$ according to Equation (3.31). This means the pseudo-time t describes the deformation of the morphing object according to the evolution of the control curve $\mathcal{C}(t)$. This *control curve induced deformation* of the morphing object according to the pseudo-time t is used in the in-silico SG placement. Independently of the control curve induced deformation of the morphing object, a prescribed *change in the radius* of the morphing object and a prescribed *release of the morphing constraints* are used in the proposed in-silico EVAR model.

A prescribed change in the radius of the morphing object by the factor Δr is induced by redefining Equation (3.28) such that the local radius r^i of the morphing object is given by

$$r^i = r^i_{\mathrm{I}} + \Delta r, \quad \forall\, i = 1, 2, ..., n^{\mathrm{B}}_{\mathrm{node}}, \tag{3.39}$$

where r^i_{I} are the local radii of the morphing object in the initial state corresponding to the initial configuration $\mathcal{C}_{\mathrm{I}}$ of the control curve and $n^{\mathrm{B}}_{\mathrm{node}}$ is the number of nodes of the morphing object. This prescribed change in the radius is used in the in-silico SG placement to apply radial crimp-

ing to the SG. Moreover, this prescribed change in the radius of the morphing object will be used in a novel stent predeformation methodology.

A prescribed release of the morphing constraints is induced by the redefinition of the morphing sets A^j with $j = 1, 2, ..., n_\mathrm{C}$ according to Equation (3.23). If the deformation of a node of the morphing object is prescribed by the morphing induced deformation or not, depends on whether this node is part of the total set of morphed nodes

$$\mathsf{A} = \bigcup_{j=1}^{n_\mathrm{C}} \mathsf{A}^j, \tag{3.40}$$

i.e., whether this nodes is assigned to any of the points of the control curve $\mathcal{C}$, cf. Equation (3.21). This means that by emptying the sets A^j a prescribed release of the morphing constraints is possible. A prescribed release of the morphing constraints will be used in the in-silico SG deployment.

As the three morphing operations, *control curve induced deformation*, *radius change of the morphing object* and *release of the morphing constraints* shall be independent of each other, a second pseudo-time $\xi \in [0, 1]$ is introduced which defines the progress of the applied morphing maps $\tilde{\boldsymbol{M}}(\xi)$ and $\tilde{\boldsymbol{m}}(\xi)$. Hence, $t(\xi)$ defining the control curve induced deformation, $\Delta r(\xi)$ defining the radius change of the morphing object and $\mathsf{A}^j(\xi)$ defining the release of the morphing constraints are functions of the pseudo-time ξ, i.e., they depend on the progress of the applied morphing map. Although, the morphing algorithm as introduced in previous sections operates on discretized bodies, the following morphing maps are formulated with respect to the continuous representations of $\boldsymbol{X} \in \Omega_0$ and $\boldsymbol{x} \in \Omega$, respectively. Hence, the continuous coordinates $\boldsymbol{X}$ and $\boldsymbol{x}$ are used instead of the nodal coordinates $\boldsymbol{X}^i$ and $\boldsymbol{x}^i$ which are related by the finite element discretization as introduced in Section 2.2.

Accordingly, the change in the *reference configuration* from $\Omega_0|_{\xi=0}$ to $\Omega_0|_{\xi=1}$ by a geometrically prescribed morphing process is defined by the diffeomorphic morphing map

$$\tilde{\boldsymbol{M}}\big(t(\xi), \Delta r(\xi), \mathsf{A}^j(\xi)\big) : \begin{cases} \Omega_0|_{\xi=0} & \rightarrow & \Omega_0|_{\xi=1} \\ \boldsymbol{X}|_{\xi=0} & \mapsto & \boldsymbol{X}|_{\xi=1} \end{cases}, \tag{3.41}$$

where $\Omega_0|_{\xi=0}$, $\boldsymbol{X}|_{\xi=0} \in \Omega_0|_{\xi=0}$ describes the stress-free reference configuration at the beginning of the morphing process ($(\bullet)\,|_{\xi=0}$), i.e., at $\xi = 0$. At the end of the morphing process ($(\bullet)\,|_{\xi=1}$), the reference configuration is given by $\Omega_0|_{\xi=1}$, $\boldsymbol{X}|_{\xi=1} \in \Omega_0|_{\xi=1}$. In-between, i.e., for $\xi \in (0, 1)$, the reference configuration is determined by an interpolation between the configurations $\Omega_0|_{\xi=0}$ and $\Omega_0|_{\xi=1}$ which is driven by $t(\xi)$, $\Delta r(\xi)$ and $\mathsf{A}^j(\xi)$.

Analogously, the change in the *current configuration* from $\Omega|_{\xi=0}$ to $\Omega|_{\xi=1}$ by a geometrically prescribed morphing process is defined by the diffeomorphic morphing map

$$\tilde{\boldsymbol{m}}\big(t(\xi), \Delta r(\xi), \mathsf{A}^j(\xi)\big) : \begin{cases} \Omega|_{\xi=0} & \rightarrow & \Omega|_{\xi=1} \\ \boldsymbol{x}|_{\xi=0} & \mapsto & \boldsymbol{x}|_{\xi=1} \end{cases}, \tag{3.42}$$

where $\Omega|_{\xi=0}$, $\boldsymbol{x}|_{\xi=0} \in \Omega|_{\xi=0}$ describes the current configuration at the beginning of the morphing process ($(\bullet)\,|_{\xi=0}$). At the end of the morphing process ($(\bullet)\,|_{\xi=1}$), the current configuration is

determined by $\Omega|_{\xi=1}$, $\boldsymbol{x}|_{\xi=1} \in \Omega|_{\xi=1}$. In-between, i.e., for $\xi \in (0,1)$, the current configuration is determined by a $t(\xi)$-$\Delta r(\xi)$-$\mathsf{A}^j(\xi)$-driven interpolation between the configurations $\Omega|_{\xi=0}$ and $\Omega|_{\xi=1}$.

These abstract definitions of $\tilde{\boldsymbol{M}}(\xi)$ changing a reference configuration and $\tilde{\boldsymbol{m}}(\xi)$ changing a current configuration will be further specified when applied to the in-silico EVAR model.

3.3. Vessel modeling

In the following, first the semi-automatic model generation process of patient-specific vessels including vessel wall, ILT and calcifications is described in Section 3.3.1. This includes the segmentation, the 3D reconstruction as well as the discretization of the vessel. Afterwards, constitutive models for the different vessel constituents are presented in Section 3.3.2. Finally, the vessel prestressing methodology is described in Section 3.3.3.

3.3.1. Patient-specific vessel segmentation, model construction and discretization

Figure 3.6 provides an overview of major steps of the vessel model generation such as vessel segmentation, vessel discretization and mapping of patient-specific quantities.

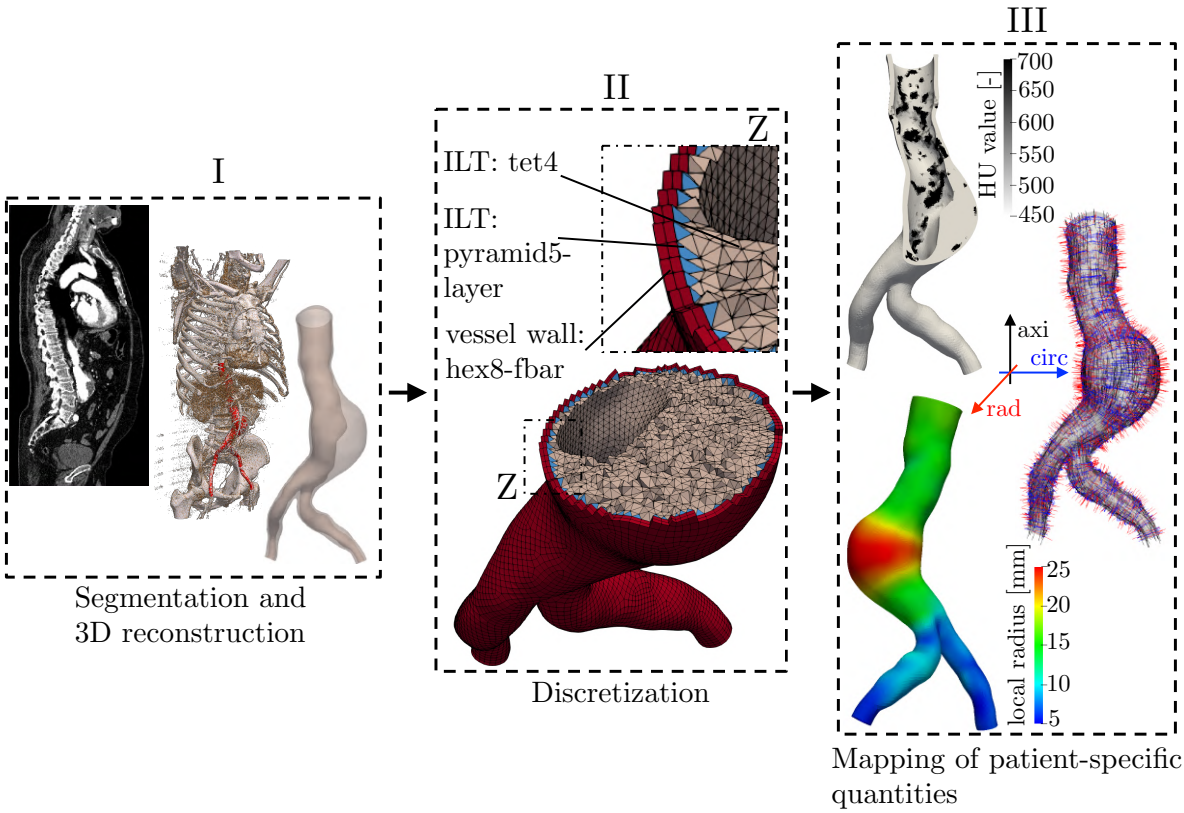

Figure 3.6 Vessel segmentation and 3D reconstruction (I), vessel discretization (II) and mapping of patient-specific quantities onto the discretized vessel model (III).

These three major steps, (i) vessel segmentation, (ii) vessel discretization and (iii) mapping of patient-specific quantities, are described in the following.

Vessel segmentation

Patient-specific vessel geometries including ILT are segmented from preinterventional CT data in a semi-automatic fashion using the segmentation software Mimics 12.1 (Materialise, Leuven, Belgium). The region of interest is limited to the abdominal aorta including AAA and iliac arteries. Vessel geometries are cut approximately 20 mm above the branching of the renal arteries and distally approximately 20 mm below the branching of the common iliac arteries into the internal and external iliac arteries. Renal arteries and internal iliac arteries are not part of the model. Thus, the renal arteries and internal iliac arteries are cut prior to the 3D reconstruction of the vessel (cf. Figure 3.6I).

To obtain comparable results, the operator-dependency on the segmentation result of the semi-automatic segmentation process should be kept to a minimum. Hence, the segmentation process of all patients, that are considered in this thesis, is based on the segmentation protocol for the 3D geometry reconstruction of AAAs from CT data by Maier [164]. This segmentation process consists of the following main steps:

1. Segmentation of the lumen in the region of interest mainly by the use of a threshold filter with respect to the voxel Hounsfield unit (HU). 3D reconstruction of the segmented lumen mask and extraction of the centerline of the lumen.

2. Segmentation of the complete vessel in the region of interest (including lumen and ILT). Since contrast between ILT and surrounding tissue is very small, i.e., the HU values are very similar, automated segmentation of ILT is very challenging and requires substantial manual interaction. 3D reconstruction of the segmented mask of the total geometry and extraction of the centerline of the total vessel geometry.

3. Laplacian smoothing [263] in combination with advanced volume preserving algorithms [249] is applied to the 3D reconstructions of the lumen (from step 1) and the total geometry (from step 2).

4. To obtain the 3D reconstruction of the pure ILT, the smoothed 3D reconstruction of the lumen is subtracted from the smoothed 3D reconstruction of the total geometry by the use of a Boolean subtraction.

Since the resolution of the available preinterventional CT data is close to the dimensions of the vessel wall thickness, the segmentation of the vessel wall with reliable wall thickness reconstruction is impossible [28, 220]. Therefore, the vessel wall is not considered in the segmentation process, but will be added later during the discretization of the vessel. In general, vessel calcifications can be easily detected in CT images due to relatively high HU values. However, since calcifications can have a very irregular shape and since they can be located at a large number of separated spots, modeling and discretization of calcifications as separate constituents is not practicable. Thus, vessel calcifications are not segmented explicitly, but are considered implicitly within the domains of ILT and aortic wall as described in Section 3.3.2.3.

Vessel discretization

A fully automated mesh generation (cf. Figure 3.6II) is used based on the commercial software Trelis 15.1 (Csimsoft, Utah, USA). Input for the generation of the discretized vessel model is the 3D reconstruction of the pure ILT geometry, i.e., without lumen. The main steps of the fully automated vessel discretization using a Trelis-Python script are stated below:

1. Discretization of the abluminal surface of the ILT geometry by quadrilateral elements.
2. Generation of the discretized vessel wall by extrusion of the meshed abluminal ILT surface in outward normal direction which results in hexahedral elements for the vessel wall. The number of element layers over the wall thickness as well as the wall thickness can be specified in the input of the automated meshing script. In the context of this thesis, a constant wall thickness of $1.5\,\mathrm{mm}$ [219] is assumed distributed over two layers of elements if not specified differently.
3. Discretization of the total ILT volume by tetrahedral elements. Pyramid elements are utilized to guarantee conforming meshes between ILT and the vessel wall.

Linear, tetrahedral and pyramid elements in the domain of the ILT and linear, hexahedral elements with F-bar based element technology (cf. Section 2.2) in the domain of the vessel wall are applied. Unless stated differently, in the context of this thesis, a mean edge length of $h^{\mathrm{Ao}} = 1\,\mathrm{mm}$ is used both for the vessel wall discretization and the ILT discretization.

Mapping of patient-specific quantities

As a prerequisite for the constitutive models of the vessel, three patient-specific quantities need to be mapped to the discretized vessel geometry (cf. Figure 3.6III):

- **HU values**: Based on the preinterventional CT data, the voxel HU values are mapped onto the elements of the discretized vessel geometry. Constant HU values are assigned to each element where the value corresponds to the interpolated voxel HU value at the location of the element's centroid. The local HU values will be used in Section 3.3.2.3 to implicitly consider calcifications, which correspond to locally high HU values, in the constitutive models of the vessel.
- **Local radial, axial and circumferential coordinate systems**: Using the centerline of the total vessel geometry, the local radial, axial and circumferential directions of the vessel are calculated at each element's centroid of the vessel wall according to [56], where the axial direction is assumed to be the direction of the tangent to the centerline at the point of the centerline that is closest to the element's centroid. The local circumferential, axial and radial bases are required for the definition of the anisotropic constitutive model of the vessel wall that will be introduced in Section 3.3.2.1.
- **Local vessel wall radius**: Using the centerline of the lumen, the local radius of each element's centroid of the vessel wall is approximated by the distance to the closest point on the centerline. The local vessel wall radius is used to smoothly blend between "healthy" vessel wall and AAA wall material as will be described in Section 3.3.2.1.

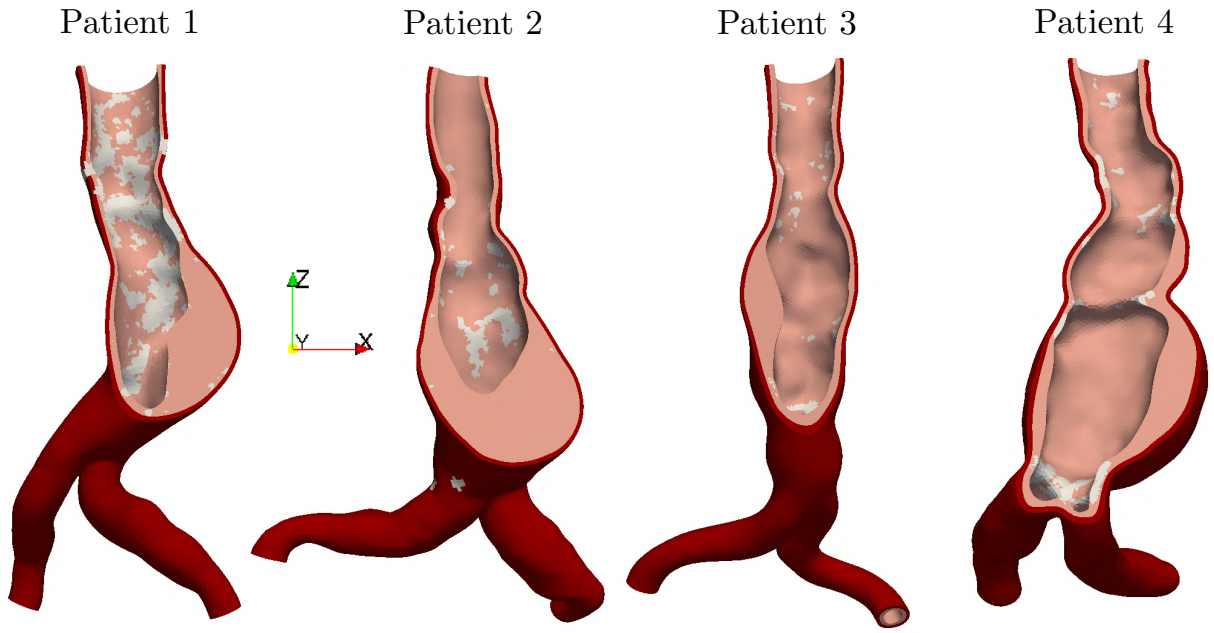

#DOFs:		#DOFs:		#DOFs:		#DOFs:	
Wall:	104,958	Wall:	131,823	Wall:	106,785	Wall:	110,556
ILT:	100,308	ILT	150,474	ILT:	83,043	ILT:	114,825
$\sum$:	205,266	$\sum$:	282,297	$\sum$:	189,828	$\sum$:	225,381

Figure 3.7 Patient-specific vessel models of patient 1-4 as listed in Appendix A.1: vessel wall (dark red), ILT (light pink) and calcifications (white). Modified figure reproduced with permission from [107].

The vessel models of all four patient-specific cases that are considered in this thesis are visualized in Figure 3.7. Both the geometry as well as the degree of calcification (white spots in Figure 3.7) vary among the four patient-specific vessels.

3.3.2. Constitutive modeling

In the following sections, the constitutive models of the vessel wall (Section 3.3.2.1), the ILT (Section 3.3.2.2) and calcifications (Section 3.3.2.3) are introduced. Model parameters of the proposed constitutive models are summarized in Table 3.1. Although patient-specific vessel geometries are studied, throughout this thesis population averaged mean values are used for constitutive models and model parameters, i.e., neither interpatient nor intrapatient variability in the constitutive models and model parameters is considered.

Since arterial tissue is almost incompressible [35], an additive split of the corresponding SEF $\Psi^{(\bullet)}$ of all vessel constituents $(\bullet)$ into a volumetric and an isochoric part is used according to

$$\Psi^{(\bullet)} = \Psi^{(\bullet)}_{\text{iso}}(\bar{\boldsymbol{C}}) + \Psi^{(\bullet)}_{\text{vol}}(J), \tag{3.43}$$

where $J = \det(\boldsymbol{F})$ and $\bar{\boldsymbol{C}} = J^{-\frac{2}{3}}\boldsymbol{C}$ is the modified right Cauchy-Green deformation tensor. Similarly, the modified invariants are given by

$$\bar{I}_1 = J^{-\frac{2}{3}} I_1, \quad \bar{I}_2 = J^{-\frac{4}{3}} I_2, \quad \bar{I}_3 = \det(\bar{\boldsymbol{C}}) = 1. \tag{3.44}$$

The isochoric-volumetric split enables the penalization of volumetric changes to sustain the almost incompressibility of the material. An Ogden volumetric SEF [65, 195] of type

$$\Psi_{\text{vol}}^{(\bullet)}(J) = \frac{K^{(\bullet)}}{4}(J^2 - 2\ln J - 1), \tag{3.45}$$

where $K^{(\bullet)}$ is the volumetric bulk modulus, is applied to all vessel constituents $(\bullet)$ considered in the model, i.e., for the SEF of "healthy" vessel wall (AA), "aneurysmatic" vessel wall (AAA), intraluminal thrombus (ILT) and calcifications (calc).

3.3.2.1. Vessel wall

From a modeling perspective, the abdominal aortic wall as well as the wall of iliac arteries can be seen as fibrous composites that consist of a ground matrix and embedded families of collagen fibers. The isotropic ground matrix is associated with mechanically relevant, non-collagenous tissue components, such as elastin and smooth muscle cells [80, 115]. While this general framework of most anisotropic models of vessel walls is the same, both two-fiber models (e.g., [102]) and four fiber-models (e.g., [222]) have been applied extensively in the recent two decades. In recent years, the dispersed orientation of these fibers, which has a significant effect on the mechanical response of the vessel wall, has been included into the model [119].

AAA progression is often associated with a loss of elastin [103, 230] and substantial structural changes of the complex network of elastin and collagen [103, 192] in the AAA wall. Hence, in the AAA wall, the collagen fibers generally are more dispersed such that isotropic models are widely used (e.g., [163, 217]).

In the context of in-silico EVAR, the vessel model should include both the AAA as well as the "healthy" parts of the vessel proximal and distal of the AAA since the SG landing zones are generally located in the "healthy" parts of the vessel. Therefore, the vessel model should include both a sophisticated model of the "healthy" vessel wall and the AAA wall.

Recently, Holzapfel et al. [118] published an arterial wall model with non-symmetric collagen fiber dispersion which is an extension to available two-fiber models without fiber dispersion [115] and available two-fiber models with rotationally symmetric collagen fiber dispersion [80]. This model is of elevated interest for this thesis since this model can be fitted to data of "healthy" aortic walls as well as to AAA walls [192], i.e., both the constitutive relation of the "healthy" vessel wall as well as the constitutive relation of the AAA wall can be expressed by the same SEF. However, so far experimental fitting of the material parameters of this model as proposed in [192] was based only on a small cohort ($n = 11$ AAAs and $n = 17$ "healthy" abdominal aortas). Hence, a different approach is followed in this thesis. However, the model of Holzapfel et al. [118] may be a useful alternative as soon as larger studies on the experimental fitting of the material model parameters are available in literature.

In this thesis, a modular approach is employed that is able to combine any sophisticated model of the "healthy" vessel wall with any sophisticated model of the AAA wall. The SEF of the

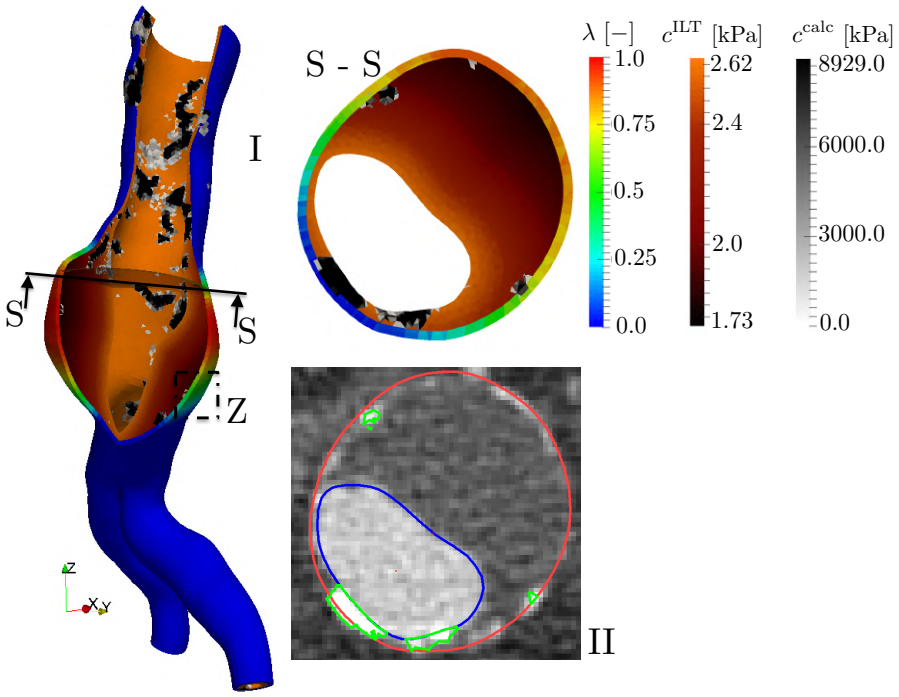

Figure 3.8 Cut view of the vessel model of patient 1 and visualization of the different vessel constituents: "healthy" vessel wall, AAA wall, ILT and calcifications (I). Transversal CT image (II) with contour lines of blood lumen (blue), abluminal ILT surface (red) and calcifications (green). Reproduced with permission from [107].

vessel wall using this modular approach incorporates a convex combination of two SEF, which was originally proposed by Thon et al. [250], where this approach was used to combine the SEF of aortic tissue and foam cells in the context of atherosclerosis. Accordingly, the SEF of the vessel wall reads

$$\Psi^{\text{wall}} = (1 - \lambda(r))\Psi^{\text{AA}} + \lambda(r)\Psi^{\text{AAA}}, \tag{3.46}$$

where $\lambda(r) \in [0, 1]$ is a geometrical parameter that blends smoothly between the SEF Ψ^{AA} of the "healthy" vessel wall and the SEF Ψ^{AAA} of the AAA wall (cf. Figure 3.8I). The geometrical parameter $\lambda(r)$ is defined by

$$\lambda(r) = \begin{cases} 0, & r < r_0, \\ \frac{1}{2}\left(1 - \cos\left(\pi \frac{r - r_0}{r_1 - r_0}\right)\right), & r_0 \leq r \leq r_1, \\ 1, & r > r_1, \end{cases} \tag{3.47}$$

where r is the local preinterventional vessel wall radius that is mapped onto the patient-specific discretized vessel model as described in Section 3.3.1. In this thesis, the bounds r_0 and r_1 are chosen heuristically as $r_0 = 1.2r^{\text{AA}}$ and $r_1 = 1.5r^{\text{AA}}$ with r^{AA} being the subrenal radius of the preinterventional vessel which is assumed to be in "healthy" state. Accordingly, regions of the vessel with a local radius r smaller than r_0 are fully described by the SEF Ψ^{AA} of a "healthy"

vessel wall whereas regions with a local radius r larger than r_1 are fully described by the SEF Ψ^{AAA} of an "aneurysmatic" vessel wall. In-between a smooth transition zone of partly "aneurysmatic" vessel material arises as shown in Figure 3.8I. It should be noted that (3.46) is a purely heuristic distinction between "healthy" vessel wall and the AAA wall parts according to the preinterventional local vessel radius r. It does not incorporate any biomechanical or biochemical law generally associated with the disease progression. In a same fashion as in (3.46), the material model could be extended to smoothly blend between iliac and abdominal aortic wall material. However, since the focus of this thesis is mainly on the proximal landing zone of the SG, the same material model and model parameters are used for the "healthy" abdominal aortic wall and the "healthy" iliac arteries, i.e., no blend between those two regions is incorporated.

In this thesis, the "healthy" vessel wall is described by the anisotropic, hyperelastic two-fiber model proposed by Gasser et al. [80]. The isochoric component of the SEF is a superposition of an isotropic ground substance $\Psi^{\mathrm{AA}}_{\mathrm{iso}}$ and an anisotropic part $\Psi^{\mathrm{AA}}_{\mathrm{fi}}$ considering the collagen fibers of the vessel wall. The total SEF of the "healthy" vessel wall reads

$$\begin{aligned}\Psi^{\mathrm{AA}}(\bar{I}_1, \bar{I}_4, \bar{I}_6, J) &= \Psi^{\mathrm{AA}}_{\mathrm{iso}}(\bar{I}_1) + \Psi^{\mathrm{AA}}_{\mathrm{fi}}(\bar{I}_4, \bar{I}_6) + \Psi^{\mathrm{AA}}_{\mathrm{vol}}(J) \\ &= c^{\mathrm{AA}}(\bar{I}_1 - 3) + \frac{k_1}{2k_2} \sum_{i=4,6} (e^{k_2[\kappa \bar{I}_1 + (1-3\kappa)\bar{I}_i - 1]^2} - 1) + \Psi^{\mathrm{AA}}_{\mathrm{vol}}(J), \end{aligned} \tag{3.48}$$

where c^{AA} is the isotropic shear modulus and k_1 as well as k_2 are fiber-specific stiffness parameters. The transversely isotropic dispersion parameter $\kappa \in [0, 1/3]$ accounts for the dispersion of the collagen fiber orientation and $\bar{I}_1$ refers to the first modified invariant of the right Cauchy-Green deformation tensor as given in Equation (3.44). $\bar{I}_4$ as well as $\bar{I}_6$ refer to the squares of the stretches in fiber direction according to

$$\bar{I}_i = \bar{\boldsymbol{C}} : \boldsymbol{A}_i \otimes \boldsymbol{A}_i, \quad i = 4, 6. \tag{3.49}$$

In (3.49), $\boldsymbol{A}_i = [0, \sin(\theta_i), \cos(\theta_i)]^{\mathrm{T}}$ defines the mean fiber direction of the two fibers in the local radial, axial and circumferential coordinate system of the preinterventional vessel as described in Section 3.3.1. The two angles θ_4 and θ_6 are material constants. For a dispersion parameter $\kappa = 0$, the SEF in (3.48) reduces to the original two-fiber model without dispersion of the collagen fiber orientation [115] and for $\kappa = 1/3$, the SEF in (3.48) reduces to a purely isotropic SEF.

In the AAA wall, the collagen fibers are more dispersed. Thus, the well established isotropic model by Raghavan and Vorp [217] is employed for the "aneurysmatic" part of the vessel wall. Accordingly, the SEF for the AAA wall reads

$$\Psi^{\mathrm{AAA}}(\bar{I}_1, J) = \Psi^{\mathrm{AAA}}_{\mathrm{iso}}(\bar{I}_1) + \Psi^{\mathrm{AAA}}_{\mathrm{vol}}(J) = a(\bar{I}_1 - 3) + b(\bar{I}_1 - 3)^2 + \Psi^{\mathrm{AAA}}_{\mathrm{vol}}(J), \tag{3.50}$$

where a and b are material parameters according to [217].

3.3.2.2. Intraluminal thrombus

ILT is a fibrin structure incorporated with blood cells and proteins, platelets and cellular debris [270] whose formation follows a complex physico-biochemical process and which adheres to the arterial wall. The existence and the shape of ILT are very irregular and depend on various

factors such as the hemodynamic conditions [18]. While in some patients the ILT deposit in the AAA sac is very thick, inducing a narrowing of the blood lumen, other patients show only thin layers of ILT. It is well accepted that ILT has a significant impact on the biomechanics of AAAs [81], such as on the stress sate in the AAA wall. Most studies assume a mechanically protective behavior of ILT on the AAA wall that is based on two main reasons. First, although ILT is much softer than the tissue of the AAA wall, it can have a certain load bearing effect [164]. Second, ILT leads to a narrowing of the lumen and hence to a reduction in the luminal surface on which the blood pressure acts [112]. However, no consensus view is given on this point in literature. For instance, the study by Schurink et al. [235] indicates that ILT within an aortic aneurysm does not reduce the blood pressure on the aneurysmal wall. Besides the effect of ILT on AAA wall stresses, the existence of ILT can have an important role on the shape of the deployed SG. Therefore, considering ILT in the vessel model can improve the predictive quality of the in-silico EVAR model.

In this thesis, the isotropic SEF

$$\Psi^{\mathrm{ILT}}(\bar{I}_1, \bar{I}_2, J) = \Psi^{\mathrm{ILT}}_{\mathrm{iso}}(\bar{I}_1, \bar{I}_2) + \Psi^{\mathrm{ILT}}_{\mathrm{vol}}(J) = c^{\mathrm{ILT}}(\bar{I}_1^2 - 2\bar{I}_2 - 3) + \Psi^{\mathrm{ILT}}_{\mathrm{vol}}(J) \tag{3.51}$$

proposed by Gasser et al. [81] is utilized to model the mechanical properties of ILT. The constitutive model resolves the material properties of three different ILT layers with decreasing stiffness c^{ILT}: luminal $c^{\mathrm{ILT}}_{\mathrm{lum}}$, medial $c^{\mathrm{ILT}}_{\mathrm{med}}$ and abluminal $c^{\mathrm{ILT}}_{\mathrm{abl}}$. The material parameter c^{ILT} is piecewise linearly interpolated between these distinct ILT layers from the luminal to the abluminal surface of the ILT.

3.3.2.3. Calcifications

Calcifications are a product of the degenerative process of the vessel wall in the late stage of the inflammatory disease atherosclerosis mainly proceeding at the innermost layer of the vessel wall, the intima.

As described in Section 3.3.1, calcifications are not segmented and modeled explicitly. Instead, calcifications are considered implicitly within the domains of ILT and vessel wall. This method to consider calcifications is adjusted from [164]. To implicitly consider calcifications within the domains of the ILT and the vessel wall, the SEF representing the mechanical behavior of calcifications is superimposed to the SEF of ILT

$$\hat{\Psi}^{\mathrm{ILT}} = \Psi^{\mathrm{ILT}} + \Psi^{\mathrm{calc}} \tag{3.52}$$

and the vessel wall

$$\hat{\Psi}^{\mathrm{wall}} = \Psi^{\mathrm{wall}} + \Psi^{\mathrm{calc}}, \tag{3.53}$$

respectively. The SEF Ψ^{calc} is a function of the local HU value of the vessel which are extracted from CT images as stated in Section 3.3.1. The almost linear material behavior of calcifications is modeled by a neo-Hookean material for the isochoric component of the SEF as proposed in [162]. Accordingly, the SEF Ψ^{calc} reads

$$\Psi^{\mathrm{calc}}(\bar{I}_1, J) = \Psi^{\mathrm{calc}}_{\mathrm{iso}}(\bar{I}_1) + \Psi^{\mathrm{calc}}_{\mathrm{vol}}(J) = c^{\mathrm{calc}}(\bar{I}_1 - 3) + \Psi^{\mathrm{calc}}_{\mathrm{vol}}(J), \tag{3.54}$$

where c^{calc} is the additional stiffness of the calcified regions that is added to the base material of ILT and vessel wall, respectively. As stated for instance in [162], "pure calcifications" and "calcified tissue" have to be distinguished, the latter one meaning a compound of vessel tissue and dispersed calcifications. This motivates the definition of c^{calc} as a smooth transition from "noncalcified" to "pure calcification" with

$$c^{\mathrm{calc}}(h) = \begin{cases} 0, & h < h_0, \\ f^{\mathrm{calc}}(h), & h_0 \leq h \leq h_1, \\ \hat{c}^{\mathrm{calc}}, & h > h_0 \end{cases}, \quad f^{\mathrm{calc}}(h) = \frac{1}{2}\hat{c}^{\mathrm{calc}}\left(1 - \cos\left(\pi \frac{h - h_0}{h_1 - h_0}\right)\right), \tag{3.55}$$

where h is the local HU value, h_0 is the HU value at which the transition from noncalcified vessel tissue to calcified tissue starts, h_1 is the HU value above which the material is considered as pure calcification.

Table 3.1 Constitutive model parameters of the vessel.

	Parameter	Description	Dimension	Value	Reference
Vessel wall	λ	Blend parameter	[-]	Eq. (3.47)	Eq. (3.47)
	k_1	Fiber stiffness	[kPa]	4070	[102]
	k_2	Exponential parameter of fibers	[-]	165.6	[102]
	c^{AA}	Stiffness of aortic ground material	[kPa]	100.9	[102]
	κ	Dispersion parameter	[-]	0.16	[102]
	θ_4	Orientation angle of first fiber	[°]	48.4	[102]
	θ_6	Orientation angle of second fiber	[°]	-48.4	[102]
	a	Stiffness parameter of AAA wall	[kPa]	174.0	[217]
	b	Stiffness parameter of AAA wall	[kPa]	1881	[217]
ILT	$c^{\mathrm{ILT}}_{\mathrm{lum}}$	ILT stiffness (luminal layer)	[kPa]	2.62	[81]
	$c^{\mathrm{ILT}}_{\mathrm{med}}$	ILT stiffness (medial layer)	[kPa]	1.98	[81]
	$c^{\mathrm{ILT}}_{\mathrm{abl}}$	ILT stiffness (abluminal layer)	[kPa]	1.73	[81]
Calc	c^{calc}	Stiffness of calcified tissue	[kPa]	Eq. (3.55)	Eq. (3.55)
	$\hat{c}^{\mathrm{calc}}$	Stiffness of pure calcifications	[kPa]	8929	[162]

3.3.3. Vessel prestressing

Patient-specific vessel geometries generally are reconstructed from in-vivo medical imaging such as CT scans and therefore involve an initial geometric configuration that is not stress-free. In order to initialize ("prestress") the vessel model to the in-vivo stressed configuration, a computational prestressing methodology needs to be considered. This is of elevated importance if the stress state of the vessel model is of particular interest. Further, if the model parameters of a nonlinear constitutive model are based on experiments, where ex-vivo tissue samples are tested, consideration of the "prestressed" state is essential. Disregarding the "prestressed" state would result in the evaluation of the stress-strain relation at the wrong stress level associated with unreasonable deformations of the geometry.

In this thesis, a modified updated Lagrangian formulation (MULF) proposed by Gee et al. [84] is applied to prestress the vessel model to the stress state that corresponds to the quasi-static blood pressure state at time of medical imaging. The MULF strategy has been proofed to effectively approximate the "prestressed" state of patient-specific AAA geometries [83]. By analogy, the embedding tissue, i.e., the spring boundary conditions according to Equations (3.5) and (3.6), are prestressed according to the methodology described in [113].

3.4. Stent-graft modeling

Models of two different commercial SG devices for the treatment of infrarenal AAAs are considered in this thesis. To clearly indicate that the presented SG models are only aligned to the real-world commercial devices, but do not exactly coincide with the them with respect to geometry and material behavior, the following two terms are introduced: *CZ-SG* and *ME-SG*. The CZ-SG model imitates the commercial Cook Zenith Flex/Spiral-Z® SG device and the ME-SG model is aligned to the characteristics of the commercial Medtronic Endurant™ II SG device, which were both described in Section 1.1.2.2. In the following, first the SG model construction and discretization processes are described in Section 3.4.1. Afterwards, constitutive models of stent and graft are presented in Section 3.4.2. Finally, it is focused on stent predeformation and its consideration in the SG model in Section 3.4.3.

3.4.1. Stent-graft model construction and discretization

Models of both commercial SG devices are generated by fully automated scripts using the commercial software Trelis 15.1 and its Python interface. The SG generation and meshing process are based on the following major steps which are the same for CZ-SG and ME-SG models:

1. Generation of the curve that describes the shape of the stent (cf. Figure 3.9I).
2. Generation and meshing of the stent cross-section (cf. Figure 3.9II).
3. Sweeping of the discretized stent cross-section along the curve that describes the shape of the stent. Adaptive element edge length of the hexahedral stent elements with mesh refinement in the curved parts for the stent is used (cf. Figure 3.9III).
4. Generation and meshing of the graft (cf. Figure 3.10III).

This configuration of the SG that results from this model construction and discretization process is denoted as initial configuration of stent $\Omega^{\mathrm{S}}_{\mathrm{I},0}$, $\boldsymbol{X}^{\mathrm{S}}_{\mathrm{I}} \in \Omega^{\mathrm{S}}_{\mathrm{I},0}$ and graft $\Omega^{\mathrm{G}}_{\mathrm{I},0}$, $\boldsymbol{X}^{\mathrm{G}}_{\mathrm{I}} \in \Omega^{\mathrm{G}}_{\mathrm{I},0}$ indicated by the subscript $(\bullet)_{\mathrm{I}}$.

Commercial SGs for infrarenal AAAs are modular devices that consist of a main body component and one (Medtronic Endurant™ II SG) or two (Cook Zenith Flex/Spiral-Z® SG) iliac leg components that are docked to the main SG component (cf. Section 1.1.2.2). Here, preassembled SG models are considered with a predefined prosthesis overlap length (cf. Figure 3.10). The exact overlap length for all four considered patient-specific cases is provided in Appendix A.1. This simplification of preassembled SG models has the drawback of not being able to assess the

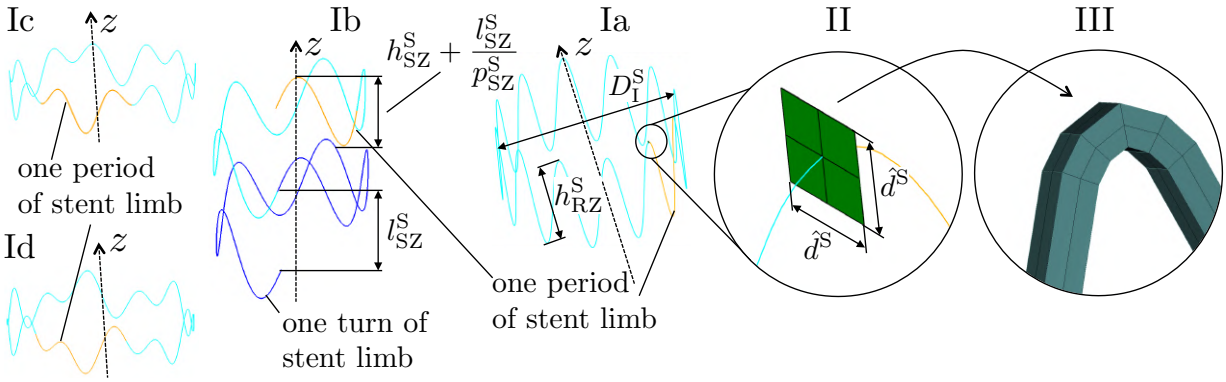

Figure 3.9 Illustration of the model generation of a ring-shaped stent limb with Z-profile (Ia) a spiral-shaped stent limb with Z-profile (Ib) and a ring-shaped stent limb with M-profile (Ic+d). Stent cross section (II) and meshing (III). Modified figure reproduced with permission from [107].

quality of the connection between the main SG component and the iliac leg components. This means these preassembled SG models are not able to make predictions on the occurrence of type III endoleaks (cf. Section 1.1.2.4). However, the impact on other areas of interest, such as the proximal and distal landing zones of the total SG, is small.

In both commercial SG devices, Cook Zenith Flex/Spiral-Z® SGs and Medtronic Endurant™ II SGs, the stent limbs are sutured on the graft. In the SG model, any elasticity of these sutures and any slippage between stent limbs and graft are neglected. Instead, stent and graft are rigidly tied which is a frequently used model assumption [49, 58, 212, 228]. Hence, mortar based mesh tying constraints according to Equation (3.4) between the outer stent surface $\Gamma^{\mathrm{S}}_{\mathrm{ex}}$ and the inner graft surface $\Gamma^{\mathrm{G}}_{\mathrm{I}}$ are used to rigidly tie the two nonconforming meshes of stent and graft. Most commercial SG devices consist of interior and exterior stent limbs. Interior stent limbs are sewn on the inner surface of the graft, whereas exterior stent limbs are sewn on the outer surface of the graft. In order to restrict the complexity of the contact interaction between SG and vessel, all stent limbs are modeled as interior stent limbs with respect to the graft. Therefore, only potential contact between graft and vessel has to be considered, but contact between stent and vessel is not possible in the in-silico EVAR model.

Remark. *Since only interior stents are considered in the SG models of this thesis, the graft diameter D^{G} determines the nominal diameter D^{SG} of the total SG, i.e., $D^{\mathrm{SG}} = D^{\mathrm{G}}$.*

To ensure hexahedral meshing of the stent and to provide proper surfaces for the mortar-based mesh tying between stent and graft, circularly shaped cross sections of the stent struts are modeled as quadratic cross sections with equivalent bending stiffness, i.e., $\hat{d}^{\mathrm{S}} = \sqrt[4]{(3/16)\pi(d^{\mathrm{S}})^4}$, where d^{S} is the diameter of the circular stent wire as provided in Table 3.2 and $\hat{d}^{\mathrm{S}}$ is the edge length of the quadratic stent strut cross-section as visualized in Figure 3.9II.

The bare proximal stents with barbs (cf. Figure 3.10I) are not modeled explicitly in a geometrical sense. In order to account for the axial fixation of the SG by the proximal barbs, mortar-based frictional contact in pure stick (no tangential sliding) is applied between SG and luminal vessel surface in the most proximal region of the SG of $5\ \mathrm{mm}$ length. This means, in this region a friction coefficient of $\mathfrak{F} \to \infty$ is used instead of the physical friction coefficient $\mathfrak{F} = 0.4$ between

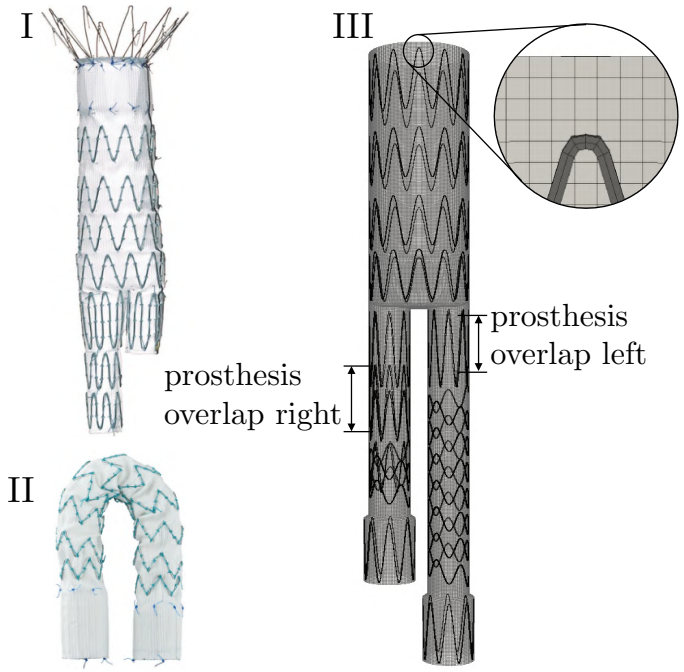

Figure 3.10 Image of a Cook Zenith Flex® main component SG (I), image of a Cook Zenith Spiral-Z® iliac leg SG (II) and the preassembled, meshed CZ-SG model (III). Modified figure reproduced with permission from [107].

SG and vessel. In some other studies the bare proximal stents are modeled [53, 205], however without modeling the anchoring of the barbs into the vessel tissue.

Although the stress-free stent diameter of most commercial SGs is substantially larger than the nominal diameter D^{SG} of the SG, in this thesis, the SG geometry initially is generated with $D_{\mathrm{I}}^{\mathrm{S}} = D_{\mathrm{I}}^{\mathrm{G}} - 2t^{\mathrm{G}} = D^{\mathrm{SG}} - 2t^{\mathrm{G}}$, where t^{G} is the graft thickness.[4] Stent predeformation will be applied afterwards in a computational approach where the stress-free stent diameter before the assembly of the SG is considered.

Three different stent shapes are considered in this thesis: ring-shaped stent limbs with Z-profile, spiral-shaped stent limbs with Z-profile and ring-shaped stent limbs with M-profile (cf. Figure 3.9I). Ring-shaped stent limbs with Z-profile are used in the CZ-SG model and the ME-SG model. Spiral-shaped stent limbs with Z-profile are applied to the iliac parts of the CZ-SG model. Ring-shaped stent limbs with M-profile are used in the proximal part of the ME-SG model.

Ring-shaped stent limbs with Z-profile are approximated by

$$\boldsymbol{X}_{\mathrm{RZ}}^{\mathrm{S}} = \begin{pmatrix} \frac{D_{\mathrm{I}}^{\mathrm{S}} - \hat{d}^{\mathrm{S}}}{2}\cos(\varphi) \\ \frac{D_{\mathrm{I}}^{\mathrm{S}} - \hat{d}^{\mathrm{S}}}{2}\sin(\varphi) \\ \frac{h_{\mathrm{RZ}}^{\mathrm{S}}}{2}\sin(\varphi p_{\mathrm{RZ}}^{\mathrm{S}}) \end{pmatrix}, \quad \varphi \in [0, 2\pi], \tag{3.56}$$

[4] To ease the notation, in the following the graft thickness t^{G} is not explicitly written, since it is very small compared to the nominal diameter D^{SG} of the SG. Hence, in the following $D_{\mathrm{I}}^{\mathrm{S}} = D_{\mathrm{I}}^{\mathrm{G}} = D_{\mathrm{I}}^{\mathrm{G}}$ is used instead.

which defines the position vector $\boldsymbol{X}_{\mathrm{RZ}}^{\mathrm{S}}$ of the centers of the stent cross sections. The stent wire thickness $\hat{d}^{\mathrm{S}}$, the height of the stent limb $h_{\mathrm{RZ}}^{\mathrm{S}}$ and the number of sinusoidal periods of the stent limb $p_{\mathrm{RZ}}^{\mathrm{S}}$ are visualized in Figure 3.9Ia.

The generation of spiral-shaped stent limbs with Z-profile is governed by the position vectors $\boldsymbol{X}_{\mathrm{SZ}}^{\mathrm{S}}$ of the centers of the stent cross sections that are given by

$$\boldsymbol{X}_{\mathrm{SZ}}^{\mathrm{S}} = \begin{pmatrix} \frac{D_{\mathrm{I}}^{\mathrm{S}} - \hat{d}^{\mathrm{S}}}{2} \cos(\varphi) \\ \frac{D_{\mathrm{I}}^{\mathrm{S}} - \hat{d}^{\mathrm{S}}}{2} \sin(\varphi) \\ \frac{h_{\mathrm{SZ}}^{\mathrm{S}}}{2} \sin(\varphi p_{\mathrm{SZ}}^{\mathrm{S}}) + l_{\mathrm{SZ}}^{\mathrm{S}} \frac{\varphi}{2\pi} \end{pmatrix}, \quad \varphi \in [0, 2\pi n_{\mathrm{SZ}}^{\mathrm{S}}], \tag{3.57}$$

where $h_{\mathrm{SZ}}^{\mathrm{S}}$ is the height of the stent limb and $p_{\mathrm{SZ}}^{\mathrm{S}}$ is the number of sinusoidal periods per turn of the stent limb. The lead of the stent limb $l_{\mathrm{SZ}}^{\mathrm{S}}$ and the number of turns per spiral-shaped stent limb $n_{\mathrm{SZ}}^{\mathrm{S}}$ are highlighted in Figure 3.9Ib.

Ring-shaped stent limbs with M-profile are approximated by a Fourier series expansion that is truncated after the second component according to

$$\boldsymbol{X}_{\mathrm{RM}}^{\mathrm{S}} = \begin{pmatrix} \frac{D_{\mathrm{I}}^{\mathrm{S}} - \hat{d}^{\mathrm{S}}}{2} \cos(\varphi) \\ \frac{D_{\mathrm{I}}^{\mathrm{S}} - \hat{d}^{\mathrm{S}}}{2} \sin(\varphi) \\ \sum_{i=1}^{2} a_i \cos(i\varphi p_{\mathrm{RM}}^{\mathrm{S}}) + \sum_{i=1}^{2} b_i \sin(i\varphi p_{\mathrm{RM}}^{\mathrm{S}}) \end{pmatrix}, \quad \varphi \in [0, 2\pi]. \tag{3.58}$$

In (3.58), $\boldsymbol{X}_{\mathrm{RM}}^{\mathrm{S}}$ is the position vector of the centers of the stent cross sections, $p_{\mathrm{SZ}}^{\mathrm{S}}$ is the number of periods of the stent limb and a_i as well as b_i are Fourier coefficients. The proximal part of the ME-SG model consists of two different ring-shaped stent limbs with M-profile. The Fourier coefficients of the most proximal covered stent limb are $a_1 = 2.2\ \mathrm{mm}$, $b_1 = 0.0\ \mathrm{mm}$, $a_2 = -2.4\ \mathrm{mm}$ and $b_2 = 0.0\ \mathrm{mm}$ (cf. Figure 3.9Ic). For all other stent limbs with M-profile of the proximal part of the ME-SG model, the coefficients are $a_1 = 2.2\ \mathrm{mm}$, $b_1 = 0.0\ \mathrm{mm}$, $a_2 = 0.0\ \mathrm{mm}$ and $b_2 = -2.4\ \mathrm{mm}$ (cf. Figure 3.9Id). These coefficients were extracted from a Medtronic Endurant™ II main body SG with a nominal diameter of $D^{\mathrm{SG}} = 32\ \mathrm{mm}$ by image processing of the uncoiled stent limb and subsequent Fourier analysis using MATLAB (The MathWorks Inc., Natick, Massachusetts, USA).

Precise descriptions of the stent shapes of commercial SGs mostly are not published in literature to safeguard company secrets. Using high resolution X-ray microtomography [51, 59] is one way to nevertheless obtain very accurate approximations of the stent shape. In this thesis, graft thickness and stent wire diameters are considered according to Table 3.2.

The geometrical parameters $h_{\mathrm{RZ}}^{\mathrm{S}}$, $p_{\mathrm{RZ}}^{\mathrm{S}}$, $h_{\mathrm{SZ}}^{\mathrm{S}}$, $p_{\mathrm{SZ}}^{\mathrm{S}}$, $l_{\mathrm{SZ}}^{\mathrm{S}}$, $n_{\mathrm{SZ}}^{\mathrm{S}}$ and $p_{\mathrm{RM}}^{\mathrm{S}}$ strongly vary within one SG and among different SG sizes. These parameters depend on the location of the specific stent limb and the nominal size of the SG. They are extracted from the Cook Zenith® manual [44] and the Medtronic Endurant™ II manual [176] as well as from own measurements of one Cook Zenith Flex® SG and one Medtronic Endurant™ II main body SG.

Table 3.2 Graft thickness and stent wire thickness of the CZ-SG model and the ME-SG model according to [60].

	CZ-SG	ME-SG
Stent: Wire diameter [mm]	0.28 (0.40)[a]	0.40
Graft: Thickness [mm]	0.08	0.08

[a] Spiral-shaped stent limbs with Z-profile

The most distal stent limb of the proximal part of the CZ-SG model and the ME-SG model are slightly elliptical with a maximum to minimum diameter ratio of 1.2. SG models of all four patient-specific cases in the respective SG size are visualized in Figure 3.11.

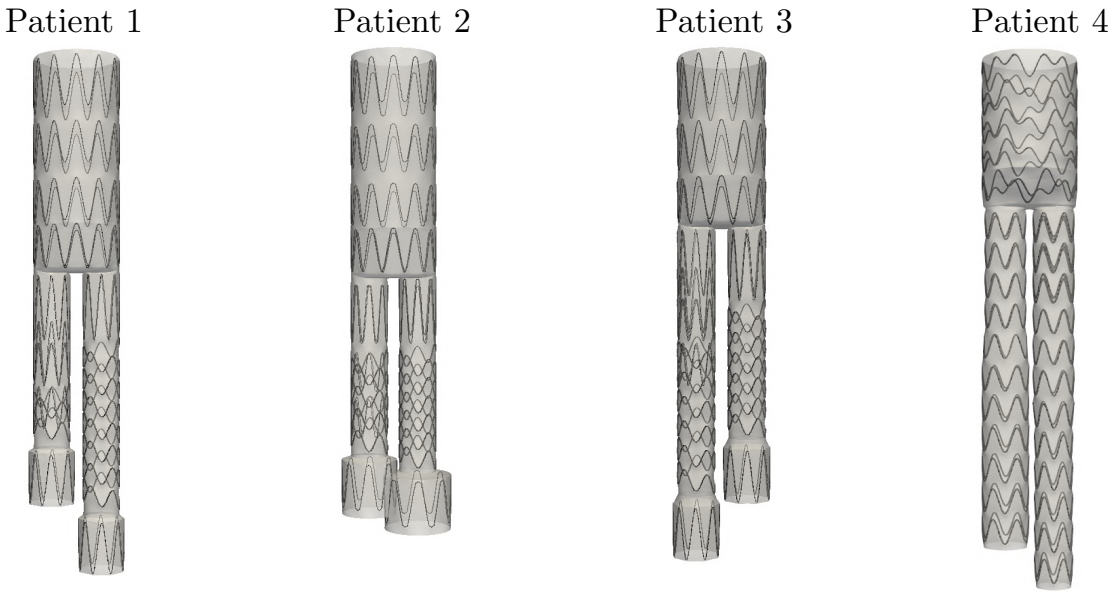

Figure 3.11 Patient-specific SG models of patient 1-4 as listed in Appendix A.1. Modified figure reproduced with permission from [107].

Stents are discretized by linear, hexahedral elements with EAS technology whereas the graft is meshed by hexahedral solid-shell elements [266] with EAS and ANS technology (cf. Section 2.2). An overview and comparison of other discretization techniques for modeling stent expansion is provided in [100].

3.4.2. Constitutive modeling

In this section, the constitutive models of stent (Section 3.4.2.1) and graft (Section 3.4.2.2) materials of the SGs that are investigated in this thesis are introduced. The model parameters of the proposed constitutive models are summarized in Table 3.3.

3.4.2.1. Stent

The stent limbs of the CZ-SG model consist of 316L stainless steel with exception of the spiral-shaped stent limbs of the iliac parts (cf. Figure 3.9Ib and Figure 3.10), which consist of nitinol. All stent limbs of ME-SG model are made of nitinol.

Nitinol is a so-called shape memory alloy of nickel and titanium. The alloy has two stable solid phases with different crystal structures and material properties: the austenitic phase and the martensitic phase. Transformations from one phase into another under stress or temperature loading are the basis of two special mechanical properties of nitinol. First, nitinol can be deformed at low temperatures but fully recovers to its original "memorized" shape when being heated. This effect is denoted as *shape memory effect*. Second, due to the phase transformation between austinite and martensite, nitinol is able to undergo large deformations without inducing plastic strains, i.e., without permanent deformations. This property is denoted as *superelasticity*.

Material models representing the superelasticity or the shape memory effect require return mapping or similar algorithms to model the associated phase transformation. These models are very similar to material models representing elastoplastic behavior. These specific models are reviewed in detail in the book of Lagoudas [146] but are not further considered in this thesis. Information given in literature [207] as well as own experiments have revealed that in the deployed state of the SG, nitinol almost fully remains in its austenitic phase. Hence, as long as the in-silico SG P&D methodology does not aim at explicitly modeling the crimping of the SG inside its delivery sheath, the material model of nitinol does not necessarily need to be able to model the phase transformation. Therefore to reduce complexity of the given problem in a reasonable range, in this thesis, the material behavior of nitinol is modeled by a purely elastic model without phase transformation as proposed in [191, 207] and material parameters corresponding to the austenitic phase of nitinol are used.

The pure elastic regime can be assumed for self-expandable SGs as reported for instance in [207, 228] since any plastic deformation would hamper the self-expansion of the SG. Thus, both nitinol and stainless steel stents are treated as hyperelastic materials and are modeled by the SEF

$$\Psi^{(\bullet)} = \frac{c^{(\bullet)}}{\beta^{(\bullet)}}(J^{-2\beta^{(\bullet)}} - 1) + \frac{c^{(\bullet)}}{2}(I_1 - 3), \quad \beta^{(\bullet)} = \frac{\nu^{(\bullet)}}{1 - 2\nu^{(\bullet)}}, \quad c^{(\bullet)} = \frac{E^{(\bullet)}}{4(1 + \nu^{(\bullet)})} \tag{3.59}$$

where $(\bullet)$ stands either for "S" or "N" indicating stainless steel and nitinol, respectively.

3.4.2.2. Graft

Grafts of endovascular SGs generally consist of polymeric materials. Most of the commercial SGs use either woven PET or ePTFE as graft material. Both of the considered commercial SG devices in this thesis use fabrics of woven PET (cf. Figure 3.12).

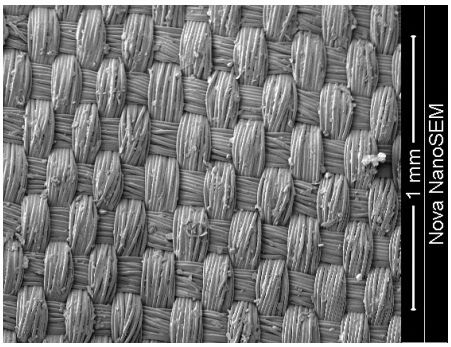

Figure 3.12 Visualization of the microscopic structure of a woven PET graft of a Medtronic Endurant™ II SG using scanning electron microscope.

Despite the inherent anisotropic material behavior of woven PET, following [9, 139, 225], an elastic and isotropic constitutive model is used in this thesis. Hence, the graft material of the CZ-SG and the ME-SG is modeled by the compressible neo-Hookean model

$$\Psi^{\mathrm{G}} = \frac{c^{\mathrm{G}}}{\beta^{\mathrm{G}}}(J^{-2\beta^{\mathrm{G}}} - 1) + \frac{c^{\mathrm{G}}}{2}(I_1 - 3), \quad \beta^{\mathrm{G}} = \frac{\nu^{\mathrm{G}}}{1 - 2\nu^{\mathrm{G}}}, \quad c^{\mathrm{G}} = \frac{E^{\mathrm{G}}}{4(1 + \nu^{\mathrm{G}})}. \tag{3.60}$$

The graft fabric usually exhibits very little bending stiffness such that it sometimes even is modeled by membrane elements without bending stiffness [9]. However, Demanget [57] showed in his thesis that full disregard of the bending stiffness of the graft does not mimic the bending behavior of SGs correctly. Therefore, Demanget [57] used another approach. Based on the bending stiffness of plates $\frac{E^{\mathrm{G}}(t^{\mathrm{G}})^3}{12(1-(\nu^{\mathrm{G}})^2)}$, a reduced bending stiffness of the graft was enforced by reducing the graft thickness t^{G} by a constant factor. To retain the membrane stiffness of the graft, the Young's modulus E^{G} was increased by the same factor. This approach, was adopted by several studies [49, 52, 228]. In this thesis, similar to [228], the graft thickness is reduced by a factor of 10 and E^{G} is increased by a factor of 10.

Table 3.3 Constitutive model parameters of the SG.

	Parameter	Description	Dimension	Value	Reference
Steel stent	E^{S}	Young's modulus of stainless steel	[GPa]	210	[60]
	ν^{S}	Poisson's ratio of stainless steel	[-]	0.3	[60]
Nitinol stent	E^{N}	Young's modulus of nitinol (austinite)	[GPa]	40	[60, 139]
	ν^{N}	Poisson's ratio of nitinol (austinite)	[-]	0.46	[60, 139]
Graft	E^{G}	Young's modulus of graft fabric	[MPa]	165[a]	[228]
	ν^{G}	Poisson's ratio of graft fabric	[-]	0.42	[228]

[a] Young's modulus in circumferential direction from Roy et al. [228]

3.4.3. Stent predeformation

Most commercial SGs are manufactured with a stent diameter $D^{\mathrm{S}}_{\mathrm{Pre}}$ larger than the associated graft diameter. During the assembling process of stent and graft, the stent rings are radially compressed resulting in an assembled SG with residual strains and stresses. This effect, known as *stent predeformation* [106] or *stent preload* [228], has to be considered in an EVAR simulation since it can have a major impact on the mechanical behavior of the SG. In particular, the stress states of the stent and the graft as well as contact tractions between SG and vessel in the deployed configuration may be affected by the degree of stent predeformation. For most commercial SGs, stent predeformation is a purely radial compression of the stent rings. However, few commercial SGs also use other stent predeformation shapes. For instance, Anaconda$^{\mathrm{TM}}$ SGs utilize stent predeformation in longitudinal direction to predeform the initially circular stent shape to a saddle shape [207]. In this thesis, stent predeformation is restricted to a purely radial compression. Thus, the degree of stent predeformation ω is defined as the ratio of the stress-free diameter $D^{\mathrm{S}}_{\mathrm{Pre}}$ of the stent, i.e., the diameter of the stent before the assembly of stent and graft, and the nominal diameter D^{SG} of the SG according to

$$\omega = \frac{D^{\mathrm{S}}_{\mathrm{Pre}}}{D^{\mathrm{SG}}} - 1. \tag{3.61}$$

The degree of stent predeformation ω depends on the SG device and size. Own measurements of commercial SG devices have shown that the degree of stent predeformation mostly is in the range between 5-20%. In the iliac leg docking zones of the main SG component, the highest degree of stent predeformation of up to 100% could be identified. This high degree of stent predeformation results in higher radial stiffness of the SG in the docking zones of the main SG component. This is required to provide enough support for the iliac leg SG components, which are deployed in the interior of the main SG component with an overlap length.

Most of the computational approaches of stent predeformation (cf. Section 1.3.2) are either very specific for one SG device [59, 60] or are based on a rule of thumb [228] which additionally requires experimental calibration. Therefore, in this section, a novel computational stent predeformation methodology is developed, which fulfills the following conditions: (i) mechanical compatibility with the BVP presented in Section 3.1, (ii) general applicability to all SG devices of different manufacturers and (iii) usage without additional assembly simulation with models of artificial assembly devices.

Novel computational stent predeformation methodology

The proposed stent predeformation methodology works in the reverse order compared to the real-world assembly process of SGs. In the real-world assembly process of SGs, the oversized stent rings are radially compressed from an initially stress-free configuration to a predeformed configuration (which is not stress-free) in which they are sewn to the graft. In the proposed computational methodology of stent predeformation, the SG model is already generated in the assembled state (cf. Section 3.4.1). Afterwards the stress-free reference configuration of the stent rings (not the graft) is changed from the initial configuration $\Omega^{\mathrm{S}}_{\mathrm{I},0}$, $\boldsymbol{X}^{\mathrm{S}}_{\mathrm{I}} \in \Omega^{\mathrm{S}}_{\mathrm{I},0}$ to the "real" stress-free configuration $\Omega^{\mathrm{S}}_{\mathrm{Pre},0}$, $\boldsymbol{X}^{\mathrm{S}}_{\mathrm{Pre}} \in \Omega^{\mathrm{S}}_{\mathrm{Pre},0}$ of the stent that corresponds to the stent diameter $D^{\mathrm{S}}_{\mathrm{Pre}}$. Due to the mesh tying constraint between stent and graft, this change of the stent reference

configuration induces residual strains and stresses within stent and graft. It consequently leads to the assembled SG model with stent predeformation.

Accordingly, the SG geometry initially is generated with $D_{\mathrm{I}}^{\mathrm{S}} = D_{\mathrm{I}}^{\mathrm{G}} = D^{\mathrm{SG}}$, i.e., stent and graft diameter are equivalent to the nominal diameter D^{SG} of the SG. The subscript $(\bullet)_{\mathrm{I}}$ is used to indicate that these diameters belong to the initial configurations $\Omega_{\mathrm{I},0}^{\mathrm{S}}$ and $\Omega_{\mathrm{I},0}^{\mathrm{G}}$ as described in Section 3.4.1. In reality, the diameter of the stress-free graft is slightly smaller than the nominal diameter D^{SG} of the assembled SG, such that after assembly of the predeformed stent and the graft the total SG diameter is D^{SG}. However, since the membrane stiffness of the graft is very high, the diameter increase of the graft after assembly is very small. Accordingly, very precise measurements of the stress-free graft diameter would be required which could not be found in literature. Hence, in this thesis $D_{\mathrm{I}}^{\mathrm{G}} = D^{\mathrm{SG}}$ is used. However, the presented stent predeformation methodology is by no means limited to this simplification.

Since $D_{\mathrm{I}}^{\mathrm{S}} = D^{\mathrm{SG}}$, initially the degree of stent predeformation of the SG model is $\omega = 0\%$. In this state, the stent is attached to the graft by applying mortar based mesh tying on the common interface $\Gamma_{\mathrm{m}} = \Gamma_{\mathrm{ex}}^{\mathrm{S}} \cap \Gamma_{\mathrm{l}}^{\mathrm{G}}$ of stent and graft according to Equation (3.4). Subsequently, using morphing maps, stent predeformation $\omega > 0$ will be induced on the assembled SG model. In Section 3.2.2.4, morphing maps were introduced in a very general way. In this section, the stent is the morphing object and a specific morphing map that changes the reference configuration of the stent is utilized as introduced in Equation (3.41). Application of the inverse morphing map $\tilde{\boldsymbol{M}}_{\mathrm{Pre}}^{-1}$ changes the reference configuration of the stent limb (not the graft) from $\Omega_{\mathrm{I},0}^{\mathrm{S}}$, $\boldsymbol{X}_{\mathrm{I}}^{\mathrm{S}} \in \Omega_{\mathrm{I},0}^{\mathrm{S}}$ to $\Omega_{\mathrm{Pre},0}^{\mathrm{S}}$, $\boldsymbol{X}_{\mathrm{Pre}}^{\mathrm{S}} \in \Omega_{\mathrm{Pre},0}^{\mathrm{S}}$ where $\tilde{\boldsymbol{M}}_{\mathrm{Pre}}^{-1}$ is defined as

$$\tilde{\boldsymbol{M}}_{\mathrm{Pre}}^{-1}\big(t_{\mathrm{Pre}}(\xi), \Delta r_{\mathrm{Pre}}(\xi), \mathsf{A}_{\mathrm{Pre}}^{j}(\xi)\big) : \begin{cases} \Omega_{\mathrm{I},0}^{\mathrm{S}}\big|_{\xi=0} & \rightarrow & \Omega_{\mathrm{Pre},0}^{\mathrm{S}}\big|_{\xi=1} \\ \boldsymbol{X}_{\mathrm{I}}^{\mathrm{S}}\big|_{\xi=0} & \mapsto & \boldsymbol{X}_{\mathrm{Pre}}^{\mathrm{S}}\big|_{\xi=1} \end{cases}, \tag{3.62}$$

$$t_{\mathrm{Pre}}(\xi) = t_{\mathrm{I}}, \tag{3.63}$$

$$\Delta r_{\mathrm{Pre}}(\xi) = \frac{1}{2}\xi(D_{\mathrm{Pre}}^{\mathrm{S}} - D_{\mathrm{I}}^{\mathrm{S}}), \tag{3.64}$$

$$\mathsf{A}_{\mathrm{Pre}}^{j}(\xi) = \mathsf{A}_{\mathrm{I}}^{\mathrm{S},j}, \quad \forall\, j = 1, 2, ..., n_{\mathrm{C}}. \tag{3.65}$$

The morphing induced deformation is a pure change in the radius of the reference configuration of the stent limb from $D_{\mathrm{I}}^{\mathrm{S}}/2 = D^{\mathrm{SG}}/2$ to $D_{\mathrm{Pre}}^{\mathrm{S}}/2$ according to Equations (3.39) and (3.64) such that after the application of the map $\tilde{\boldsymbol{M}}_{\mathrm{Pre}}^{-1}$ the new reference coordinates of the stent are given by $\boldsymbol{X}_{\mathrm{Pre}}^{\mathrm{S}} \in \Omega_{\mathrm{Pre},0}^{\mathrm{S}}$. The superscript $(\bullet)^{\mathrm{S}}$ in $\mathsf{A}_{\mathrm{I}}^{\mathrm{S},j}$ in Equation (3.65) indicates that $\mathsf{A}_{\mathrm{I}}^{\mathrm{S},j}$ holds only nodes of the stent, i.e., only the stent (not the graft) is morphed. This means that the reference configuration of the graft remains unchanged during this step, i.e., $\boldsymbol{X}_{\mathrm{Pre}}^{\mathrm{G}} = \boldsymbol{X}_{\mathrm{I}}^{\mathrm{G}}$ and $\Omega_{\mathrm{Pre},0}^{\mathrm{G}} = \Omega_{\mathrm{I},0}^{\mathrm{G}}$.

Before the stent predeformation, i.e., before application of the morphing map $\tilde{\boldsymbol{M}}_{\mathrm{Pre}}^{-1}$, the current configuration of the SG is related to the reference configuration via the deformation map $\boldsymbol{\Phi}_{\mathrm{I}}$, i.e.,

$$\boldsymbol{\Phi}_{\mathrm{I}}(\boldsymbol{X}_{\mathrm{I}}^{\{\mathrm{S,G}\}}) = \boldsymbol{x}_{\mathrm{I}}^{\{\mathrm{S,G}\}}. \tag{3.66}$$

In contrast to Chapter 2, where the deformation map $\boldsymbol{\Phi}$ was introduced, now more than one deformation map $\boldsymbol{\Phi}$ exists. Hence, the subscript $(\bullet)_{\mathrm{I}}$ is introduced to indicate that $\boldsymbol{\Phi}_{\mathrm{I}}$ relates the current configuration to the reference configuration at the initial stage, i.e., before the stent predeformation. As the morphing map $\tilde{\boldsymbol{M}}_{\mathrm{Pre}}^{-1}$ changes the reference configuration from $\Omega_{\mathrm{I},0}^{\mathrm{S}}$ to $\Omega_{\mathrm{Pre},0}^{\mathrm{S}}$, this morphing map also affects the deformation map $\boldsymbol{\Phi}$ according to

$$\boldsymbol{\Phi}_{\mathrm{Pre}} = \boldsymbol{\Phi}_{\mathrm{I}} \circ \tilde{\boldsymbol{M}}_{\mathrm{Pre}}. \tag{3.67}$$

In Equation (3.67), $\tilde{\boldsymbol{M}}_{\mathrm{Pre}}$ is the inverse of the diffeomorphic map $\tilde{\boldsymbol{M}}_{\mathrm{Pre}}^{-1}$, i.e., $\tilde{\boldsymbol{M}}_{\mathrm{Pre}} : \Omega_{\mathrm{Pre},0}^{\mathrm{S}} \rightarrow \Omega_{\mathrm{I},0}^{\mathrm{S}}$. After application of the morphing map $\tilde{\boldsymbol{M}}_{\mathrm{Pre}}^{-1}$, i.e., after application of the stent predeformation, the current configuration of the SG is related to the reference configuration via the deformation map

$$\boldsymbol{\Phi}_{\mathrm{Pre}}(\boldsymbol{X}_{\mathrm{Pre}}^{\{\mathrm{S,G}\}}) = \boldsymbol{x}_{\mathrm{Pre}}^{\{\mathrm{S,G}\}}, \tag{3.68}$$

where $\Omega_{\mathrm{Pre}}^{\{\mathrm{S,G}\}}$, $\boldsymbol{x}_{\mathrm{Pre}}^{\{\mathrm{S,G}\}} \in \Omega_{\mathrm{Pre}}^{\{\mathrm{S,G}\}}$ are the current configurations of stent and graft after the stent predeformation.

To be mathematically correct, the mesh tying constraint between stent and graft according to Equation (3.4) needs to be written more precisely, i.e., mortar based mesh tying between stent and graft induces the constraint

$$\boldsymbol{u}^{\mathrm{S}}\big|_{\boldsymbol{\Phi}_{\mathrm{I}}} = \boldsymbol{u}^{\mathrm{G}}\big|_{\boldsymbol{\Phi}_{\mathrm{I}}} \quad \text{on } \Gamma_{\mathrm{I,ex}}^{\mathrm{S}} \cap \Gamma_{\mathrm{I,l}}^{\mathrm{G}}, \tag{3.69}$$

where $\boldsymbol{u}^{(\bullet)}\big|_{\boldsymbol{\Phi}_{\mathrm{I}}} = \boldsymbol{\Phi}_{\mathrm{I}}(\boldsymbol{X}_{\mathrm{I}}^{(\bullet)}) - \boldsymbol{X}_{\mathrm{I}}^{(\bullet)}$ is the displacement of stent ("S") and graft ("G") with respect to the initial stress-free reference configurations $\Omega_{\mathrm{I},0}^{\mathrm{S}}$ and $\Omega_{\mathrm{I},0}^{\mathrm{G}}$, respectively. $\boldsymbol{u}^{(\bullet)}\big|_{\boldsymbol{\Phi}_{\mathrm{I}}}$ is not the same as $\boldsymbol{u}^{(\bullet)}$ defined in Equation (2.2), which is the displacement with respect to the underlying stress-free reference configuration at the respective stage of in-silico EVAR, since the stress-free reference configuration of the stent has changed during stent predeformation.

This methodology for stent predeformation is valid for exterior and interior stents and for all sizes of SGs. Furthermore, no additional models of artificial assembly devices and no additional SG assembly simulation to assemble stent and graft is required since the SG is initially already assembled. Stent predeformation can be accounted for at any stage of in-silico EVAR. Even after the SG deployment, the degree of stent predeformation can be changed.

For a detailed examination of the effect of stent predeformation on residual strains and stresses in the assembled SG, the interested reader is referred to Appendix A.2, where the stress and strain states of the assembled SG are illustratively investigated for the CZ-SG model.

Remark. *This stent predeformation methodology could also be applied to SGs, where the stent predeformation is not a purely radial compression (e.g., Anaconda$^{\mathrm{TM}}$ SGs). Then Equations (3.62)-(3.65) need to be adapted such that in addition to the change in the radius also other deformations of the stent can be prescribed.*

3.5. In-silico EVAR and stent-graft parameter continuation

A procedural overview of the computational approaches of this section is visualized in Figure 3.13. The objective of the proposed in-silico EVAR model is to find the final deployed SG

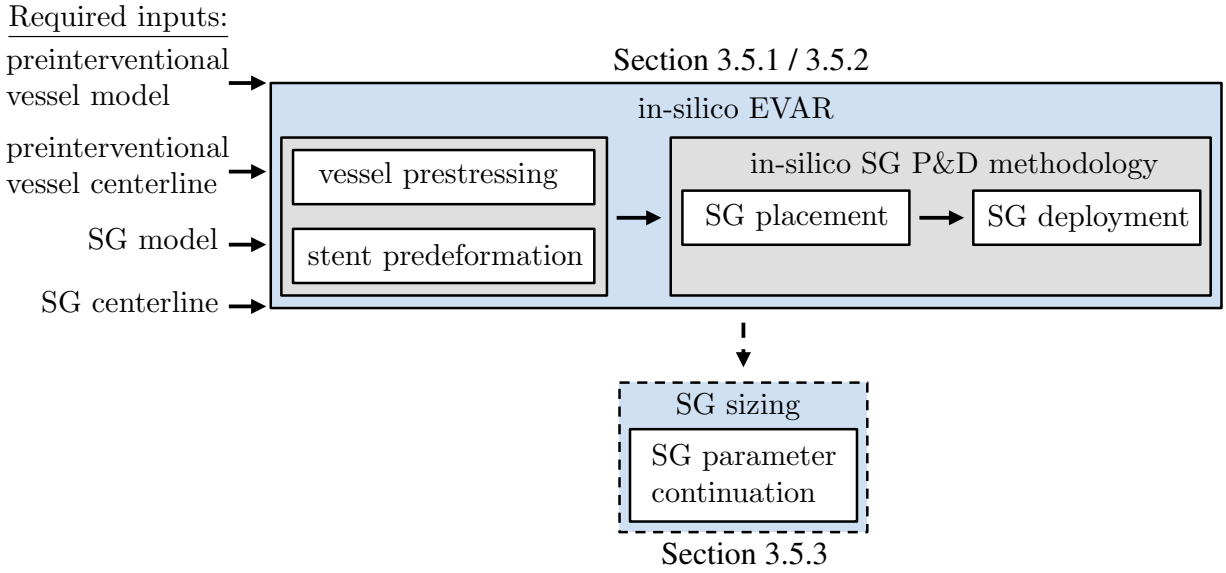

Figure 3.13 Procedural overview of the in-silico EVAR and subsequent SG sizing by SG parameter continuation.

configuration within the elastically deformable vessel under physiologically meaningful conditions, where nonetheless a pseudo-stationary problem is assumed. Required inputs to approximate the deployed configuration by in-silico EVAR are the vessel model and the SG model in the preinterventional configuration as well as their centerlines. In this section, first, the in-silico EVAR model is described for a tube SG in detail (Section 3.5.1). Afterwards, in Section 3.5.2, required extensions of the in-silico EVAR model of bifurcated SGs are elaborated. In Section 3.5.3, SG parameter continuation is used to continuously change the SG diameter starting from an already deployed SG configuration, which can be a valuable tool when investigating the issue of SG sizing.

These computational approaches strongly depend on the morphing algorithm based on control curves $\mathcal{C}$ as described in Section 3.2.2. From now on, $\mathcal{C}_\mathrm{I}$ is the centerline of the initial configuration of the SG $\Omega_{\mathrm{I},0}^{\{\mathrm{S,G}\}}$ and $\mathcal{C}_\mathrm{T}$ is the luminal centerline of the initial, preinterventional configuration of the vessel $\Omega_{\mathrm{I},0}^{\mathrm{Ao}}$. Both, $\mathcal{C}_\mathrm{I}$ and $\mathcal{C}_\mathrm{T}$ are control curves described by n_C points. In in-silico EVAR and the SG sizing by parameter continuation, a change in the reference configuration is applied, i.e., the initial configuration not necessarily has to be equivalent to the stress-free reference configuration. Depending on the particular stage, the stress-free state is defined by a different reference configuration.

Six distinct configurations of the SG are defined where the configurations visualized in Figure 3.14I-III describe reference configurations and the configurations visualized in Figure 3.14IV-VI describe current configurations. All reference configurations are denoted by

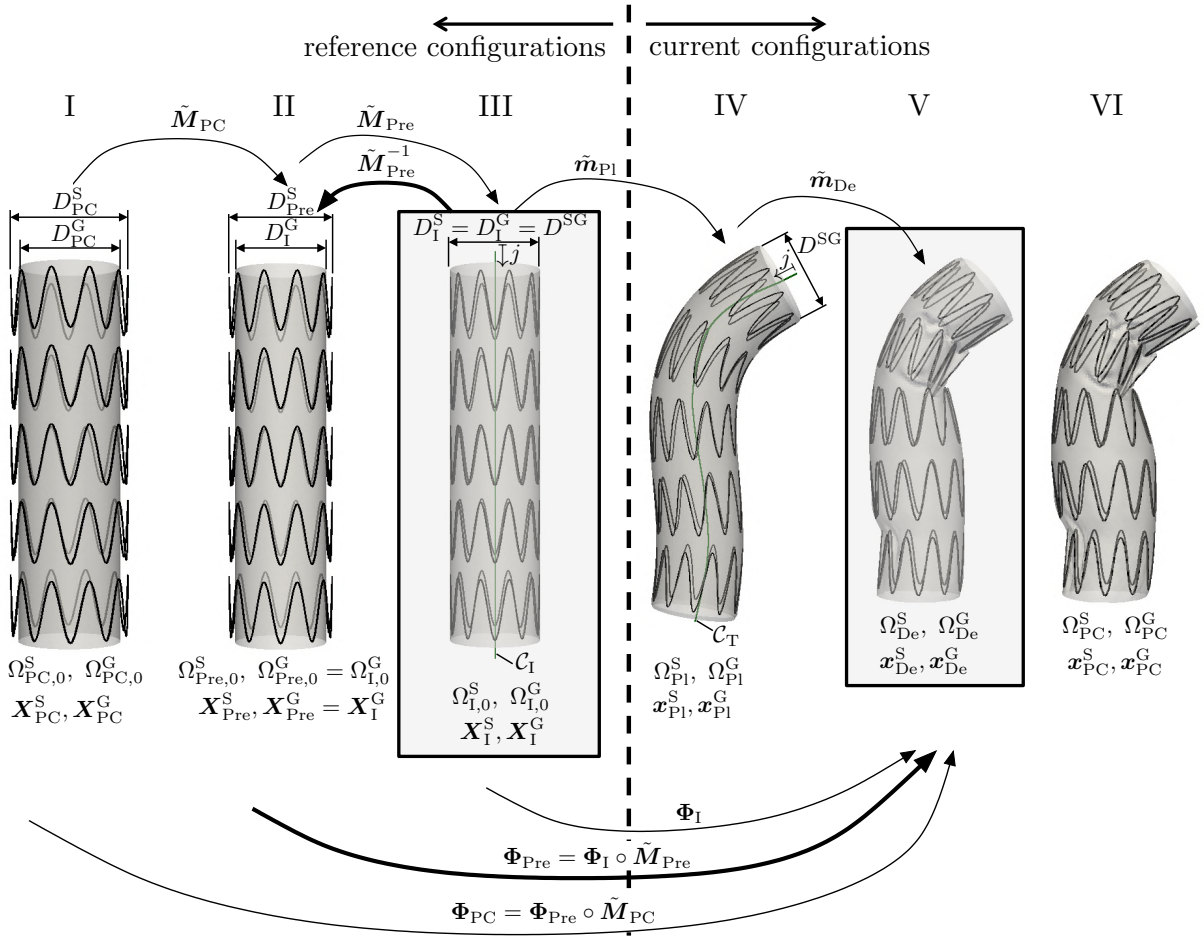

Figure 3.14 Overview of configurations of the SG $\Omega^{\{\mathrm{S,G}\}}_{(\Upsilon)}$ with $\Upsilon \in \{\mathrm{I}, \mathrm{Pre}, \mathrm{Pl}, \mathrm{De}, \mathrm{PC}\}$ of the in-silico EVAR model (initial state (I), stent predeformation (Pre), SG placement (Pl), SG deployment (De) and SG parameter continuation (PC)). Diffeomorphic morphing maps $\tilde{\boldsymbol{M}}$ and $\tilde{\boldsymbol{m}}$ as well as deformation maps $\boldsymbol{\Phi}_{\mathrm{I}}$, $\boldsymbol{\Phi}_{\mathrm{Pre}}$ and $\boldsymbol{\Phi}_{\mathrm{PC}}$ define the relation between the different configurations of the SG. Initial configuration $\mathcal{C}_{\mathrm{I}}$ and target configuration $\mathcal{C}_{\mathrm{T}}$ of the control curve (green). Modified figure reproduced with permission from [106].

the subscript $(\bullet)_0$ whereas all other configurations are current configurations. Further, the subscript $(\bullet)_{\mathrm{Pre}}$ denotes the stent predeformation, $(\bullet)_{\mathrm{Pl}}$ denotes the SG placement and $(\bullet)_{\mathrm{De}}$ the SG deployment. The subscript $(\bullet)_{\mathrm{PC}}$ describes the parameter continuation approach which is used to change the diameter of the SG, i.e., the degree of SG oversizing. Accordingly, $\Omega^{\{\mathrm{S,G}\}}_{\mathrm{Pre},0}$ describes the stress-free reference configurations of stent (superscript $(\bullet)^{\mathrm{S}}$) and graft (superscript $(\bullet)^{\mathrm{G}}$) after the stent predeformation has been applied to the SG. $\Omega^{\{\mathrm{S,G}\}}_{\mathrm{Pl}}$ are the current configurations of stent and graft after the in-silico SG placement has been performed and $\Omega^{\{\mathrm{S,G}\}}_{\mathrm{De}}$ are the current configurations of stent and graft after the in-silico SG deployment has been done. $\Omega^{\{\mathrm{S,G}\}}_{\mathrm{PC},0}$ are the stress-free reference configurations of stent and graft and $\Omega^{\{\mathrm{S,G}\}}_{\mathrm{PC}}$ are the current configurations of stent and graft after the SG diameter has been changed by the parameter continuation approach (cf. Figure3.14).

Remark. *Vessel prestressing as described in Section 3.3.3 does induce a change in the reference configuration of the vessel. Hence, to be precise another reference configuration should be introduced in Figure 3.14. However, since in this thesis vessel prestressing is only applied but not further investigated, this additional reference configuration due to vessel prestressing is not further outlined.*

The initial reference configurations of stent and graft $\Omega_{\mathrm{I},0}^{\{\mathrm{S,G}\}}$, i.e., the discretized stent and graft configurations obtained from the SG model generation process as described in Section 3.4.1, are visualized in Figure 3.14III. The final deployed configurations of stent and graft $\Omega_{\mathrm{De}}^{\{\mathrm{S,G}\}}$, i.e., the result of the in-silico EVAR without SG parameter continuation, are visualized in Figure 3.14V. The position vector of a reference configuration is described by the capital letter $\boldsymbol{X}$ and the position vector of a current configuration is described by the small letter $\boldsymbol{x}$. At any stage of the in-silico EVAR and the SG parameter continuation, the current configurations $\Omega_{(\Upsilon)}^{(\mathit{\Pi})}$ with $\mathit{\Pi} \in \{\mathrm{Ao}, \mathrm{G}, \mathrm{S}\}$ and $\Upsilon \in \{\mathrm{I}, \mathrm{Pre}, \mathrm{Pl}, \mathrm{De}, \mathrm{PC}\}$ are related to the corresponding stress-free reference configurations $\Omega_{(\Upsilon),0}^{(\mathit{\Pi})}$ via the mapping $\boldsymbol{\Phi}$ (cf. Section 2.1.1) based on the BVP of in-silico EVAR according to Equations (3.1)-(3.7). However, as the stress-free reference configurations of stent and graft are modified during progression of in-silico EVAR (e.g., during stent predeformation as described in Section 3.4.3), the subscripts $(\bullet)_{\mathrm{I}}$, $(\bullet)_{\mathrm{Pre}}$ and $(\bullet)_{\mathrm{PC}}$ are introduced. $\boldsymbol{\Phi}_{\mathrm{I}}$ initially relates the current configurations to the corresponding stress-free reference configurations, i.e., before any change of the stress-free reference configuration has been applied. $\boldsymbol{\Phi}_{\mathrm{Pre}}$ relates the current configurations to the corresponding stress-free reference configurations after the stent predeformation has been applied. $\boldsymbol{\Phi}_{\mathrm{PC}}$ relates the current configurations to the corresponding stress-free reference configurations after the parameter continuation has been applied (cf. Figure 3.14).

3.5.1. In-silico EVAR with tube stent-grafts

In this section, a simplified scenario of tube SGs and synthetic vessels without bifurcation into the iliac arteries is considered to describe theoretical aspects of the in-silico EVAR model. The presented in-silico EVAR approach is subdivided into three major steps (cf. Figure 3.13), where all three steps depend on morphing maps $\tilde{\boldsymbol{M}}$ and $\tilde{\boldsymbol{m}}$ as introduced in Section 3.2.2.4. First, the vessel and SG model are preconditioned (Section 3.5.1.1), i.e., the vessel is prestressed and stent predeformation is applied to the SG. Afterwards, the SG is placed inside the vessel (Section 3.5.1.2). Finally, the SG is deployed (Section 3.5.1.3).

3.5.1.1. Vessel and stent-graft preconditioning

The vessel prestressing as well as the stent predeformation methodology were already discussed in Section 3.3.3 and 3.4.3, where the vessel and the SG model were introduced. Here, the two vessel and SG preconditioning steps are only restated for the sake of completeness of the in-silico EVAR model and to state specific parameters associated with vessel prestressing and stent predeformation.

Throughout this thesis, the vessel and the embedding tissue, i.e., the surrounding spring boundary conditions according to Equations (3.5) and (3.6), are prestressed to an assumed diastolic pressure level of $p^{\mathrm{diast}} = 80\ \mathrm{mmHg}$ (cf. Figure 3.15I). The degree of stent predeforma-

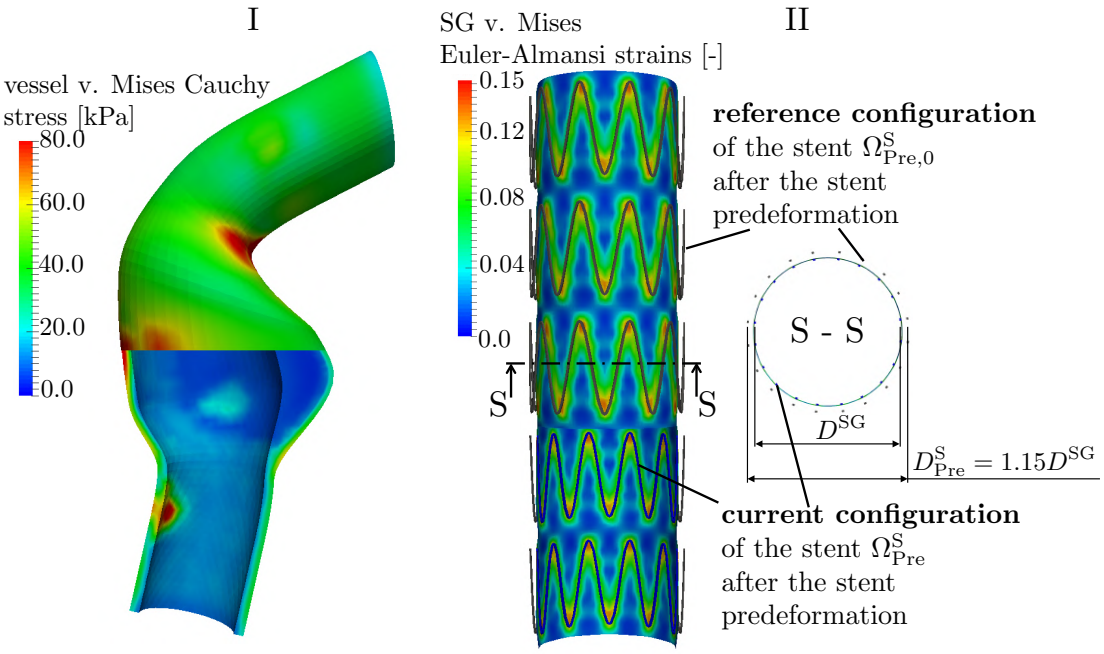

Figure 3.15 Vessel prestressing (I) and stent predeformation (II). Modified figure reproduced with permission from [106].

tion significantly varies among SG devices and sizes and even varies among the different stent limbs of one SG. For simplicity and due to the limited availability of data, in this thesis constant stent predeformation of $\omega = 15\%$ (cf. Figure 3.15II) for each stent limb is used if not stated differently. It is important to note, that the stent predeformation methodology, described in Section 3.4.3, changes the stress-free reference configuration of the stent from $\Omega^{S}_{I,0}$ to $\Omega^{S}_{Pre,0}$, whereas the stress-free reference configuration of the graft remains unchanged, i.e., $\Omega^{G}_{Pre,0} = \Omega^{G}_{I,0}$ (cf. Figure 3.14II). Hence, after stent predeformation, the current configuration of the SG is related to the reference configuration via the deformation map $\boldsymbol{\Phi}_{Pre}(\boldsymbol{X}^{\{S,G\}}_{Pre}) = \boldsymbol{x}^{\{S,G\}}_{Pre}$, where $\boldsymbol{\Phi}_{Pre} = \boldsymbol{\Phi}_{I} \circ \tilde{\boldsymbol{M}}_{Pre}$ as stated in Equations (3.67) and (3.68).

3.5.1.2. Stent-graft placement

The maximum length of the proximal landing zone is proximally limited by the branch-offs into the renal arteries which must not be occluded by the covered part of the SG after the deployment. The proximal landing zone of the SG is assumed to be as long as possible. Thus, the SG is positioned slightly distal to the branches to the renal arteries according to the preinterventional CT data. The distal landing zones are not a priori determined but evolve from the deployment process.

The in-silico SG placement is a sequence of two steps (cf. Figure 3.16I+II). The first step is a transformation of the SG from the initial, straight configuration $\Omega^{\{S,G\}}_{I}$ onto the vessel centerline with a reduced SG diameter of D_{Pl} such that the SG entirely fits into the vessel (cf. Figure 3.16I). No contact constraints between vessel and SG are considered in this step. A subsequent reenlargement of the SG to the nominal diameter D^{SG} establishes potential contact between SG and vessel (cf. Figure 3.16II) which is modeled by the frictional contact con-

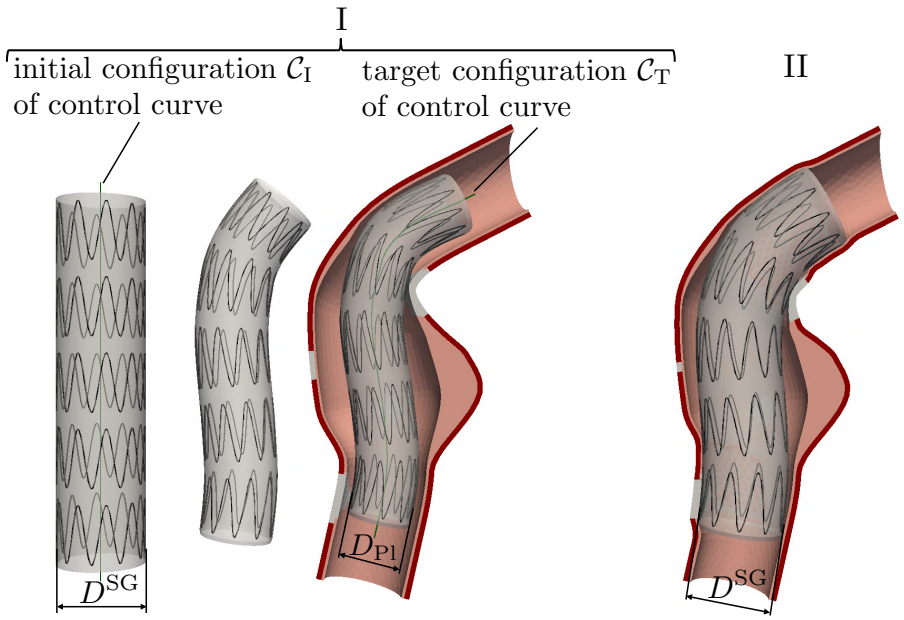

Figure 3.16 In-silico SG placement: radial crimping and morphing of the SG (I); radial reenlargement of the SG (II). Intermediate SG configuration in (I) is only shown for better visualization. This intermediate configuration is not required for computation. Modified figure reproduced with permission from [106].

straints stated in (3.7). Both steps of the in-silico SG placement are described by the morphing map $\tilde{\boldsymbol{m}}_\mathrm{Pl}$ which changes the current configuration (cf. Section 3.2.2.4) of stent and graft from $\Omega_\mathrm{I}^{\{\mathrm{S,G}\}}$, $\boldsymbol{x}_\mathrm{I}^{\{\mathrm{S,G}\}} \in \Omega_\mathrm{I}^{\{\mathrm{S,G}\}}$ (cf. Figure 3.14III) to $\Omega_\mathrm{Pl}^{\{\mathrm{S,G}\}}$, $\boldsymbol{x}_\mathrm{Pl}^{\{\mathrm{S,G}\}} \in \Omega_\mathrm{Pl}^{\{\mathrm{S,G}\}}$ (cf. Figure 3.14IV) according to

$$\tilde{\boldsymbol{m}}_\mathrm{Pl}\big(t_\mathrm{Pl}(\xi), \Delta r_\mathrm{Pl}(\xi), \mathsf{A}_\mathrm{Pl}^j(\xi)\big) : \begin{cases} \Omega_\mathrm{I}^{\{\mathrm{S,G}\}}\big|_{\xi=0} & \rightarrow \quad \Omega_\mathrm{Pl}^{\{\mathrm{S,G}\}}\big|_{\xi=1} \\ \boldsymbol{x}_\mathrm{I}^{\{\mathrm{S,G}\}}\big|_{\xi=0} & \mapsto \quad \boldsymbol{x}_\mathrm{Pl}^{\{\mathrm{S,G}\}}\big|_{\xi=1} \end{cases}, \tag{3.70}$$

$$t_\mathrm{Pl}(\xi) = \begin{cases} t_\mathrm{I} + 2\xi(t_\mathrm{T} - t_\mathrm{I}), & \xi < \frac{1}{2} \\ t_\mathrm{T}, & \xi \geq \frac{1}{2} \end{cases}, \tag{3.71}$$

$$\Delta r_\mathrm{Pl}(\xi) = \begin{cases} -\xi(D^\mathrm{SG} - D_\mathrm{Pl}), & \xi < \frac{1}{2} \\ (\xi - 1)(D^\mathrm{SG} - D_\mathrm{Pl}), & \xi \geq \frac{1}{2} \end{cases}, \tag{3.72}$$

$$\mathsf{A}_\mathrm{Pl}^j(\xi) = \mathsf{A}_\mathrm{I}^j, \quad \forall\, j = 1, 2, ..., n_\mathrm{C}. \tag{3.73}$$

Equation (3.71) triggers a control curve induced deformation of the current configuration of the SG from the initial configuration of the control curve $\mathcal{C}_\mathrm{I}$ (centerline of the SG configuration $\Omega_{\mathrm{I},0}^{\{\mathrm{S,G}\}}$) to the target configuration of the control curve $\mathcal{C}_\mathrm{T}$ (centerline of the vessel configuration $\Omega_{\mathrm{I},0}^{\mathrm{Ao}}$) for $\xi < \frac{1}{2}$. For $\xi \geq \frac{1}{2}$, no further control curve induced deformation takes place.

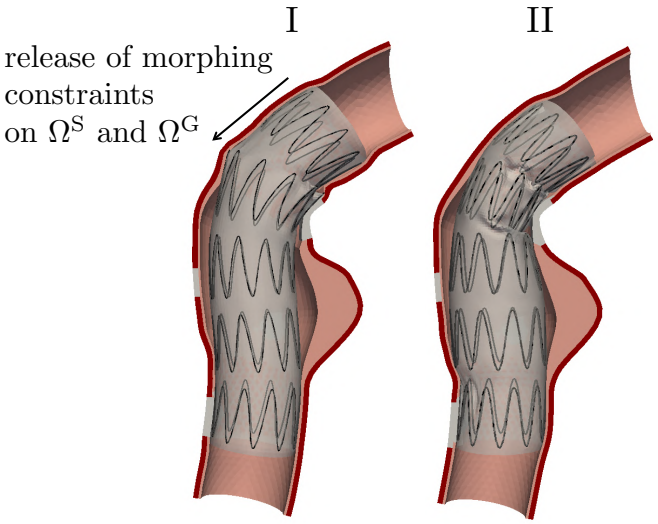

Figure 3.17 In-silico SG deployment: release of morphing constraints (I) and final deployed configuration (II). Reproduced with permission from [106].

The configuration of the control curve $\mathcal{C}(t(\xi))$ for $\xi \geq \frac{1}{2}$ is equal to the target configuration $\mathcal{C}_{\mathrm{T}}$ of the control curve. Equation (3.72) states a change in the radius of stent and graft from $D^{\mathrm{SG}}/2$ to $D_{\mathrm{Pl}}/2$ for $\xi < \frac{1}{2}$ and a change in the radius from $D_{\mathrm{Pl}}/2$ to $D^{\mathrm{SG}}/2$ for $\xi \geq \frac{1}{2}$.

According to Equation (3.73) all nodes of the SG are morphed for any $\xi \in [0, 1]$. Hence, during the total in-silico SG placement step, the current configuration of the entire SG is prescribed by the morphing map $\tilde{\boldsymbol{m}}_{\mathrm{Pl}}(\xi)$. Therefore, buckling of the SG is prevented during the whole placement process. Moreover, since the deformation of the entire SG is prescribed, the contact between SG and vessel reduces to a computationally simple *Signorini contact problem*. Still, the BVP of Equation (3.1)-(3.7) has to be solved for the vessel Ω_0^{Ao}. Those aspects make the in-silico placement computationally very efficient and robust.

It is important to note that only the initial and the target configuration of the control curve as well as the initial configurations of the vessel and the SG (the morphing object) are required. Based on these inputs, the target configuration of the SG in the interior of the vessel is computed, where no intermediate configurations of the control curve and the SG need to be computed.

3.5.1.3. Stent-graft deployment

Before the SG is deployed, the systolic pressure state $\hat{\boldsymbol{t}}^{\mathrm{Ao}} = \hat{\boldsymbol{t}}^{\mathrm{G}} = -p^{\mathrm{sys}}\boldsymbol{n}$ on $(\gamma_{\mathrm{l,n}}^{\mathrm{Ao}} \cup \gamma_{\mathrm{l}}^{\mathrm{G}})$ is applied with $p^{\mathrm{sys}} = 130\ \mathrm{mmHg}$ and the internal vessel pressure on the luminal vessel surface $\gamma_{\mathrm{l,c}}^{\mathrm{Ao}}$ covered by the SG is removed, i.e., $\hat{\boldsymbol{t}}^{\mathrm{Ao}} = \boldsymbol{0}$ on $\gamma_{\mathrm{l,c}}^{\mathrm{Ao}}$ (cf. Equation (3.8)). During the SG deployment, the morphing constraints on the SG are gradually removed starting from the proximal end (cf. Figure 3.17I) by application of the map

$$\tilde{\boldsymbol{m}}_{\mathrm{De}}\big(t_{\mathrm{De}}(\xi), \Delta r_{\mathrm{De}}(\xi), \mathsf{A}_{\mathrm{De}}^{j}(\xi)\big) : \begin{cases} \Omega_{\mathrm{Pl}}^{\{\mathrm{S,G}\}}\Big|_{\xi=0} & \rightarrow & \Omega_{\mathrm{De}}^{\{\mathrm{S,G}\}}\Big|_{\xi=1} \\ \boldsymbol{x}_{\mathrm{Pl}}^{\{\mathrm{S,G}\}}\Big|_{\xi=0} & \mapsto & \boldsymbol{x}_{\mathrm{De}}^{\{\mathrm{S,G}\}}\Big|_{\xi=1} \end{cases}, \tag{3.74}$$

$$t_{\mathrm{De}}(\xi) = t_{\mathrm{T}}, \tag{3.75}$$

$$\Delta r_{\mathrm{De}}(\xi) = 0, \tag{3.76}$$

$$\mathsf{A}^{j}_{\mathrm{De}}(\xi) = \begin{cases} \mathsf{A}^{j}_{\mathrm{I}}, & \xi < \frac{j}{n_{\mathrm{C}}} \\ \emptyset, & \xi \geq \frac{j}{n_{\mathrm{C}}} \end{cases}, \quad \forall\, j = 1, 2, ..., n_{\mathrm{C}}, \tag{3.77}$$

where $\Omega^{\{\mathrm{S,G}\}}_{\mathrm{Pl}}$, $\boldsymbol{x}^{\{\mathrm{S,G}\}}_{\mathrm{Pl}} \in \Omega^{\{\mathrm{S,G}\}}_{\mathrm{Pl}}$ (cf. Figure 3.14IV) are the current configurations of stent and graft before the in-silico SG deployment ($\xi = 0$) and $\Omega^{\{\mathrm{S,G}\}}_{\mathrm{De}}$, $\boldsymbol{x}^{\{\mathrm{S,G}\}}_{\mathrm{De}} \in \Omega^{\{\mathrm{S,G}\}}_{\mathrm{De}}$ (cf. Figure 3.14V) are the current configurations of stent and graft after the in-silico deployment ($\xi = 1$). Equation (3.77) induces a gradual release of the morphing constraints from the nodes of the SG by gradual emptying of the morphing sets $\mathsf{A}^{j}_{\mathrm{De}}(\xi)$. Only nodes that are part of the total morphing set A_{De} are prescribed by morphing constraints, cf. Equation (3.40). As

$$\mathsf{A}_{\mathrm{De}}(\xi = 1) = \bigcup_{j=1}^{n_{\mathrm{C}}} \mathsf{A}^{j}_{\mathrm{De}}(\xi = 1) = \emptyset \tag{3.78}$$

for $\xi = 1$, in the deployed state all morphing constraints are removed. Consequently, the current configurations $\Omega^{(\Pi)}_{\mathrm{De}}$ in the deployed state are related to the corresponding stress-free reference configurations $\Omega^{(\Pi)}_{\mathrm{Pre},0}$ solely by means of the deformation map

$$\boldsymbol{\Phi}_{\mathrm{Pre}}(\boldsymbol{X}^{(\Pi)}_{\mathrm{Pre}}) = (\boldsymbol{\Phi}_{\mathrm{I}} \circ \tilde{\boldsymbol{M}}_{\mathrm{Pre}})(\boldsymbol{X}^{(\Pi)}_{\mathrm{Pre}}) = \boldsymbol{x}^{(\Pi)}_{\mathrm{De}} \tag{3.79}$$

(cf. Figure 3.14) with $\Pi \in \{\mathrm{Ao}, \mathrm{G}, \mathrm{S}\}$ based on the BVP of in-silico EVAR (cf. Section (3.1). This means that the SG can elastically deform within the elastically deformable vessel. A prescribed decay of the damping coefficients c_{M} and c_{K} is applied in the dynamic relaxation scheme (cf. Section 2.2) used in this thesis. Hence, high damping coefficients of $c_{\mathrm{M}} = 0.5\ \mathrm{ms}^{-1}$ and $c_{\mathrm{K}} = 0.5\ \mathrm{ms}$ are used at the beginning of the release of the morphing constraints and when the system approaches toward the steady-state, the coefficients tend toward zero, i.e., $c_{\mathrm{M}} \to 0\ \mathrm{ms}^{-1}$ and $c_{\mathrm{K}} \to 0\ \mathrm{ms}$. The final state of SG and vessel after the in-silico SG deployment is visualized in Figure 3.17II.

3.5.2. In-silico EVAR with bifurcated stent-grafts

This section provides relevant aspects for the extension of in-silico EVAR proposed in Section 3.5.1 to patient-specific cases with bifurcated SGs. Bifurcated SGs as introduced in Section 3.4 are a modular composition of three tube-shaped parts: the proximal SG part and two iliac parts. In-silico EVAR with bifurcated SGs functions equally than in-silico EVAR with tube SGs. The only difference is that the presented algorithms have to be applied to all three tube-shaped parts of the bifurcated SG. Hence, in the following it is distinguished between the proximal SG part (blue), the left iliac SG part (orange) and the right iliac SG part (green), cf. Figure 3.18IIIc.

Further, in-silico EVAR with bifurcated SGs demands three control curves: one control curve of the proximal part $\mathcal{C}^{\mathrm{P}}$, one control curve of the left iliac part $\mathcal{C}^{\mathrm{L}}$ and one control curve of the right iliac part $\mathcal{C}^{\mathrm{R}}$ of the SG. Each of the three control curves has to be given in the initial $\mathcal{C}^{(\Theta)}_{\mathrm{I}}$ and

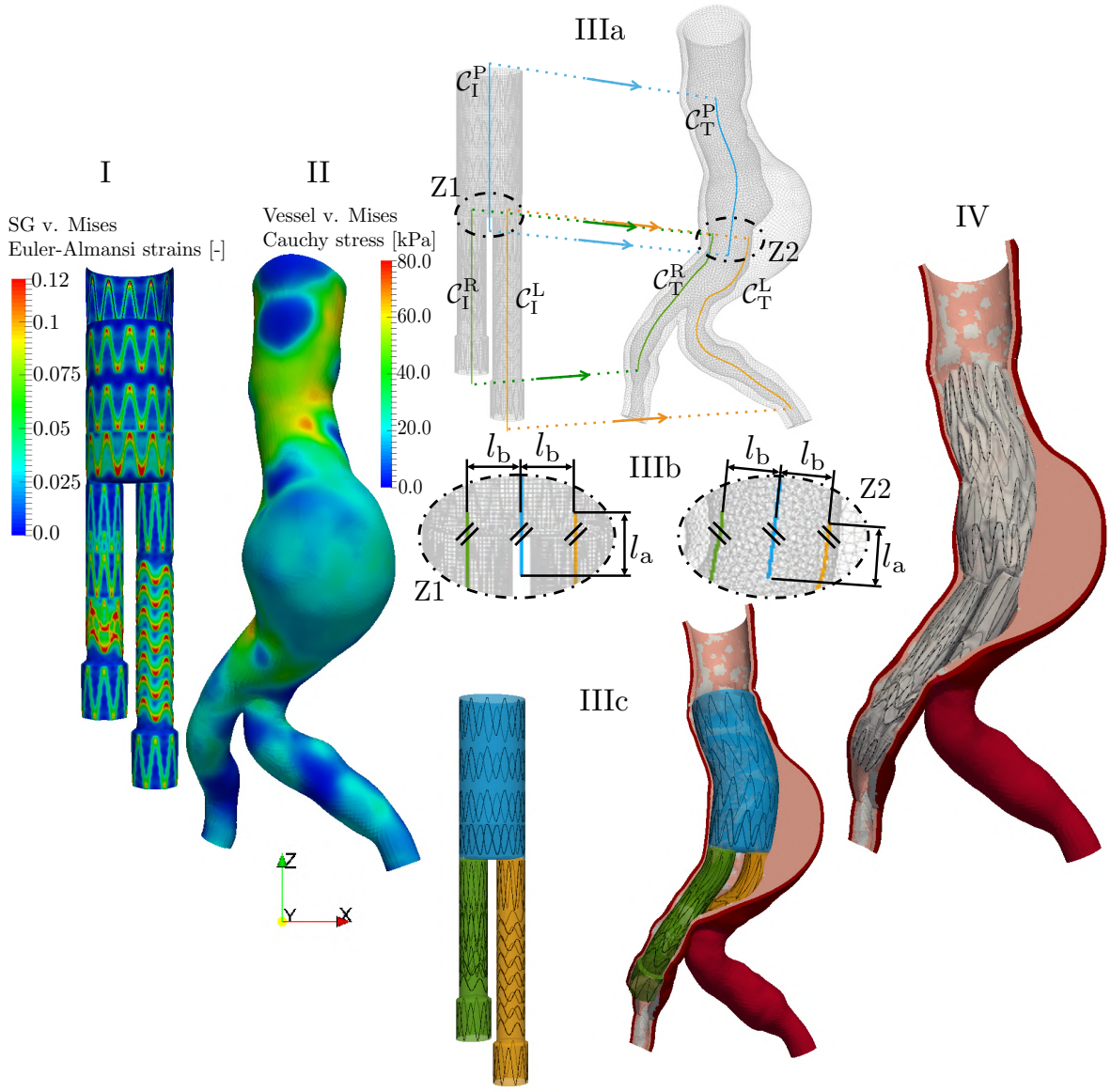

Figure 3.18 In-silico EVAR with bifurcated stent-grafts applied to patient 1: stent predeformation (I), vessel prestressing (II), SG placement (IIIa-c) and final deployed state under static conditions (IV). Overview of the control curves $\mathcal{C}$ of the proximal part $(\bullet)^{\mathrm{P}}$, the left iliac part $(\bullet)^{\mathrm{L}}$ and the right iliac part $(\bullet)^{\mathrm{R}}$ in the initial $(\bullet)_{\mathrm{I}}$ and the target configuration $(\bullet)_{\mathrm{T}}$ (IIIa). Colors of the SG indicate affiliation to the proximal control curve (blue), the left iliac control curve (orange) and the right iliac control curve (green) (IIIc). Reproduced with permission from [107].

the target configuration $\mathcal{C}_{\mathrm{T}}^{(\Theta)}$ with $\Theta \in \{\mathrm{P}, \mathrm{L}, \mathrm{R}\}$ (cf. Figure 3.18IIIa). The initial configurations of the control curves $\mathcal{C}_{\mathrm{I}}^{(\Theta)}$ are the centerlines of the three SG parts in the initial undeformed configuration. These three centerlines are known from the SG model generation process described in Section 3.4. The target configurations of the control curves $\mathcal{C}_{\mathrm{T}}^{(\Theta)}$ correspond to the luminal centerlines of the vessel in the preinterventional imaged configuration which are known from the segmentation process (cf. Section 3.3).

For bifurcated SGs, the in-silico EVAR steps based on morphing maps $\tilde{\boldsymbol{m}}$ and $\tilde{\boldsymbol{M}}$ (Section 3.2.2.4) are combinations of three morphing maps, i.e.,

$$(\tilde{\boldsymbol{M}}^{\mathrm{bif}}_{\mathrm{Pre}})^{-1}\Big((\tilde{\boldsymbol{M}}^{\mathrm{P}}_{\mathrm{Pre}})^{-1},(\tilde{\boldsymbol{M}}^{\mathrm{L}}_{\mathrm{Pre}})^{-1},(\tilde{\boldsymbol{M}}^{\mathrm{R}}_{\mathrm{Pre}})^{-1}\Big):\ \Omega^{\mathrm{S}}_{\mathrm{I},0}\rightarrow\Omega^{\mathrm{S}}_{\mathrm{Pre},0}, \tag{3.80}$$

$$\tilde{\boldsymbol{m}}^{\mathrm{bif}}_{\mathrm{Pl}}(\tilde{\boldsymbol{m}}^{\mathrm{P}}_{\mathrm{Pl}},\tilde{\boldsymbol{m}}^{\mathrm{L}}_{\mathrm{Pl}},\tilde{\boldsymbol{m}}^{\mathrm{R}}_{\mathrm{Pl}}):\ \Omega^{\{\mathrm{S,G}\}}_{\mathrm{I}}\rightarrow\Omega^{\{\mathrm{S,G}\}}_{\mathrm{Pl}}, \tag{3.81}$$

$$\tilde{\boldsymbol{m}}^{\mathrm{bif}}_{\mathrm{De}}(\tilde{\boldsymbol{m}}^{\mathrm{P}}_{\mathrm{De}},\tilde{\boldsymbol{m}}^{\mathrm{L}}_{\mathrm{De}},\tilde{\boldsymbol{m}}^{\mathrm{R}}_{\mathrm{De}}):\ \Omega^{\{\mathrm{S,G}\}}_{\mathrm{Pl}}\rightarrow\Omega^{\{\mathrm{S,G}\}}_{\mathrm{De}}. \tag{3.82}$$

In Equations (3.80)-(3.82), the superscript $(\bullet)^{\mathrm{bif}}$ denotes the total morphing map of the bifurcated SG which is a superposition of the local morphing maps of the three tube-shaped parts of the SG (the proximal part $(\bullet)^{\mathrm{P}}$, the left iliac part $(\bullet)^{\mathrm{L}}$ and the right iliac part $(\bullet)^{\mathrm{R}}$), where the local morphing maps function exactly like defined in Equations (3.62)-(3.65), (3.70)-(3.73) and (3.74)-(3.77), respectively. Each local morphing map $(\bullet)^{(\Theta)}$ with $\Theta\in\{\mathrm{P},\mathrm{L},\mathrm{R}\}$ is only associated with its given control curve in the initial configuration $\mathcal{C}^{(\Theta)}_{\mathrm{I}}$ and target configuration $\mathcal{C}^{(\Theta)}_{\mathrm{T}}$.

Since stent predeformation is only applied to the stent limbs (not to the graft), which are not interconnected, no special treatment between the local morphing maps $(\tilde{\boldsymbol{M}}^{\mathrm{P}}_{\mathrm{Pre}})^{-1}$, $(\tilde{\boldsymbol{M}}^{\mathrm{L}}_{\mathrm{Pre}})^{-1}$ and $(\tilde{\boldsymbol{M}}^{\mathrm{R}}_{\mathrm{Pre}})^{-1}$ is required. Each local morphing map governs the stent predeformation process of the stent limbs of the respective parts. A bifurcated CZ-SG after stent predeformation is visualized in Figure 3.18I.

The SG placement, which is governed by the morphing map $\tilde{\boldsymbol{m}}^{\mathrm{bif}}_{\mathrm{Pl}}$ according to Equation (3.81), is a transformation of the SG from the undeformed SG configuration into the vessel geometry according to the evolution of the control curves $\mathcal{C}^{(\Theta)}_{\mathrm{I}}$ from their initial configuration into their target configuration $\mathcal{C}^{(\Theta)}_{\mathrm{T}}$ with $\Theta\in\{\mathrm{P},\mathrm{L},\mathrm{R}\}$ (cf. Figure 3.18III). During the SG placement step, the deformation of the SG is completely prescribed by the morphing algorithm based on control curves, where each SG part (proximal part, left iliac part, right iliac part) is morphed individually by the respective local morphing map $\tilde{\boldsymbol{m}}^{\mathrm{P}}_{\mathrm{Pl}}$, $\tilde{\boldsymbol{m}}^{\mathrm{L}}_{\mathrm{Pl}}$ and $\tilde{\boldsymbol{m}}^{\mathrm{R}}_{\mathrm{Pl}}$, respectively. The local morphing maps $\tilde{\boldsymbol{m}}^{(\Theta)}_{\mathrm{Pl}}$ with $\Theta\in\{\mathrm{P},\mathrm{L},\mathrm{R}\}$ of the single tube-shaped SG parts function equally as defined in Equations (3.70)-(3.73). This means, the deformation of the proximal SG part (blue) is fully described by the evolution of the control curve $\mathcal{C}^{\mathrm{P}}$ from $\mathcal{C}^{\mathrm{P}}_{\mathrm{I}}$ to $\mathcal{C}^{\mathrm{P}}_{\mathrm{T}}$ and independent of the evolution of the control curves $\mathcal{C}^{\mathrm{L}}$ and $\mathcal{C}^{\mathrm{R}}$. Similar independencies are given for the left iliac SG part and the right iliac SG part, respectively (cf. Figure 3.18III). To ensure continuity between the three SG parts $\Theta\in\{\mathrm{P},\mathrm{L},\mathrm{R}\}$ during the entire SG placement, the following conditions between the initial configurations $\mathcal{C}^{(\Theta)}_{\mathrm{I}}$ and the target configurations $\mathcal{C}^{(\Theta)}_{\mathrm{T}}$ of the control curves have to be satisfied (cf. Figure 3.18IIIb):

- The distal end of the control curve $\mathcal{C}^{\mathrm{P}}_{\mathrm{I}}$ and the proximal ends of the control curves $\mathcal{C}^{\mathrm{L}}_{\mathrm{I}}$ and $\mathcal{C}^{\mathrm{R}}_{\mathrm{I}}$ have to be piecewise parallel and have to be in one plane. Same holds for the target configurations of the control curves $\mathcal{C}^{\mathrm{P}}_{\mathrm{T}}$, $\mathcal{C}^{\mathrm{L}}_{\mathrm{T}}$ and $\mathcal{C}^{\mathrm{R}}_{\mathrm{T}}$.

- The longitudinal overlap l_{a} of the three control curves as well as the transverse distance l_{b} between the three control curves has to be the same in the initial configurations $\mathcal{C}^{(\Theta)}_{\mathrm{I}}$ and the target configurations $\mathcal{C}^{(\Theta)}_{\mathrm{T}}$.

During the in-silico SG placement, the deformation of the SG is fully prescribed by morphing constraints. After the placement of the SG in the interior of the vessel, the morphing constraints

of the SG are gradually removed starting at the proximal end of the SG. This process is governed by the map $\tilde{\boldsymbol{m}}_{\mathrm{De}}^{\mathrm{bif}}$, where first the proximal part of the SG is released by $\tilde{\boldsymbol{m}}_{\mathrm{De}}^{\mathrm{P}}$. After the full removal of all morphing constraints of the proximal SG part, the release of the morphing constraints of both iliac SG parts starts simultaneously from the proximal end governed by the maps $\tilde{\boldsymbol{m}}_{\mathrm{De}}^{\mathrm{L}}$ and $\tilde{\boldsymbol{m}}_{\mathrm{De}}^{\mathrm{R}}$, respectively. After the in-silico SG deployment, i.e., after the release of all morphing constraints of all three SG parts, the SG can elastically deform within the elastically deformable vessel. Additional frictional contact is considered between the two iliac parts of the SG with a friction coefficient of $\mathfrak{F} = 0.4$. The final state of SG and vessel after the in-silico SG deployment of patient 1 is visualized in Figure 3.18IV.

3.5.3. Stent-graft parameter continuation

As stated in the introduction of this thesis in Section 1.2, correct sizing of the SG in diameter and length is one of the major challenges in the preinterventional planning phase of EVAR. In this thesis, SG sizing is restricted to SG sizing with respect to the SG diameter, i.e., with respect to the degree of SG oversizing (cf. Section 1.1.2.3). In classical in-silico studies investigating the issue of SG sizing [53, 212], for each considered SG diameter a separate EVAR simulation was required. This can be computationally very expensive if many different SG diameters are studied. Therefore, in this section a parameter continuation approach to model different SG diameters within one simulation is proposed which can be used as a computationally very efficient SG sizing tool. This approach requires only one "computationally expensive" in-silico placement and deployment of a SG of a specific size. Afterwards, this deployed state is used as initial guess and the SG diameter is continuously changed by changing the stress-free reference configuration of the SG. As a result, one obtains the deployed state of several different SG sizes without having to perform again an in-silico SG placement and deployment. In Figure 3.19, the procedure of SG parameter continuation is visualized for a SG with initial degree of SG oversizing of $o = 5\%$. This means initially, the SG with $o = 5\%$ is placed and deployed within the vessel and afterwards parameter continuation is used to continuously change the SG diameter to the diameter that corresponds to $o = 35\%$.

In the following the theoretical aspects of the SG parameter continuation approach, which incorporates the use of the morphing algorithm proposed in Section 3.2.2, are stated. After the in-silico deployment of a SG with the nominal diameter $D^{\mathrm{SG}} = D_{\mathrm{I}}^{\mathrm{SG}}$, the nominal diameter of the SG can be modified continuously from $D_{\mathrm{I}}^{\mathrm{SG}}$ ($\xi = 0$ in Figure 3.19) to $D_{\mathrm{PC}}^{\mathrm{SG}}$ ($\xi = 1$ in Figure 3.19). Hence, all degrees of SG oversizing in the range $[o_{\mathrm{I}} = \frac{D_{\mathrm{I}}^{\mathrm{SG}}}{D^{\mathrm{Ao}}} - 1, o_{\mathrm{PC}} = \frac{D_{\mathrm{PC}}^{\mathrm{SG}}}{D^{\mathrm{Ao}}} - 1]$ can be investigated where D^{Ao} is the inner vessel wall diameter in the landing zone.

The continuous change in the nominal diameter of the SG is realized by alteration the reference configuration of the SG from $\Omega_{\mathrm{Pre},0}^{\{\mathrm{S,G}\}}$, $\boldsymbol{X}_{\mathrm{Pre}}^{\{\mathrm{S,G}\}} \in \Omega_{\mathrm{Pre},0}^{\{\mathrm{S,G}\}}$ (cf. Figure 3.14II) to $\Omega_{\mathrm{PC},0}^{\{\mathrm{S,G}\}}$, $\boldsymbol{X}_{\mathrm{PC}}^{\{\mathrm{S,G}\}} \in \Omega_{\mathrm{PC},0}^{\{\mathrm{S,G}\}}$ (cf. Figure 3.14I) according to the morphing map

$$\tilde{\boldsymbol{M}}_{\mathrm{PC}}^{-1}\big(t_{\mathrm{PC}}(\xi), \Delta r_{\mathrm{PC}}^{\mathrm{S}}(\xi), \Delta r_{\mathrm{PC}}^{\mathrm{G}}(\xi), \mathsf{A}_{\mathrm{PC}}^{j}(\xi)\big) : \begin{cases} \Omega_{\mathrm{Pre},0}^{\{\mathrm{S,G}\}}\Big|_{\xi=0} & \rightarrow & \Omega_{\mathrm{PC},0}^{\{\mathrm{S,G}\}}\Big|_{\xi=1} \\ \boldsymbol{X}_{\mathrm{Pre}}^{\{\mathrm{S,G}\}}\Big|_{\xi=0} & \mapsto & \boldsymbol{X}_{\mathrm{PC}}^{\{\mathrm{S,G}\}}\Big|_{\xi=1} \end{cases}, \tag{3.83}$$

$$t_{\mathrm{PC}}(\xi) = t_{\mathrm{I}}, \tag{3.84}$$

$$\Delta r^{\mathrm{S}}_{\mathrm{PC}}(\xi) = \frac{1}{2}\xi(D^{\mathrm{S}}_{\mathrm{PC}} - D^{\mathrm{S}}_{\mathrm{Pre}}), \tag{3.85}$$

$$\Delta r^{\mathrm{G}}_{\mathrm{PC}}(\xi) = \frac{1}{2}\xi(D^{\mathrm{G}}_{\mathrm{PC}} - D^{\mathrm{SG}}_{\mathrm{I}}), \tag{3.86}$$

$$\mathsf{A}^{j}_{\mathrm{PC}}(\xi) = \mathsf{A}^{j,\{\mathrm{S,G}\}}_{\mathrm{I}}, \quad \forall\, j = 1, 2, ..., n_{\mathrm{C}}. \tag{3.87}$$

The morphing map $\tilde{\boldsymbol{M}}^{-1}_{\mathrm{PC}}$ is a pure change in the diameter of the stent from $D^{\mathrm{S}}_{\mathrm{Pre}}$ to $D^{\mathrm{S}}_{\mathrm{PC}}$ (cf. Equation (3.85)) and the diameter of the graft from $D^{\mathrm{SG}}_{\mathrm{I}}$ to $D^{\mathrm{G}}_{\mathrm{PC}}$ (cf. Equation (3.86)). The diameter $D^{\mathrm{S}}_{\mathrm{PC}}$ of the stent reference configuration $\Omega^{\mathrm{S}}_{\mathrm{PC},0}$ after the parameter continuation is chosen such that the degree of stent predeformation

$$\omega = \frac{D^{\mathrm{S}}_{\mathrm{Pre}}}{D^{\mathrm{SG}}_{\mathrm{I}}} - 1 = \frac{D^{\mathrm{S}}_{\mathrm{PC}}}{D^{\mathrm{SG}}_{\mathrm{PC}}} - 1 \tag{3.88}$$

is kept constant during the entire parameter continuation.

After the change in the nominal diameter of the SG from $D^{\mathrm{SG}}_{\mathrm{I}}$ to $D^{\mathrm{SG}}_{\mathrm{PC}}$, the relation between the stress-free reference configuration $\Omega^{\{\mathrm{S,G}\}}_{\mathrm{PC},0}$ (cf. Figure 3.14I) and the current configuration $\Omega^{\{\mathrm{S,G}\}}_{\mathrm{PC}}$ (cf. Figure 3.14VI) is determined by the deformation map $\boldsymbol{\Phi}_{\mathrm{PC}}$, where

$$\boldsymbol{\Phi}_{\mathrm{PC}} = \boldsymbol{\Phi}_{\mathrm{Pre}} \circ \tilde{\boldsymbol{M}}_{\mathrm{PC}} = \boldsymbol{\Phi}_{\mathrm{I}} \circ \tilde{\boldsymbol{M}}_{\mathrm{Pre}} \circ \tilde{\boldsymbol{M}}_{\mathrm{PC}}. \tag{3.89}$$

In Equation (3.89), $\tilde{\boldsymbol{M}}_{\mathrm{PC}}$ is the inverse of the diffeomorphic map $\tilde{\boldsymbol{M}}^{-1}_{\mathrm{PC}}$, i.e., $\tilde{\boldsymbol{M}}_{\mathrm{PC}} : \Omega^{\mathrm{S}}_{\mathrm{PC},0} \rightarrow \Omega^{\mathrm{S}}_{\mathrm{Pre},0}$. Consequently,

$$\boldsymbol{\Phi}_{\mathrm{PC}}(\boldsymbol{X}^{(\Pi)}_{\mathrm{PC}}) = (\boldsymbol{\Phi}_{\mathrm{I}} \circ \tilde{\boldsymbol{M}}_{\mathrm{Pre}} \circ \tilde{\boldsymbol{M}}_{\mathrm{PC}})(\boldsymbol{X}^{(\Pi)}_{\mathrm{PC}}) = \boldsymbol{x}^{(\Pi)}_{\mathrm{PC}} \tag{3.90}$$

with $\Pi \in \{\mathrm{Ao}, \mathrm{G}, \mathrm{S}\}$ (cf. Figure 3.14).

As the given problem is nonlinear, the results may be path-dependent. Especially, the parameter continuation approach has to be validated carefully with respect to this issue. Therefore, in Appendix A.4 it is shown at one example that the influence of the path-dependency on the outcome using the parameter continuation approach is small.

Similar to in-silico EVAR for bifurcated SGs (Section 3.5.2), the SG parameter continuation approach can be extended to bifurcated SGs by using three control curves: one for the proximal SG part $\mathcal{C}^{\mathrm{P}}$, one for the left iliac SG part $\mathcal{C}^{\mathrm{L}}$ and one for the right iliac SG part $\mathcal{C}^{\mathrm{R}}$. Analogously to Equations (3.80)-(3.82), the morphing map for SG parameter continuation of a bifurcated SG is a combination of three single morphing maps

$$(\tilde{\boldsymbol{M}}^{\mathrm{bif}}_{\mathrm{PC}})^{-1}\Big((\tilde{\boldsymbol{M}}^{\mathrm{P}}_{\mathrm{PC}})^{-1}, (\tilde{\boldsymbol{M}}^{\mathrm{L}}_{\mathrm{PC}})^{-1}, (\tilde{\boldsymbol{M}}^{\mathrm{R}}_{\mathrm{PC}})^{-1}\Big) : \Omega^{\{\mathrm{S,G}\}}_{\mathrm{Pre},0} \rightarrow \Omega^{\{\mathrm{S,G}\}}_{\mathrm{PC},0}, \tag{3.91}$$

where $(\tilde{\boldsymbol{M}}^{\mathrm{P}}_{\mathrm{PC}})^{-1}$, $(\tilde{\boldsymbol{M}}^{\mathrm{L}}_{\mathrm{PC}})^{-1}$ and $(\tilde{\boldsymbol{M}}^{\mathrm{R}}_{\mathrm{PC}})^{-1}$ are the morphing maps of the three tube-shaped parts of the SG: the proximal, the left iliac part and the right iliac part. SG parameter continuation of bifurcated SGs can also be applied only to selected parts of the SG such as only the proximal part whereas the diameters of the iliac parts of the SG remain unchanged.

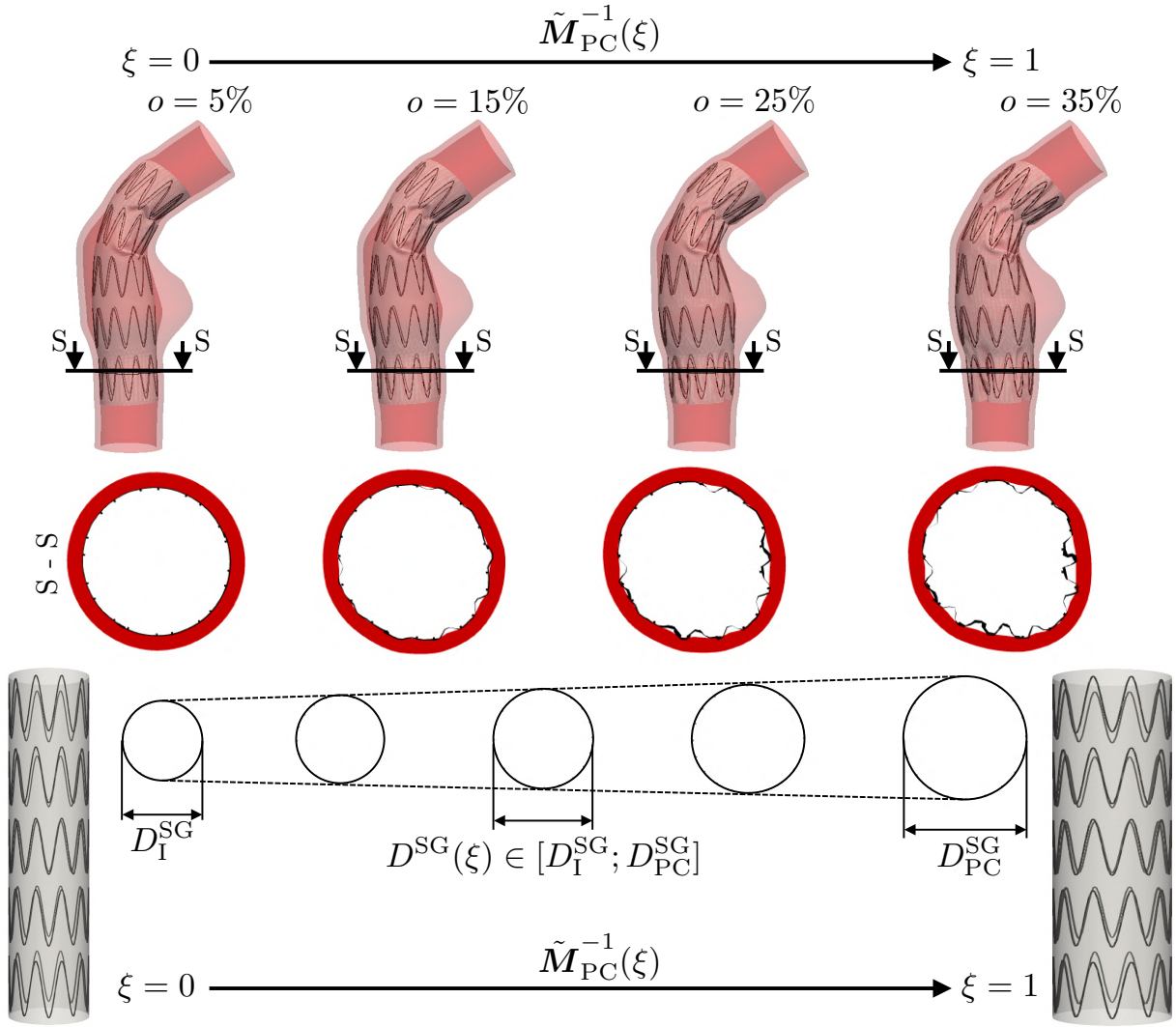

Figure 3.19 Procedure of the continuous change of the degree of SG oversizing o using the SG parameter continuation approach.

3.6. Postprocessing of the in-silico EVAR outcome

Based on the predicted postinterventional configuration of SG and vessel by the in-silico EVAR model, in this section some postprocessing steps are presented to assess the in-silico EVAR outcome and estimate the potential complication likelihood from an engineering perspective. First, some fundamental equations to evaluate the shape of the deployed SG configuration are derived in Section 3.6.1. Afterwards, in Section 3.6.2, mechanical and geometrical parameters are proposed to assess the in-silico EVAR outcome with respect to the quality of EVAR and the likelihood of potential EVAR related complications.

3.6.1. Shape of the deployed stent-graft configuration

According to the morphing algorithm based on control curves (cf. Section 3.2.2), which is used for in-silico SG placement and deployment, all nodes with the reference coordinates $\boldsymbol{X}_{\mathrm{I}}^{(\Theta),i} \in \Omega_{\mathrm{I},0}^{\{\mathrm{S,G}\},(\Theta)} = (\Omega_{\mathrm{I},0}^{\mathrm{S},(\Theta)} \cup \Omega_{\mathrm{I},0}^{\mathrm{G},(\Theta)})$ of the SG model in its undeformed configuration with $i = 1, 2, ..., n_{\mathrm{node}}^{\mathrm{SG},(\Theta)}$ are grouped into subsets $\mathsf{A}_{\mathrm{I}}^{(\Theta),j}$ according to Equations (3.21)-(3.22). $\Omega_{\mathrm{I},0}^{\mathrm{S},(\Theta)} \subset \Omega_{\mathrm{I},0}^{\mathrm{S}}$ and $\Omega_{0}^{\mathrm{G},(\Theta)} \subset \Omega_{\mathrm{I},0}^{\mathrm{G}}$ are the undeformed configurations of stent and graft of SG part $\Theta \in \{\mathrm{P,L,R}\}$. To ease the notation, in the following, the superscript $(\bullet)^{(\Theta)}$ is omitted. Unless specified differently, the variables are valid for any of the three tube-shaped parts of the SG $\Theta \in \{\mathrm{P,L,R}\}$. Obviously, the derived quantities are equally valid for non-bifurcated SGs.

Based on the valid assumption that the relative deformation of the SG tangentially to its centerline is small, the centerline $\mathcal{C}_{\mathrm{De}}$ of the deployed SG can be computed. The points of the centerline $\mathcal{C}_{\mathrm{De}}$ are the centers of gravity of the SG nodes i in the sets $\mathsf{A}_{\mathrm{I}}^{j}$ according to

$$\boldsymbol{x}_{\mathrm{C,De}}^{j} = \frac{1}{\sum\limits_{i \in \mathsf{A}_{\mathrm{I}}^{j}} \bar{\theta}^{i}} \sum_{i \in \mathsf{A}_{\mathrm{I}}^{j}} \bar{\theta}^{i} \boldsymbol{x}_{\mathrm{De}}^{i} = \frac{1}{2\pi} \sum_{i \in \mathsf{A}_{\mathrm{I}}^{j}} \bar{\theta}^{i} \boldsymbol{x}_{\mathrm{De}}^{i}, \quad \forall j = 1, 2, ..., n_{\mathrm{C}}, \tag{3.92}$$

where n_{C} is the number of points of the centerline $\mathcal{C}_{\mathrm{I}}$ of the SG in the undeformed configuration, $\boldsymbol{x}_{\mathrm{De}}^{i}$ are the current coordinates of all nodes i in the set $\mathsf{A}_{\mathrm{I}}^{j}$ in the deployed state and $\bar{\theta}^{i} = \frac{1}{2}(\theta^{i+1} - \theta^{i-1})$ is the mean angular distance between two adjacent nodes in set $\mathsf{A}_{\mathrm{I}}^{j}$. The nodes i in the sets $\mathsf{A}_{\mathrm{I}}^{j}$ are ordered counterclockwise according to the local angular coordinate θ^{i} of the local cylindrical coordinate systems tangentially aligned to the centerline $\mathcal{C}_{\mathrm{I}}$ (cf. Figure 3.4). Hence, the nodes i and $i+1$ are adjacent nodes. The mean angular distance $\bar{\theta}^{i}$ is used as weighting to account for irregularly distributed nodes in the set $\mathsf{A}_{\mathrm{I}}^{j}$. In case of a regular SG mesh, the mean angular distance $\bar{\theta}^{i}$ between two adjacent nodes in the set $\mathsf{A}_{\mathrm{I}}^{j}$ is $\bar{\theta}^{i} = \frac{2\pi}{n_{\mathrm{node}}^{j}}$ for each node i where n_{node}^{j} is the number of nodes in the set $\mathsf{A}_{\mathrm{I}}^{j}$. Therefore, the calculation of the center of gravity of all nodes i in the set $\mathsf{A}_{\mathrm{I}}^{j}$ according to Equation (3.92) reduces to the arithmetic mean

$$\boldsymbol{x}_{\mathrm{C,De}}^{j} = \frac{1}{2\pi} \sum_{i \in \mathsf{A}_{\mathrm{I}}^{j}} \bar{\theta}^{i} \boldsymbol{x}_{\mathrm{De}}^{i} = \frac{1}{n_{\mathrm{node}}^{j}} \sum_{i \in \mathsf{A}_{\mathrm{I}}^{j}} \boldsymbol{x}_{\mathrm{De}}^{i}, \quad \forall j = 1, 2, ..., n_{\mathrm{C}}. \tag{3.93}$$

Further, the arc length parameterization is introduced

$$s_{\mathrm{De}}^{j} = s_{\mathrm{De}}^{j-1} + ||\boldsymbol{x}_{\mathrm{C,De}}^{j} - \boldsymbol{x}_{\mathrm{C,De}}^{j-1}||, \quad \forall j = 2, 3, ..., n_{\mathrm{C}}, \quad s_{\mathrm{De}}^{1} = 0,$$

where $\boldsymbol{x}_{\mathrm{C,De}}^{j}$ is the position vector of point j of the centerline $\mathcal{C}_{\mathrm{De}}$ according to Equation (3.92) and n_{C} is the total number of points $j = 1, 2, ..., n_{\mathrm{C}}$ that describe the piecewise linear centerline $\mathcal{C}_{\mathrm{De}}$ of the SG in the deployed state. Consequently, s_{De}^{j} are discrete values of the arc length of the centerline $\mathcal{C}_{\mathrm{De}}$ with

$$\{s_{\mathrm{De}}^{j} | 0 \leq s_{\mathrm{De}}^{j} \leq L_{\mathrm{De}}^{\mathrm{SG}}, \forall j = 1, 2, ..., n_{\mathrm{C}}\}, \tag{3.94}$$

where $L_{\mathrm{De}}^{\mathrm{SG}}$ is the total arc length of the centerline $\mathcal{C}_{\mathrm{De}}$, which corresponds to the arc length of the SG in the deployed state. Using the local cylindrical coordinates θ_{De}^{i} and r_{De}^{i} (cf. Figure 3.4),

the average diameter of each set $\mathsf{A}_{\mathrm{I}}^{j}$ can be calculated. In contrast to Figure 3.4 where the local cylindrical coordinate systems are aligned to the centerline $\mathcal{C}_{\mathrm{I}}$ of the undeformed SG, the local coordinates θ_{De}^{i} and r_{De}^{i} correspond to the local coordinate systems that are tangentially aligned to the centerline $\mathcal{C}_{\mathrm{De}}$ of the deployed SG which is given by Equation (3.92).

The average SG diameter of all nodes in the set $\mathsf{A}_{\mathrm{I}}^{j}$, i.e., the average SG diameter in an orthogonal slice $\gamma_{\perp}^{\mathrm{SG}}(s_{\mathrm{De}})$ to the centerline $\mathcal{C}_{\mathrm{De}}$ at location s_{De}^{j}, is given by

$$\bar{d}^{j} = \bar{d}(s_{\mathrm{De}}^{j}) = \frac{1}{2\pi}\sum_{i\in\mathsf{A}_{\mathrm{I}}^{j}} 2\bar{\theta}_{\mathrm{De}}^{i} r_{\mathrm{De}}^{i} = \frac{1}{\pi}\sum_{i\in\mathsf{A}_{\mathrm{I}}^{j}} \bar{\theta}_{\mathrm{De}}^{i} r_{\mathrm{De}}^{i}, \quad \forall j = 1,2,...,n_{\mathrm{C}}, \tag{3.95}$$

where $\bar{\theta}_{\mathrm{De}}^{i} = \frac{1}{2}(\theta_{\mathrm{De}}^{i+1} - \theta_{\mathrm{De}}^{i-1})$ is the mean angular distance between two adjacent nodes in the set $\mathsf{A}_{\mathrm{I}}^{j}$ according to the local cylindrical coordinate systems tangentially aligned to the centerline $\mathcal{C}_{\mathrm{De}}$ of the deployed SG (cf. Figure 3.4).

At this point, it is important to clearly distinguish between r_{De}^{i} and $\bar{d}^{j}$.The radius r_{De}^{i} is the local radius of node i in set $\mathsf{A}_{\mathrm{I}}^{j}$ according to the local cylindrical coordinate system that is tangentially aligned to the centerline $\mathcal{C}_{\mathrm{De}}$. In contrast, $\bar{d}^{j}$ is the average diameter of all nodes belonging to one common set $\mathsf{A}_{\mathrm{I}}^{j}$. The term *average* refers to the average of the diameters $2r_{\mathrm{De}}^{i}$ of a all nodes i in the set $\mathsf{A}_{\mathrm{I}}^{j}$.

Further, the average diameters of the pure stent $\bar{d}^{\mathrm{S},j}$ and the pure graft $\bar{d}^{\mathrm{G},j}$ can be calculated by

$$\bar{d}^{\mathrm{S},j} = \frac{1}{\pi}\sum_{i\in\mathsf{A}_{\mathrm{I}}^{\mathrm{S},j}} \bar{\theta}_{\mathrm{De}}^{\mathrm{S},i} r_{\mathrm{De}}^{\mathrm{S},i}, \quad \forall j = 1,2,...,n_{\mathrm{C}} \tag{3.96}$$

and

$$\bar{d}^{\mathrm{G},j} = \frac{1}{\pi}\sum_{i\in\mathsf{A}_{\mathrm{I}}^{\mathrm{G},j}} \bar{\theta}_{\mathrm{De}}^{\mathrm{G},i} r_{\mathrm{De}}^{\mathrm{G},i}, \quad \forall j = 1,2,...,n_{\mathrm{C}}, \tag{3.97}$$

respectively. In Equation (3.96) and (3.97), the superscripts $(\bullet)^{\mathrm{S}}$ and $(\bullet)^{\mathrm{G}}$ indicate variables of the stent and the graft, respectively. In contrast to $\mathsf{A}_{\mathrm{I}}^{j}$, $\mathsf{A}_{\mathrm{I}}^{\mathrm{S},j}$ and $\mathsf{A}^{\mathrm{G},j}$ only hold nodes of the stent and the graft, respectively. Since the number of discrete locations s_{De}^{j} at which the average diameters $\bar{d}(s_{\mathrm{De}}^{j})$ are measured is very high, the diameter measure is called *pseudo-continuous* diameter measure. Hence, the average diameters $\bar{d}(s_{\mathrm{De}}^{j})$ are given almost continuously along the total length $L_{\mathrm{De}}^{\mathrm{SG}}$ of the deployed SG. Therefore, in the following, $s_{\mathrm{De}} \in [0, L_{\mathrm{De}}^{\mathrm{SG}}]$ is used as the abbreviated continuous representation of (3.94). Variables with superscript $(\bullet)^{j}$ denote discrete variables and variables without superscript $(\bullet)^{j}$ denote variables that are given pseudo-continuously along $s_{\mathrm{De}} \in [0, L_{\mathrm{De}}^{\mathrm{SG}}]$.

Similarly to Equation (3.95), the minimum and maximum radius within the set $\mathsf{A}^{(\bullet),j}$, i.e., within the orthogonal slice $\gamma_{\perp}^{\mathrm{SG}}(s_{\mathrm{De}})$, can be determined by

$$r_{\min}^{(\bullet),j} = \min_{i\in\mathsf{A}^{(\bullet),j}} r_{\mathrm{De}}^{(\bullet),i}, \quad \forall j = 1,2,...,n_{\mathrm{C}} \tag{3.98}$$

and

$$r_{\max}^{(\bullet),j} = \max_{i \in \mathsf{A}^{(\bullet),j}} r_{\mathrm{De}}^{(\bullet),i}, \quad \forall j = 1, 2, ..., n_{\mathrm{C}}, \tag{3.99}$$

where $(\bullet)$ denotes either the stent "S" or the graft "G".

3.6.2. EVAR quality parameters

Currently, in clinical practice, preinterventional EVAR planning tools are limited to 3D visualizations and measurement functions, but mechanical and geometrical assessment of the predicted postinterventional state is not used. In-silico EVAR, as presented in Section 3.5, is able to make predictions of the deployed state under realistic conditions. However, the major question of how to evaluate the in-silico EVAR results with respect to the quality of the EVAR outcome still is largely unsolved. This aspect raises the need for the definition of a set of mechanical and geometrical parameters (e.g., SG drag force [75, 157, 186], SG fixation force [177], tissue stresses [6, 139] and the quality of seal [7, 224]) to assess the quality of the in-silico EVAR outcome and their validation of being able to indicate EVAR related complications (cf. Section 1.1.2.4), such as endoleaks, stress induced aortic neck dilatation and SG fracture. This bridging of the gap between predictive in-silico EVAR outcome and interpretation of the potential success of EVAR is an important step toward the usage of in-silico EVAR in clinical practice.

In this section, mechanical and geometrical parameters are defined to estimate the quality of the EVAR outcome. Medical, biological or other parameters that also may have an influence on the quality of the EVAR outcome are not considered. The proposed parameters will be denoted as *EVAR quality parameters*. The selection and definition of these EVAR quality parameters is based on a detailed literature study. The EVAR quality parameters have to satisfy the following basic demands:

- Ability to provide indications of potential EVAR related complications
- Quantifiability from in-silico EVAR outcomes
- Applicability to patient-specific cases

The EVAR quality parameters must be able to provide indications of the following major EVAR related complications which were discussed in detail in Section 1.1.2.4:

- Type I endoleak
- SG migration
- Aortic neck dilatation
- SG fatigue
- SG kinking
- Aortic compliance mismatch

The in-silico EVAR outcome, i.e., the deployed state of SG and vessel, is postprocessed according to the EVAR quality parameters. The focus is on quantifiable parameters to enable quantitative and statistical investigations. The EVAR quality parameters assess the complication likelihood and thus estimate the potential success of the EVAR outcome. EVAR is considered to be successful if the patient is free of EVAR related complications for several years after the intervention. Nevertheless, all EVAR quality parameters are quantities measured directly after the

in-silico SG deployment, i.e., they are postinterventional quantities. No growth and remodeling of the aortic tissue is considered which could be used to trace the change of the EVAR quality parameters over time. It is assumed that the EVAR quality parameters as postinterventional quantities already can give hints on potential complications that will occur after several years.

For the sake of clarity, in the following the subscripts $(\bullet)_{\mathrm{Pre}}$ and $(\bullet)_{\mathrm{De}}$ are not explicitly stated for the configurations and boundaries of SG and vessel. Any reference configuration $\boldsymbol{X}^{(II)} \in \Omega_0^{(II)}$ and its boundaries $\Gamma^{(II)}$ denotes the stress-free reference configuration at time of the deployed SG, which is $\Omega_{0,\mathrm{Pre}}^{(II)}$. Similarly, any current configuration $\boldsymbol{x}^{(II)} \in \Omega^{(II)}$ and its boundaries $\gamma^{(II)}$ denotes the current configuration at time of the deployed SG, which is $\Omega_{\mathrm{De}}^{(II)}$ as described in Section 3.5.

Many EVAR quality parameters are related to the landing zones, where in this section it is not distinguished between the proximal or the distal landing zone. Accordingly, L_{lz} is denoted as the length of the landing zone (proximal or distal) in the following. Further, the area of the landing zone of the cylindrical SG in the preinterventional configuration is given by

$$A_{\mathrm{lz}} = \pi D^{\mathrm{SG}} L_{\mathrm{lz}}. \tag{3.100}$$

The area of the landing zone of the SG in the current configuration Ω^{SG} (i.e., in the deployed state) can be calculated using Nanson's formula according to

$$a_{\mathrm{lz}} = \int_{\gamma_{\mathrm{ex,lz}}^{\mathrm{G}}} \mathrm{d}a_{\mathrm{lz}} = \int_{\Gamma_{\mathrm{ex,lz}}^{\mathrm{G}}} ||J^{\mathrm{G}}(\boldsymbol{F}^{\mathrm{G}})^{-\mathrm{T}}\boldsymbol{N}^{\mathrm{G}}||\mathrm{d}A_{\mathrm{lz}}, \tag{3.101}$$

where $\mathrm{d}a_{\mathrm{lz}}$ is the differential area element of the outer graft surface in the current configuration, $\boldsymbol{N}^{\mathrm{G}}$ is the unit outward surface normal on the differential area element $\mathrm{d}A_{\mathrm{lz}}$ of the outer graft surface in the reference configuration, $\boldsymbol{F}^{\mathrm{G}}$ is the deformation gradient and $J^{\mathrm{G}} = \det(\boldsymbol{F}^{\mathrm{G}})$ is the determinant of the deformation gradient. The boundaries $\gamma_{\mathrm{ex,lz}}^{\mathrm{G}}$ and $\Gamma_{\mathrm{ex,lz}}^{\mathrm{G}}$ are the outer graft surfaces of the landing zone in the current and in the reference configuration, respectively.

In the following, it is distinguished between *vessel and stent-graft stresses and tractions* (Section 3.6.2.1), *fixation and drag forces* (Section 3.6.2.2), parameters to evaluate the *quality of seal* (Section 3.6.2.3), *geometrical parameters of the deployed SG* (Section 3.6.2.4) and *parameters depending on the pulsatile blood pressure* (Section 3.6.2.5). In Section 3.6.2.6, a summary of all proposed EVAR quality parameters with references to available studies in literature as well as indications of their potential impact on EVAR related complications is given.

3.6.2.1. Vessel and stent-graft stresses and tractions

In this thesis, the Cauchy von Mises equivalent stress measure, denoted by σ, is applied which describes the stress state after the SG deployment. The Cauchy von Mises equivalent stress measure is frequently used to asses the stress state in vessels [139, 163, 212] and SGs [139, 175]. Instead of considering maximum values of stresses, stress percentiles are used which had been proven to be more suitable in the evaluation of vessel stresses [163, 165, 244]. Accordingly, $\sigma_{99}^{\mathrm{wall}}$ denotes the 99-percentile Cauchy von Mises vessel wall stress which is the stress such that in 99% of the domain Ω_0^{wall} the Cauchy von Mises stress is smaller than $\sigma_{99}^{\mathrm{wall}}$. A precise mathematical definition of the proposed quantiles is given in Appendix A.5. Although the 99-percentile

and 1-percentile are used for stresses and tractions in this thesis, these quantities are denoted as "maximum" and "minimum" stresses and tractions in the following for simplicity.

Aortic neck dilatation (cf. Section 1.1.2.4) is a frequently stated complication after EVAR which is associated with an enlargement of the vessel in the proximal landing zone and subsequent SG migration or endoleak type Ia. Among other reasons, the additional vessel stress induced by the oversized SG is often named as source of aortic neck dilatation [47, 197]. Hence, the vessel wall overstress

$$\bar{\sigma}^{\mathrm{wall}}(\boldsymbol{X}) = \sigma(\boldsymbol{X}) - \sigma_{\mathrm{pre}}(\boldsymbol{X}), \quad \forall \boldsymbol{X} \in \Omega_0^{\mathrm{wall}} \tag{3.102}$$

is defined to measure the additional vessel stress induced by the oversized SG, where $\sigma_{\mathrm{pre}}(\boldsymbol{X})$ are the von Mises Cauchy stresses before EVAR and $\sigma(\boldsymbol{X})$ are the von Mises Cauchy stresses after EVAR (cf. Figure 3.20I). Here, $\sigma_{\mathrm{pre}}(\boldsymbol{X})$ and $\sigma(\boldsymbol{X})$ both are Cauchy stress measures of the current configuration evaluated at the same material point $\boldsymbol{X} \in \Omega_0^{\mathrm{wall}}$. Accordingly, $\bar{\sigma}_{99}^{\mathrm{wall}}$ is the 99-percentile vessel wall overstress of all material points of the vessel wall $\boldsymbol{X} \in \Omega_0^{\mathrm{wall}}$, where $\Omega_0^{\mathrm{wall}} \subset \Omega_0^{\mathrm{Ao}}$ defines the vessel wall. A second possible explanation of aortic neck dilatation is the continuation of the aneurysm disease process [62, 234]. Actually the SG should protect the diseased vessel by removing the pulsatile blood pressure from the vessel and stopping the disease process. However, if the SG fixation zone is in a region with partly "aneurysmatic" vessel material, the diseased vessel may not be properly protected. On the contrary, the additional vessel stress induced by the oversized SG may even increase the progression of the disease process in this region since besides biochemical processes vessel stress is considered as one of the triggers of aneurysm growth [27, 279]. Hence, the aneurysmatic vessel wall overstress

$$\bar{\sigma}^{\lambda,\mathrm{wall}}(\boldsymbol{X}) = \lambda(r(\boldsymbol{X}))\,(\sigma(\boldsymbol{X}) - \sigma_{\mathrm{pre}}(\boldsymbol{X})) = \lambda(r(\boldsymbol{X}))\,\bar{\sigma}^{\mathrm{wall}}(\boldsymbol{X}), \quad \forall \boldsymbol{X} \in \Omega_0^{\mathrm{wall}} \tag{3.103}$$

is explicitly defined, where $\lambda(r(\boldsymbol{X})) \in [0,1]$ is the blend parameter to distinguish between "healthy" ($\lambda = 0$) and "aneurysmatic" ($\lambda = 1$) vessel wall material as defined in Equation (3.47). Accordingly, $\bar{\sigma}_{99}^{\lambda,\mathrm{wall}}$ denotes the 99-percentile aneurysmatic vessel wall overstress, which describes the "maximum" additional stress in the "aneurysmatic" vessel wall material compared to the preinterventional vessel wall stresses.

Major goal of EVAR is the reduction of the blood pressure and the reduction of vessel wall stresses in the aneurysm sac. Thus, also the maximum relief $|\bar{\sigma}_1^{\lambda,\mathrm{wall}}|$ of the stresses in the "aneurysmatic" vessel wall material is quantified, where $\bar{\sigma}_1^{\lambda,\mathrm{wall}}$ denotes the 1-percentile aneurysmatic vessel wall overstress.

It clearly has to be pointed out that the definition of the "aneurysmatic" region by $\lambda(r(\boldsymbol{X}))$ is purely heuristic according to the preinterventional local vessel radius $r(\boldsymbol{X})$. Hence, the stress measure $\bar{\sigma}^{\lambda,\mathrm{wall}}(\boldsymbol{X})$ is affected by this heuristic decision that vessel wall material with an abnormally large local vessel radius is considered to be in an "aneurysmatic" state.

The 99-percentile stent stresses σ_{99}^{S} of the stent in the deployed state are considered to estimate the tendency of SG fatigue. The permanent interaction of vessel and SG with high contact pressures may induce local remodeling of the surrounding tissue or even may lead to erosion of the vessel wall often associated with the emergence of aortoenteric fistula [101, 166]. Thus, the 99-percentile value $p_{\mathrm{n},99}$ of the normal contact pressure between SG and vessel is considered.

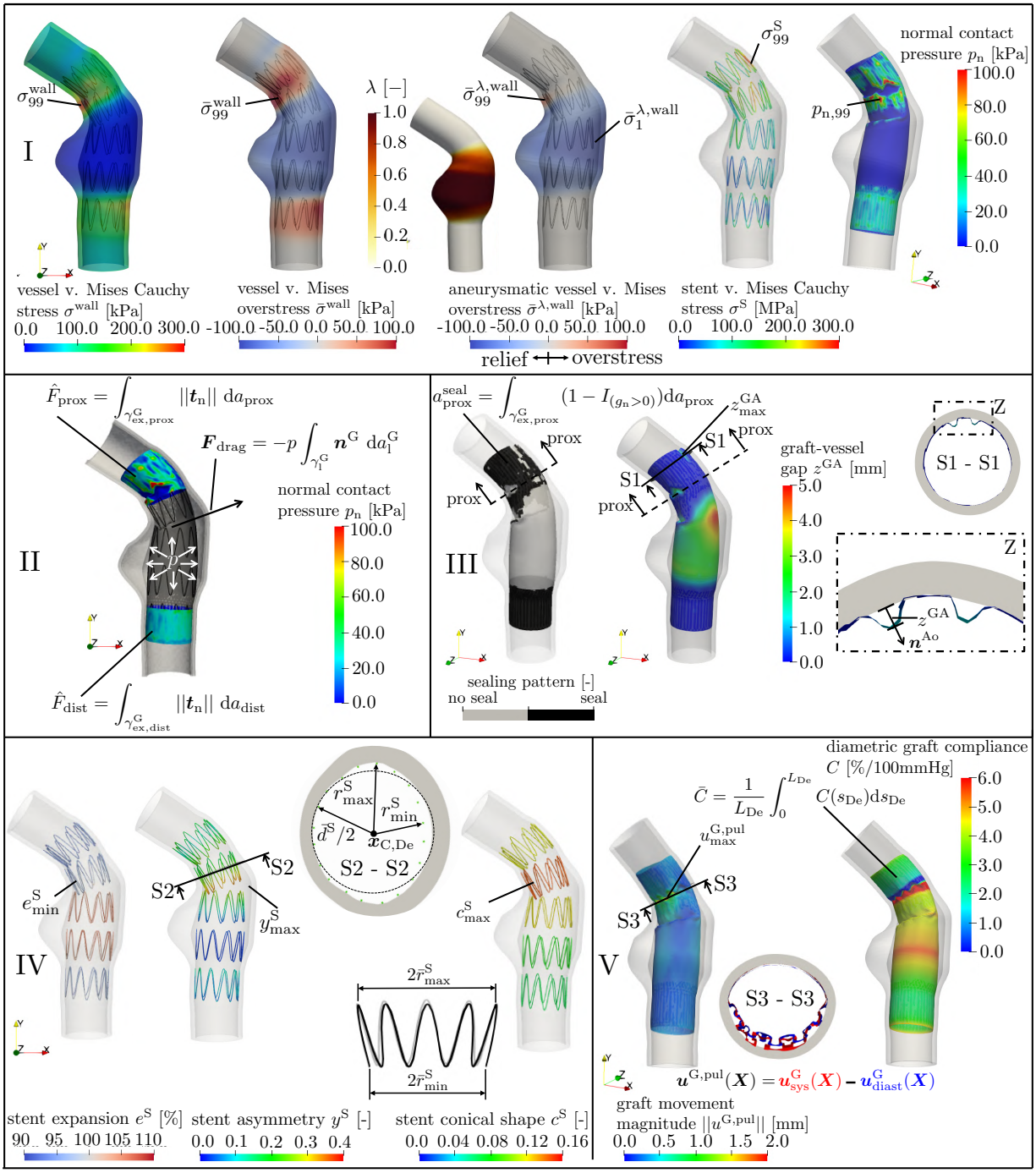

Figure 3.20 Qualitative visualization of the EVAR quality parameters: vessel and stent-graft stresses and tractions (I), drag and fixation forces (II), quality of seal (III), geometrical parameters of the deployed SG (IV) and parameters depending on the pulsatile blood pressure (V). Modified figure reproduced with permission from [109].

3.6.2.2. Drag and fixation forces

In the deployed state of the SG, the SG has to sustain the permanent and pulsatile load of the blood flow and pressure. This force resulting from the load by the blood is denoted as SG drag force. In this thesis, inertial effects and shear tractions acting on the luminal graft surface are neglected since their contribution to the SG drag force is assumed to be negligibly small compared to the hydrostatic blood pressure [120, 128, 154, 157, 158]. Hence, the SG drag force is approximated by

$$\boldsymbol{F}_{\mathrm{drag}} = \int_{\gamma_{\mathrm{l}}^{\mathrm{G}}} \hat{\boldsymbol{t}}^{\mathrm{G}} \, \mathrm{d}a_{\mathrm{l}}^{\mathrm{G}} = -p \int_{\gamma_{\mathrm{l}}^{\mathrm{G}}} \boldsymbol{n}^{\mathrm{G}} \, \mathrm{d}a_{\mathrm{l}}^{\mathrm{G}}, \tag{3.104}$$

where $\hat{\boldsymbol{t}}^{\mathrm{G}}$ is the nonlinear hydrostatic traction load of the blood on the luminal graft surface $\gamma_{\mathrm{l}}^{\mathrm{G}}$, $\boldsymbol{n}^{\mathrm{G}}$ is the unit outward surface normal on the differential area element $\mathrm{d}a_{\mathrm{l}}^{\mathrm{G}}$ of the luminal graft surface in the current configuration and p is the hydrostatic blood pressure.

In order to resist the SG drag force $\boldsymbol{F}_{\mathrm{drag}}$ and prevent the SG from migrating, SGs generally are designed with an oversize with respect to the vessel diameter as defined in Equation (1.1). The SG oversizing results in a passive fixation force

$$\hat{F}_{\mathrm{lz}} = \int_{\gamma_{\mathrm{ex,lz}}^{\mathrm{G}}} ||\boldsymbol{t}_{\mathrm{n}}|| \, \mathrm{d}a_{\mathrm{lz}}, \tag{3.105}$$

where $(\bullet)_{\mathrm{lz}}$ denotes either the proximal landing zone $(\bullet)_{\mathrm{prox}}$ or the distal landing zone $(\bullet)_{\mathrm{dist}}$ (cf. Figure 3.20II). In (3.105), $\mathrm{d}a_{\mathrm{lz}}$ is the differential area element of the luminal graft surface $\gamma_{\mathrm{ex,lz}}^{\mathrm{G}}$ and $\boldsymbol{t}_{\mathrm{n}}$ is the normal contact traction at the contact interface between SG and luminal surface of the vessel.

3.6.2.3. Quality of seal

To obtain an optimal seal between SG and vessel in the landing zones, the fixation areas in the landing zones of the SG should be as large as possible. The fixation area is defined by

$$a_{\mathrm{lz}}^{\mathrm{seal}} = \int_{\gamma_{\mathrm{ex,lz}}^{\mathrm{G}}} (1 - I_{(g_{\mathrm{n}}>0)}) \mathrm{d}a_{\mathrm{lz}}, \tag{3.106}$$

where g_{n} is the normal projection of the gap function between the potential contact surfaces in the current configuration as defined in Equation (2.31) and $I_{(g_{\mathrm{n}}>0)}$ is the indicator function as defined in Appendix A.5. According to the Karush-Kuhn-Tucker conditions of unilateral contact (cf. Section 2.1.5), the normal projection of the gap function is $g_{\mathrm{n}} \geq 0$ and consequently for points being in contact, $I_{(g_{\mathrm{n}}>0)}$ is zero and for points not being in contact $I_{(g_{\mathrm{n}}>0)}$ is one. In contrast to the area a_{lz} of the landing zone, the fixation area $a_{\mathrm{lz}}^{\mathrm{seal}}$ is only the portion of a_{lz} that is in contact with the vessel (cf. Figure 3.20III). From a mechanical perspective, $a_{\mathrm{lz}}^{\mathrm{seal}}$ should be as large as possible, such that SG fixation forces are distributed over a larger area and therefore the fixation is more uniform and stable against SG migration.

Type I endoleaks occur when a gap between SG and vessel in the landing zones allows blood to flow into the aneurysm sac. Thus, to further assess the quality of seal, the closest point dis-

tance z^{GA} of each point $\boldsymbol{x}^{\mathrm{G}} \in \gamma^{\mathrm{G}}_{\mathrm{lz,ex}}$ of the outer graft surface in the landing zone on the luminal vessel surface with $\boldsymbol{x}^{\mathrm{Ao}} \in \gamma^{\mathrm{Ao}}_{\mathrm{l}}$ as well as the closest point distance z^{SA} of each point $\boldsymbol{x}^{\mathrm{S}} \in \gamma^{\mathrm{S}}_{\mathrm{lz,ex}}$ of the outer stent surface in the landing zone are determined and their maximum values are evaluated by

$$z^{\mathrm{GA}}_{\mathrm{max}} = \max_{\boldsymbol{x}^{\mathrm{G}} \in \gamma^{\mathrm{G}}_{\mathrm{lz,ex}}} z^{\mathrm{GA}}(\boldsymbol{x}^{\mathrm{G}}) = \max_{\boldsymbol{x}^{\mathrm{G}} \in \gamma^{\mathrm{G}}_{\mathrm{lz,ex}}} \left(\boldsymbol{n}^{\mathrm{Ao}}(\check{\boldsymbol{x}}^{\mathrm{Ao,G}}) \cdot (\boldsymbol{x}^{\mathrm{G}} - \check{\boldsymbol{x}}^{\mathrm{Ao,G}}) \right) \tag{3.107}$$

and

$$z^{\mathrm{SA}}_{\mathrm{max}} = \max_{\boldsymbol{x}^{\mathrm{S}} \in \gamma^{\mathrm{S}}_{\mathrm{lz,ex}}} z^{\mathrm{SA}}(\boldsymbol{x}^{\mathrm{S}}) = \max_{\boldsymbol{x}^{\mathrm{S}} \in \gamma^{\mathrm{S}}_{\mathrm{lz,ex}}} \left(\boldsymbol{n}^{\mathrm{Ao}}(\check{\boldsymbol{x}}^{\mathrm{Ao,S}}) \cdot (\boldsymbol{x}^{\mathrm{S}} - \check{\boldsymbol{x}}^{\mathrm{Ao,S}}) \right), \tag{3.108}$$

respectively. The definition of the outward surface normal $\boldsymbol{n}^{\mathrm{Ao}}$ on $\gamma^{\mathrm{Ao}}_{\mathrm{l}}$ in the current configuration is visualized in Figure 3.20III, detail Z. In (3.107), $\check{\boldsymbol{x}}^{\mathrm{Ao,G}}(\boldsymbol{x}^{\mathrm{G}})$ is the point on the luminal vessel surface $\gamma^{\mathrm{Ao}}_{\mathrm{l}}$ that is closest to the point $\boldsymbol{x}^{\mathrm{G}} \in \gamma^{\mathrm{G}}_{\mathrm{lz,ex}}$, i.e.,

$$\check{\boldsymbol{x}}^{\mathrm{Ao,G}}(\boldsymbol{x}^{\mathrm{G}}) = \underset{\boldsymbol{x}^{\mathrm{Ao}} \in \gamma^{\mathrm{Ao}}_{\mathrm{l}}}{\mathrm{argmin}} ||\boldsymbol{x}^{\mathrm{G}} - \boldsymbol{x}^{\mathrm{Ao}}||. \tag{3.109}$$

Analogously, $\check{\boldsymbol{x}}^{\mathrm{Ao,S}}(\boldsymbol{x}^{\mathrm{S}})$ in (3.108) is determined by

$$\check{\boldsymbol{x}}^{\mathrm{Ao,S}}(\boldsymbol{x}^{\mathrm{S}}) = \underset{\boldsymbol{x}^{\mathrm{Ao}} \in \gamma^{\mathrm{Ao}}_{\mathrm{l}}}{\mathrm{argmin}} ||\boldsymbol{x}^{\mathrm{S}} - \boldsymbol{x}^{\mathrm{Ao}}||. \tag{3.110}$$

In the following, $z^{\mathrm{SA}}_{\mathrm{max}}$ and $z^{\mathrm{GA}}_{\mathrm{max}}$ are denoted as the maximum stent-vessel gap and the maximum graft-vessel gap, respectively. It is important to note, that the occurrence of type I endoleaks strongly depends on the sealing pattern of the deployed SG. As long as a complete circumferential seal of sufficient length exists in the landing of the SG, large graft-vessel gaps do not necessarily lead to a type I endoleak.

3.6.2.4. Geometrical parameters of the deployed stent-graft

In this section, only the geometrical shape of the stent is evaluated since the geometrical shape of the graft is dominated by its buckling pattern and does not represent the effects that shall be investigated in this section.

Accordingly, the degree of stent expansion (cf. Figure 3.20IV) is defined by

$$e^{\mathrm{S}}(s_{\mathrm{De}}) = \frac{\bar{d}^{\mathrm{S}}(s_{\mathrm{De}})}{D^{\mathrm{SG}}}, \quad \forall s_{\mathrm{De}} \in [0, L^{\mathrm{SG}}_{\mathrm{De}}], \tag{3.111}$$

where D^{SG} is the nominal diameter of the SG and $\bar{d}^{\mathrm{S}}(s_{\mathrm{De}})$ is the average diameter of the stent in the plane $\gamma^{\mathrm{SG}}_{\perp}(s_{\mathrm{De}})$ as defined in Equation (3.96). The stent expansion expresses the degree of expansion of the stent rings and hence may have an influence on the fatigue behavior of the SG. The minimum stent expansion

$$e^{\mathrm{S}}_{\mathrm{min}} = \min_{s_{\mathrm{De}} \in [0, L^{\mathrm{SG}}_{\mathrm{De}}]} e^{\mathrm{S}}(s_{\mathrm{De}}) \tag{3.112}$$

is primarily found in the landing zones where the full expansion of the stent is restricted by the surrounding vessel. Furthermore, the effective degree of SG oversizing at a specific location s_{De} can be calculated by

$$o^{\mathrm{eff}}(s_{\mathrm{De}}) = \frac{D^{\mathrm{SG}}}{\bar{d}^{\mathrm{S}}(s_{\mathrm{De}})} - 1 = \frac{1}{e^{\mathrm{S}}(s_{\mathrm{De}})} - 1, \quad \forall s_{\mathrm{De}} \in [0, L_{\mathrm{De}}^{\mathrm{SG}}]. \tag{3.113}$$

In contrast to the nominal degree of SG oversizing o as defined in Equation (1.1), the effective degree of SG oversizing o_{eff} expresses the degree of SG oversizing in the deployed state of the SG. Since the vessel is elastically deformable, the insertion of a SG generally induces an enlargement of the vessel diameter in the landing zones. Hence, if the SG is perfectly aligned to the luminal vessel surface, the effective degree of SG oversizing o^{eff} generally is smaller than the nominal value of SG oversizing o in an elastically deformable vessel. For a rigid vessel, nominal and effective degree of SG oversizing would be identical in this case. The mean value of the effective degree of SG oversizing in the landing zone is denoted by

$$\bar{o}_{\mathrm{lz}}^{\mathrm{eff}} = \frac{1}{L_{\mathrm{lz}}} \int_0^{L_{\mathrm{lz}}} o^{\mathrm{eff}}(s_{\mathrm{De}}) \mathrm{d}s_{\mathrm{De}}, \tag{3.114}$$

where L_{lz} is the length of the landing zone.

The best seal and the most uniform fixation of the SG between a cylindrical SG and a cylindrical vessel can be assumed for a perfectly cylindrical shape of the SG in the deployed state. Any asymmetric shape of the SG in the deployed state may have negative effects on the seal and the fixation of the SG [32, 273]. Moreover, the fatigue behavior of the SG may be affected since asymmetric stent shapes go hand in hand with nonuniform loading of the SG with local stress hot spots. The in-plane stent asymmetry y^{S} and its maximum value are defined by

$$y_{\mathrm{max}}^{\mathrm{S}} = \max_{s_{\mathrm{De}} \in [0, L_{\mathrm{De}}^{\mathrm{SG}}]} y^{\mathrm{S}}(s_{\mathrm{De}}) = \max_{s_{\mathrm{De}} \in [0, L_{\mathrm{De}}^{\mathrm{SG}}]} \left(\frac{r_{\mathrm{max}}^{\mathrm{S}}(s_{\mathrm{De}})}{r_{\mathrm{min}}^{\mathrm{S}}(s_{\mathrm{De}})} - 1 \right). \tag{3.115}$$

This means that $y^{\mathrm{S}}(s_{\mathrm{De}})$ is a measure of the ovalization of the stent which is zero in the case of a perfectly circular shape and $y^{\mathrm{S}}(s_{\mathrm{De}}) > 0$ for any elliptic shape of the stent (cf. Figure 3.20IV). If the SG is forced in a conical shape, this can also lead to negative effects on the fixation and the fatigue behavior of the SG [174, 273]. The conical shape of a stent limb $i \in [1, n^{\mathrm{S}}]$ is defined as

$$c_i^{\mathrm{S}} = \frac{\max\limits_{s_{\mathrm{De}} \in \mathsf{S}_i} \bar{d}^{\mathrm{S}}(s_{\mathrm{De}})}{\min\limits_{s_{\mathrm{De}} \in \mathsf{S}_i} \bar{d}^{\mathrm{S}}(s_{\mathrm{De}})} - 1, \tag{3.116}$$

where n^{S} is the number of stent limbs of the SG and S_i is the interval of the arc length s_{De} of the centerline $\mathcal{C}_{\mathrm{De}}$ that corresponds to the position of stent limb i. For a perfectly cylindrical stent limb c_i^{S} is zero and $c_i^{\mathrm{S}} > 0$ for any stent limb of conical shape (cf. Figure 3.20IV). The stent limb with the maximum conical shape is denoted as

$$c_{\mathrm{max}}^{\mathrm{S}} = \max_{i \in [1, n^{\mathrm{S}}]} c_i^{\mathrm{S}}. \tag{3.117}$$

Besides negative effects on the nonuniform loading of the SG, strongly asymmetric and conical stent shapes may also be an indicator of local SG kinking.

3.6.2.5. Parameters depending on the pulsatile blood pressure

The SG is subjected to the permanent pulsatile nature of blood flow with the relative displacement

$$\boldsymbol{u}^{\mathrm{pul}}(\boldsymbol{X}) = \boldsymbol{u}^{\mathrm{sys}}(\boldsymbol{X}) - \boldsymbol{u}^{\mathrm{diast}}(\boldsymbol{X}), \quad \forall \boldsymbol{X} \in \Omega_0^{\mathrm{SG}}, \tag{3.118}$$

where $\boldsymbol{u}^{\mathrm{sys}}(\boldsymbol{X})$ is the displacement of material point $\boldsymbol{X}$ at the systolic pressure state and $\boldsymbol{u}^{\mathrm{diast}}(\boldsymbol{X})$ is the displacement of the same material point $\boldsymbol{X}$ at the diastolic pressure state according to the solution of the elastostatic BVP of Section 3.1.

Quantitatively, the maximum movement of the stent $u_{\max}^{\mathrm{S,pul}}$ and the graft $u_{\max}^{\mathrm{G,pul}}$ during one heart beat are determined by

$$u_{\max}^{\mathrm{G,pul}} = \max_{\boldsymbol{X} \in \Omega_0^{\mathrm{G}}} ||\boldsymbol{u}^{\mathrm{pul}}(\boldsymbol{X})|| \tag{3.119}$$

and

$$u_{\max}^{\mathrm{S,pul}} = \max_{\boldsymbol{X} \in \Omega_0^{\mathrm{S}}} ||\boldsymbol{u}^{\mathrm{pul}}(\boldsymbol{X})||, \tag{3.120}$$

respectively (cf. Figure 3.20V). Obviously, large permanent movements of a material point $\boldsymbol{X}$ together with high strains and stresses at this point may increase the risk of SG fatigue dramatically.

As stated in the introduction of this thesis in Section 1.1.2.4, the reduced compliance of the SG compared to the native aorta may affect the sensitive cardiovascular system. Instead of measuring the volume change mostly the change in diameter or the change in cross section is used to determine arterial compliance [156, 190, 265, 276]. Analogously, the compliance of the graft in the deployed state is calculated by

$$C(s_{\mathrm{De}}) = \frac{\left(\frac{\bar{d}^{\mathrm{sys,G}}(s_{\mathrm{De}}) - \bar{d}^{\mathrm{diast,G}}(s_{\mathrm{De}})}{\bar{d}^{\mathrm{diast,G}}(s_{\mathrm{De}})} \right)}{p^{\mathrm{sys}} - p^{\mathrm{diast}}}, \quad \forall s_{\mathrm{De}} \in [0, L_{\mathrm{De}}^{\mathrm{SG}}], \tag{3.121}$$

where p^{diast} is the diastolic blood pressure, p^{sys} is the systolic blood pressure and $s_{\mathrm{De}} \in [0, L_{\mathrm{De}}^{\mathrm{SG}}]$ is the arc length of the SG centerline in the deployed state. Further, $\bar{d}^{\mathrm{diast,G}}(s_{\mathrm{De}})$ and $\bar{d}^{\mathrm{sys,G}}(s_{\mathrm{De}})$ are the average graft diameters in orthogonal slices $\gamma_{\perp}^{\mathrm{SG}}(s_{\mathrm{De}})$ at the diastolic and the systolic blood pressure state according to Equation (3.97). Only the average diameters of the graft $\bar{d}^{\mathrm{diast,G}}(s_{\mathrm{De}})$ and $\bar{d}^{\mathrm{sys,G}}(s_{\mathrm{De}})$, but not the average diameters of the stent, are considered since the domain of the lumen is fully described by the graft. Obviously, in the landing zones the compliance $C(s_{\mathrm{De}})$ is smaller than in the aneurysm sac, since in the landing zones the compliance is a combination of the compliance of the SG and the surrounding vessel. In the aneurysm sac, where generally there is only partial contact between SG and vessel, the compliance $C(s_{\mathrm{De}})$ is dominated solely by the compliance of the SG. Hence, depending on the position $s_{\mathrm{De}} \in [0, L_{\mathrm{De}}^{\mathrm{SG}}]$, the compliance $C(s_{\mathrm{De}})$ is either a combination of the compliance of SG and vessel or the com-

pliance of the SG only (cf. Figure 3.20V). Quantitatively, only the mean diametric compliance $\bar{C}$ is considered which is given by

$$\bar{C} = \frac{1}{L_{\mathrm{De}}^{\mathrm{SG}}} \int_0^{L_{\mathrm{De}}^{\mathrm{SG}}} C(s_{\mathrm{De}}) \mathrm{d}s. \tag{3.122}$$

3.6.2.6. Summary of the EVAR quality parameters

In Figure 3.20, a visualization of the EVAR quality parameters for a synthetic SG and vessel is provided. To indicate quantities of the proximal and quantities of the distal landing zone, the subscripts $(\bullet)_{\mathrm{prox}}$ and $(\bullet)_{\mathrm{dist}}$ are used instead of $(\bullet)_{\mathrm{lz}}$. The EVAR quality parameters can similarly be used for assessment of the in-silico EVAR outcome of patient-specific cases as will be shown in Chapter 5.

In Table 3.4, all EVAR quality parameters are summarized, their potential impact on the quality of the EVAR outcome is indicated and their related complications are named. In practice, single EVAR complications cannot clearly be separated. For instance, SG migration mostly goes hand in hand with a type I endoleak. However, in Table 3.4 the intention is to state the relation of the EVAR quality parameter to the EVAR complication it has initiated. It is important to note, that this is only a proposal of parameters that may be able to estimate the likelihood of certain EVAR related complications from an engineering perspective. However, the clear correlation between the proposed EVAR quality parameters and EVAR related complications still needs to be proven in a future study of patient-specific cases of appropriate cohort size. Many different namings of the single EVAR quality parameters are available in literature and often slightly different definitions are used. In Table 3.4, available studies related to the single EVAR quality parameters are stated.

3.7. Summary of assumptions

In this section, the major assumption that are incorporated in the proposed approach of in-silico EVAR are summarized. The assumptions are separated into assumptions of the vessel model, the SG model, the in-silico SG P&D methodology and assumptions of the EVAR quality parameters.

Assumptions of the vessel model

- Inter- and intrapatient variability of vessel wall material parameters and vessel wall thickness are neglected. Instead, population-averaged mean values are used. A constant vessel wall thickness of $1.5\ \mathrm{mm}$ [219] is assumed.
- Same material models and model parameters are used for iliac arteries and the abdominal aorta.
- Residual sac pressure after EVAR [41, 145] is not considered. Instead, zero sac pressure after the insertion of the SG is assumed.
- The model does not include any tissue growth and remodeling after EVAR which often is observed in reality [142, 245, 267].

Table 3.4 Summary of all EVAR quality parameters. Reproduced with permission from [107].

	EVAR quality parameter	Reference	Symbol [dimension]	Equation	Potential influence[b]	Associated complication
Tractions / stresses	Max. vessel stress	[6, 138, 139, 187]	$\sigma_{99}^{\mathrm{wall}}$ [kPa]	-	$\downarrow$	Aortic neck dilatation
	Max. vessel overstress		$\bar{\sigma}_{99}^{\mathrm{wall}}$ [kPa]	(3.102)	$\downarrow$	
	Max. vessel relief[a]	-	$\lvert\bar{\sigma}_{1}^{\lambda,\mathrm{wall}}\rvert$ [kPa]	(3.103)	$\uparrow$	
	Max. aneurysmatic overstress[a]		$\bar{\sigma}_{99}^{\lambda,\mathrm{wall}}$ [kPa]	(3.103)	$\downarrow$	
	Max. normal contact pressure	[6, 7, 138]	$p_{\mathrm{n},99}$ [kPa]	-	$\downarrow$	
	Max. stent stress	[6, 7, 139]	σ_{99}^{S} [GPa]	-	$\downarrow$	SG fatigue
Fixation / drag forces	Passive fixation force	[237, 264] [7, 143, 177, 216][d]	$\hat{F}_{\mathrm{lz}}$ [N]	(3.105)	$\uparrow$	SG migration
	Drag force	[45, 75, 133, 186]	$\boldsymbol{F}_{\mathrm{drag}}$ [N]	(3.104)	$\downarrow$	
Quality of seal	Fixation area	[7, 236]	$a_{\mathrm{lz}}^{\mathrm{seal}}$ [mm^2]	(3.106)	$\uparrow$	Type I endoleak
	Max. graft-vessel gap	[53, 206, 224]	$z_{\mathrm{max}}^{\mathrm{GA}}$ [mm]	(3.107)	$\downarrow$	
	Max. stent-vessel gap		$z_{\mathrm{max}}^{\mathrm{SA}}$ [mm]	(3.108)	$\downarrow$	
SG geometry	Effective SG oversizing	[257][c]	$\bar{o}_{\mathrm{lz}}^{\mathrm{eff}}$ [%]	(3.114)	$-$	Type I endoleak, SG migration
	Min. stent expansion	[53, 138][d]	$e_{\mathrm{min}}^{\mathrm{S}}$ [%]	(3.112)	$\downarrow$	SG fatigue, SG kinking
	Max. stent asymmetry	[32, 39, 53][d]	$y_{\mathrm{max}}^{\mathrm{S}}$ [-]	(3.115)	$\downarrow$	
	Max. conical stent shape	[174, 273][c,d]	$c_{\mathrm{max}}^{\mathrm{S}}$ [-]	(3.117)	$\downarrow$	
Pulsatile parameters	Max. graft movement[a]	-	$u_{\mathrm{max}}^{\mathrm{G,pul}}$ [mm]	(3.119)	$\downarrow$	SG fatigue
	Max. stent movement[a]		$u_{\mathrm{max}}^{\mathrm{S,pul}}$ [mm]	(3.120)	$\downarrow$	
	Mean diametric graft compliance	[128, 139, 190, 276]	$\bar{C}$ [%/100mmHg]	(3.122)	$-$	Aortic compliance mismatch

[a] newly introduced EVAR quality parameter; no other publications about this or a closely related parameter is available (to the best of the author's knowledge)

[b] expected or reported influence of the parameter on the quality of EVAR; $\uparrow$: high value has positive influence on quality of EVAR; $\downarrow$: high value has negative influence on quality of EVAR; $-$: no unambiguous influence reported

[c] only qualitative assessment/discussion of the EVAR quality parameters but no quantitative considerations of the parameters

[d] consideration of closely related parameters

Assumptions of the stent-graft model

- The geometry of commercial SGs is approximated based on own measurements and data given in literature [44, 60, 176].
- The three SG components are modeled as one pre-assembled SG with fixed overlap lengths between the main, the left iliac and the right iliac component.
- The uncovered proximal stents with barbs are not modeled explicitly in a geometrical sense. In order to account for the axial fixation of the SG by the proximal barbs, mortar based frictional contact in pure stick (no tangential sliding) is applied between SG and luminal vessel surface in the most proximal region of the SG of $5\ \mathrm{mm}$ length.
- Any elasticity of the sutures and any slippage between stent limbs and graft are neglected. Instead, rigid connection by mortar based mesh tying is applied to model the suture between stent and graft.
- Commercial SG devices consist of interior and exterior stent limbs. In the proposed SG models, all stent limbs are modeled as interior stent limbs with respect to the graft.
- Circularly shaped cross sections of the stent struts are modeled as quadratic cross sections with equivalent bending stiffness to ensure hexahedral meshing of the stent and to provide proper surfaces for the mortar based mesh tying between stent and graft.
- Woven PET grafts are modeled as isotropic material.
- Superelasticity of nitinol stents is neglected.

Assumptions of the in-silico SG P&D methodology

- Compared to the real-world medical intervention, the in-silico SG P&D methodology is a strongly simplified process. The final deployed state of SG and vessel under steady-state conditions is the only point of interest. Any intrainterventional results cannot be obtained by this in-silico SG P&D methodology. No medical tools, other than the SG itself are considered. Hence, it is assumed that the simplified intrainterventional steps only have a minor influence on the final deployed SG configuration.
- The in-vivo deployed SG configuration may depend on clinician-specific factors that are not considered in the in-silico SG P&D methodology such as the speed of SG deployment and the application of a molding angioplasty to further unfold the SG.
- Treatment as purely solid mechanics problem. Fluid dynamics of the blood flow is neglected. A quasi-static blood pressure state is considered.
- Friction between SG and vessel is modeled as dry friction using Coulomb's law. Lubrication is neglected.

Assumptions of the EVAR quality parameters

- The EVAR quality parameters are proposed parameters to assess the likelihood of certain EVAR related complications from an engineering perspective. However, the clear link between the proposed EVAR quality parameters and EVAR related complications still needs to be proven.
- Mechanical and geometrical EVAR quality parameters may give indications of potential EVAR related complications. However, the EVAR related complication and its consequences are not modeled. For instance, modeling of a type I endoleak would require modeling of blood flow.
- The proposed EVAR quality parameters assess the EVAR outcome from a purely engineering perspective. Medical, biological or other parameters that also may have an influence on the occurrence of EVAR related complications are not evaluated.
- The proposed EVAR quality parameters are intended to provide likelihoods of potential EVAR related complications, but they are not a sure sign of these complications. For instance, a large graft-vessel gap in the landing zone may increase the risk of a type I endoleak. However, as long as there is a full circumferential seal, large graft-vessel gaps do not necessarily lead to a type I endoleak.
- All EVAR quality parameters are quantities taken directly after the SG deployment. This means it is assumed that these postinterventional parameters may give indications of potential EVAR related complications that arise several years after EVAR. The model would need to include growth and remodeling of vessel tissue to be able to consider the development of the EVAR quality parameters over several years.
- Ranges of acceptable values of the EVAR quality parameters are not provided in this thesis but would need to be determined in a future study of patient-specific cases of appropriate cohort size.

3.8. Summary

In this chapter, an in-silico EVAR model has been presented that is based solely on preinterventional data and which predicts the final postinterventional configuration of the deployed SG and the vessel. The in-silico EVAR model can be applied to patient-specific cases and provides a high level of detail of the postinterventional state of SG and vessel. It incorporates patient-specific vessel models, models of commercial SG devices and an in-silico SG P&D methodology to place and deploy the SG model in the vessel model. The vessel model considers several different vessel constituents such as the “healthy” vessel wall, the AAA wall, ILT and calcifications. SG models of two commercial SG devices as well as a novel stent predeformation methodology for the SG assembly has been proposed. The newly developed in-silico SG P&D methodology uses a suitable morphing algorithm that is directly applied to the SG model. This novel morphing algorithm is based on RMFs along the control curves that govern the deformation of the morphing object, i.e., the deformation of the SG model. Furthermore, SG parameter continuation has

been proposed for the assessment of several different SG sizes within a single EVAR simulation. Based on the predicted configuration of SG and vessel, several mechanical and geometrical parameters have been proposed to assess the in-silico EVAR outcome with respect to EVAR related complication likelihoods from an engineering perspective.

This continuous process chain of the vessel and SG model generation, the in-silico prediction of the final postinterventional configuration and the assessment of the in-silico EVAR outcome can be a promising tool in the preinterventional planning of EVAR. The validation of the in-silico EVAR model and the versatile application of this process chain will be presented in the subsequent chapters.

Part II.

In-silico EVAR application and validation

4. Validation of the in-silico EVAR model

In the previous chapter, all computational tools for in-silico EVAR were presented. In-silico EVAR is an idealization of the real-world medical EVAR procedure which incorporates several assumptions (cf. Section 3.7). Hence, the proposed approximation of the EVAR outcome by in-silico methods requires careful validation.

Some studies used in-vitro validation of their in-silico EVAR models [51, 122]. However, most in-silico EVAR results are validated by qualitative or quantitative comparison to in-vivo imaging data [9, 122, 188, 205, 207]. In-silico EVAR as defined in this thesis uses only preinterventional information, such as the patient-specific vessel geometry from preinterventional CT data. Thus, an appropriate validation can be obtained by comparison of the deployed state obtained from in-silico EVAR and the deployed state extracted from postinterventional CT data of the same patient. On postinterventional patient-specific CT data, the stent as metallic object is visible whereas the thin graft as plastic object is not visible. Hence, the comparison of in-silico results and postinterventional CT data is mostly restricted to the comparison of the stent configuration. A validation methodology that uses the postinterventional stent configuration extracted from CT data has to cope with distracting artifacts that frequently occur when imaging metallic objects such as stents by CT [25, 49, 161, 214].

Quantitative validation methodologies that compare the deployed stent configuration from postinterventional CT data and from in-silico EVAR have been proposed by [9, 205, 207]. Auricchio et al. [9] used the mean stent diameter in three distinct slices orthogonal to the postinterventional vessel centerline to compare in-silico EVAR results with in-vivo data of one patient with an ascending aortic pseudo aneurysm treated by a tube SG. Measuring the diameter of the stent from postinterventional CT data at distinct locations can be sensitive to small variations of the location due to local distracting artifacts in the postinterventional CT data. Therefore, the validation result may be strongly dependent on the subjective choice of the location where the stent diameter is measured. By far a more objective and more elaborated validation methodology was used by Perrin et al. for the validation of in-silico EVAR of patient-specific cases of three Medtronic Endurant^{TM} II SGs [205] and three Anaconda^{TM} SGs [207]. Perrin et al. used one average diameter per stent limb in their quantitative validation methodology. In addition to the diameter comparison, Perrin et al. compared the position of each stent limb quantitatively between in-silico EVAR results and the stent extracted from postinterventional CT data. Calculating only one mean diameter for each stent limb is less susceptible to local artifacts in the postinterventional CT data. However, this method is not able to capture nonuniform stent shapes such as a conical shape. But particularly in the landing zones of the SG, nonuniform vessel shapes and consequently nonuniform stent shapes can have a major impact on the applicability and the success of EVAR [42, 185]. Hence, a validation methodology should also be able to assess how well such nonuniform stent shapes are represented.

In this chapter, a novel qualitative and quantitative validation methodology, that is based on a comparison between in-silico EVAR results and postinterventional CT data, is presented. The validation methodology compares average stent diameters in slices orthogonal to the postinterventional SG centerline pseudo-continuously along the total length of the deployed SG. This validation methodology is used to validate the in-silico EVAR model presented in Chapter 3 by considering three patient-specific cases (patient 1-3, Appendix A.1).

The outline of this chapter is as follows: first, the validation methodology using postinterventional CT data is described in Section 4.1. Afterwards, in Section 4.2, this validation methodology is used for qualitative and quantitative validation of the in-silico EVAR model considering three patient-specific cases. Results of this validation process are discussed in Section 4.3. Finally, limitations and conclusions are stated in Section 4.4 and 4.5, respectively.

This chapter is primarily based on the previous publication [107] by the author of this thesis, which is reused here with permission.

4.1. Validation methodology using postinterventional CT data

In this section, the validation methodology of in-silico EVAR is described. The validation is a qualitative and quantitative comparison of the final configuration of the stent after the in-silico SG deployment with the configuration of the stent extracted from postinterventional CT data. Thus, first in-silico EVAR is applied to the real clinical cases of patient 1-3 with the clinical characteristics as stated in Appendix A.1. Perfect placement of the SG slightly distal to the branches to the renal arteries according to the preinterventional CT data is assumed in the in-silico EVAR model. The distal landing zones evolve from the deployment process.

The comparison of the stent configuration after in-silico EVAR with the stent configuration extracted from real-world postinterventional CT data requires the assumption that within the time period between the EVAR intervention and the day of the postinterventional CT scan, no growth and remodeling and other reasons have changed the configurations of vessel and SG. Due to the short time period (patient 1: 2 days, patient 2: 5 days, patient 3: 2 days) between the EVAR intervention and the day of the postinterventional CT scan as well as relatively slow growth and remodeling rates of vessel tissue, this assumption seems reliable.

In the quantitative validation, the diameters of the stent from in-silico EVAR are compared to the diameters of the stent from postinterventional CT data. The single steps of the proposed validation methodology are discussed in the following and are summarized in Figure 4.1.

In-silico EVAR is based on the vessel geometry of preinterventional CT data which in general is aligned in a different coordinate system than the postinterventional CT data. Hence, after the segmentation of the stent from postinterventional CT data, a rigid registration based on a minimal point distance filter of the stent from postinterventional CT data onto the stent from in-silico EVAR is used to align both stent configurations in the same coordinate system (cf. Figure 4.1II). Next, the three parts of the stent $\Theta \in \{\mathrm{P}, \mathrm{L}, \mathrm{R}\}$ (proximal part, left iliac part and right iliac part) are considered separately (cf. Figure 4.1III).

In Section 3.6.1, a postprocessing methodology to measure the stent diameter after in-silico EVAR pseudo-continuously along the total SG length in the deployed state was presented. This

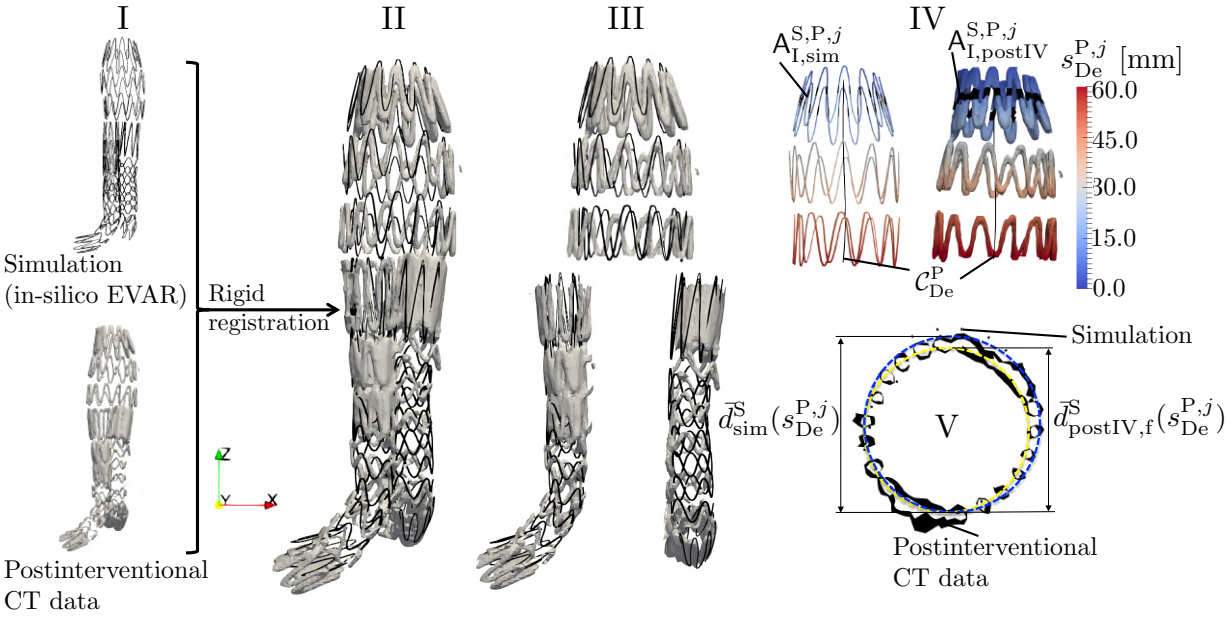

Figure 4.1 Validation methodology using postinterventional CT data visualized for patient 3. Stent from simulation and segmented stent from postinterventional CT data (I). Rigid registration of stents from simulation and postinterventional CT data (II). Cut of stents into three SG parts (proximal part, left iliac part and right iliac part) (III). Exemplary illustration of one set $\mathsf{A}^{\mathrm{S,P},j}_{\mathrm{I,postIV}}$ and $\mathsf{A}^{\mathrm{S,P},j}_{\mathrm{I,sim}}$ of the proximal stent part (IV) and exemplary comparison of the stent diameter $\bar{d}^{\mathrm{S}}_{\mathrm{sim}}(s^{\mathrm{P},j}_{\mathrm{De}})$ from simulation and the stent diameter $\bar{d}^{\mathrm{S}}_{\mathrm{postIV,f}}(s^{\mathrm{P},j}_{\mathrm{De}})$ from postinterventional CT data at the same arc length $s^{\mathrm{P},j}_{\mathrm{De}}$ (V). Reproduced with permission from [107].

methodology consists of the following two major steps. Using Equation (3.92), the centerlines $\mathcal{C}^{(\Theta)}_{\mathrm{De}}$ of the three SG parts $\Theta \in \{\mathrm{P},\mathrm{L},\mathrm{R}\}$ in the deployed state are determined. Afterwards, according to Equation (3.96), the average diameter $\bar{d}^{\mathrm{S},(\Theta),j}$ of all nodes in the morphing set $\mathsf{A}^{\mathrm{S},(\Theta),j}_{\mathrm{I}}$ (cf. Figure 4.1IV) is determined which corresponds to the average diameter of the stent in an orthogonal slice at the location of point j of the centerline $\mathcal{C}^{(\Theta)}_{\mathrm{De}}$. The superscript $(\bullet)^j$ indicates that the average diameter $\bar{d}^{\mathrm{S},(\Theta),j} = \bar{d}^{\mathrm{S}}(s^{(\Theta),j}_{\mathrm{De}})$ is measured at the discrete location of point j described by the arc length $s^{(\Theta),j}_{\mathrm{De}}$.

In the following, the same methods are applied to evaluate the deployed stent configuration extracted from postinterventional CT data with a resolution of $0.75 \times 0.75 \times 1.0\ \mathrm{mm}^3$ for patient 1, $0.79 \times 0.79 \times 1.0\ \mathrm{mm}^3$ for patient 2 and $0.76 \times 0.76 \times 1.0\ \mathrm{mm}^3$ for patient 3. The same centerlines $\mathcal{C}^{(\Theta)}_{\mathrm{De}}$ and the same methods as for the simulated SG are used to evaluate the average diameters $\bar{d}^{\mathrm{S},(\Theta),j}$ of the stent segmented from postinterventional CT data (cf. Figure 4.2). The subscripts $(\bullet)_{\mathrm{sim}}$ and $(\bullet)_{\mathrm{postIV}}$ are introduced to distinguish between variables of the simulation and variables of the postinterventional CT data.

Measuring the diameter of the stent from postinterventional CT data at distinct locations $s^{(\Theta),j}_{\mathrm{De}}$, i.e., measuring the average diameter of distinct sets $\mathsf{A}^{\mathrm{S},(\Theta),j}_{\mathrm{I,postIV}}$, can be sensitive to small variations of the location due to local artifacts in the postinterventional CT data. The main source of these artifacts is given by the well known problem of imaging metallic objects by CT [25, 161, 214].

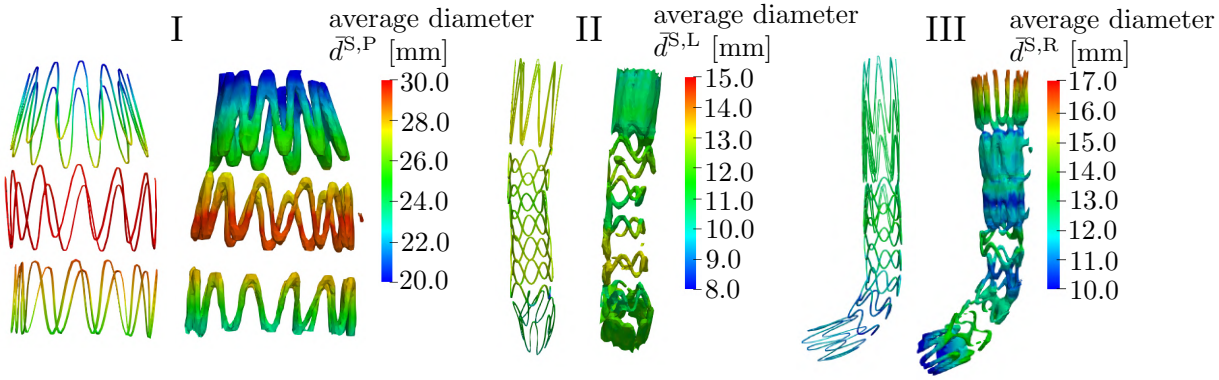

Figure 4.2 Visualization of the average stent diameters $\bar{d}^{\mathrm{S},(\Theta)}_{\mathrm{sim}}$ from simulation and the average stent diameters $\bar{d}^{\mathrm{S},(\Theta)}_{\mathrm{postIV}}$ from postinterventional CT data for the proximal SG part (I), the left iliac SG part (II) and the right iliac SG part (III) of patient 3. Reproduced with permission from [107].

Due to these metal-related artifacts, stent struts appear to be thicker than they are and a clear segmentation process of the stent is more difficult. Additionally, calcifications often cannot be separated clearly from stents. Hence, in the validation methodology with the objective to measure the stent diameter pseudo-continuously along the total SG length, an outlier detection by a moving average filter is applied to reduce the variance of the measured average stent diameters from postinterventional CT data due to the presence of local artifacts. This filtering process is described in Appendix A.6. Filtered data is indicated by the subscript $(\bullet)_{\mathrm{f}}$ in the following. A quality estimation of the segmented data from postinterventional CT scans, i.e., an estimation to which extent the stent diameter measurement from postinterventional CT data is influenced by the vagueness in the segmentation process, is provided in Appendix A.7.

The quantitative comparison of the simulation results with the postinterventional CT data is done by comparing the average stent diameters $\bar{d}^{\mathrm{S}}_{\mathrm{sim}}(s^{(\Theta),j}_{\mathrm{De}}) = \bar{d}^{\mathrm{S},(\Theta),j}_{\mathrm{sim}}$ from simulation with the average stent diameters $\bar{d}^{\mathrm{S}}_{\mathrm{postIV,f}}(s^{(\Theta),j}_{\mathrm{De}}) = \bar{d}^{\mathrm{S},(\Theta),j}_{\mathrm{postIV,f}}$ from postinterventional CT data (cf. Figure 4.1V) at same arc length $\{s^{(\Theta),j}_{\mathrm{De}} | 0 \leq s^{(\Theta),j}_{\mathrm{De}} \leq L^{\mathrm{SG},(\Theta)}_{\mathrm{De}}, \forall j = 1,2,...,n^{(\Theta)}_{\mathrm{C}}\}$, where $s^{(\Theta),j}_{\mathrm{De}}$ are discrete values of the arc length of the centerline $\mathcal{C}^{(\Theta)}_{\mathrm{De}}$ of SG part $\Theta \in \{\mathrm{P},\mathrm{L},\mathrm{R}\}$ as described in Section 3.6.1. As the exact blood pressure state of the patients in the postinterventional CT data is unknown, the simulation results at an assumed diastolic blood pressure state of $p^{\mathrm{diast}} = 80\ \mathrm{mmHg}$ are used as lower bound and the simulation results at an assumed systolic blood pressure state of $p^{\mathrm{sys}} = 130\ \mathrm{mmHg}$ are used as upper bound for the validation. Thus, the postinterventional CT data is compared to the in-silico EVAR results at the internal diastolic pressure state and at the internal systolic pressure state. The relative error $\varepsilon^{(\Lambda)}(s^{(\Theta),j}_{\mathrm{De}})$ of the in-silico EVAR model at the discrete location $s^{(\Theta),j}_{\mathrm{De}}$ and at the respective pressure state is

$$\varepsilon^{(\Lambda)}(s^{(\Theta),j}_{\mathrm{De}}) = \frac{\bar{d}^{\mathrm{S},(\Lambda)}_{\mathrm{sim}}(s^{(\Theta),j}_{\mathrm{De}}) - \bar{d}^{\mathrm{S}}_{\mathrm{postIV,f}}(s^{(\Theta),j}_{\mathrm{De}})}{\bar{d}^{\mathrm{S}}_{\mathrm{postIV,f}}(s^{(\Theta),j}_{\mathrm{De}})} \tag{4.1}$$

with $\Lambda \in \{\mathrm{diast},\mathrm{sys}\}$. The mean error ε at the discrete location $s^{(\Theta),j}_{\mathrm{De}}$ out of the error at the

diastolic pressure state $\varepsilon^{\mathrm{diast}}$ and the error at the systolic pressure state $\varepsilon^{\mathrm{sys}}$ is given by

$$\varepsilon(s_{\mathrm{De}}^{(\Theta),j}) = \frac{1}{2}\left(\varepsilon^{\mathrm{diast}}(s_{\mathrm{De}}^{(\Theta),j}) + \varepsilon^{\mathrm{sys}}(s_{\mathrm{De}}^{(\Theta),j})\right). \tag{4.2}$$

In the following, the patient specific cases $\Xi \in \{1,2,3\}$ (cf. Appendix A.1) are used for validation. The mean error $\mu_{\varepsilon,(\Xi)}^{(\Theta)}$ and standard deviation $\sigma_{\varepsilon,(\Xi)}^{(\Theta)}$ for each SG part $\Theta \in \{\mathrm{P},\mathrm{L},\mathrm{R}\}$ and each patient $\Xi \in \{1,2,3\}$ over all discrete locations $s_{\mathrm{De},(\Xi)}^{(\Theta),j}$ are calculated according to

$$\mu_{\varepsilon,(\Xi)}^{(\Theta)} = \frac{1}{n_{\mathrm{C},(\Xi)}^{(\Theta)}} \sum_{j=1,2,\ldots,n_{\mathrm{C},(\Xi)}^{(\Theta)}} \varepsilon(s_{\mathrm{De},(\Xi)}^{(\Theta),j}) \tag{4.3}$$

and

$$\sigma_{\varepsilon,(\Xi)}^{(\Theta)} = \sqrt{\frac{1}{n_{\mathrm{C},(\Xi)}^{(\Theta)}} \sum_{j=1,2,\ldots,n_{\mathrm{C},(\Xi)}^{(\Theta)}} \left(\varepsilon(s_{\mathrm{De},(\Xi)}^{(\Theta),j}) - \mu_{\varepsilon,(\Xi)}^{(\Theta)}\right)^2}. \tag{4.4}$$

In (4.3) and (4.4), $s_{\mathrm{De},(\Xi)}^{(\Theta),j}$ are discrete values of the arc length of the centerline $\mathcal{C}_{\mathrm{De},(\Xi)}^{(\Theta)}$ with $\{s_{\mathrm{De},(\Xi)}^{(\Theta),j} | 0 \leq s_{\mathrm{De},(\Xi)}^{(\Theta),j} \leq L_{\mathrm{De},(\Xi)}^{\mathrm{SG},(\Theta)}, \forall j = 1,2,...,n_{\mathrm{C},(\Xi)}^{(\Theta)}\}$. The discrete values of the arc length $s_{\mathrm{De},(\Xi)}^{(\Theta),j}$ describe the discrete locations at which the average diameters $\bar{d}_{\mathrm{sim}}^{\mathrm{S}}(s_{\mathrm{De},(\Xi)}^{(\Theta),j}) = \bar{d}_{\mathrm{sim},(\Xi)}^{\mathrm{S},(\Theta),j}$ as well as $\bar{d}_{\mathrm{postIV}}^{\mathrm{S}}(s_{\mathrm{De},(\Xi)}^{(\Theta),j}) = \bar{d}_{\mathrm{postIV},(\Xi)}^{\mathrm{S},(\Theta),j}$ and consequently the relative errors $\varepsilon(s_{\mathrm{De},(\Xi)}^{(\Theta),j}) = \varepsilon_{(\Xi)}^{(\Theta),j}$ are measured. $n_{\mathrm{C},(\Xi)}^{(\Theta)}$ is the total number of these discrete locations and $L_{\mathrm{De},(\Xi)}^{\mathrm{SG},(\Theta)}$ is the total arc length of the centerline $\mathcal{C}_{\mathrm{De},(\Xi)}^{(\Theta)}$ of patient $\Xi \in \{1,2,3\}$ and SG part $\Theta \in \{\mathrm{P},\mathrm{L},\mathrm{R}\}$ in the deployed state. Accordingly, for instance, $\mu_{\varepsilon,1}^{\mathrm{P}}$ denotes the mean error of the proximal SG part of patient 1.

The number of discrete locations $s_{\mathrm{De},(\Xi)}^{(\Theta),j}$ at which the average diameters $\bar{d}^{\mathrm{S}}(s_{\mathrm{De},(\Xi)}^{(\Theta),j})$ are measured is very high. Hence, as stated in Section 3.6, the diameter measure is denoted as *pseudo-continuous* diameter measure. Accordingly, variables with superscript $(\bullet)^j$ feature discrete variables and variables without superscript $(\bullet)^j$ feature variables that are given pseudo-continuously along $s_{\mathrm{De},(\Xi)}^{(\Theta)} \in [0, L_{\mathrm{De},(\Xi)}^{\mathrm{SG},(\Theta)}]$.

4.2. Results

The in-silico EVAR model is validated by qualitative (Section 4.2.1) and quantitative (Section 4.2.2) comparison between the simulation results and postinterventional CT data for patient 1-3.

4.2.1. Qualitative validation

In Figure 4.3, the simulated stent configurations of patient 1-3 at an internal pressure state of $80\ \mathrm{mmHg}$ are superimposed to the stent configuration segmented from postinterventional CT data. Qualitatively, the simulated and real-world postinterventional stent shapes are almost iden-

tical by visual comparison. Even specific SG deformations, such as the conical stent shape of the most proximal stent limb of patient 3 or the highly curved SG part of the left iliac part of patient 1 are properly predicted by the in-silico EVAR model as can be seen in Figure 4.3. Only slight mismatches in the relative position of the right iliac SG parts of all three patients exist, whereas for the proximal and the left iliac SG part no significant position mismatches are visible.

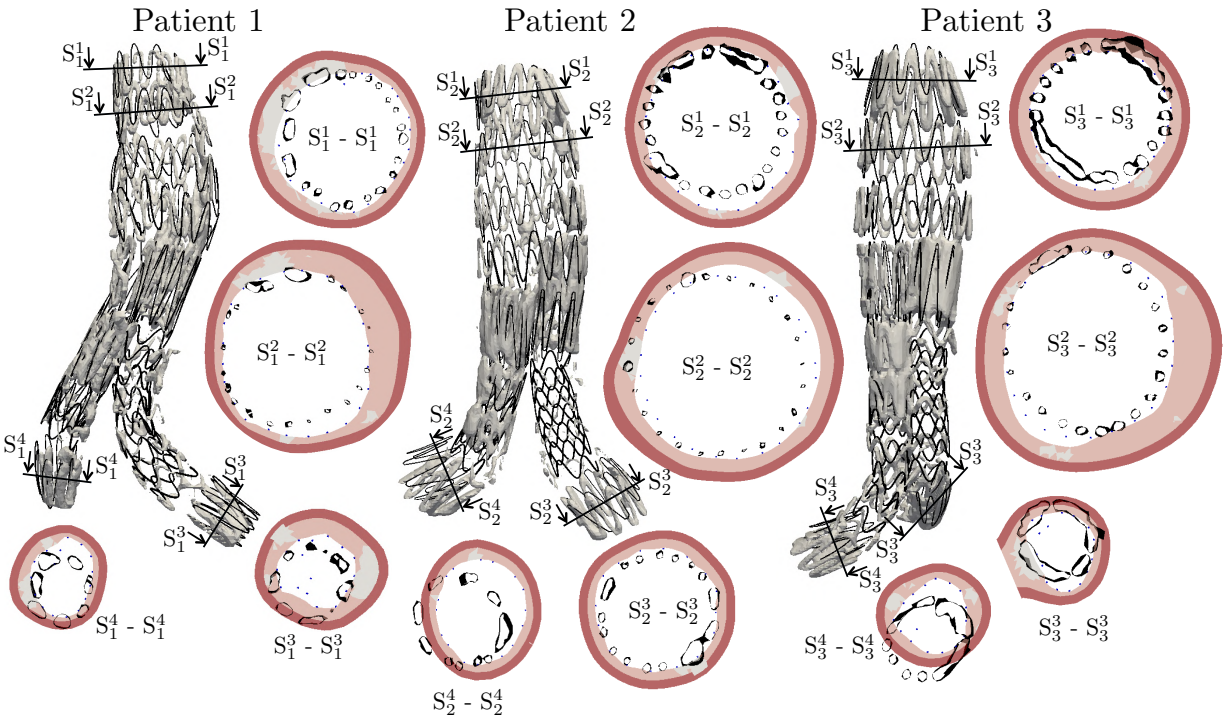

Figure 4.3 Qualitative validation of the patient-specific cases 1-3. Comparison of the average diameters of the stent from in-silico EVAR and the stent from postinterventional CT data. Reproduced with permission from [107].

For each patient four slices are considered qualitatively: one slice through the first stent limb of the proximal part (slice $S^1_{(\Xi)}$), one slice through the second stent limb of the proximal part (slice $S^2_{(\Xi)}$), one slice through the last stent limb of the left iliac part (slice $S^3_{(\Xi)}$) and one slice through the last stent limb of the right iliac part (slice $S^4_{(\Xi)}$), where $\Xi \in \{1, 2, 3\}$ denotes the number of the patient. The slices $S^1_{(\Xi)}$, $S^3_{(\Xi)}$ and $S^4_{(\Xi)}$ are of elevated relevance as they are within the proximal and the distal landing zones that are involved in several EVAR related complications such as endoleaks type 1a and 1b (cf. Section 1.1.2.4).

The deployed stent diameters in the slices S^1_1, S^1_2 and S^1_3, which define slices through the proximal landing zone, are well predicted. Slight discrepancies in slice S^1_2 of patient 2 can be observed where the simulated stent diameter is slightly larger than the stent diameter extracted from postinterventional CT data. In the slices S^2_1 and S^2_3 some mismatches in the predicted stent expansion can be identified, whereas the prediction of the stent expansion in slice S^2_2 is almost perfect.

The diameter of the simulated stents and the diameter of the stents from postinterventional CT data in the slices S^3_1, S^3_2 and S^3_3, which are slices through the landing zone of the left iliac part, are almost identical from a qualitative perspective. The slices S^4_1, S^4_2 and S^4_3 through the landing zone

of the right iliac part highlight the previously mentioned relative position error of the simulated right iliac SG part compared to the postinterventional CT data. The prediction of the diameter expansion is relatively good. The largest discrepancies by visual comparison can be identified for patient 2 (slice S_2^4) where the simulated stent diameter is too large.

4.2.2. Quantitative validation

In Table 4.1, the average stent diameters and relative errors of the distinct slices are shown. These distinct slices were qualitatively evaluated in Section 4.2.1 and are visualized in Figure 4.3. The in-silico EVAR results are quantitatively evaluated at the assumed diastolic pressure state of $p^{\mathrm{diast}} = 80\ \mathrm{mmHg}$ and at the assumed systolic pressure state of $p^{\mathrm{sys}} = 130\ \mathrm{mmHg}$.

Table 4.1 Measured average diameters from in-silico EVAR $\bar{d}^{\mathrm{S},(\Lambda)}_{\mathrm{sim}}$ and from postinterventional CT data $\bar{d}^{\mathrm{S}}_{\mathrm{postIV,f}}$ as well as relative errors $\varepsilon^{(\Lambda)}$ at the assumed diastolic pressure state $(\bullet)^{\mathrm{diast}}$ ($80\ \mathrm{mmHg}$) and at the assumed systolic pressure state $(\bullet)^{\mathrm{sys}}$ ($130\ \mathrm{mmHg}$) according to Equation (4.1) in the exemplary four slices per patient visualized in Figure 4.3. Reproduced with permission from [107].

	Patient 1				Patient 2				Patient 3			
Slice	S_1^1	S_1^2	S_1^3	S_1^4	S_2^1	S_2^2	S_2^3	S_2^4	S_3^1	S_3^2	S_3^3	S_3^4
$\bar{d}^{\mathrm{S,diast}}_{\mathrm{sim}}$ [mm]	21.9	25.3	10.4	10.8	25.5	28.6	20.5	16.9	23.3	30.0	10.9	11.4
$\bar{d}^{\mathrm{S,sys}}_{\mathrm{sim}}$ [mm]	22.3	25.9	10.8	11.1	26.0	28.7	20.9	17.1	24.0	30.4	11.1	11.6
$\bar{d}^{\mathrm{S}}_{\mathrm{postIV,f}}$ [mm]	21.1	24.3	10.7	10.2	23.3	28.9	19.5	14.5	22.2	28.6	11.9	11.0
$\varepsilon^{\mathrm{diast}}$ [%]	3.8	4.1	-2.8	5.9	9.4	-1.0	5.1	16.6	5.0	4.9	-8.4	3.6
$\varepsilon^{\mathrm{sys}}$ [%]	5.7	6.6	0.9	8.8	11.6	-0.7	7.2	17.9	8.1	6.3	-6.7	5.5

In Figure 4.4, the average stent diameters of in-silico EVAR at $80\ \mathrm{mmHg}$ ($\bar{d}^{\mathrm{S,diast}}_{\mathrm{sim}}(s^{(\Theta)}_{\mathrm{De},(\Xi)})$) and at $130\ \mathrm{mmHg}$ ($\bar{d}^{\mathrm{S,sys}}_{\mathrm{sim}}(s^{(\Theta)}_{\mathrm{De},(\Xi)})$) as well as the filtered average diameters $\bar{d}^{\mathrm{S}}_{\mathrm{postIV,f}}(s^{(\Theta)}_{\mathrm{De},(\Xi)})$ of the stent from postinterventional CT data are plotted pseudo-continuously along the arc length $s^{(\Theta)}_{\mathrm{De},(\Xi)} \in [0, L^{\mathrm{SG},(\Theta)}_{\mathrm{De},(\Xi)}]$ for all three SG parts $\Theta \in \{\mathrm{P}, \mathrm{L}, \mathrm{R}\}$ and all three patients $\Xi \in \{1, 2, 3\}$. Each asterisk corresponds to a discrete average diameter $\bar{d}^{\mathrm{S},(\Theta),j}_{\mathrm{sim},(\Xi)}$, $\bar{d}^{\mathrm{S},(\Theta),j}_{\mathrm{postIV,f},(\Xi)}$ measured in a distinct set $\mathsf{A}^{\mathrm{S},(\Theta),j}_{\mathrm{I,sim},(\Xi)}$ and $\mathsf{A}^{\mathrm{S},(\Theta),j}_{\mathrm{I,postIV},(\Xi)}$, respectively (cf. Section 3.6.1). Additionally, the relative error $\varepsilon(s^{(\Theta)}_{\mathrm{De},(\Xi)})$ between in-silico EVAR and the postinterventional CT data according to Equation (4.2) is visualized in Figure 4.4 (right scale).

At the bifurcations of the SG, the stent diameters of the postinterventional CT data could not be measured properly as the proximal part and the iliac parts of the stent are slightly overlapping. Further, in the range $s^{\mathrm{L}}_{\mathrm{De},2} \in [34\ \mathrm{mm}, 65\ \mathrm{mm}]$ of the left iliac part of patient 2, the quality of the segmented stent from postinterventional CT data is inappropriate to be able to measure stent diameters. Those regions, in which the average stent diameters of the postinterventional CT data could not be measured, are highlighted by orange color in the plots of Figure 4.4 and are neglected in the calculation of the relative errors $\varepsilon(s^{(\Theta)}_{\mathrm{De},(\Xi)})$. Table 4.2 provides a summary of the mean $\mu^{(\Theta)}_{\varepsilon,(\Xi)}$ and the standard deviation $\sigma^{(\Theta)}_{\varepsilon,(\Xi)}$ of the relative errors $\varepsilon(s^{(\Theta)}_{\mathrm{De},(\Xi)})$

according to Equation (4.3) and (4.4) over all SG parts $\Theta \in \{\mathrm{P}, \mathrm{L}, \mathrm{R}\}$ and all patient-specific cases $\Xi \in \{1, 2, 3\}$.

Table 4.2 Mean and standard deviation of the relative errors $\varepsilon(s^{(\Theta)}_{\mathrm{De},(\Xi)})$ according to Equation (4.3) and (4.4) over all SG parts $\Theta \in \{\mathrm{P}, \mathrm{L}, \mathrm{R}\}$ and all patient-specific cases $\Xi \in \{1, 2, 3\}$. Reproduced with permission from [107].

$\mu^{(\Theta)}_{\varepsilon,(\Xi)} \pm \sigma^{(\Theta)}_{\varepsilon,(\Xi)}$ [%]	Patient 1 ($\Xi = 1$)	Patient 2 ($\Xi = 2$)	Patient 3 ($\Xi = 3$)	Total
Proximal part ($\Theta = \mathrm{P}$)	6.0 ± 1.6	5.8 ± 5.0	7.2 ± 1.9	6.4 ± 3.4
Left iliac part ($\Theta = \mathrm{L}$)	-3.4 ± 7.6	7.6 ± 6.0	2.0 ± 10.2	2.1 ± 9.3
Right iliac part ($\Theta = \mathrm{R}$)	12.4 ± 7.9	4.2 ± 9.3	4.7 ± 9.9	6.6 ± 9.8
Total	6.7 ± 8.7	5.5 ± 7.4	5.0 ± 8.2	5.6 ± 8.1

Referring to Figure 4.4, in the proximal parts of the three patients, average stent diameters of in-silico EVAR at $80\ \mathrm{mmHg}$ (blue curve) and at 130 mmHg (red curve) are very close to the average stent diameters $\bar{d}^{\mathrm{S}}_{\mathrm{postIV,f}}(s^{\mathrm{P}}_{\mathrm{De},(\Xi)})$ of the postinterventional CT data (black curve). Largest discrepancies between in-silico EVAR and postinterventional CT data can be observed in the proximal SG part of patient 2. The relative error is $|\varepsilon(s^{\mathrm{P}}_{\mathrm{De},(\Xi)})| < 12\%$ for any of the three patients with $s^{\mathrm{P}}_{\mathrm{De},(\Xi)} \in [0, L^{\mathrm{SG,P}}_{\mathrm{De},(\Xi)}]$, where $L^{\mathrm{SG,P}}_{\mathrm{De},(\Xi)}$ is the length of the proximal SG part of patient $\Xi \in \{1, 2, 3\}$ in the deployed state. The good prediction of the average stent diameters of the proximal SG part results in a mean relative error of $\mu^{\mathrm{P}}_{\varepsilon} = 6.4\%$ and a small standard deviation of $\sigma^{\mathrm{P}}_{\varepsilon} = 3.4\%$ (cf. Table 4.2). $\mu^{\mathrm{P}}_{\varepsilon}$ and $\sigma^{\mathrm{P}}_{\varepsilon}$ denote the mean and standard deviation of the error ε for the proximal SG part over all three patients according to Equation (4.3) and (4.4). It is also worth mentioning that the in-silico EVAR model is able to reproduce the conical shapes of the stent in the proximal landing zone (indicated by green color in Figure 4.4). Whereas the most proximal stent limb of patient 1 is only slightly conical, the most proximal stent limbs of patient 2 and 3 are strongly conical with a smaller average diameter at the proximal end and a larger average diameter at the distal end.

The SGs of all three patients are strongly compressed in the proximal landing zone, i.e., the measured average stent diameters (blue, red and black curve in Figure 4.4) are significantly smaller than the nominal diameter $D^{\mathrm{SG}}(s^{\mathrm{P}}_{\mathrm{De},(\Xi)})$ (cyan curve in Figure 4.4). In the aneurysm sac ($s^{\mathrm{P}}_{\mathrm{De},(\Xi)} \gtrsim 30\ \mathrm{mm}$), the SG fully expands to its nominal diameter $D^{\mathrm{SG}}(s^{\mathrm{P}}_{\mathrm{De},(\Xi)})$ with exception of patient 1. Due to a pronounced ILT layer, patient 1 has a relatively small luminal diameter in the aneurysm sac of the preinterventional vessel. The SG cannot fully expand to its nominal diameter in this region.

Very similar behavior of the left and right iliac SG parts can be observed in Figure 4.4. A relative error in the left iliac SG parts of $|\varepsilon(s^{\mathrm{L}}_{\mathrm{De},(\Xi)})| < 20\%$ and a relative error in the right iliac SG parts of $|\varepsilon(s^{\mathrm{R}}_{\mathrm{De},(\Xi)})| < 25\%$ is found for any $s^{\mathrm{L}}_{\mathrm{De},(\Xi)} \in [0, L^{\mathrm{SG,L}}_{\mathrm{De},(\Xi)}]$ and $s^{\mathrm{R}}_{\mathrm{De},(\Xi)} \in [0, L^{\mathrm{SG,R}}_{\mathrm{De},(\Xi)}]$, respectively. Here, $L^{\mathrm{SG,L}}_{\mathrm{De},(\Xi)}$ and $L^{\mathrm{SG,R}}_{\mathrm{De},(\Xi)}$ denote the length of the left and the right SG part in the deployed state of patient $\Xi \in \{1, 2, 3\}$. The mean error and the standard deviation of the iliac parts are given by $\mu^{\mathrm{L}}_{\varepsilon} \pm \sigma^{\mathrm{L}}_{\varepsilon} = 2.1 \pm 9.3\%$ for the left iliac part and $\mu^{\mathrm{R}}_{\varepsilon} \pm \sigma^{\mathrm{R}}_{\varepsilon} = 6.6 \pm 9.8\%$ for the right iliac part (cf. Table 4.2). $\mu^{\mathrm{L}}_{\varepsilon}$ and $\sigma^{\mathrm{L}}_{\varepsilon}$ denote the mean and standard deviation of the relative

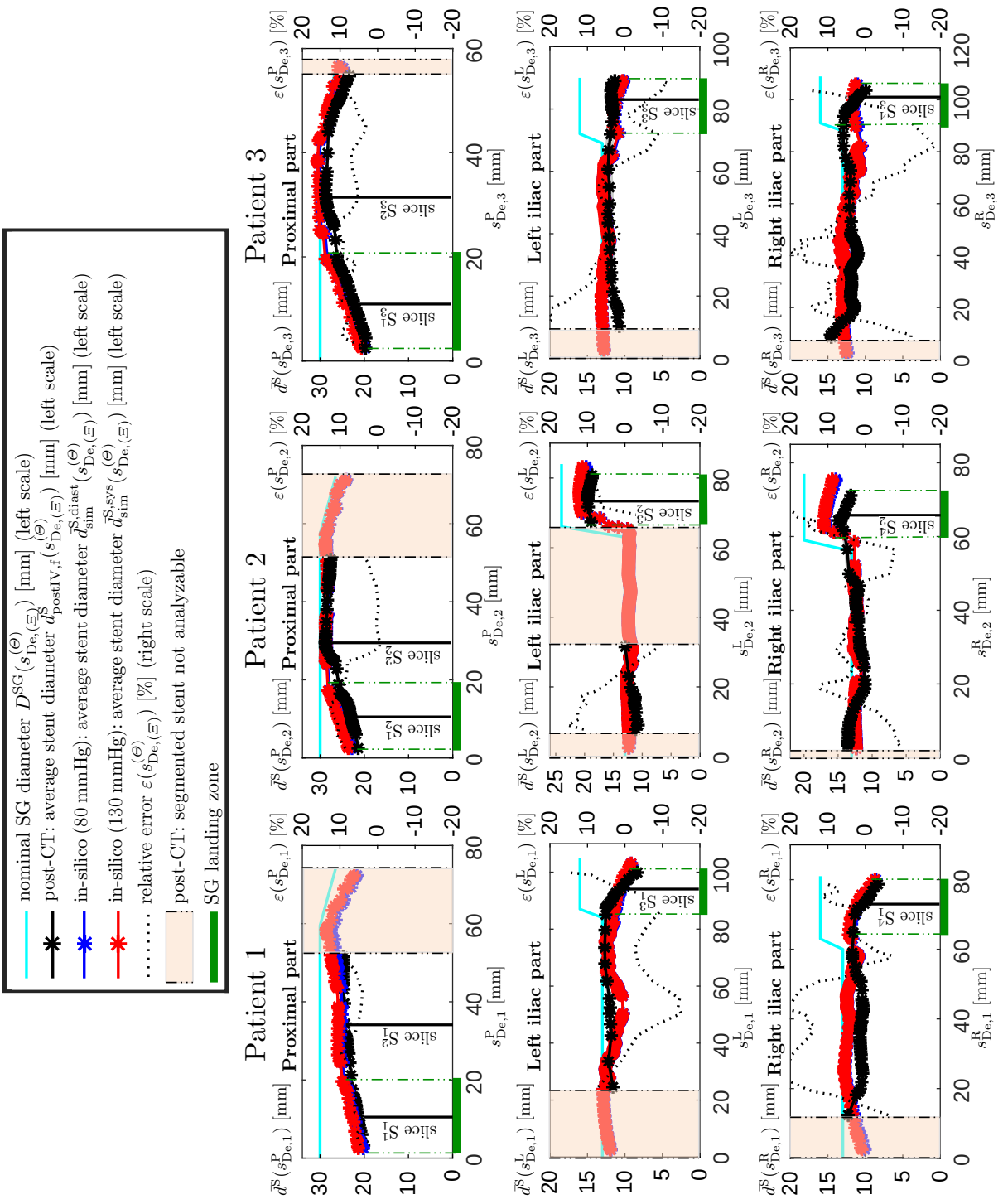

Figure 4.4 Quantitative validation of the patient-specific cases 1-3. Comparison of the average diameters of the stent from in-silico EVAR and the stent from postinterventional CT data pseudo-continuously along the total arc length $s^{(\Theta)}_{\mathrm{De},(\Xi)} \in [0, L^{\mathrm{SG},(\Theta)}_{\mathrm{De},(\Xi)}]$ of the respective SG part $\Theta \in \{\mathrm{P}, \mathrm{L}, \mathrm{R}\}$ of patient $\Xi \in \{1, 2, 3\}$. Reproduced with permission from [107].

error ε for the left iliac SG part over all three patients. $\mu_{\varepsilon}^{\mathrm{R}}$ and $\sigma_{\varepsilon}^{\mathrm{R}}$ is the mean and standard deviation of the relative error ε for the right iliac SG part over all three patients according to Equation (4.3) and (4.4). In contrast to the proximal SG parts, where the simulated average diameters $\bar{d}_{\mathrm{sim}}^{\mathrm{S,diast}}$ are slightly larger than the average diameters $\bar{d}_{\mathrm{postIV,f}}^{\mathrm{S}}$ from postinterventional CT data for the total length of the SG part $s_{\mathrm{De},(\Xi)}^{\mathrm{P}} \in [0, L_{\mathrm{De},(\Xi)}^{\mathrm{SG,P}}]$, in the iliac SG parts there are regions where the simulated stent diameters are too large and regions where the simulated stent diameters are too small. This is the reason for the relatively small mean relative errors but higher standard deviations for the iliac SG parts as provided in Table 4.2. The prediction of the stent expansion diameters in the landing zones of the iliac SG parts (indicated by green color in Figure 4.4) is relatively good with exception of the landing zone of the right iliac SG part of patient 2. In the landing zone of the right iliac SG part of patient 2, the predicted average stent diameters by in-silico EVAR are too large compared to the postinterventional CT data with relative errors up to 25%. The average stent diameters of the deployed SG (blue, red and black curve) in the iliac SG parts are close to the nominal diameter (cyan curve) with exception of the regions of the distal landing zones (indicated by green color) where the SG is strongly compressed.

In summary, the mean and the standard deviation of the relative error ε are very similar for all three patients with $\mu_{\varepsilon,1} \pm \sigma_{\varepsilon,1} = 6.7 \pm 8.7\%$, $\mu_{\varepsilon,2} \pm \sigma_{\varepsilon,2} = 5.5 \pm 7.4\%$ and $\mu_{\varepsilon,3} \pm \sigma_{\varepsilon,3} = 5.0 \pm 8.2\%$. $\mu_{\varepsilon,(\Xi)}$ and $\sigma_{\varepsilon,(\Xi)}$ are the mean and the standard deviation of the relative error ε of all three SG parts of patient $\Xi \in \{1, 2, 3\}$ according to Equation (4.3) and (4.4). The total relative error over all patients and all SG parts is $\mu_{\varepsilon} \pm \sigma_{\varepsilon} = 5.6 \pm 8.1\%$ (cf. Table 4.2).

Considering the change of the average stent diameters induced by the blood pressure change, the average diameters of the stent at 80 mmHg ($\bar{d}_{\mathrm{sim}}^{\mathrm{S,diast}}(s_{\mathrm{De},(\Xi)}^{(\Theta)})$) (blue curve in Figure 4.4) are only slightly smaller than the average diameters of the stent at $130\ \mathrm{mmHg}$ ($\bar{d}_{\mathrm{sim}}^{\mathrm{S,sys}}(s_{\mathrm{De},(\Xi)}^{(\Theta)})$) (red curve in Figure 4.4).

4.3. Discussion

In this chapter, it was shown that the in-silico EVAR model is applicable to patient-specific geometries with bifurcated SGs. The qualitative comparison of the deployed stent configuration of in-silico EVAR and the deployed stent extracted from postinterventional CT data showed very good agreement despite the fact that certain model parameters, such as constitutive vessel parameters and the vessel wall thickness, are uncertain. Instead of fully patient-specific parameters, cohort-averaged and literature-based values had to be used.

Since the exact blood pressure state of the patients at time of the postinterventional CT scans is unknown, the average diameters of the deployed stent from in-silico EVAR at the assumed diastolic blood pressure of 80 mmHg and at the assumed systolic blood pressure of $130\ \mathrm{mmHg}$ were computed. The in-silico results at the systolic blood pressure can be seen as upper bound and the in-silico results at the diastolic blood pressure as lower bound when comparing to postinterventional CT data. However, the difference of the deployed stent diameters induced by the blood pressure change of 50 mmHg is rather small ($\mathrm{mean} \pm \mathrm{std} = 2.0 \pm 1.2\%$ at the proximal SG parts and $\mathrm{mean} \pm \mathrm{std} = 0.7 \pm 0.8\%$ at the iliac SG parts).

The newly developed quantitative validation methodology allowed to plot the average diameters of the stents from in-silico EVAR and the stents extracted from postinterventional CT data pseudo-continuously along the total length of the SG in the deployed state. The quantitative comparison of the average stent diameters of the deployed SG from in-silico EVAR and the average stent diameters from postinterventional CT data showed very good agreement for the proximal SG parts with the maximum error smaller than 12% and $\mu_\varepsilon^{\mathrm{P}} \pm \sigma_\varepsilon^{\mathrm{P}} = 6.4 \pm 3.4\%$ over all three patient-specific cases. The comparison of the iliac SG components showed good agreement with $\mu_\varepsilon^{\mathrm{L}} \pm \sigma_\varepsilon^{\mathrm{L}} = 2.1 \pm 9.3\%$ for the left iliac parts and $\mu_\varepsilon^{\mathrm{R}} \pm \sigma_\varepsilon^{\mathrm{R}} = 6.6 \pm 9.8\%$ for the right iliac parts. In total, the prediction of the stent diameters by the in-silico EVAR model led to slightly too large diameters compared to the stents extracted from postinterventional CT data. It was also shown that the in-silico EVAR model is able to properly reproduce nonuniform stent shapes such as a conical shape in the proximal landing zone. A conical stent shape means that the expansion diameter of the stent is not constant, i.e., the stent compression is larger at the location of smaller stent diameter than at the location of larger stent diameter. Mechanically, this results in higher contact tractions between SG and vessel as well as higher stresses in the stent at the location of large stent compression. In contrast to [205], only the comparison of stent diameters was used for validation of the in-silico EVAR model. The position of the stent limbs was not compared since pre- and postinterventional CT data generally are aligned in different coordinate systems. Hence, the results of the position comparison strongly depend on the quality of the registration between pre- and postinterventional CT data. As the order of the position comparison should be in the range of a few millimeters, this effect would dominate the results. In contrast to the position comparison, the diameter comparison is independent of the global position of the stent.

Although the preinterventional vessel diameters and the degree of SG oversizing in the proximal landing zone are in the same range for all three considered patients ($o = 17 - 20\%$, Appendix A.1), the deployed SG configurations of the three patient-specific cases are very different in the proximal landing zone. The SG diameter in the deployed state in the proximal landing zone of patient 1 with a mean diameter of $22.9\ \mathrm{mm}$ is significantly smaller than the corresponding SG diameters of patient 2 with a mean diameter of $25.9\ \mathrm{mm}$ and patient 3 with a mean diameter of $24.5\ \mathrm{mm}$. Here, the mean diameter corresponds to the in-silico EVAR results in the proximal landing zones at $130\ \mathrm{mmHg}$ blood pressure. One possible explanation is the highest degree of calcification of patient 1 compared to the other two patient-specific vessels. Calcifications are very stiff vessel constituents which reduce the widening of the vessel by the oversized SG. Thus, the deployed SG diameter is smaller. These different characteristics of the deployed SGs in the landing zones of potentially similar clinical cases (similar with respect to the SG device, the preinterventional proximal vessel diameter and the degree of SG oversizing) raise the need for patient-specific simulations which consider the patient-specific geometry of the vessel and which incorporate ILT and calcifications as additional vessel constituents. However, as in this study only three clinical cases were considered, these results do not allow for general conclusions.

4.4. Limitations

Apart from the basic model assumptions of the vessel model, the SG model and the in-silico SG P&D methodology stated in Section 3.7, this study is affected by the following limitations.

First, the resolution of patient-specific CT scans both of the preinterventional and postinterventional data limits the accuracy of both the prediction by in-silico EVAR and the validation using postinterventional CT data.

Second, the blood pressure at time of imaging had not been recorded. Hence, the blood pressure corresponding to the stent configuration segmented from postinterventional CT data is unknown. Instead, diastolic and systolic blood pressures are considered in in-silico EVAR and were used as lower and upper bound in the comparison between in-silico results and postinterventional CT data.

Third, the quantitative comparison of in-silico results and postinterventional CT data was based on average diameters only. In future work, the cross-sectional shape, such as the ovalization of stents, could be compared as well.

Finally, the validation study is only a comparison of the deployed stent configurations, i.e., a pure validation of the kinematic behavior. However, other important quantities such as vessel stresses or contact tractions between SG and vessel could not be directly validated by this validation methodology.

4.5. Conclusions

In this chapter, a qualitative and quantitative validation methodology has been developed, which is based on a comparison of average stent diameters between in-silico results and postinterventional CT data. The validation methodology measures average stent diameters pseudo-continuously along the total length of the deployed SG and is applicable to any SG device.

The validation of the in-silico EVAR model was performed for three patient-specific cases treated by Cook Zenith Flex/Spiral-Z® SGs. The good agreement between in-silico results and real-world postinterventional CT data with a total relative error in the prediction of the SG expansion diameter over all patients of $\mathrm{mean} \pm \mathrm{std} = 5.6 \pm 8.1\%$ makes the use of the in-silico EVAR model very promising.

5. Application to patient-specific cases: toward a predictive tool

EVAR as standard method of treating AAAs requires a complex preinterventional planning process which must be individually adapted to the patient-specific case. As the only patient-specific information for assessment of the applicability of EVAR, the SG selection and the SG sizing is the data obtained from medical imaging, this assessment is a great challenge, requires a lot of experience and is to a certain extent the subjective choice of the clinician (cf. Section 1.2). Due to the good predictive quality of in-silico EVAR, as demonstrated in Chapter 4, it can be a promising planning tool in the preinterventional planning phase of EVAR with versatile applications.

Available patient-specific in-silico EVAR studies are mostly restricted to the prediction of the deployed state of the SG and investigations directly associated to the predicted deployed state (cf. Section 1.3.4). However, the bridge to an advanced clinical application with a multivariate assessment of the in-silico EVAR outcome by several EVAR quality parameters, as proposed in Section 3.6.2, is rarely given. In this chapter, possible approaches for how the use of in-silico EVAR as objective tool can optimize the preinterventional planning process and hence reduce EVAR complication rates are investigated. The following three applications are illustratively demonstrated in this chapter to indicate the potential benefit of using in-silico EVAR in the preinterventional planning process of EVAR:

- Predictive assessment of the likelihood of EVAR related complications based on a subset of mechanical and geometric parameters as proposed in Section 3.6.2.
- Optimization of the SG selection from the portfolio of common commercial SG devices.
- Assessment of SG misplacement, i.e., assessment of the outcome if the SG is not perfectly placed at a location slightly distal to the branch-offs into the renal arteries.

This list of demonstrated applications of in-silico EVAR as predictive tool is by far not complete (cf. Section 1.2). Rather, the intention of this chapter is to show illustratively some major potential applications than provide a full overview. While the first two points test the applicability of EVAR and are aimed at giving the best possible outcome for the patient-specific case, the third point investigates the impact of potential non-ideal performance of the clinician during the EVAR intervention.

This chapter is structured as follows: in Section 5.1, the process chain to use in-silico EVAR as predictive tool is summarized. Afterwards in Section 5.2, the aforementioned applications of in-silico EVAR are illustratively shown. The results of Section 5.2 are discussed in Section 5.3. Finally, limitations and conclusions of this study regarding the application of in-silico EVAR as predictive tool for clinical cases are stated in Section 5.4 and Section 5.5, respectively.

The content of this chapter is largely based on work previously published by the author of the present thesis, namely [107, 108].

5.1. Methods

To use in-silico EVAR as predictive tool for clinical cases, a continuous and largely fully automated process chain is utilized, which is shown in Figure 5.1. The methodologies of the single steps of this process chain were stated in Chapter 3. In this section, only the sequence of the sequential steps of the process chain are summarized.

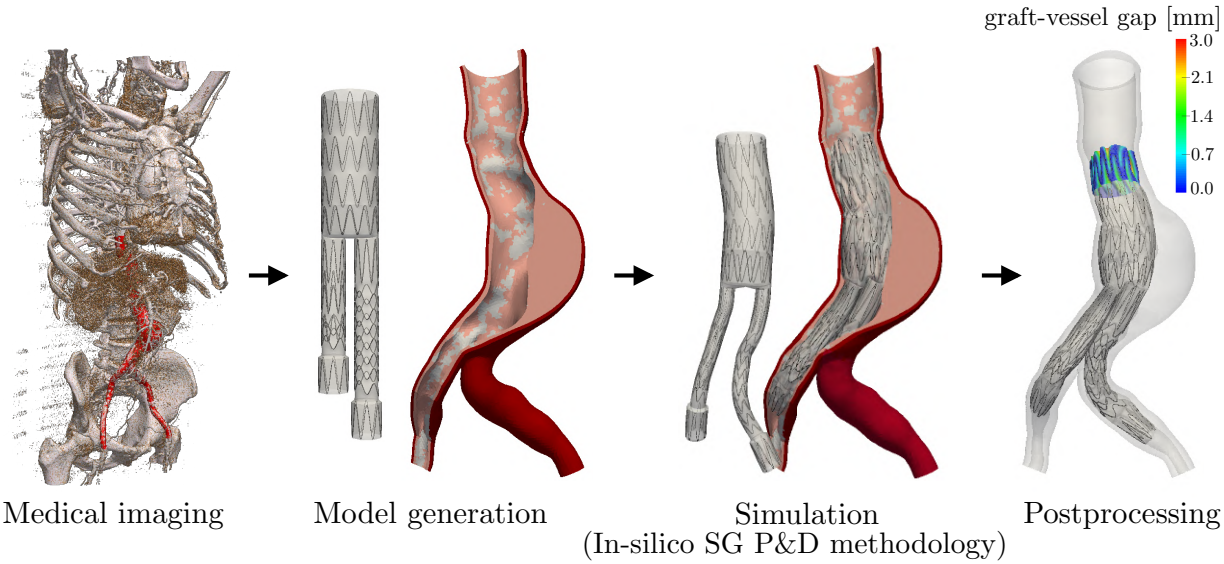

Figure 5.1 Process chain for the predictive use of in-silico EVAR in the preinterventional planning phase. Modified figure reproduced with permission from [108].

First, the patient-specific vessel geometry is semi-automatically segmented from preinterventional CT data using commercial segmentation software. Subsequently, a realistic vessel simulation model is fully automatically created from the segmented vessel geometry (cf. Section 3.3). The vessel model includes ILT and calcification and considers a physiological blood pressure state. Throughout this chapter, the systolic blood pressure state is considered which is assumed to be $p^{\mathrm{sys}} = 130\,\mathrm{mmHg}$. In addition, a SG model is generated fully automatically by specifying a SG device and a SG size (cf. Section 3.4). Afterwards, using the in-silico SG P&D methodology proposed in Section 3.5, the postinterventional vessel and SG configuration is predicted.

Based on the predicted postinterventional vessel and SG configuration, the complication likelihood after EVAR is estimated. For this purpose, geometric and mechanical parameters, such as SG induced tissue overstresses and the graft-vessel gap, are used (cf. Section 3.6). SG induced tissue overstresses are characterized by an overloading of the surrounding arterial wall. The gap between graft and the luminal vessel surface is a measure of the quality of seal between the SG and vessel in the SG landing zones. A large gap between SG and vessel in the landing zones increases the likelihood of type I endoleaks.

Four clinical cases are considered in this study with patient characteristics provided in Appendix A.1. The overview of the respective vessel and SG models is provided in Section 3.3 (cf. Figure 3.7) and Section 3.4 (cf. Figure 3.11), respectively.

Throughout this chapter, it is assumed that the most proximal $20\ \mathrm{mm}$ of the SG serve as proximal SG landing zone. Hence, in the calculation of EVAR quality parameters (cf. Section 3.6) related to the proximal landing zone, a length of $L_{\mathrm{prox}} = 20\ \mathrm{mm}$ is assumed for all patient-specific cases to obtain comparable results. For improved visualization of the results that correspond to the proximal landing zone, a projection of the results into the flat auxiliary $\breve{X}\breve{Z}$-plane is used in the presentation of the results. The auxiliary $\breve{X}\breve{Z}$-plane represents the uncoiled lateral surface of a virtual cylinder with radius $\breve{R} = 15\ \mathrm{mm}$ (cf. Appendix A.8), where $\breve{X}$ describes the circumferential direction of the SG and $\breve{Z}$ describes the axial direction of the SG with positive values of $\breve{Z}$ pointing in proximal direction of the SG.

5.2. Illustrative applications and selected results

In this section, three different applications of in-silico EVAR as patient-specific, predictive tool are presented. First, in Section 5.2.1, the complication likelihood is estimated by considering four patient-specific cases. Then, in Section 5.2.2, it is demonstrated how in-silico EVAR can be used to assist the clinician in the selection of the most suitable SG device during the preinterventional planning process. Finally, the influence of a potential SG misplacement in the medical intervention is assessed for one patient-specific case in Section 5.2.3.

5.2.1. Assessment of EVAR complication likelihoods

For the sake of clarity, in the following only the results with regard to some EVAR quality parameters are presented. Since this section is supposed to demonstrate the idea of how in-silico EVAR can be used to predict the patient-specific complication likelihood, it is not essential to evaluate the four patient-specific cases with respect to all EVAR quality parameters proposed in Section 3.6.2. First, in Section 5.2.1.1, the in-silico EVAR outcome is assessed with respect to the postinterventional configuration of SG and vessel. Then, SG induced tissue overstresses are considered in Section 5.2.1.2. Finally, it is focused on some EVAR quality parameters related to the SG landing zone in Section 5.2.1.3.

5.2.1.1. Postinterventional configuration of stent-graft and vessel

In Figure 5.2, the postinterventional configuration of the elastically deformable vessel and SG model based on in-silico EVAR are presented for an internal blood pressure of $p^{\mathrm{sys}} = 130\ \mathrm{mmHg}$. For patient 2, 3 and 4, radial graft buckling is only apparent in the proximal and distal landing zones and longitudinal graft buckling in the curved iliac parts. In contrast, for patient 1 radial graft buckling is apparent across almost the entire SG since the SG is in contact with the ILT even in the aneurysm sac. Additionally, patient 1 possesses the highest degree of calcification, i.e., additional stiffening of the vessel, which may reduce the widening of the vessel by the SG and may lead to increased buckling of the SG. The SG almost fully adapts to the vessel geometry in all four cases, i.e., straightening of the vessel is insignificantly small even in

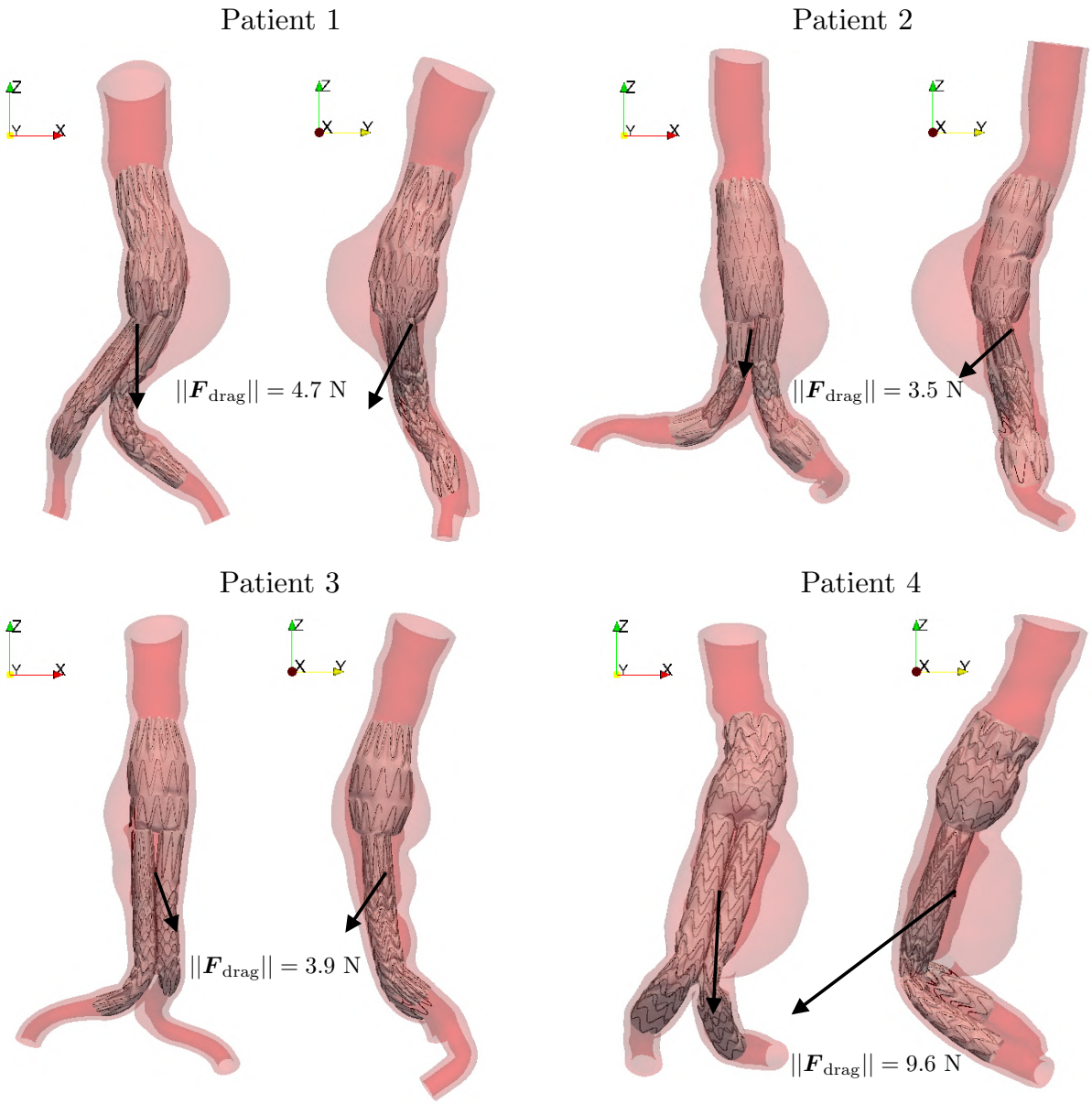

Figure 5.2 Postinterventional SG and vessel configurations as well as SG drag force $\boldsymbol{F}_{\text{drag}}$ of the four patient-specific cases for an internal blood pressure of $p^{\text{sys}} = 130$ mmHg.

the strongly angulated iliac arteries. In case of patient 4, slight SG kinking at the bifurcation into the iliac arteries is visible due to high angulation of the iliac arteries and a luminal narrowing at this location.

The SG drag force, as defined in Equation (3.104), is directly related to the deployed SG configuration since it is the integration of the spatially constant hydrostatic blood pressure over the luminal surface of the SG in the deployed state. Substantial differences in the magnitude of the SG drag force are visible in Figure 5.2. While patient 2 reveals the smallest SG drag force ($||\boldsymbol{F}_{\text{drag}}|| = 3.5$ N), patient 4 shows a relatively large SG drag force ($||\boldsymbol{F}_{\text{drag}}|| = 9.6$ N) that may indicate an increased likelihood of SG migration. This is mainly due to the high angulation of

the iliac arteries of patient 4 with respect to the proximal part of the vessel. While the magnitude of the SG drag force is substantially different among the four patient-specific cases, the direction of the SG drag force is orientated in anterior (negative Y-direction) and distal direction (negative Z-direction) in all four patient-specific cases.

5.2.1.2. Tissue overstress after EVAR

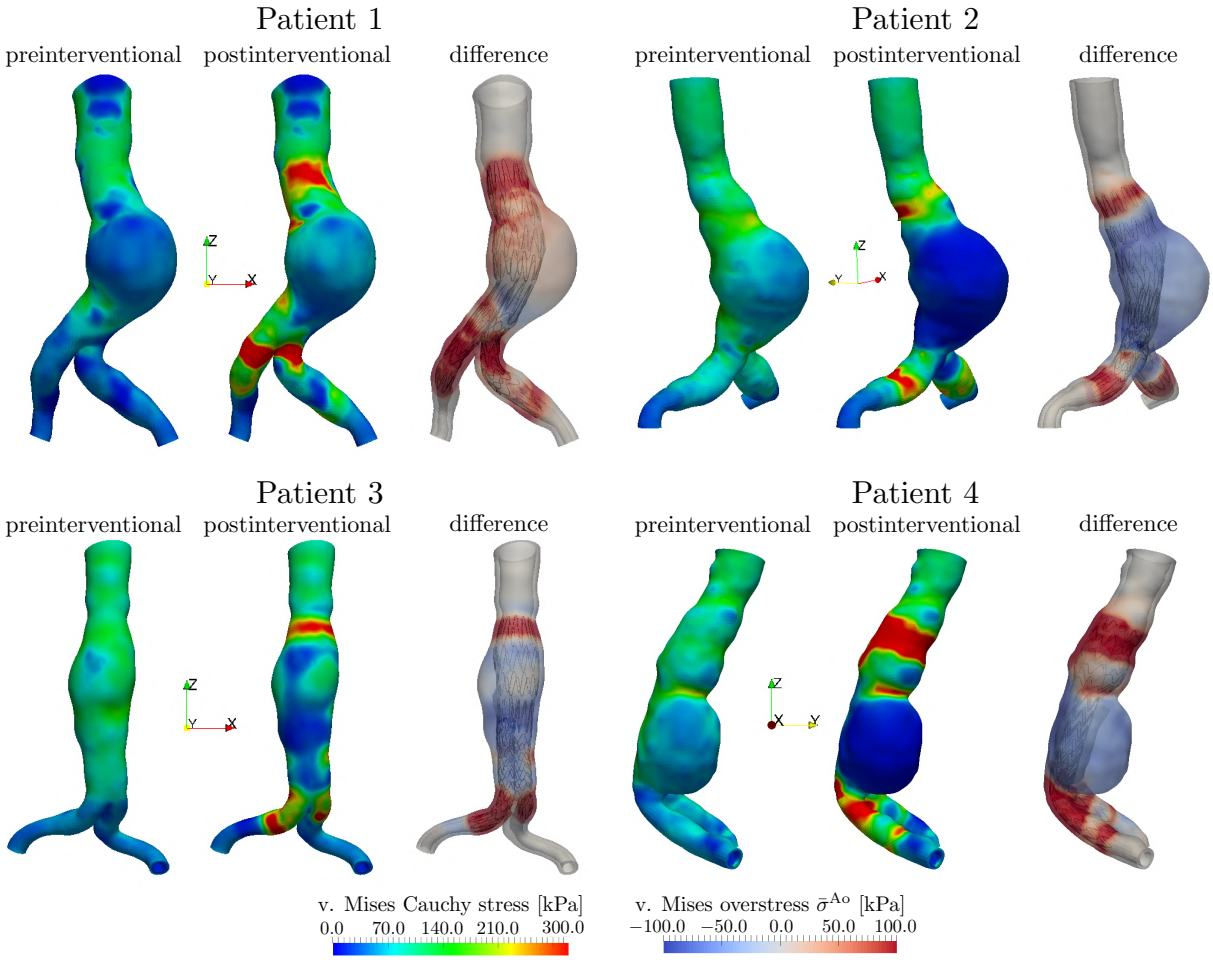

Figure 5.3 Preinterventional and postinterventional vessel stresses as well as SG induced vessel overstresses $\bar{\sigma}^{\mathrm{Ao}}$. Modified figure reproduced with permission from [107].

In Figure 5.3, preinterventional and postinterventional vessel stresses at the systolic blood pressure state of $p^{\mathrm{sys}} = 130\ \mathrm{mmHg}$ are shown. Furthermore, vessel overstresses $\bar{\sigma}^{\mathrm{Ao}}$ being the difference between the post- and preinterventional stresses, as defined in Section 3.6.2.1, are visualized. Positive overstresses characterize regions of the arterial wall in which the postinterventional tissue stresses are larger than the preinterventional tissue stresses. Negative overstresses indicate regions in which the tissue stresses before EVAR are larger than the tissue stresses after EVAR.

The insertion of the SG yields vessel stresses above $300\ \mathrm{kPa}$ in the proximal and distal landing zones in the model of all four patient-specific cases as well as in the highly curved iliac parts

of patient 1. In all four patient-specific cases local tissue overstresses $\bar{\sigma}^{\mathrm{Ao}}$ of up to $100\ \mathrm{kPa}$ exist mainly in the proximal and distal landing zones where passive fixation by SG oversizing is desired. The insertion of the SG reduces the wall stresses in the aneurysm sac in case 2, 3 and 4. In case of patient 2 and 4, the SG is not in contact with the ILT in the aneurysm sac. Hence, the load on the vessel wall is fully removed resulting in zero vessel stresses in the aneurysm sac. In case of patient 1 the luminal diameter in the aneurysm sac is relatively small due to a relatively thick ILT layer. This means the SG is almost fully in contact with the ILT in the aneurysm sac. Therefore, the wall stresses in the aneurysm sac do not decrease in the model.

5.2.1.3. A focus on the landing zone

In Figure 5.4, geometrical and mechanical characteristics of the proximal SG landing zone in the deployed state are visualized for the four patient-specific cases. The graft-vessel gap $z_{\max}^{\mathrm{GA}}$ and the sealing pattern as introduced in Section 3.6.2.3 are shown to investigate the quality of seal in the proximal landing of the four patient-specific cases. Further, the normal contact pressure is considered to assess how uniformly the SG is pressed against the vessel.

All four models of the patient-specific cases have in common that the SG is mainly attached to the luminal vessel surface at the locations where the stent rings are attached to the graft. This results from the radial buckling of the graft whose buckling pattern is mainly driven by the shape of the stent rings. At locations of the graft where the stent rings are attached, the relatively stiff stent wires prevent the graft from buckling. Hence, if radially compressed the graft buckles mainly in-between the stent wires. While patient 3 and 4 show a very uniform attachment of the SG to the luminal vessel surface for the total lateral surface of the SG in the proximal landing zone with no severe graft-vessel gaps, the SG-vessel attachment in case of patient 1 and 2 is much more nonuniform.

The in-silico deployment of the SG model in the vessel geometry of patient 1 reveals one region of relatively large graft-vessel gaps of up to $z_{\max}^{\mathrm{GA}} = 5\ \mathrm{mm}$ in which the likelihood of a type I endoleak may be increased. In this region, the stent ring is not able to fully attach to the luminal vessel surface inducing relatively large gaps between SG and vessel.

Without showing large graft-vessel gaps, the SG-vessel attachment of patient 2 is nonuniform. At one side ($\breve{X} > 0$) the SG is almost fully in contact with the luminal vessel surface, i.e., only very little graft buckling is present. This means that at this side, graft-vessel gaps are mainly zero. In total, this leads to the largest SG fixation area $a_{\mathrm{prox}}^{\mathrm{seal}}$ in the proximal landing zone of all four patient-specific cases. The SG fixation area $a_{\mathrm{prox}}^{\mathrm{seal}}$ as introduced in Equation (3.106) defines the area of the outer graft surface in the SG landing zone that is in contact with the luminal vessel surface. However, the normal contact pressure p_{n} between SG and luminal vessel surface is relatively small on this side ($\breve{X} > 0$) as well. This means that although the SG fixation area $a_{\mathrm{prox}}^{\mathrm{seal}}$ is relatively large, the force transmission between SG and vessel, which is required for the passive fixation of the SG in the landing zone, is small. Consequently, although patient 2 has the largest fixation area $a_{\mathrm{prox}}^{\mathrm{seal}} = 790\ \mathrm{mm}$ in the proximal landing zone, the SG fixation force $\hat{F}_{\mathrm{prox}} = 51.0\ \mathrm{N}$ as defined in Equation (3.105) is the smallest of all four patient-specific cases. If the SG simultaneously is subjected to large drag forces (cf. Figure 5.2), this circumstance may be an indicator that patient 2 is subject to an increased likelihood of SG migration.

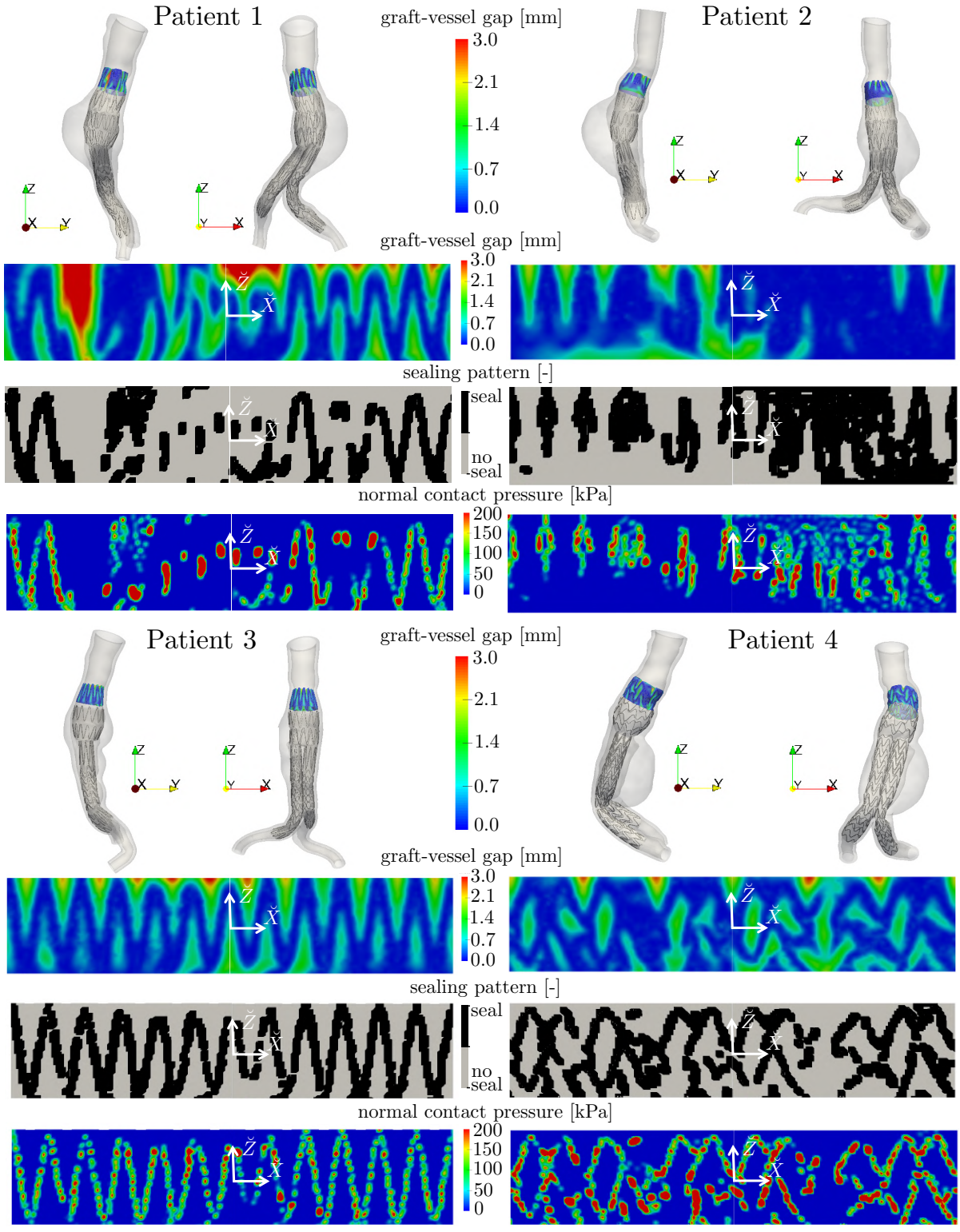

Figure 5.4 EVAR quality parameters in the proximal SG landing zone: graft-vessel gap, sealing pattern and normal contact pressure between SG and luminal vessel surface. Representation in 3D and in the auxiliary $\check{X}\check{Z}$-plane (cf. Appendix A.8).

5.2.2. Assistance in stent-graft device selection

The clinician usually has to choose the SG from a large portfolio of different SG manufacturers and different SG sizes, where the final choice of the SG is to a large extent the subjective decision of the clinician. How in-silico EVAR can make this SG selection more objective and optimized is demonstrated in Figure 5.5 by comparing the in-silico EVAR outcome of two different SG devices (stent-graft A and B) in the same patient-specific vessel geometry of patient 1. To represent a realistic setting, SG models of two different manufacturers are compared, where the SG sizing is based on the manufacturer's IFU. Based on the IFU of manufacturer A, a SG with a proximal diameter of $D^{\mathrm{SG}} = 30\ \mathrm{mm}$ is used for patient 1. Based on the IFU of manufacturer B, a SG with a proximal diameter of $D^{\mathrm{SG}} = 32\ \mathrm{mm}$ is recommended for the same patient-specific vessel. The clinician now has to decide which of the two SGs represents the better solution for patient 1.

Remark. *In this section, the comparison is restricted to the comparison between two different SG devices of different SG manufacturers. However, in a similar manner the in-silico assistance in the SG device selection could be extended by comparing different SG sizes, such as different SG diameters or different SG lengths. Since the influence of SG sizing is extensively studied in Chapter 6 and in order to not repeat results in this thesis, the comparison of different SG sizes is skipped here.*

In the following comparison, only selected EVAR quality parameters are considered. In Figure 5.5, the quality of seal in the proximal landing zone of the two SG devices is compared. While stent-graft A results in a slight stent collapse in the proximal landing zone, stent-graft B provides a very good and uniform seal. The stent collapse of stent-graft A results in a region in the proximal landing zone where the SG is incapable of properly attaching to the luminal vessel surface. The occurrence of stent collapse depends on many factors such as the degree of SG oversizing, the SG design and the morphology of the vessel in the landing zone. While in general SGs with large SG oversizing are rather prone to stent collapse [135, 247], in this example, the SG with a smaller SG oversizing (stent-graft A) is associated with stent collapse. Due to the larger stent height of stent-graft A compared to stent-graft B, stent-graft A rather tends towards a stent collapse in the vessel geometry of patient 1. Based on the results of the quality of seal in the proximal landing zone of patient 1, the likelihood of a type I endoleak could be higher using stent-graft A than with stent-graft B.

The stent ring height of stent-graft B is smaller. Therefore, in case of stent-graft B two stent rings are attached to the graft in the region of the proximal landing zone of assumed length of $20\ \mathrm{mm}$. In contrast, in case of stent-graft A only one stent ring of larger stent height is attached to the graft in the region of the proximal landing zone. Additionally, stent-graft B leads to substantially larger normal contact tractions between SG and luminal vessel surface, which may be associated with both the additional stent ring in the proximal landing zone and the larger degree of SG oversizing of stent-graft B compared to stent-graft A. The substantially larger normal contact tractions of stent-graft B induce an approximately twofold greater SG fixation force $\hat{F}_{\mathrm{prox}}$ in the proximal landing zone compared to stent-graft A. Since the SG drag force $\boldsymbol{F}_{\mathrm{drag}}$ does not substantially vary between the two SG devices, the likelihood of SG migration may be higher using stent-graft A than using stent-graft B for patient 1.

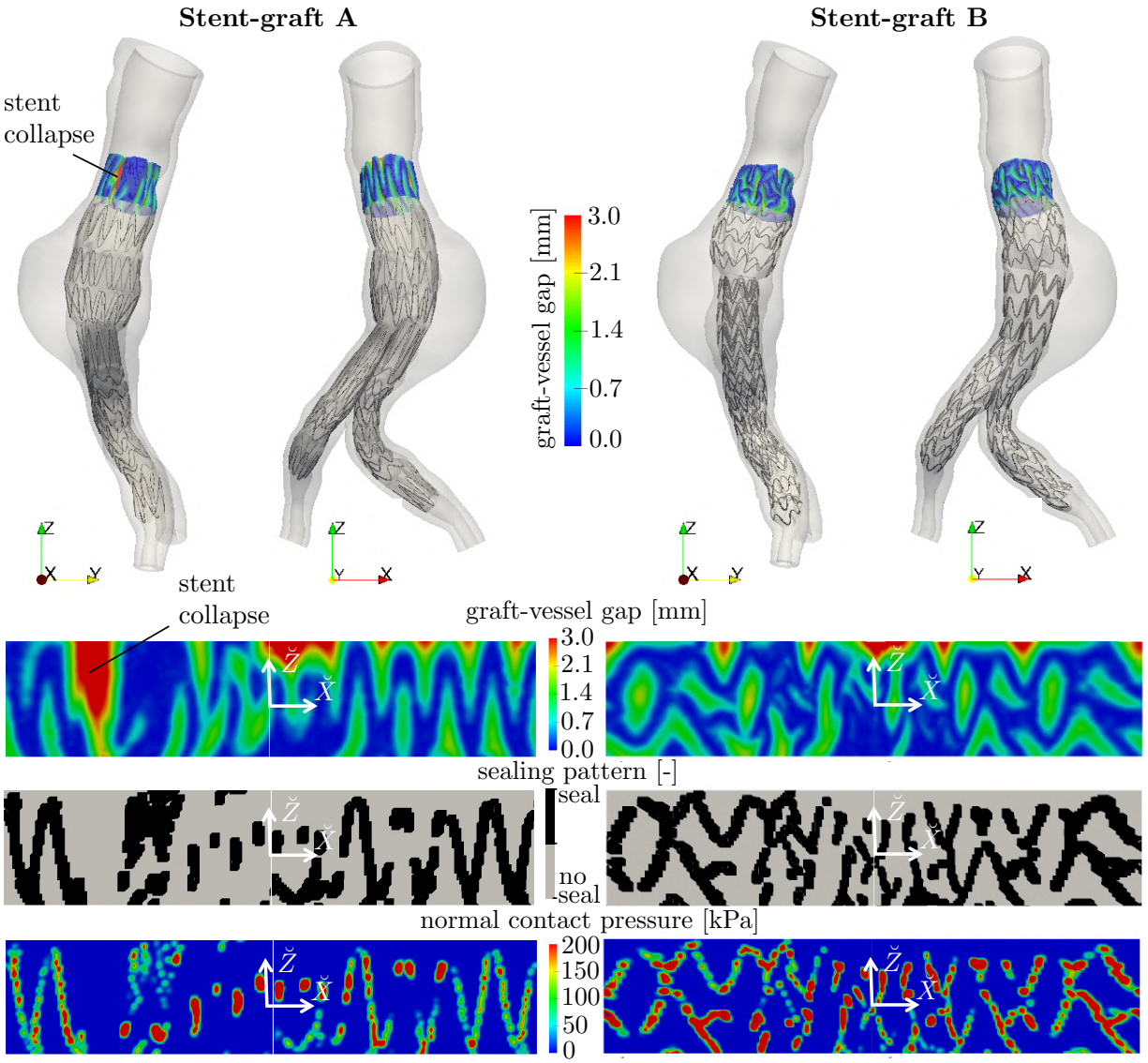

Figure 5.5 Comparison of the performance in the proximal landing zone of two different SG devices deployed in the patient-specific vessel of patient 1. Representation in 3D and in the auxiliary $\check{X}\check{Z}$-plane (cf. Appendix A.8). Modified figure reproduced with permission from [108].

5.2.3. Assessment of stent-graft misplacement

The proximal landing zone is proximally limited by the branch-offs into the renal arteries that must not be occluded by the covered part of the SG. Since a sufficiently long SG landing zone is a prerequisite for a proper seal and fixation of the SG, in an ideal medical EVAR intervention the SG should be placed directly distal to the most inferior renal artery to achieve the maximum possible length of the proximal landing zone. The medical EVAR procedure is performed under permanent pulsatile blood flow. Further, fluoroscopy imaging is used to be able to position the SG. Both limited resolution of intrainterventional medical imaging and the pulsatile forces on the SG resulting from the blood flow hamper the exact placement of the SG directly distal to the most inferior renal artery. Since occlusion of the renal arteries by the covered part of the SG is a

severe complication that requires secondary interventions [26, 104], the clinician rather tends to place the SG a bit more distally to ensure that the renal arteries are not covered. However, such a conservative placement of the SG leaves certain portions of the valuable potential length of the proximal landing zone unused. How this shortened length of the proximal landing zone influences the quality of the EVAR outcome is illustratively demonstrated in this section considering the vessel geometry of patient 2.

In Figure 5.6, the impact of SG misplacement in distal direction is visualized for patient 2. The SG misplacement of x_{mis} is measured from the most inferior renal artery as visualized in Figure 5.6, detail Z. The renal arteries visualized in Figure 5.6 are not part of the vessel model but are only used for better visualization of the SG misplacement measure x_{mis}. The in-silico EVAR results of a SG placed perfectly distal to the most inferior renal artery, i.e., $x_{\mathrm{mis}} = 0\ \mathrm{mm}$ (blue), a SG placed $x_{\mathrm{mis}} = 5\ \mathrm{mm}$ distal of the perfect position (green) and a SG placed $x_{\mathrm{mis}} = 10\ \mathrm{mm}$ distal of the perfect position (red) are opposed.

Remark. *Using a SG misplacement $x_{\mathrm{mis}} > 0$, actually, the overlap lengths of the three SG components should be increased so as not to cover the bifurcation into the internal iliac arteries by the distal ends of the iliac SG legs. However, since the focus of this example is only on the evaluation of the proximal landing zone, the overlap lengths of the three SG components is kept constant independent of the SG misplacement x_{mis}.*

In Figure 5.6, a clear impact of the SG misplacement x_{mis} on the in-silico EVAR outcome is visible, both qualitatively and quantitatively. Qualitatively, the sealing pattern of the three cases $x_{\mathrm{mis}} = 0\ \mathrm{mm}$, $x_{\mathrm{mis}} = 5\ \mathrm{mm}$ and $x_{\mathrm{mis}} = 10\ \mathrm{mm}$ are compared for the most proximal $20\ \mathrm{mm}$ of the SG model. While in the case of $x_{\mathrm{mis}} = 0\ \mathrm{mm}$, i.e., perfect placement of the SG, seal is given almost over the full assumed axial length $L_{\mathrm{prox}} = 20\ \mathrm{mm}$ of the proximal landing zone, the sealing is clearly reduced in the case of a SG misplacement of $x_{\mathrm{mis}} = 5\ \mathrm{mm}$ and $x_{\mathrm{mis}} = 10\ \mathrm{mm}$ (sealing pattern in Figure 5.6). For a SG misplacement of $x_{\mathrm{mis}} = 10\ \mathrm{mm}$, only the most proximal $5\ \mathrm{mm}$ of the SG provide seal which may not be sufficient. Since in case of $x_{\mathrm{mis}} > 0$, the considered most proximal $20\ \mathrm{mm}$ of the SG are placed already in the dilated part of the aorta, i.e., at the proximal shoulder of the AAA, the SG is not fully in contact with the aorta. This impact of SG misplacement on patient 2 is also visible when comparing quantitatively the proximal fixation area $a_{\mathrm{prox}}^{\mathrm{seal}}$, i.e., the area of the SG that is in contact with the vessel in this proximal region of $L_{\mathrm{prox}} = 20\ \mathrm{mm}$ length (black area in the sealing pattern of Figure 5.6). While for a perfect placement ($x_{\mathrm{mis}} = 0\ \mathrm{mm}$), a fixation area of $a_{\mathrm{prox}}^{\mathrm{seal}} = 790\ \mathrm{mm}^2$ is given, for $x_{\mathrm{mis}} = 10\ \mathrm{mm}$ the fixation area reduces to $a_{\mathrm{prox}}^{\mathrm{seal}} = 640\ \mathrm{mm}^2$ (cf. Figure 5.6).

The impact of the SG misplacement for patient 2 is even more severe if the normal contact pressure p_{n} and the fixation force $\hat{F}_{\mathrm{prox}}$ are considered in the proximal landing zone of the deployed SGs. The reduced fixation area $a_{\mathrm{prox}}^{\mathrm{seal}}$ in combination with reduced normal contact pressures p_{n}, potentially resulting from the reduced degree of SG oversizing in the dilated part of the aorta, results in a substantially smaller SG fixation force $\hat{F}_{\mathrm{prox}}$ for $x_{\mathrm{mis}} > 0$. While the perfectly placed SG ($x_{\mathrm{mis}} = 0\ \mathrm{mm}$) results in a proximal fixation force of $\hat{F}_{\mathrm{prox}} = 51\ \mathrm{N}$, the SG with misplacement of $x_{\mathrm{mis}} = 10\ \mathrm{mm}$ results only in a SG fixation force of $\hat{F}_{\mathrm{prox}} = 25\ \mathrm{N}$ (cf. Figure 5.6).

Consequently, a substantially reduced quality of seal and reduced SG fixation are given for patient 2 in the case of a certain SG misplacement. Hence, such a predictive assessment of the

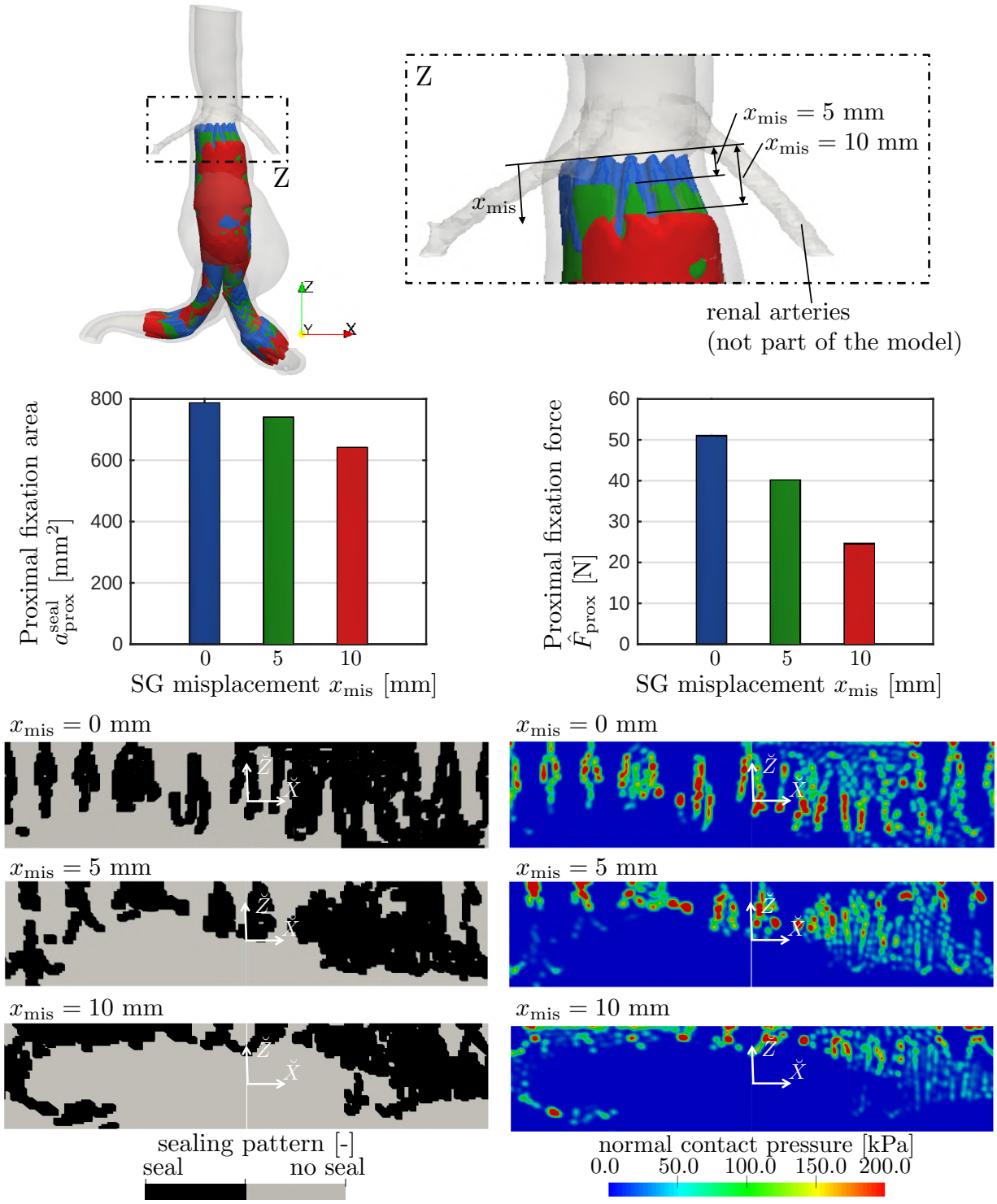

Figure 5.6 Comparison of the in-silico EVAR outcome in the proximal landing zone of patient 2 for SG misplacement of $x_{\text{mis}} = 0$ mm, $x_{\text{mis}} = 5$ mm and $x_{\text{mis}} = 10$ mm in distal direction. The SG misplacement x_{mis} is measured from the most inferior renal artery. Representation in 3D and in the auxiliary $\breve{X}\breve{Z}$-plane (cf. Appendix A.8).

impact of SG misplacement by in-silico EVAR can indicate already in the preinterventional planning phase that the clinician should focus especially on achieving exact placement of the SG. Otherwise the EVAR related complication likelihood of for instance type I endoleaks or SG migration may be substantially increased.

5.3. Discussion

In this chapter, potential applications of in-silico EVAR as predictive tool in the preinterventional planning phase were illustratively demonstrated. Application of the EVAR quality parameters, that were introduced in Section 3.6.2, to four patient-specific cases showed substantial differences in the SG drag force resulting from the internal blood pressure. In all four patient-specific cases, the drag force is mainly pointing in the anterior and distal directions. This finding is similar to most CFD and FSI studies on SG drag forces (e.g., [75, 187]), which in contrast to this study also considered shear forces acting on the SG.

Using in-silico EVAR, it was shown that the insertion of the SG reduced the vessel stresses in the aneurysm sac and led to instant shrinkage of the sac diameter in three of four cases. Shrinkage of the sac diameter is often considered as evidence of clinical success [70, 243] as this is an indicator that the luminal pressure is removed from the AAA wall. However, local tissue overstresses of up to $100\ \mathrm{kPa}$ could be observed in the SG landing zones, which can lead to negative effects such as tissue remodeling and aortic neck dilatation [142, 245, 267].

A focus on the landing zone revealed insights into the sealing pattern and gaps between graft and vessel in the deployed state of the four patient-specific cases. However, it is important to note, that large gaps between graft and vessel do not necessarily mean that this is a source of a type I endoleak. It only indicates that in this case the likelihood of developing an endoleak may be increased. In the landing zone, the SG is usually oversized with respect to the luminal vessel diameter, which induces radial buckling of the graft. Since graft buckling can also lead to relatively large graft-vessel gaps of a few millimeters, which may not be severe for the detection of endoleaks, the stent-vessel gap as introduced in Equation (3.108) may be a better measure for the detection of stent collapse and the associated increased risks of type I endoleaks.

The comparison of two commercial SGs in the same patient-specific vessel geometry was presented and it was indicated how this comparison with respect to EVAR quality parameters can support the clinician in the SG selection during the preinterventional planning process. In this illustrative example, only two SG devices were compared. However, in a clinical setting this process is even more complex and multivariate comparison, where not only the SG device but also the SG size must be considered.

Misplacement of the SG during the medical EVAR intervention is discussed in the literature mainly with respect to misplacement in proximal direction, i.e., coverage of renal arteries and resulting renal ischemia [26, 168]. However, the influence of SG misplacement in distal direction, where parts of the potential proximal landing zone remain unused, is insufficiently discussed in the literature. For the studied patient-specific case, SG misplacement in distal direction showed a crucial impact on the quality of the in-silico EVAR outcome. A SG misplacement in distal direction of $10\ \mathrm{mm}$ lead to a substantial decrease in the fixation area and the proximal SG fixation force for the considered patient-specific case. The main reason for this finding is that the most proximal parts of the SG, that are supposed to build the sealing zone, are partly positioned in the

dilated part of the vessel. Hence, only a small portion of the SG is in contact with the vessel in the potential landing zone. Further, the degree of SG oversizing is much smaller in the dilated part of the vessel which usually induces smaller SG fixation forces. The relation between SG oversizing and SG fixation forces will be studied in detail in Chapter 6. However,the extent to which the quality of seal and the SG fixation are reduced by SG misplacement in distal direction strongly depends on the vessel geometry of the patient-specific case and should be assessed individually in the preinterventional planning phase. Especially in the case of a short proximal neck length, the impact of SG misplacement in distal direction may be essential.

5.4. Limitations

Besides the basic assumptions stated in Section 3.7, this illustrative study on the application of in-silico EVAR as predictive tool is subject to the following limitations. First, the in-silico EVAR model used to predict the postinterventional SG and vessel geometry so far was only validated with respect to the postinterventional stent configuration (cf. Chapter 4), i.e., with respect to its kinematic behavior. However, direct validation of the mechanical and geometrical EVAR quality parameters that were used to assess the quality of the EVAR outcome has not yet been performed. Validation of these mechanical and geometrical parameters is technically impossible or at least extremely challenging with respect to the development of suitable experiments for validation.

Second, in this chapter, the EVAR quality parameters were considered separately. However, for the assessment of the overall likelihood of EVAR related complications, these parameters need to be considered in combination with one another. For instance, large SG drag forces do not necessarily mean that the likelihood of SG migration is large so long as the SG fixation forces are large enough to resist these SG drag forces. However, a valid metric using these EVAR quality parameters in combination first needs to be developed in future studies. The metric combining these mechanical and geometrical parameters should group the in-silico EVAR results in the range between “high risk of complications” and “no risk of complications” and thus make the in-silico EVAR outcome easily interpretable by a clinician.

Finally, setting up the computational model is a largely automated process. Nevertheless, the semi-automated segmentation process of the patient-specific vessel geometry required approximately 3 h per patient and should be further automated for clinical applicability. Running the simulations required approximately 36 h per patient on 112 cores (Intel Haswell nodes, SuperMUC, Leibniz Supercomputing Centre). Algorithmic optimizations and model reduction techniques [4] should be considered in future studies to use in-silico EVAR as predictive tool in clinical practice.

5.5. Conclusions

As a first step toward a patient-specific, predictive tool, in-silico EVAR was applied to four clinical cases with bifurcated SGs and sophisticated models of the vessel that include ILT, calcifications and an anisotropic, hyperelastic material model for the vessel wall. Patient-specific AAAs have extreme variance in their geometric characteristics. Since the optimal treatment of the AAA depends strongly on the vessel geometry, preinterventional planning of EVAR requires

personalized medicine where decisions regarding the treatment process need to be adapted to the patient-specific case. This study provided basic ideas of how in-silico EVAR can improve these individual decisions and hence reduce EVAR related complication rates.

6. In-silico EVAR study of parameterized vessel and stent-graft models

EVAR requires SG devices that interact perfectly with the vessel such that the aneurysm sac is permanently excluded from the main blood flow and the AAA is prevented from rupture. Especially in case of unfavorable vessel geometries, EVAR may fail or lead to possible secondary interventions. In contrast, EVAR is considered to be successful if the aneurysm stays excluded and has no expansion for several years after the intervention. Reasons for immediate or long-term failure of EVAR are difficult to identify, but both wrong SG sizing [46, 143, 245, 257] and inappropriate vessel geometries [63, 233, 275] are frequent explanations in literature.

The objective of this chapter is to investigate the influence of the vessel and SG geometry on EVAR outcomes from an engineering perspective. A large parameter study of parameterized vessels and SGs may help to give answers to open question such as the best value for SG oversizing [34, 257] depending on the vessel geometry. It may provide clarification on specific questions, such as whether excessive SG oversizing can compensate the drawbacks of EVAR in unfavorable aortic morphologies. This hypothesis is presumed by van Keulen et al. [256] whereas Canaud et al. [34] report adverse effects of excessive SG oversizing especially in unfavorable aortic morphologies such as large neck angles.

Some studies (e.g., [6, 7, 53, 206, 212]) have already been conducted to evaluate the influence of vessel and SG parameters on EVAR outcomes based on in-silico approaches (cf. Section 1.3.4). However, most of these studies used only a very limited number of EVAR quality parameters and a very limited number of variations of the vessel and SG geometry. De Bock et al. [53] varied the neck angle, the SG position and the degree of SG oversizing in a full factorial analysis of in total 72 simulations in an angulated tube-shaped vessel with linear elastic material properties and without consideration of ILT and calcifications. To asses the quality of the EVAR outcome, they defined four EVAR quality parameters.

In this chapter, a full parameterization of an AAA by 16 parameters is proposed. Furthermore, a full parameterization of a SG by seven parameters is used. The deployed state of the elastically deformable SG in a hyperelastic, anisotropic vessel with consideration of ILT and calcifications is approximated by the in-silico SG P&D methodology presented in Chapter 3. The in-silico EVAR outcome is investigated at the diastolic as well as at the systolic blood pressure state by consideration of several mechanical and geometrical parameters to assess the quality of the in-silico EVAR outcome with respect to EVAR complication likelihoods. These mechanical and geometrical parameters have been introduced in Section 3.6.2 and are denoted as *EVAR quality parameters*. In total, 146 EVAR simulations of 146 different realizations of the parameters of the vessel and the SG are performed. For each of these EVAR simulations, SG parameter con-

tinuation (Section 3.5.3) is used to investigate SG oversizing between 5% to 40% in a computationally efficient way. A large statistical analysis of the influence of vessel and SG parameters, inlcuding the degree of SG oversizing, on the EVAR quality parameters is given in this chapter. Furthermore, the impacts of specific parameters, such as the influence of patient-specific vessel uncertainties [23], the influence of aortic neck calcification and the influence of the aortic blood pressure state on the quality of the in-silico EVAR outcome are investigated in this chapter.

This chapter is structured as follows: in Section 6.1, a full parameterization of vessel and SG is defined and the framework of the proposed parameter study is described. In Section 6.2, the results of the parameter study are evaluated statistically, quantitatively and qualitatively. The discussion of these findings is done in Section 6.3. Finally, limitations and conclusions of this study are provided in Section 6.4 and 6.5, respectively.

This chapter is a revised version of the previously published work by the author of this thesis, namely [109].

6.1. Methods

In the following, first a full parameterization of the vessel (Section 6.1.1) by 16 parameters and a full parameterization of a tube SG (Section 6.1.2) by 7 parameters are presented. Subsequently, the framework of the proposed parameter study is outlined in Section 6.1.3.

6.1.1. Vessel parameterization

Although most EVAR related complications are associated with inappropriate conditions at the aortic neck, a realistic representation of the total AAA is used due to two main reasons. First, some EVAR quality parameters, such as the SG drag force and the mean diametric graft compliance, require the consideration of the total aorta covered by the SG and not only the neck region (cf. Section 3.6.2). Second, all results presented in this study shall be transferable to real, patient-specific cases. Nevertheless, this study is restricted to an AAA and a SG without bifurcation into the iliac arteries to reduce the complexity of the vessel and SG parameterizations.

The proposed parameterized vessel is rotationally symmetric around the plane and smooth curve $\mathcal{C}^{\mathrm{Ao}}(s) \subset \mathbb{R}^2$, which is a higher order spline (Trelis 15.1, Csimsoft, Utah) in the global XY-plane through the five points $\mathrm{E_p}$, $\mathrm{S_p}$, O, $\mathrm{S_d}$, $\mathrm{E_d}$ according to Figure 6.1I. The locations of the five points are defined by the seven parameters: proximal neck angle α_{p}, distal neck angle α_{d}, proximal neck length l_{p}, distal neck length l_{d}, proximal eccentricity e_{p}, distal eccentricity e_{d} and aneurysm length l_{AAA}. Further, the three-dimensional representation of the vessel is defined by the six parameters: proximal neck diameter d_{p}, distal neck diameter d_{d}, AAA diameter d_{AAA}, proximal shoulder length l_{sp}, distal shoulder length l_{sd}, vessel wall thickness t_{w} and maximum ILT thickness t_{ILT}. The proximal shoulder length l_{sp} and the distal shoulder length l_{sd} define the length of the transition zone between the diameter of the "aneurysmatic" vessel and the "healthy" vessel in the neck and the distal part, respectively.

The luminal region is rotationally symmetric around the plane curve $\hat{\mathcal{C}}^{\mathrm{Ao}}(\hat{s}) \subset \mathbb{R}^2$ through the five points $\mathrm{E_p}$, $\mathrm{S_p}$, $\hat{\mathrm{O}}$, $\mathrm{S_d}$, $\mathrm{E_d}$ according to Figure 6.1II where the point $\hat{\mathrm{O}}$ is shifted by the eccentricity e_{l} with respect to the point O. The eccentricity e_{l} of the luminal centerline is

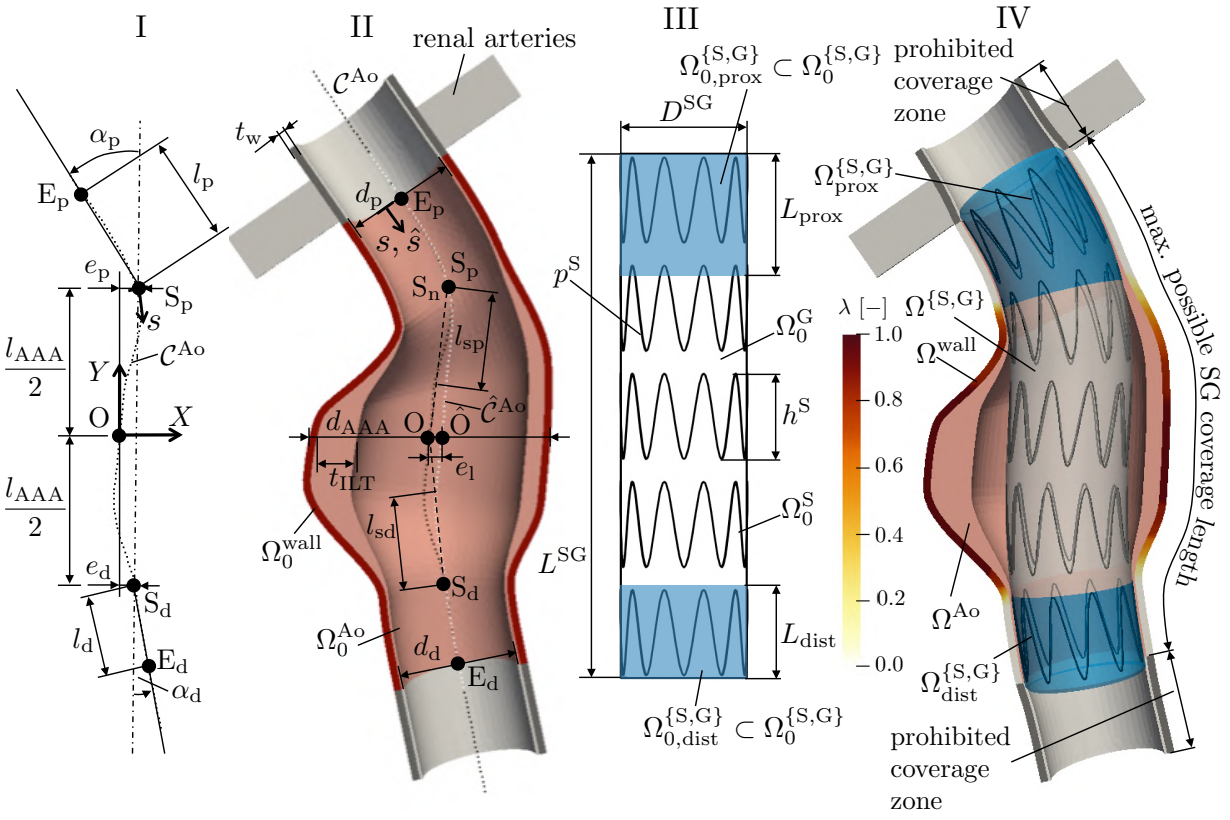

Figure 6.1 Definition of the curve $\mathcal{C}^{\mathrm{Ao}}(s)$ through the five points $\mathrm{E_p}$, $\mathrm{S_p}$, O, $\mathrm{S_d}$ and $\mathrm{E_d}$ (I). Definition of the curve $\hat{\mathcal{C}}^{\mathrm{Ao}}(\hat{s})$ through the five points $\mathrm{E_p}$, $\mathrm{S_p}$, $\hat{\mathrm{O}}$, $\mathrm{S_d}$ and $\mathrm{E_d}$ and 3D geometry of the parameterized vessel (II); renal arteries are not part of the computational model. Geometry of the parameterized SG and visualization of the proximal and distal landing zones (blue) of length L_{prox} and L_{dist}, respectively (III). Placed SG distal to the branch-offs into the renal arteries (IV). Reproduced with permission from [109].

implicitly given by

$$e_{\mathrm{l}} = l_{\mathrm{AAA}} \left(\mathrm{sgn}\left(\alpha_{\mathrm{p}}\right) \kappa_{\mathrm{p}} - \mathrm{sgn}\left(\alpha_{\mathrm{d}}\right) \kappa_{\mathrm{d}} \right) \tag{6.1}$$

where $\mathrm{sgn}(\bullet)$ is the sign function and $\kappa_{\mathrm{p}} = ||\boldsymbol{\mathcal{C}}^{\mathrm{Ao}''}(s = \mathrm{S_p})||$ as well as $\kappa_d = ||\boldsymbol{\mathcal{C}}^{\mathrm{Ao}''}(s = \mathrm{S_d})||$ are the curvatures of the curve $\mathcal{C}^{\mathrm{Ao}}$ at the points $\mathrm{S_p}$ and $\mathrm{S_d}$, respectively. The heuristic definition of e_{l} in Equation (6.1) is motivated by the fact, that the ILT thickness generally is larger at the flow averted side than at the flow faced side.

Spots of calcified tissue are considered in the domain of the vessel Ω_0^{Ao} according to Section 3.3. In this chapter, calcifications spots are predominantly located in the proximal landing zone. To assess the degree of calcification, the percentage circumferential proximal neck calcification $\bar{c}_{\mathrm{prox}}^{\mathrm{calc}}$ is introduced which is the ratio of the luminal surface in the proximal landing zone of the vessel covered by calcifications and the total luminal vessel surface of the proximal landing zone. Vessel uncertainties [23] (e.g., the vessel wall thickness t_{w} and the vessel wall stiffness) are quantities of the vessel model that are usually not easy to obtain and which are mostly incorporated in terms of population-averaged quantities. To investigate the impact of the vessel wall

stiffness in a strongly simplified manner, the scaled SEF of the vessel wall

$$\tilde{\Psi}^{\mathrm{wall}} = \gamma \Psi^{\mathrm{wall}} \tag{6.2}$$

is defined, where γ is a scalar-valued scaling parameter. The parameter γ is spatially constant for any $\boldsymbol{X} \in \Omega_0^{\mathrm{wall}}$, i.e., intrapatient variability of γ is not considered.

In total, the set $\mathcal{G}^{\mathrm{Ao}} = \{\alpha_{\mathrm{p}}, \alpha_{\mathrm{d}}, l_{\mathrm{p}}, l_{\mathrm{d}}, e_{\mathrm{p}}, e_{\mathrm{d}}, l_{\mathrm{AAA}}, d_{\mathrm{p}}, d_{\mathrm{d}}, d_{\mathrm{AAA}}, l_{\mathrm{sp}}, l_{\mathrm{sd}}, t_{\mathrm{w}}, t_{\mathrm{ILT}}, \bar{c}^{\mathrm{calc}}_{\mathrm{prox}}, \gamma\}$ of 16 parameters $g^{\mathrm{Ao}} \in \mathcal{G}^{\mathrm{Ao}}$ uniquely describes the vessel model with an AAA as visualized in Figure 6.1I+II.

6.1.2. Stent-graft parameterization

In clinical practice, the length of a SG generally is chosen as long as possible to obtain relatively long landing zones at the proximal and distal ends where the maximum length in the given problem is limited by the renal arteries at the proximal end. For simplicity, an AAA without bifurcation into the iliac arteries is considered. Further, the renal arteries are not part of the computational model. However, the points $\mathrm{E_p}$ and $\mathrm{E_d}$ define the locations of the renal arteries and the bifurcation of the iliac arteries, respectively (cf. Figure 6.1II+IV). Therefore, in the model the location of the two points $\mathrm{E_p}$ and $\mathrm{E_d}$ define the maximal possible coverage length of the SG (cf. Figure 6.1IV). The aorta proximal of the point $\mathrm{E_p}$ and distal of the point $\mathrm{E_d}$ must not be covered by the SG as this would occlude the renal arteries and parts of the iliac arteries, respectively. Under the assumption that the maximal possible coverage length of the SG is used, the length L^{SG} of the SG is implicitly given by the length of the luminal vessel centerline $\hat{\mathcal{C}}^{\mathrm{Ao}}$ between the two points $\mathrm{E_p}$ and $\mathrm{E_d}$ (cf. Figure 6.1II) according to

$$L^{\mathrm{SG}} = \int_{\mathrm{E_p}}^{\mathrm{E_d}} \mathrm{d}\hat{s} = \int_{Y_{\mathrm{E_p}}}^{Y_{\mathrm{E_d}}} \sqrt{1 + \left(\frac{\mathrm{d}X_{\hat{\mathcal{C}}^{\mathrm{Ao}}}}{\mathrm{d}Y_{\hat{\mathcal{C}}^{\mathrm{Ao}}}} \right)^2} \, \mathrm{d}Y_{\hat{\mathcal{C}}^{\mathrm{Ao}}}, \tag{6.3}$$

where $X_{\hat{\mathcal{C}}^{\mathrm{Ao}}}$ and $Y_{\hat{\mathcal{C}}^{\mathrm{Ao}}}$ are the coordinates of the curve $\hat{\mathcal{C}}^{\mathrm{Ao}}$ in the XY-plane.

Given the degree of SG oversizing o as defined in Equation (1.1), the nominal diameter of the SG is implicitly given by

$$D^{\mathrm{SG}} = (o+1) D^{\mathrm{Ao}} = (o+1) d_{\mathrm{p}}, \tag{6.4}$$

where $D^{\mathrm{Ao}} = d_{\mathrm{p}}$ is the inner wall diameter of the parameterized vessel in the proximal landing zone. Sinusoidally shaped stent limbs according to Equation (3.56) are considered, where h^{S} is the height of the stent limb and p^{S} is the number of sinusoidal periods per stent limb. All n^{S} stent limbs are equally distributed along the graft length and are predeformed by ω according to Equation (3.61). Graft thickness of $t^{\mathrm{G}} = 0.05 \ \mathrm{mm}$ and thickness of $\hat{d}^{\mathrm{S}} = 0.33 \ \mathrm{mm}$ of the stent wires with quadratic cross section are chosen to be in the range of commercial SGs [60] and are not modified in this chapter. Constitutive SG parameters are chosen to be in the range of commercial SGs with stainless steel stent and ePTFE graft ($E^{\mathrm{S}} = 210 \ \mathrm{GPa}$ [60], $\nu^{\mathrm{S}} = 0.3$ [60], $E^{\mathrm{G}} = 55.2 \ \mathrm{MPa}$ [139], $\nu^{\mathrm{G}} = 0.46$ [139], cf. Section 3.4.2).

In total, the set $\mathcal{G}^{\mathrm{SG}} = \{h^{\mathrm{S}}, p^{\mathrm{S}}, n^{\mathrm{S}}, \omega, t^{\mathrm{G}}, \hat{d}^{\mathrm{S}}\}$ uniquely defines (uniquely with exception of its diameter D^{SG}) the geometry of the SG in the preinterventional configuration

$\Omega_0^{\{\mathrm{S,G}\}} = \Omega_0^{\mathrm{S}} \cup \Omega_0^{\mathrm{G}}$ by six parameters $g^{\mathrm{SG}} \in \mathcal{G}^{\mathrm{SG}}$ (cf. Figure 6.1III). In contrast to the discrete parameters $g \in \mathcal{G} = \mathcal{G}^{\mathrm{Ao}} \cup \mathcal{G}^{\mathrm{SG}}$, the degree of SG oversizing $o(D^{\mathrm{SG}})$, which implicitly defines the nominal diameter of the SG, is treated as continuous parameter by a SG parameter continuation approach as described in Section 3.5.3.

6.1.3. Framework of the parameter study

In the following, variations of vessel parameters $g^{\mathrm{Ao}} \in \mathcal{G}^{\mathrm{Ao}}$ and SG parameters $g^{\mathrm{SG}} \in \mathcal{G}^{\mathrm{SG}}$ around the basic vessel and SG with the parameters $\hat{g}$ (cf. Table 6.2) are considered and their influence on the EVAR quality parameters is investigated. In total, 20 EVAR quality parameters are considered quantitatively to assess the quality of the in-silico EVAR outcome with respect to EVAR complication likelihoods. Accordingly, the set of EVAR quality parameters $\mathcal{Q}$ with the single parameters $q \in \mathcal{Q}$ is introduced. A summary of the considered EVAR quality parameters is provided in Table 6.1. For the definitions of these parameters, the reader is referred to Section 3.6.2.

Several EVAR quality parameters are related to the landing zones, i.e., to the sealing and fixation quality in the landing zones. In Section 3.6.2, the EVAR quality parameters were defined without specifying the location of the landing zone. In this chapter, the passive SG fixation force $\hat{F}_{\mathrm{lz}}$ is evaluated in the proximal landing zone $\hat{F}_{\mathrm{prox}}$ and the distal landing zone $\hat{F}_{\mathrm{dist}}$. All other parameters related to the landing zone are only evaluated in the proximal landing zone. Further, the SG drag force $\boldsymbol{F}_{\mathrm{drag}}$ is divided into a lateral component $F_{\mathrm{drag,x}}$ and an axial component $F_{\mathrm{drag,y}}$.

The lengths and areas of the proximal and distal landing zones of the parameterized vessel and SG model in the preinterventional configuration are given by (cf. Figure 6.1)

$$A_{\mathrm{prox}} = \pi D^{\mathrm{SG}} L_{\mathrm{prox}} = \pi D^{\mathrm{SG}} \int_{\mathrm{E_p}}^{\mathrm{S_p}} \mathrm{d}\hat{s} \approx \pi D^{\mathrm{SG}} l_{\mathrm{p}}, \tag{6.5}$$

$$A_{\mathrm{dist}} = \pi D^{\mathrm{SG}} L_{\mathrm{dist}} = \pi D^{\mathrm{SG}} \int_{\mathrm{S_d}}^{\mathrm{E_d}} \mathrm{d}\hat{s} \approx \pi D^{\mathrm{SG}} l_{\mathrm{d}}. \tag{6.6}$$

The area of the proximal (distal) landing zone of the SG in the current configuration, i.e., in the deployed state, is given by (cf. Equation (3.101))

$$a_{\mathrm{prox}} = \int_{\Gamma^{\mathrm{G}}_{\mathrm{ex,prox}}} ||J^{\mathrm{G}}(\boldsymbol{F}^{\mathrm{G}})^{-\mathrm{T}} \boldsymbol{N}^{\mathrm{G}}|| \mathrm{d}A_{\mathrm{prox}}, \tag{6.7}$$

$$a_{\mathrm{dist}} = \int_{\Gamma^{\mathrm{G}}_{\mathrm{ex,dist}}} ||J^{\mathrm{G}}(\boldsymbol{F}^{\mathrm{G}})^{-\mathrm{T}} \boldsymbol{N}^{\mathrm{G}}|| \mathrm{d}A_{\mathrm{dist}}. \tag{6.8}$$

Using the 22 geometrical parameters $g \in \mathcal{G} = \mathcal{G}^{\mathrm{Ao}} \cup \mathcal{G}^{\mathrm{SG}}$ and the degree of SG oversizing o, the vessel and the SG are uniquely defined in their preinterventional configuration Ω_0^{Ao} and Ω_0^{SG}, respectively (cf. Figure 6.1). Since a full factorial analysis for the given number of parameters $g \in \mathcal{G}$ and the number of parameter variations is not achievable, a basic vessel and SG geometry with the parameters $\hat{g}$ (cf. Table 6.2) is used from which single parameters $g \in \mathcal{G}$ are modified while all others are kept constant. For each realization of the parameters $g \in \mathcal{G}$,

Table 6.1 Summary of the considered EVAR quality parameters $q \in \mathcal{Q}$. The definitions of these parameters have been introduced in Section 3.6.2.

Symbol	Description	Symbol	Description
$\sigma_{99}^{\mathrm{wall}}$	Max. vessel stress	$a_{\mathrm{prox}}^{\mathrm{seal}}$	Proximal fixation area
$\bar{\sigma}_{99}^{\mathrm{wall}}$	Max. vessel overstress	$z_{\mathrm{max}}^{\mathrm{GA}}$	Max. graft-vessel gap
$\lvert\bar{\sigma}_{1}^{\lambda,\mathrm{wall}}\rvert$	Max. vessel relief	$z_{\mathrm{max}}^{\mathrm{SA}}$	Max. stent-vessel gap
$\bar{\sigma}_{99}^{\lambda,\mathrm{wall}}$	Max. aneurysmatic overstress	$\bar{o}_{\mathrm{prox}}^{\mathrm{eff}}$	Effective SG oversizing
$p_{\mathrm{n},99}$	Max. normal contact pressure	$e_{\mathrm{min}}^{\mathrm{S}}$	Min. stent expansion
σ_{99}^{S}	Max. stent stress	$y_{\mathrm{max}}^{\mathrm{S}}$	Max. stent asymmetry
$\hat{F}_{\mathrm{prox}}$	Proximal passive fixation force	$c_{\mathrm{max}}^{\mathrm{S}}$	Max. conical stent shape
$\hat{F}_{\mathrm{dist}}$	Distal passive fixation force	$u_{\mathrm{max}}^{\mathrm{G,pul}}$	Max. graft movement
$F_{\mathrm{drag,x}}$	Lateral drag force	$u_{\mathrm{max}}^{\mathrm{S,pul}}$	Max. stent movement
$F_{\mathrm{drag,y}}$	Axial drag force	$\bar{C}$	Mean diametric graft compliance

the deployed SG configuration is evaluated at the hydrostatic, diastolic blood pressure level of $p^{\mathrm{diast}} = 80\ \mathrm{mmHg}$ and at the hydrostatic, systolic blood pressure level of $p^{\mathrm{sys}} = 130\ \mathrm{mmHg}$ since some EVAR quality parameters may be critical in the diastolic state, others in the systolic state. 73 different realizations of the parameters $g \in \mathcal{G}$ (cf. Table 6.2) are considered which together with the two considered blood pressure states result in $n = 73 \cdot 2 = 146$ required simulations. This includes $n^{\mathrm{Ao}} = 120$ and $n^{\mathrm{SG}} = 26$ different realizations of the vessel parameters and the SG parameters, respectively.

Figure 6.2 provides an overview of the proposed framework to assess relations between the vessel as well as SG parameters $g \in \mathcal{G}$ and the EVAR quality parameters $q \in \mathcal{Q}$. For each realization of the parameters $g \in \mathcal{G}$, the in-silico SG P&D methodology proposed in Section 3.5.1 is used to deploy the SG with a degree of oversizing of $o_{\mathrm{I}} = 5\%$. Subsequently, the degrees of SG oversizing in the range between $o_{\mathrm{I}} = 5\%$ to $o_{\mathrm{PC}} = 40\%$ are investigated in a computationally efficient way by using SG parameter continuation (cf. Section 3.5.3). Using parameter continuation, it is possible to model all degrees of SG oversizing in the range $o \in [o_{\mathrm{I}}, o_{\mathrm{PC}}] = [\frac{D_{\mathrm{I}}^{\mathrm{SG}}}{d_{\mathrm{p}}} - 1, \frac{D_{\mathrm{PC}}^{\mathrm{SG}}}{d_{\mathrm{p}}} - 1]$ within a single EVAR simulation.

Starting from the results of an EVAR simulation, i.e. the postinterventional state of SG and vessel, with a SG of diameter $D_{\mathrm{I}}^{\mathrm{SG}}$ the stress-free reference configuration of the SG is continuously changed to the larger diameter $D_{\mathrm{PC}}^{\mathrm{SG}}$, which corresponds to the degree of SG oversizing of o_{PC} (cf. Figure 6.2III). The stress-free reference configurations of stent and graft are modified such that the degree of stent predeformation ω remains constant during SG parameter continuation.

Such a study would be computationally extremely expensive if SG parameter continuation is not used since for each considered degree of SG oversize, a separate EVAR simulation would be required. Assuming that the degree of SG oversizing should be investigated in increments of 5% in the range from 5% to 40%, such a study would require eight EVAR simulations per considered parameter realization. Together with the large amount of considered realizations of the parameters $g \in \mathcal{G}$ in this study, this would result in $8 \cdot 146 = 1168$ required EVAR simulations which

Table 6.2 Overview of vessel and SG parameters: basic parameters $\hat{g}$ that describe the basic vessel and SG configuration, range $[g_{\min}, g_{\max}]$ as well as number of variations $\#g_i$ of the parameters used in the parameter study. Parameters highlighted in gray are varied in the parameter study. Reproduced with permission from [109].

	Vessel parameters $g^{\mathrm{Ao}} \in \mathcal{G}^{\mathrm{Ao}}$													
	α_{p}	α_{d}	l_{p}	l_{d}	d [a]	e [b]	l_{AAA}	d_{AAA}	$l_{\mathrm{sp}}^{\mathrm{c,d}}$	l_{sd}	t_{w}	t_{ILT}	γ	$\bar{c}_{\mathrm{prox}}^{\mathrm{Ao\ e}}$
	[°]	[°]	[mm]	[mm]	[mm]	[mm]	[mm]	[mm]	[mm]	[mm]	[mm]	[mm]	[-]	[%]
$\hat{g}$	50	0	25	15	24	5	60	45	20	20	1.5	10	1	0
$g_{\min}$	-80	0	5	15	16	0	40	45	10	20	0.68	0	0.125	0
$g_{\max}$	80	0	30	15	32	12	100	45	40	20	2.6	28	8	70
$\#g_i$	13	1	6	1	5	6	4	1	8	1	7	6	7	7

	SG parameters $g^{\mathrm{SG}} \in \mathcal{G}^{\mathrm{SG}}$					
	h^{S}	p^{S}	n^{S}	ω	$\hat{d}^{\mathrm{S}}$	t^{G}
	[mm]	[-]	[-]	[%]	[mm]	[mm]
$\hat{g}$	16	10	5	5	0.33	0.05
$g_{\min}$	8	4	(5)[f]	0	0.33	0.05
$g_{\max}$	28	14	(5)[f]	25	0.33	0.05
$\#g_i$	6	4	(1)[f]	6	1	1

[a] same vessel diameters $d = d_{\mathrm{p}} = d_{\mathrm{d}}$ are used in the proximal and distal neck

[b] same neck eccentricities $e = e_{\mathrm{p}} = e_{\mathrm{d}}$ are used

[c] use of shortened neck length $l_{\mathrm{p}} = 5$ mm to increase potential influence of l_{sp}

[d] 4 variations of l_{sp} at $\alpha_{\mathrm{p}} = 0°$ and 4 variations of l_{sp} at $\alpha_{\mathrm{p}} = 50°$

[e] variation of percentage circumferential proximal neck calcification $\bar{c}_{\mathrm{prox}}^{\mathrm{calc}}$ and location of the calcification spots

[f] n^{S} adapted to SG length L^{SG}; gap between stent limbs is kept constant

is not achievable with a reasonable amount of computational power. Further, SG parameter continuation not only provides results of discrete degrees of SG oversizing but provides the results continuously over different degrees of SG oversizing within the provided range $o \in [o_{\mathrm{I}}, o_{\mathrm{PC}}]$.

Each deployed SG configuration with $o \in [o_{\mathrm{I}}, o_{\mathrm{PC}}]$ is postprocessed according to the EVAR quality parameters $q \in \mathcal{Q}$ (Section 3.6) to assess the quality of the EVAR outcome with respect to EVAR complication likelihoods (cf. Figure 6.2IV). Hence, as a result of the proposed parameter study, the EVAR quality parameters $q(g^{\mathrm{Ao}}, g^{\mathrm{SG}}, o)$ are given as a function of g^{Ao}, g^{SG} and o where g^{Ao} and g^{SG} are discrete function parameters and o is a continuously given function parameter.

For the purpose of a statistical analysis, the coefficient of variation is considered, which is defined as

$$\mathrm{CV}q(o) = \frac{\sigma_q(o)}{\mu_q(o)}, \quad \forall q \in \mathcal{Q}, \tag{6.9}$$

where

$$\mu_q(o) = \underset{i=1,2,...,n}{\mathrm{mean}}\, q_i(o), \quad \forall q \in \mathcal{Q} \tag{6.10}$$

is the mean value and

$$\sigma_q(o) = \underset{i=1,2,...,n}{\mathrm{std}}\, q_i(o), \quad \forall q \in \mathcal{Q} \tag{6.11}$$

is the standard deviation. q_i is the value of EVAR quality parameter $q \in \mathcal{Q}$ for the specific realization $i = 1, 2, ..., n$ that is described by the vessel and SG parameters g_i. Coefficients of variation $\mathrm{CV}q(o)$, mean values $\mu_q(o)$ and standard deviations $\sigma_q(o)$ are continuously given for

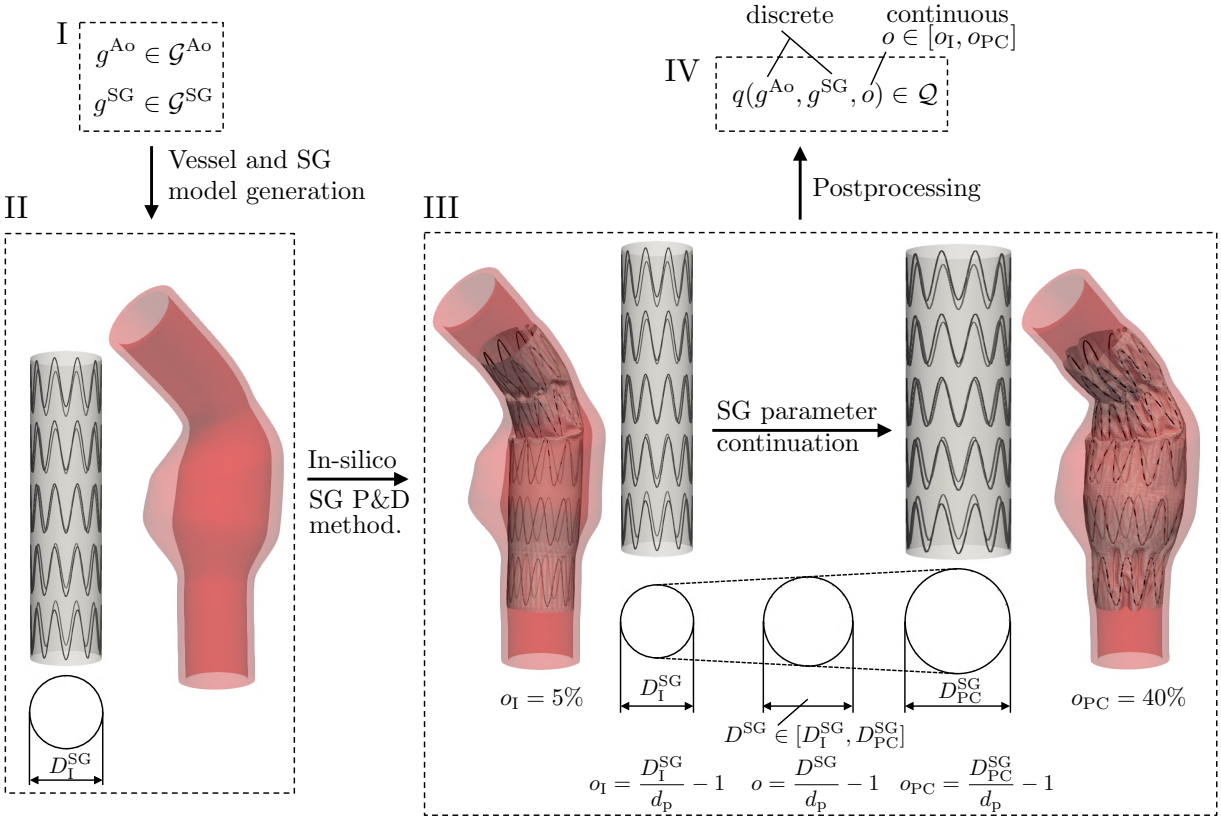

Figure 6.2 Framework of the parameter study: vessel and SG parameter selection (I); vessel and SG model generation with an initial degree of SG oversizing of $o_{\mathrm{I}} = 5\%$ (II); SG parameter continuation from $o_{\mathrm{I}} = 5\%$ to $o_{\mathrm{PC}} = 40\%$ (III); evaluation of EVAR quality parameters $q \in \mathcal{Q}$ for $o \in [o_{\mathrm{I}}, o_{\mathrm{PC}}]$ (IV). Modified figure reproduced with permission from [109].

all considered degrees of SG oversizing $o \in [5\%, 40\%]$ since the EVAR quality parameters $q_i(o)$ are evaluated continuously in this range of SG oversizing.

Furthermore, in order to investigate correlations, the degree of SG oversizing is not considered as continuous but also as discrete design variable. This leads to $\tilde{n} = n \cdot n_o = 146 n_o$ realizations at which the EVAR quality parameters $q \in \mathcal{Q}$ are given by discrete values q_i where n_o is the number of discrete evaluations of the continuously given degree of SG oversizing o. The Pearson product-moment correlation coefficient between the EVAR quality parameter $q \in \mathcal{Q}$ and the nominal degree of SG oversizing o is given by

$$r_{q,o} = \frac{\sum_{i=1}^{\tilde{n}} (q_i - \bar{q})(o_i - \bar{o})}{\sqrt{\sum_{i=1}^{\tilde{n}} (q_i - \bar{q})^2} \sqrt{\sum_{i=1}^{\tilde{n}} (o_i - \bar{o})^2}}, \quad \forall q \in \mathcal{Q},\ o \in [o_{\mathrm{I}}, o_{\mathrm{PC}}], \tag{6.12}$$

where $\bar{q}$ and $\bar{o} = 22.5\%$ are the mean values over all $\tilde{n}$ realizations of the EVAR quality parameter $q \in \mathcal{Q}$ and the degree of SG oversizing o, respectively. The correlation between two EVAR quality parameters $\hat{q} \in \mathcal{Q}$ and $\check{q} \in \mathcal{Q}$ is given by

$$r_{\hat{q},\check{q}} = \frac{\sum_{i=1}^{\tilde{n}} (\hat{q}_i - \bar{\hat{q}})(\check{q}_i - \bar{\check{q}})}{\sqrt{\sum_{i=1}^{\tilde{n}} (\hat{q}_i - \bar{\hat{q}})^2} \sqrt{\sum_{i=1}^{\tilde{n}} (\check{q}_i - \bar{\check{q}})^2}}, \quad \forall \hat{q}, \check{q} \in \mathcal{Q}, \tag{6.13}$$

where $\bar{\hat{q}}$ and $\bar{\check{q}}$ are the mean values of the EVAR quality parameter $\hat{q} \in \mathcal{Q}$ and the EVAR quality parameter $\check{q} \in \mathcal{Q}$, respectively.

6.2. Results

Due to the large amount of data, only the most interesting findings are shown in this section. The interested reader is referred to Appendix A.9 for a more detailed summary of the simulation results. This section is organized as follows: first, statistical studies on the total cohort of $n = 146$ realizations are performed with respect to the influence of vessel and SG parameters as well as the degree of SG oversizing on the EVAR quality parameters (Section 6.2.1). Afterwards more specific quantitative and qualitative results are presented for variations of the degree of SG oversizing (Section6.2.2), variations of the vessel (Section 6.2.3), variations of the SG (Section 6.2.4) and variations of the arterial blood pressure state (Section 6.2.5).

6.2.1. Overall impact of vessel and stent-graft parameters

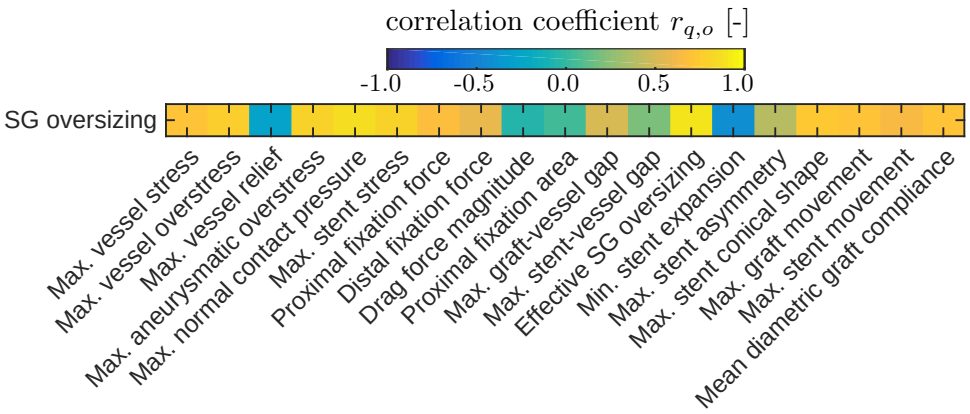

Figure 6.3 Correlation coefficients $r_{q,o}$ between EVAR quality parameters $q \in \mathcal{Q}$ and the degree of SG oversizing o as defined in Equation (6.12). Reproduced with permission from [109].

Strong positive correlation with correlation coefficients $r_{q,o} > 0.75$ is given between the degree of SG oversizing o and the following EVAR quality parameters (cf. Figure 6.3): maximum vessel overstress $\bar{\sigma}_{99}^{\text{wall}}$, maximum aneurysmatic overstress $\bar{\sigma}_{99}^{\lambda,\text{wall}}$, maximum normal contact pressure $p_{\text{n},99}$, maximum stent stress σ_{99}^{S} and the effective degree of SG oversizing $\bar{o}_{\text{prox}}^{\text{eff}}$. No correlation is given between the nominal degree of SG oversizing o and the SG drag force $\boldsymbol{F}_{\text{drag}}$ ($r_{q,o} = -0.05$) as well as between the nominal degree of SG oversizing o and the proximal fixation area $a_{\text{prox}}^{\text{seal}}$ ($r_{q,o} = 0.04$). The last point indicates that a larger area A_{prox} that results

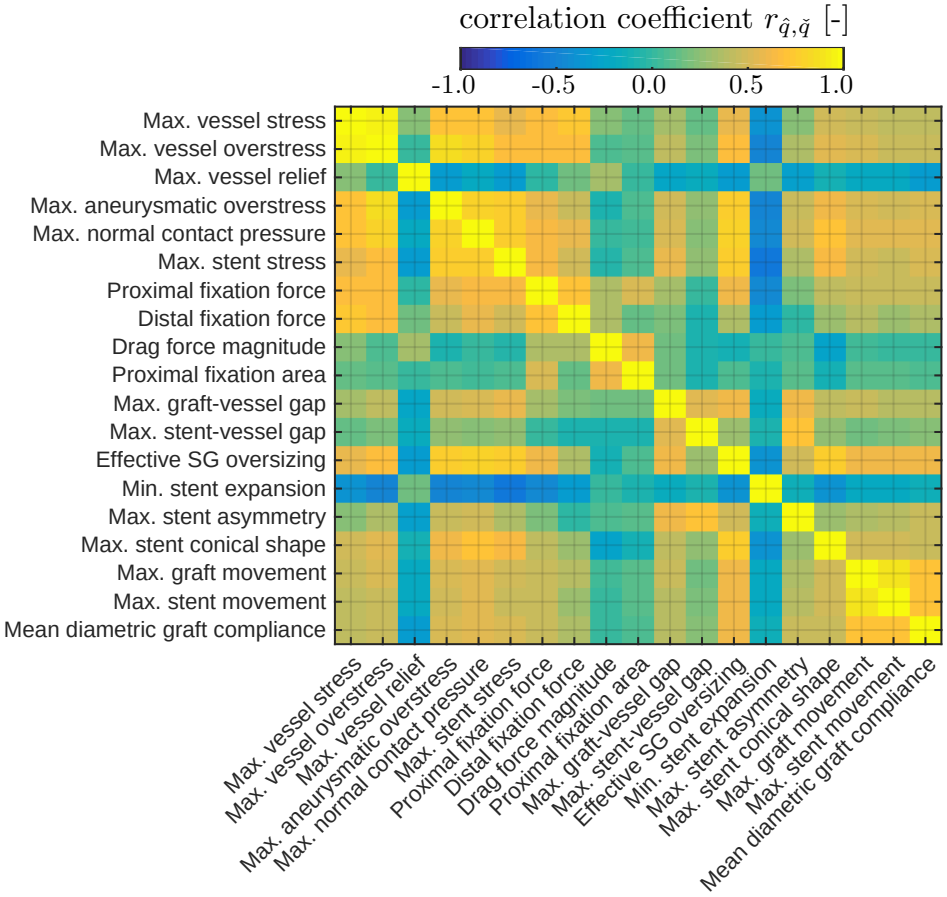

Figure 6.4 Correlation coefficients $r_{\hat{q},\check{q}}$ between EVAR quality parameters $\hat{q}$ and $\check{q}$ (II) as defined in Equation (6.13). Reproduced with permission from [109].

from a larger SG diameter D^{SG} does not necessarily lead to a larger proximal fixation area $a^{\mathrm{seal}}_{\mathrm{prox}}$ since buckling of the graft reduces the graft-vessel attachment in case of larger degrees of SG oversizing o.

According to Figure 6.4, strong correlation between the maximum aneurysmatic overstress $\bar{\sigma}^{\lambda,\mathrm{wall}}_{99}$ and the maximum normal contact pressure $p_{\mathrm{n},99}$ ($r_{\hat{q},\check{q}} = 0.81$), between the maximum aneurysmatic overstress $\bar{\sigma}^{\lambda,\mathrm{wall}}_{99}$ and the maximum stent stress σ^{S}_{99} ($r_{\hat{q},\check{q}} = 0.76$) as well as between the normal contact pressure $p_{\mathrm{n},99}$ and the maximum stent stress σ^{S}_{99} ($r_{\hat{q},\check{q}} = 0.75$) is given. Further, the effective degree of SG oversizing $\bar{o}^{\mathrm{eff}}_{\mathrm{prox}}$ strongly correlates with the maximum aneurysmatic overstress $\bar{\sigma}^{\lambda,\mathrm{wall}}_{99}$ ($r_{\hat{q},\check{q}} = 0.76$), the maximum normal contact pressure $p_{\mathrm{n},99}$ ($r_{\hat{q},\check{q}} = 0.78$) and the maximum stent stresses σ^{S}_{99} ($r_{\hat{q},\check{q}} = 0.75$). Strong, but less surprising correlations are given between the maximum vessel stress $\sigma^{\mathrm{wall}}_{99}$ and the maximum vessel overstress $\bar{\sigma}^{\mathrm{wall}}_{99}$ ($r_{\hat{q},\check{q}} = 0.94$), the maximum vessel overstress $\bar{\sigma}^{\mathrm{wall}}_{99}$ and the maximum aneurysmatic overstress $\bar{\sigma}^{\lambda,\mathrm{wall}}_{99}$ ($r_{\hat{q},\check{q}} = 0.85$) as well as between the maximum graft movement $u^{\mathrm{G,pul}}_{\mathrm{max}}$ and the maximum stent movement $u^{\mathrm{S,pul}}_{\mathrm{max}}$ ($r_{\hat{q},\check{q}} = 0.89$).

In Figure 6.5, the coefficient of variation $\mathrm{CV}q$ is considered for all EVAR quality parameters $q \in \mathcal{Q}$ at the nominal degree of SG oversizing of $o = 15\%$. In Appendix A.9, the coefficient of variation $\mathrm{CV}q$ is continuously given over all degrees of SG oversizing in the range

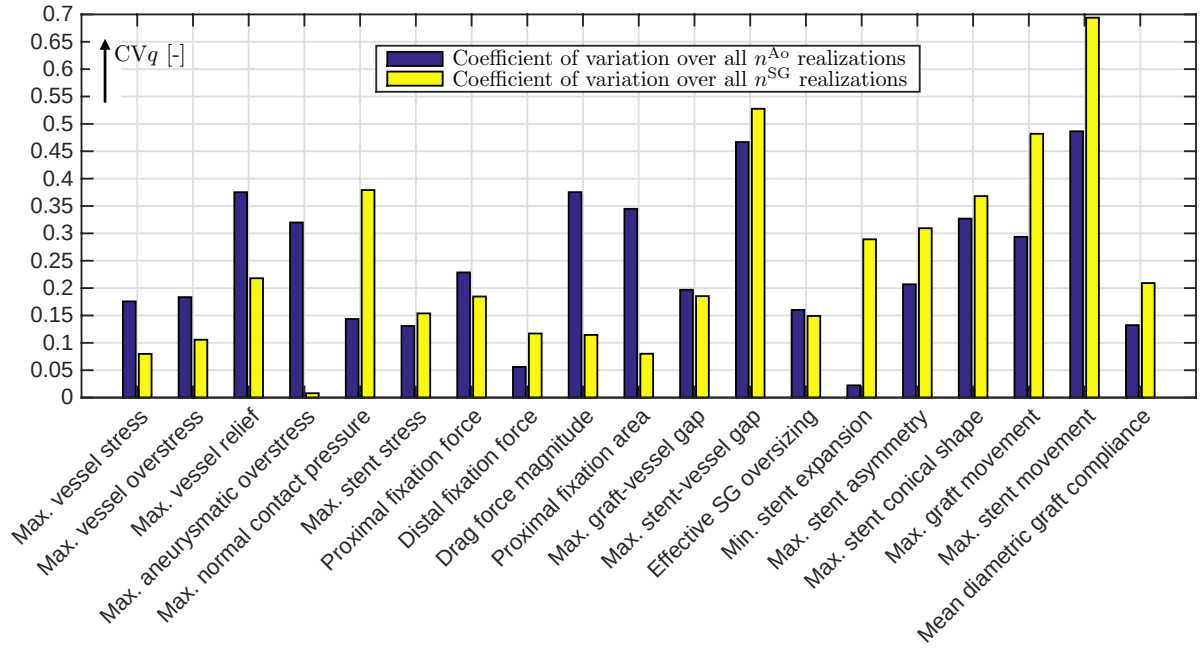

Figure 6.5 Coefficient of variation $\mathrm{CV}q$ according to Equation (6.9) over all $n^{\mathrm{Ao,diast}}$ realizations with different vessel geometries (blue bars) as well as over all $n^{\mathrm{SG,diast}}$ realizations with different SG geometries (yellow bars) at the diastolic pressure level of $p^{\mathrm{diast}} = 80\ \mathrm{mmHg}$. Reproduced with permission from [109].

$o \in [5\%, 40\%]$. The coefficients of variation $\mathrm{CV}q$ over all $n^{\mathrm{Ao,diast}} = 61$ realizations of the vessel parameters $g^{\mathrm{Ao}} \in \mathcal{G}^{\mathrm{Ao}}$ and over all $n^{\mathrm{SG,diast}} = 13$ realizations of the SG parameters $g^{\mathrm{SG}} \in \mathcal{G}^{\mathrm{SG}}$ are considered separately at the diastolic blood pressure state $p^{\mathrm{diast}} = 80\ \mathrm{mmHg}$. Hence, the coefficient of variation $\mathrm{CV}q$ over all $n^{\mathrm{Ao,diast}} = 60$ realizations (blue bars in Figure 6.5) indicates by how much the EVAR quality parameters $q \in \mathcal{Q}$ are influenced by the vessel parameters $g^{\mathrm{Ao}} \in \mathcal{G}^{\mathrm{Ao}}$ and the coefficient of variation $\mathrm{CV}q$ over all $n^{\mathrm{SG,diast}} = 13$ realizations (yellow bars in Figure 6.5) indicates by how much the EVAR quality parameters $q \in \mathcal{Q}$ are influenced by the SG parameters $g^{\mathrm{SG}} \in \mathcal{G}^{\mathrm{SG}}$.

According to Figure 6.5, the following EVAR quality parameters are strongly influenced by the vessel parameters $g^{\mathrm{Ao}} \in \mathcal{G}^{\mathrm{Ao}}$ with coefficients of variation $\mathrm{CV}q > 0.35$ (blue bars in Figure 6.5): the maximum vessel relief $|\bar{\sigma}_1^{\lambda,\mathrm{wall}}|$, the SG drag force $\boldsymbol{F}_{\mathrm{drag}}$, the maximum stent-vessel gap $z_{\mathrm{max}}^{\mathrm{SA}}$ and the maximum stent movement $u_{\mathrm{max}}^{\mathrm{S,pul}}$. Further, the following EVAR quality parameters are strongly influenced by the SG parameters $g^{\mathrm{SG}} \in \mathcal{G}^{\mathrm{SG}}$ with coefficients of variation $\mathrm{CV}q > 0.35$ (yellow bars in Figure 6.5): the maximum normal contact pressure $p_{\mathrm{n},99}$, the maximum stent-vessel gap $z_{\mathrm{max}}^{\mathrm{SA}}$, the maximum conical stent shape $c_{\mathrm{max}}^{\mathrm{S}}$, the maximum graft movement $u_{\mathrm{max}}^{\mathrm{G,pul}}$ and the maximum stent movement $u_{\mathrm{max}}^{\mathrm{S,pul}}$.

6.2.2. Influence of the degree of stent-graft oversizing

SG fixation forces increase almost linearly with increasing degree of SG oversizing. However, above a critical degree of SG oversizing o_{crit}, the SG fixation force does not further increase (cf.

Figure 6.6). The value of the critical degree of SG oversizing, i.e., the degree of SG oversizing above which the fixation force does not further increase, depends amongst other parameters on the geometry of the landing zone and the blood pressure state. For the distal landing zone of the vessel geometry visualized in Figure 6.6, the critical degrees of SG oversizing are $o_{\text{crit}}^{\text{diast}} \approx 15\%$ at the diastolic blood pressure state $p^{\text{diast}} = 80$ mmHg and $o_{\text{crit}}^{\text{sys}} \approx 20\%$ at the systolic blood pressure state $p^{\text{sys}} = 130$ mmHg.

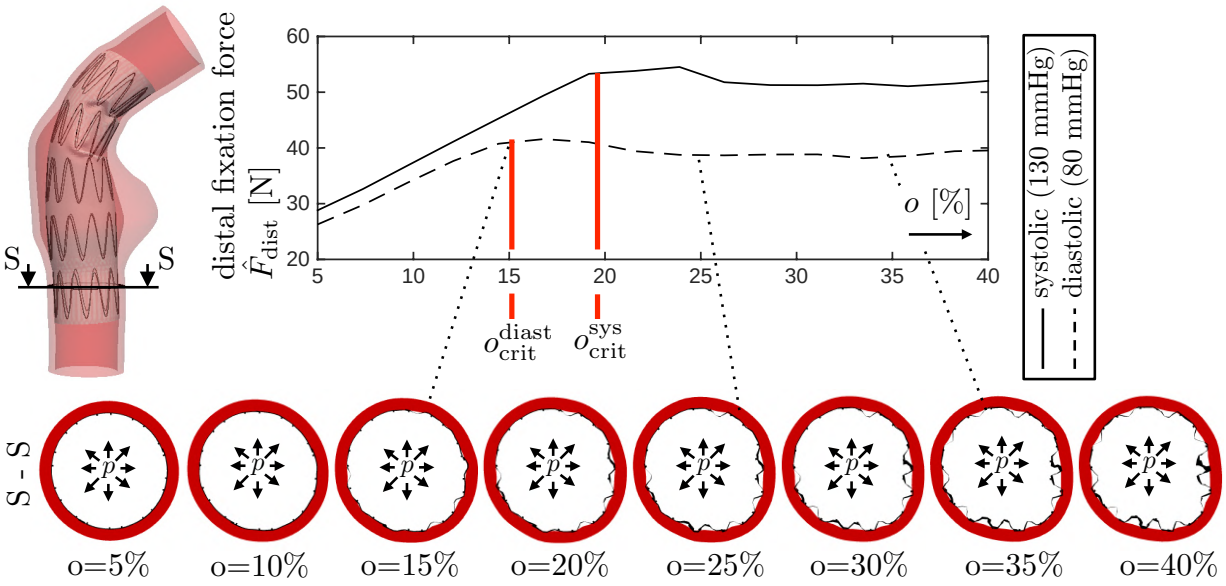

Figure 6.6 Distal fixation force $\hat{F}_{\text{dist}}$ as a function of the degree of SG oversizing o. Reproduced with permission from [108].

Increased radial graft buckling and associated negative effects on the force transmission between SG and vessel is a potential reason for the plateau in SG fixation forces above the critical degree of SG oversizing o_{crit}. Below the critical degree of SG oversizing ($o < o_{\text{crit}}$), the SG is almost perfectly attached to the vessel in the relatively straight distal landing zone of the vessel geometry visualized in Figure 6.6. Above the critical degree of SG oversizing ($o > o_{\text{crit}}$), the degree of radial graft buckling increases drastically with increasing degree of SG oversizing. The SG fixation force of a SG in the deployed state is a superposition of the force resulting from the oversized SG plus the force resulting from the internal blood pressure p which presses the SG against the luminal vessel surface. The internal blood pressure p results in a nonlinear traction load $\hat{\boldsymbol{t}}^{\text{G}} = -p \cdot \boldsymbol{n}^{\text{G}}$ on the luminal graft surface $\gamma_{\text{l}}^{\text{G}}$ as stated in Equation (3.8). If the SG is well attached to the vessel in the landing zone, the majority of the traction load $\hat{\boldsymbol{t}}^{\text{G}}$ is in radial direction. Thus, it is transmitted from the SG to the vessel and results in a SG fixation force. In case of graft buckling, a large portion of the traction load $\hat{\boldsymbol{t}}^{\text{G}}$ is not in radial direction. Hence, a large portion of the traction load $\hat{\boldsymbol{t}}^{\text{G}}$ does not contribute to the SG fixation force leading to the plateau of SG fixation force above o_{crit}.

Since graft buckling is more pronounced in the diastolic than in the systolic pressure state, $o_{\text{crit}}^{\text{diast}}$ is smaller than $o_{\text{crit}}^{\text{sys}}$. For landing zones in angulated vessels, the plateau in SG fixation force is less pronounced since in angulated vessels, longitudinal graft buckling dominates radial graft buckling induced by excessive SG oversizing.

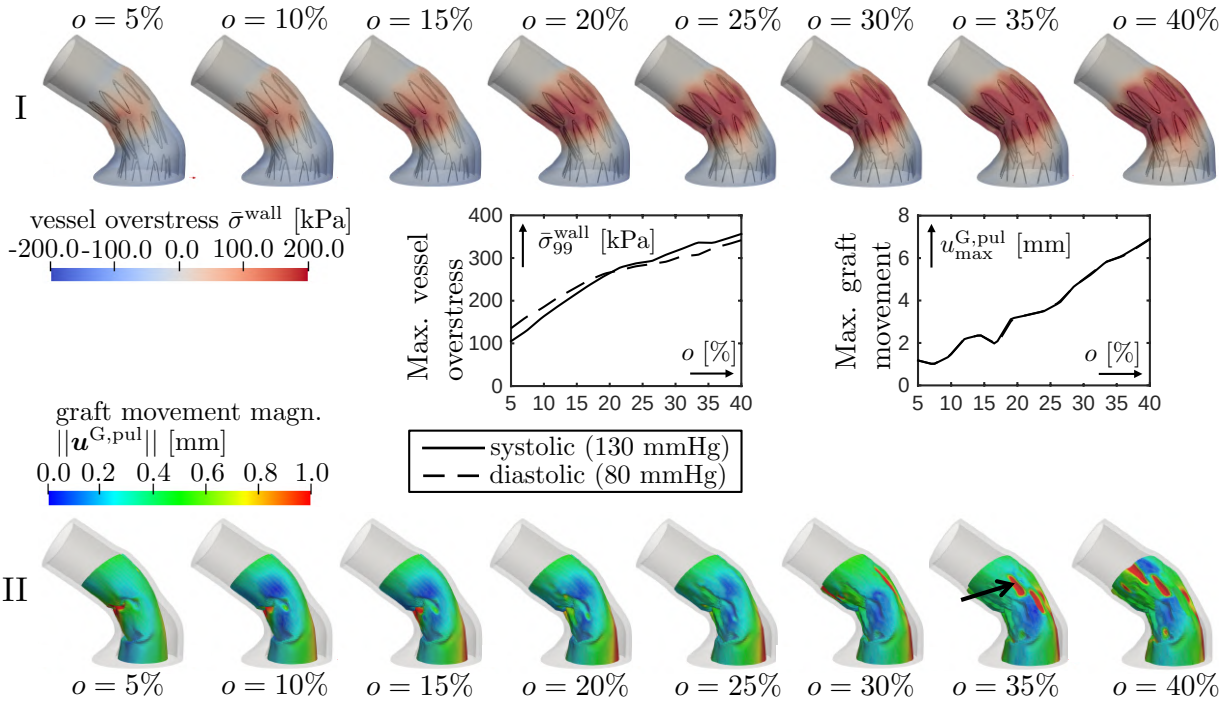

Figure 6.7 Visualization of the vessel overstress $\bar{\sigma}^{\text{wall}}$ (I) and the magnitude of the graft movement $||\boldsymbol{u}^{\text{G,pul}}||$ (II) for different degrees of SG oversizing o at the systolic pressure level of $p^{\text{sys}} = 130$ mmHg. Reproduced with permission from [109].

In Figure 6.7I, the impact of the degree of SG oversizing o on the vessel overstresses $\bar{\sigma}^{\text{wall}}$ is highlighted. The vessel overstresses $\bar{\sigma}^{\text{wall}}$ increase with increasing degree of SG oversizing o. Furthermore, increased radial buckling associated with large local graft movements $\boldsymbol{u}^{\text{G,pul}}$ of the resulting folds can be identified for large degrees of SG oversizing in Figure 6.7II, black arrow.

6.2.3. Influence of vessel parameters

In Figure 6.8, some EVAR quality parameters are exemplarily shown for the variation of the proximal neck angle α_{p} (cf. Figure 6.8I), the variation of the proximal neck length l_{p} (cf. Figure 6.8II) and the proximal neck diameter d_{p} (cf. Figure 6.8III).

Larger neck angles α_{p} lead both to a larger in-plane asymmetry $y^{\text{S}}_{\text{max}}$ of the stent rings in the curved region of the vessel and to a substantially increase in the SG drag force $\boldsymbol{F}_{\text{drag}}$ (cf. Figure 6.8I). Qualitative investigations of those two findings are provided in Figure 6.9 for proximal neck angles in the range $\alpha_{\text{p}} \in [0°, 80°]$. Additionally, in Figure 6.9I, stent collapse is visible for the deployed SG in vessels with a neck angle of $\alpha_{\text{p}} \geq 70°$.

A short neck length l_{p} causes a small fixation area $a^{\text{seal}}_{\text{prox}}$ (cf. Figure 6.8II) associated with a relatively poor quality of seal as well as a small fixation force $\hat{F}_{\text{prox}}$ (cf. Figure 6.10). Increasing the degree of SG oversizing o may be one potential way of improving the quality of seal and the SG fixation force in a vessel with short neck length l_{p}. The downside of this approach is visualized in Figure 6.10 by comparing the results of a SG oversized by $o = 5\%$ and a SG oversized by $o = 35\%$ in the vessel with short neck length $l_{\text{p}} = 5$ mm. A larger degree of

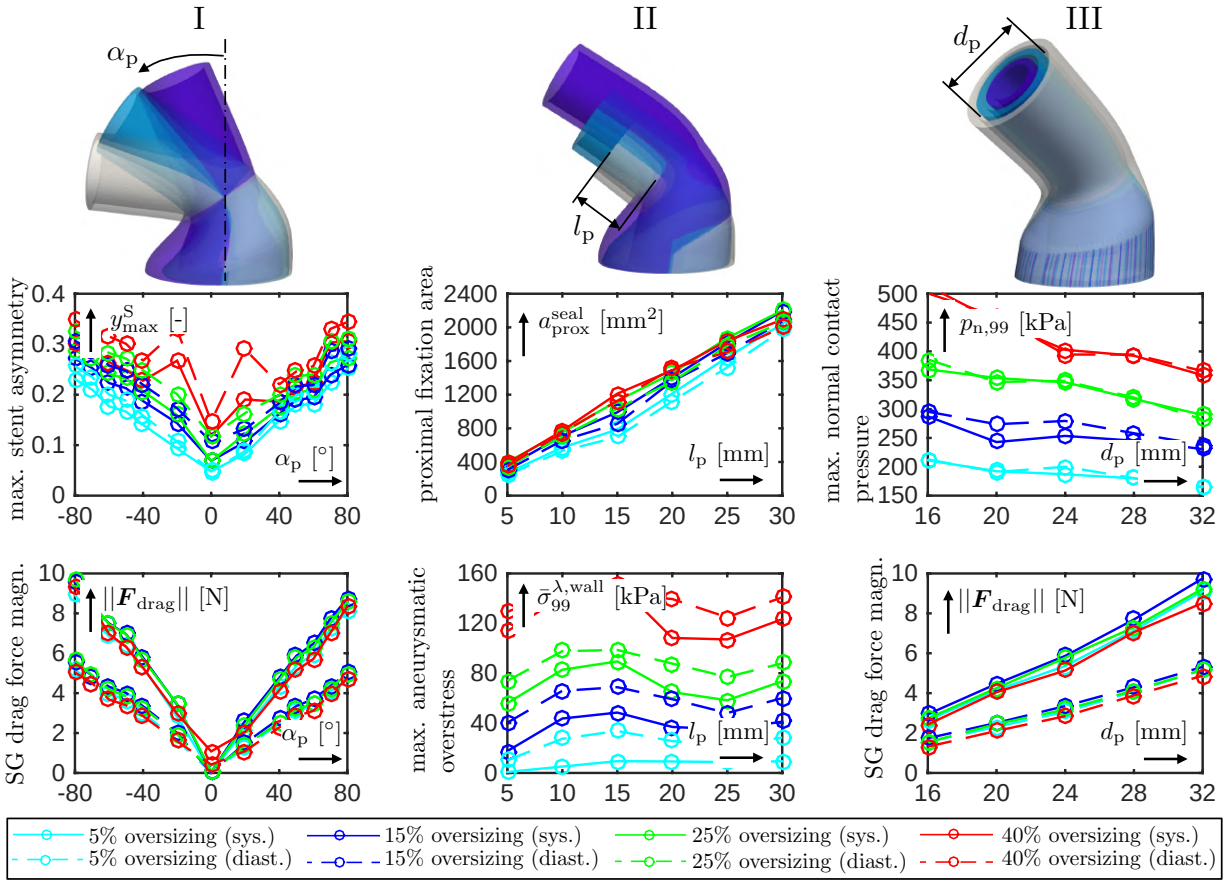

Figure 6.8 Influence of the proximal neck angle α_p (I), the proximal neck length l_p (II) and the proximal neck diameter d_p (III) on selected EVAR quality parameters $q \in \mathcal{Q}$ for different degrees of SG oversizing o as well as different blood pressure states $p^{diast} = 80$ mmHg and $p^{sys} = 130$ mmHg. Reproduced with permission from [109].

SG oversizing improves the quality of seal and the proximal fixation force of the SG. However, this is at the expense of increased aneurysmatic vessel overstresses in the AAA shoulder region which may trigger negative effects such as ongoing AAA growth in this region. Thus, it is at the expense of the potential long-term durability.

The magnitude of the SG drag force $||\boldsymbol{F}_{drag}||$ increases approximately linearly with increasing neck diameter d_p since the luminal area on which the blood pressure acts increases approximately linearly with increasing neck diameter d_p (cf. Figure 6.8III). Although the sealing area between SG and vessel increases as well with increasing neck diameter d_p, the fixation force $\hat{F}_{prox}$ does not substantially increase with increasing d_p since simultaneously the normal contact pressure between SG and vessel decreases (cf. Figure 6.8III). Thus, vessels with a larger neck diameter d_p may be rather prone to SG migration since the drag-fixation ratio of the SG is worse.

The following vessel uncertainties are investigated in this study: the vessel wall thickness t_w (cf. Figure 6.11I) and the vessel wall stiffness γ (cf. Figure 6.11II) according to Equation (6.2). In Figure 6.11I+II, the effective degree of SG oversizing $\bar{o}^{eff}_{prox}$ is plotted against the nominal degree of SG oversizing o for vessel walls of different thickness t_w and vessel walls of different stiffness γ. The softer and the thinner the vessel wall, the larger is the immediate postimplant

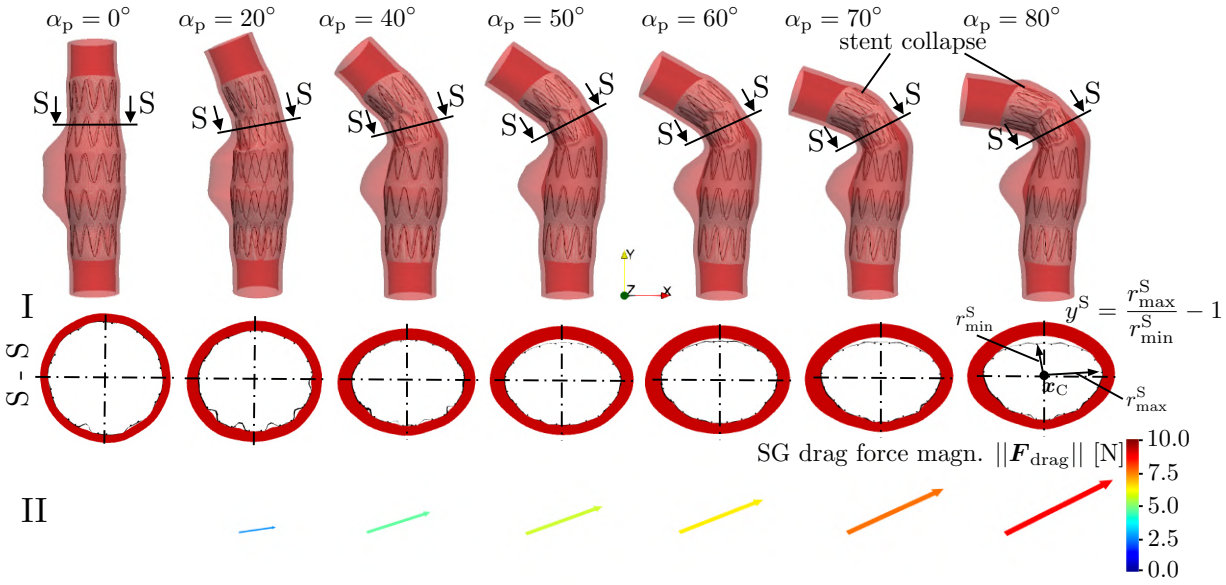

Figure 6.9 Visualization of the in-plane stent asymmetry y^S (I) and the SG drag force $\boldsymbol{F}_{drag}$ (II) for different proximal neck angles α_p with a nominal SG oversizing of $o = 15\%$ at the systolic pressure level of $p^{sys} = 130$ mmHg. Reproduced with permission from [109].

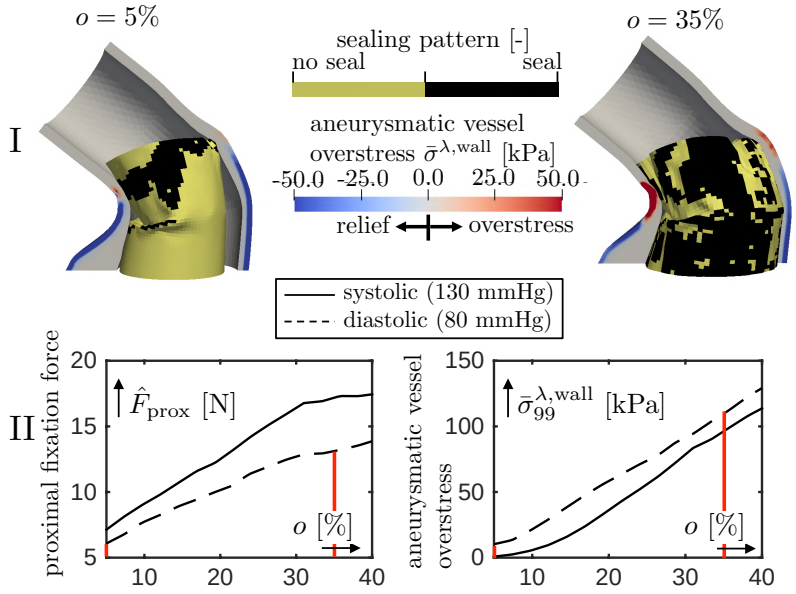

Figure 6.10 Qualitative comparison of the sealing pattern and the aneurysmatic vessel overstress (I) as well as quantitative comparison of the proximal SG fixation force $\hat{F}_{prox}$ and the aneurysmatic vessel overstress $\bar{\sigma}^{\lambda,wall}_{99}$ (II) of a vessel with short proximal neck length $l_p = 5$ mm. Red bars indicate the degree of SG oversizing $o = 5\%$ and $o = 35\%$ as well as the diastolic blood pressure state $p^{diast} = 80$ mmHg at which the qualitative results are evaluated. Reproduced with permission from [109].

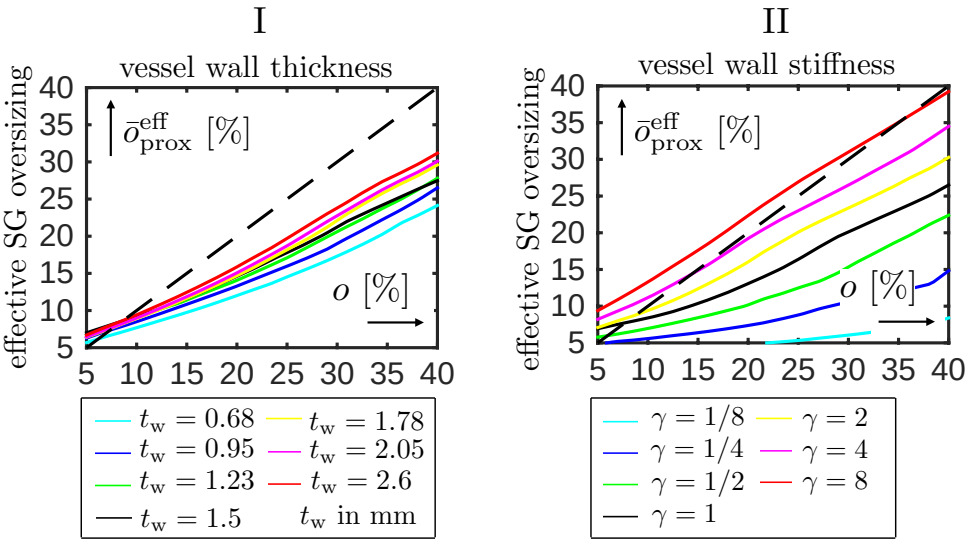

Figure 6.11 Investigation of vessel uncertainties at $p^{\text{sys}} = 130$ mmHg: influence of the vessel wall thickness t_w (I) and the vessel wall stiffness γ (II) on the effective degree of SG oversizing $\bar{o}^{\text{eff}}_{\text{prox}}$ for different degrees of SG oversizing o. Dashed line indicates reference of $o = \bar{o}^{\text{eff}}_{\text{prox}}$. Reproduced with permission from [109].

vessel dilatation and therefore the larger is the difference between nominal and effective degree of SG oversizing. In the case of the very stiff vessel ($\gamma = 8$, red curve in Figure 6.11II), the SG induced vessel deformation is very small. Thus, the local stent expansion diameter $\bar{d}^{\text{S}}(s_{\text{De}})$ is approximately equivalent to the preinterventional vessel diameter d_{p}. Consequently, the nominal and the effective degree of SG oversizing are approximately the same (cf. Equations (1.1) and (3.113)):

$$o^{\text{eff}}(s_{\text{De}}) = \frac{D^{\text{SG}}}{\bar{d}^{\text{S}}(s_{\text{De}})} - 1 \approx \frac{D^{\text{SG}}}{d_{\text{p}}} - 1 = o \tag{6.14}$$

In contrast to the stiff vessel, the soft vessel ($\gamma = 1/8$, cyan curve in Figure 6.11II) exhibits enormous immediate postimplant SG induced vessel dilatation such that the stent almost fully expands and the local stent expansion diameter $\bar{d}^{\text{S}}(s_{\text{De}})$ is close to the nominal diameter D^{SG} of the SG. Thus,

$$o^{\text{eff}}(s_{\text{De}}) = \frac{D^{\text{SG}}}{\bar{d}^{\text{S}}(s_{\text{De}})} - 1 \approx \frac{D^{\text{SG}}}{D^{\text{SG}}} - 1 = 0. \tag{6.15}$$

In Figure 6.12, the influence of vessel calcifications in the proximal landing zone is investigated. The difference in the vessel deformation between a non-calcified vessel and a highly calcified vessel (cf. Figure 6.12, detail Z) seems to be small. However, considering the effective degree of SG oversizing $\bar{o}^{\text{eff}}_{\text{prox}}$, this difference may be very essential. Having in mind that in clinical practice a nominal degree of SG oversizing of approximately $o \in [10\%, 20\%]$ is aspired, a difference in 3.7 % effective SG oversizing o^{eff} between the highly calcified ($\bar{c}^{\text{calc}}_{\text{prox}} = 70$ %) and the non-calcified aortic neck ($\bar{c}^{\text{calc}}_{\text{prox}} = 0$ %) is substantial (cf. Figure 6.12IV, $o = 15\%$).

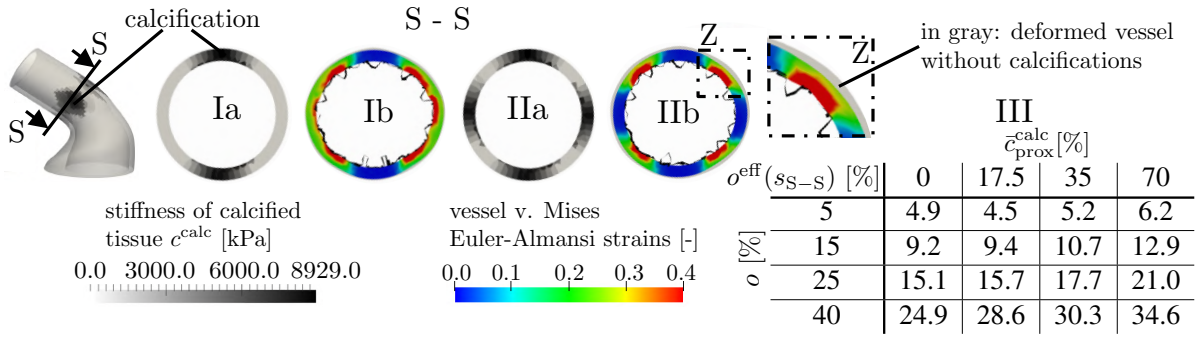

III

o [%] \ $\bar{c}^{\text{calc}}_{\text{prox}}$ [%]	0	17.5	35	70
5	4.9	4.5	5.2	6.2
15	9.2	9.4	10.7	12.9
25	15.1	15.7	17.7	21.0
40	24.9	28.6	30.3	34.6

$o^{\text{eff}}(s_{\text{S-S}})$ [%]

Figure 6.12 Influence of vessel calcifications in the proximal landing zone. Visualization of the calcification spots of the vessel with two calcified spots (Ia) and the vessel with four calcification spots (IIa). Visualization of the vessel von Mises Euler-Almansi strains for a vessel with two calcification spots (Ib) and a vessel with four calcification spots (IIb). Effective degree of SG oversizing $o^{\text{eff}}(s_{\text{S-S}})$ at location of slice S-S for different degrees of percentage circumferential proximal neck calcification $\bar{c}^{\text{calc}}_{\text{prox}}$ and different nominal degrees of SG oversizing o at $p^{\text{sys}} = 130$ mmHg (III). Modified figure reproduced with permission from [109].

6.2.4. Influence of stent-graft parameters

In this chapter, in the variation of the stent height h^{S}, the number of stent limbs n^{S} of the SG is adapted to keep the total SG length L^{SG} and the length of the gap between stent limbs constant over all considered variations of the stent height h^{S}. SGs with many short stent limbs are radially stiffer than SGs with few long stent limbs. Hence, the mean diametric graft compliance $\bar{C}$ increases with increasing stent height h^{S} (cf. Figure 6.13I and Figure 6.14I). Moreover, SGs with shorter stent limbs, i.e., smaller h^{S}, are more flexible and can better adapt to the curved vessel geometry. Thus, SGs with stent limbs of large height h^{S} have an increased tendency to SG kinking with its associated negative effects in tortuous vessels. However, whether there will be SG kinking or not also strongly depends on the position of the single stent limbs in the curved regions of the vessel. For the given vessel geometry, a SG with $h^{\text{S}} = 24$ mm shows considerable SG kinking whereas a SG with $h^{\text{S}} = 28$ mm does not show any SG kinking (cf. Figure 6.14II). Increased in-plane stent asymmetry $y^{\text{S}}_{\text{max}}$ is a side effect of the increased tendency to SG kinking. SG kinking occurs at the gaps between stent limbs. The deformation of the adjacent stent limbs is large in case of SG kinking leading to an ovalization of the stent limbs, i.e., to large in-plane stent asymmetries $y^{\text{S}}_{\text{max}}$ (cf. Figure 6.13I).

SGs with stent limbs that have a larger number of periods p^{S} per stent limb behave radially stiffer. Thus, increasing the number of periods p^{S} per stent limb leads to a reduction of the mean diametric compliance $\bar{C}$ of the SG (cf. Figure 6.13II). Further, a larger number of periods p^{S} per stent limb causes higher contact pressures $p_{\text{n,99}}$ and fixation forces $\hat{F}_{\text{prox}}$ between SG and vessel. This effect is likewise for all considered degrees of SG oversizing o (cf. Figure 6.13II).

Stent predeformation ω has positive effects on the radial buckling of the graft and the SG fixation. However, in Figure 6.13III, some downsides of stent predeformation are shown. Larger degrees of stent predeformation ω result in higher vessel overstresses $\bar{\sigma}^{\text{wall}}$. Moreover, especially in combination with large degrees of SG oversizing o, large degrees of stent predeformation ω induce very high stent stresses σ^{S}.

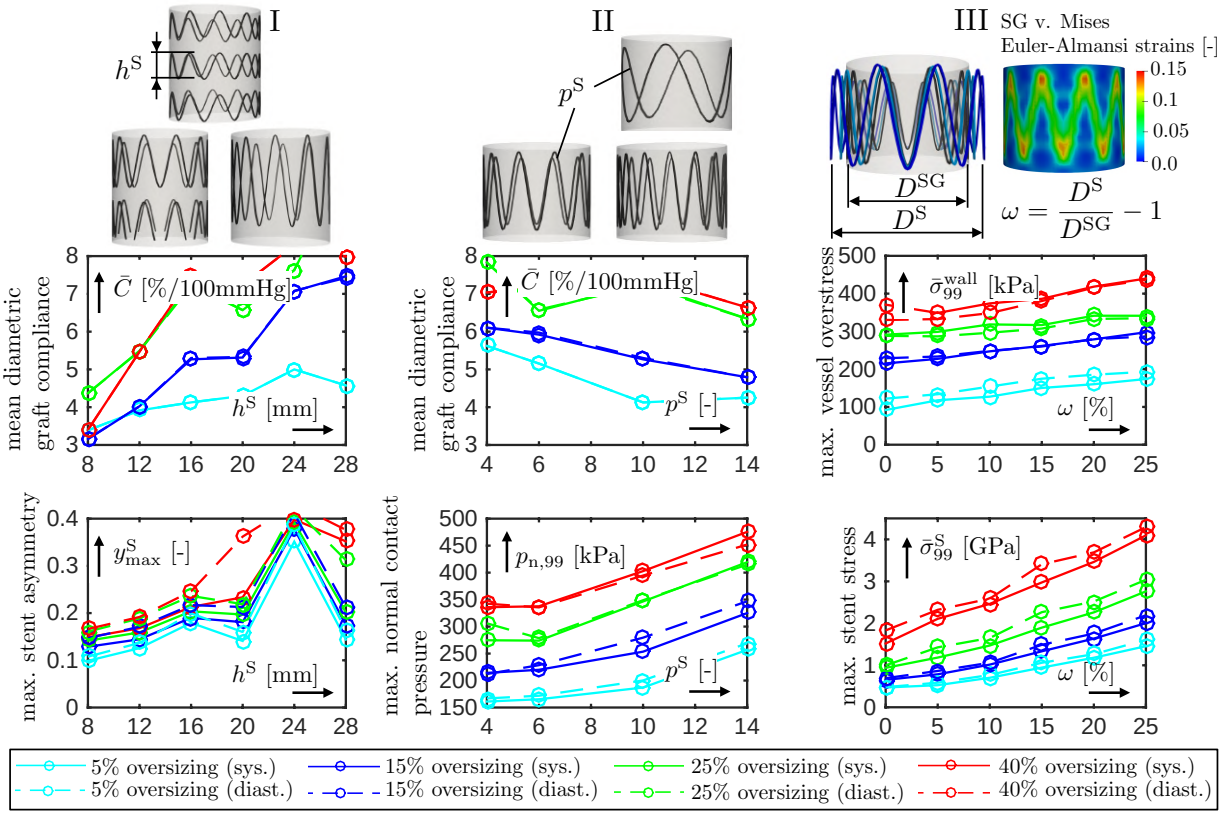

Figure 6.13 Influence of the stent height h^S (I), the number stent limb periods p^S(II) and the stent predeformation ω (III) on selected EVAR quality parameters $q \in \mathcal{Q}$ for different degrees of SG oversizing o as well as different blood pressure states $p^{diast} = 80$ mmHg and $p^{sys} = 130$ mmHg. Reproduced with permission from [109].

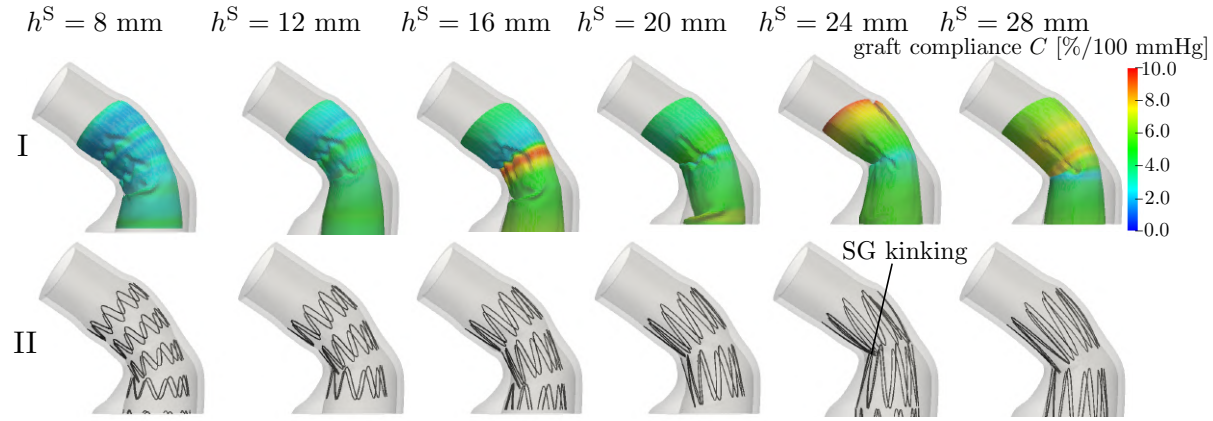

Figure 6.14 Visualization of the graft compliance C (I) and the deployed stent configuration (II) for different stent heights h^S for a SG oversized by $o = 15\%$ at the systolic pressure level of $p^{sys} = 130$ mmHg. Reproduced with permission from [109].

6.2.5. Influence of the arterial blood pressure

In Figure 6.15, the influence of the blood pressure state on the EVAR quality parameters $q \in \mathcal{Q}$ is investigated where the relative change of the EVAR quality parameter is given by

$$\Delta q(o) = \frac{\mu_q^{\mathrm{sys}}(o) - \mu_q^{\mathrm{diast}}(o)}{\mu_q^{\mathrm{diast}}(o)}, \quad \forall q \in \mathcal{Q} \tag{6.16}$$

In Equation (6.16), μ_q^{sys} is the mean value of the EVAR quality parameter q at the systolic blood pressure state of $p^{\mathrm{sys}} = 130\,\mathrm{mmHg}$ and μ_q^{diast} is the mean value of the EVAR quality parameter at the diastolic blood pressure state of $p^{\mathrm{diast}} = 80\,\mathrm{mmHg}$. The calculation of the mean values was introduced in Equation (6.10). Besides the general influence of the blood pressure state on the EVAR quality parameters, this consideration gives some insight whether the diastolic or whether the systolic blood pressure state is more crucial for the EVAR quality parameter $q \in \mathcal{Q}$.

In Figure 6.15, the influence of the arterial blood pressure state Δq is plotted for a degree of SG oversizing of $o = 15\%$. In Appendix A.9, the influence of the arterial blood pressure state $\Delta q(o)$ is continuously given over all degrees of SG oversizing in the range $o \in [5\%, 40\%]$. Figure 6.15 highlights that some EVAR quality parameters are larger at the systolic blood pressure state ($\Delta q > 0$) while others are larger at the diastolic blood pressure state ($\Delta q < 0$). The following EVAR quality parameters are strongly influenced by the blood pressure state with $|\Delta q| > 50\%$: the maximum vessel relief $|\bar{\sigma}_1^{\mathrm{wall}}|$ and the magnitude of the SG drag force $||\boldsymbol{F}_{\mathrm{drag}}||$.

Having a closer look on the results visualized in Figure 6.15, several interesting impacts of the blood pressure state can be observed. It is plausible that the vessel relief $|\bar{\sigma}_1^{\mathrm{wall}}|$, which describes the reduction of the vessel wall stresses in the "aneurysmatic" region, is much larger in the systolic than in the diastolic blood pressure state since the preinterventional vessel stresses in the aneurysm sac are larger in systolic pressure state. Thus, the difference between the preinterventional vessel stresses and the postinterventional vessel stresses in the aneurysm sac are larger having in mind that the postinterventional vessel stresses in the aneurysm sac are close to zero for most of the considered $n = 146$ realizations independent of the blood pressure state. Both, SG fixation forces $\hat{F}_{\mathrm{prox}}$ and $\hat{F}_{\mathrm{dist}}$ as well as the magnitude of the SG drag force $||\boldsymbol{F}_{\mathrm{drag}}||$ are larger at the systolic blood pressure state ($\Delta q > 0$). Since the influence of the blood pressure on the drag force $\boldsymbol{F}_{\mathrm{drag}}$ is much larger than on the fixation forces $\hat{F}_{\mathrm{prox}}$ and $\hat{F}_{\mathrm{dist}}$, the risk of SG migration may be higher at the systolic pressure state.

Furthermore, maximum stent stresses σ_{99}^{S} are around 10% larger in the diastolic than in the systolic blood pressure state ($\Delta q \approx -10\%$) since the SG in the deployed state in the landing zones, i.e., in the regions where mostly the largest stent stresses occur, is under compression. Hence, an increase of arterial blood pressure relaxes the SG in the landing zones. The proximal fixation area $a_{\mathrm{prox}}^{\mathrm{seal}}$ is larger at the systolic blood pressure state ($\Delta q > 0$) whereas the maximum graft-vessel gap $z_{\mathrm{max}}^{\mathrm{GA}}$ and the maximum stent-vessel gap $z_{\mathrm{max}}^{\mathrm{SA}}$ in the proximal landing zone are larger in the diastolic blood pressure state ($\Delta q < 0$). The main reason for this finding is that the larger the blood pressure, the more the SG is pressed against the vessel. Thus, the fixation area $a_{\mathrm{prox}}^{\mathrm{seal}}$ increases whereas the graft-vessel gap $z_{\mathrm{max}}^{\mathrm{GA}}$ and the stent-vessel gap $z_{\mathrm{max}}^{\mathrm{SA}}$ decrease with increasing blood pressure. As a consequence, the risk of leakage may be higher at the diastolic blood pressure state.

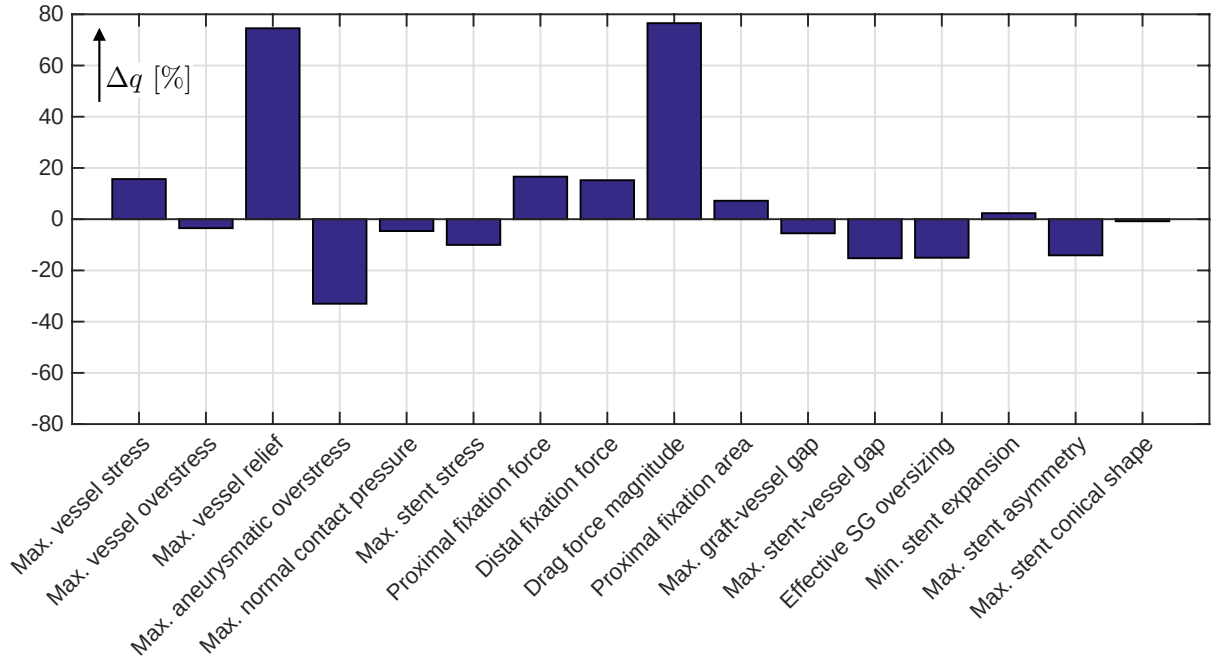

Figure 6.15 Influence of the arterial blood pressure state Δq according to Equation (6.16) on EVAR quality parameter q at a degree of SG oversizing of $o = 15\%$. A value of $\Delta q > 0$ indicates that the EVAR quality parameter q is larger in the systolic blood pressure state $p^{\mathrm{sys}} = 130\,\mathrm{mmHg}$ whereas a value of $\Delta q < 0$ indicates that the EVAR quality parameter q is larger in the diastolic blood pressure state $p^{\mathrm{diast}} = 80\,\mathrm{mmHg}$. Reproduced with permission from [109].

6.3. Summary of the results and discussion

In this chapter, a fully parameterized AAA and SG geometry was developed. A parameter study was performed on in total $n = 146$ different realizations of the vessel and SG parameters by using in-silico EVAR. In the parameter study, the degree of SG oversizing was treated as continuous variable between 5% and 40% oversizing by using a SG parameter continuation approach. 20 EVAR quality parameters were used to assess the outcome of in-silico EVAR with respect to complication likelihoods such as SG migration, endoleaks or aortic neck dilatation.

The following impacts of SG oversizing could be identified:

- SG fixation forces and maximum normal contact pressures between SG and vessel increase with increasing degree of SG oversizing. However, due to increased radial graft buckling and associated negative effects on the force transmission above a critical degree of SG oversizing, the SG fixation force does not further increase, i.e., a plateau in SG fixation force is given. In relatively straight landing zones, the plateau in SG fixation force starts above a degree of SG oversizing in the range 15%-25%, whereas for landing zones in angulated vessels, the plateau in SG fixation force is less pronounced.
- Vessel and stent stresses increase with increasing degree of SG oversizing.
- SG drag force is not substantially affected by the degree of SG oversizing.

- For large degrees of SG oversizing the effective SG oversizing is clearly smaller than the nominal SG oversizing since the SG induced immediate postimplant vessel dilatation [232] reduces the effective degree of SG oversizing.
- Increased SG oversizing leads to increased radial buckling of the SG. Locally large relative movements of the resulting folds are possible every heart beat which can have negative effects on the fatigue behavior of the graft.

It is important to note that the plateau in SG fixation force, which is stated in the first point, is not a result of the superelastic behavior of nitinol stents since linear elastic stainless steel stents were used in the study of this chapter. The plateau in SG fixation force could also be detected by Senf et al. [237]. According to Senf et al. [237], the maximum fixation force for Anaconda$^{\mathrm{TM}}$ SGs in a straight elastic vessel is given for SG oversized in the range $20\% - 24\%$ which is close to the findings of this study.

There are numerous different stent designs of marketed SGs. In this parameter study, the impact of stent design parameters on the EVAR outcome was investigated. This led to the following findings:

- A large number of periods per stent limb, i.e., a large number of loops of the sinusoidally shaped stent limb, induces radially stiffer SGs with reduced SG compliance.
- SGs with shorter stent limbs are more flexible and lead to a better SG-vessel attachment with reduced risk of SG kinking.
- Excessive stent predeformation can result in high stent stresses. Especially, if used in combination with a large degree of SG oversizing.
- None of the investigated SG designs showed significant aortic compliance mismatch. The mean diametric graft compliance was largely in the range of reported values of healthy abdominal aortas ($3.7 - 6.8\ \%/100\ \mathrm{mmHg}$) [147].

Variations of vessel parameters showed the following major impacts of the vessel geometry on the EVAR outcome:

- Vessel uncertainties [23], such as the vessel wall thickness and vessel wall stiffness, have a substantial impact on the effective degree of SG oversizing.
- The local stiffening of the vessel by calcifications leads to reduced SG expansion and a higher degree of effective SG oversizing.
- The neck angle has a very large impact on the SG drag force as often stated in literature [63, 157].
- Short neck length has the most negative impact on SG fixation as also stated for instance by [6, 278].
- The magnitude of the SG drag force increases almost linearly with increasing neck diameter since the luminal area on which the blood pressure acts increases approximately linearly with increasing neck diameter.

The last point is in accordance with several studies that mention an increase in SG drag forces and an increased risk of SG migration for patients with large vessel diameters [156, 183, 189, 203]. In contrast to the SG drag force, the SG fixation force is little affected by the neck diameter. This observation however is limited by the fact that in the current parameter study, the number of periods per stent limb was kept constant when increasing the SG diameter. However, SGs with larger diameter may require a larger number of periods per stent limb which would increase the radial stiffness of the SG.

The problematic nature of hostile necks [2, 8, 129], such as high angulation and short neck length, could clearly be shown in the parameter study. Higher degrees of SG oversizing in the case of hostile necks have proved to be a possibility to counteract small fixation areas and small SG fixation forces as suggested in some medical and experimental studies [34, 256, 257].

Even if the diameter of the deployed SG is little affected by the blood pressure state, investigations of the EVAR outcome at the diastolic blood pressure state of $80\ \mathrm{mmHg}$ and at the systolic pressure state of $130\ \mathrm{mmHg}$ have shown that it is important to consider both blood pressure states to assess the quality of the EVAR outcome. Some EVAR quality parameters are critical in the diastolic state while others are critical in the systolic state. The major findings of this parameter study with respect to the blood pressure state are:

- Maximum vessel overstresses, i.e., the difference in vessel stresses before and after EVAR, are larger in the diastolic blood pressure state.

- Maximum stent stresses are around 10% larger in the diastolic than in the systolic pressure state since a larger blood pressure reduces the compression of the stent in the landing zone and thus relaxes the stent.

- In the diastolic blood pressure state, the gap between SG and vessel is larger which increases the risk of leakage.

- The SG drag force is approximately 80% larger in the systolic blood pressure state which is in accordance with the frequently stated increased risk of SG migration in case of hypertension [157, 183, 189].

Furthermore, the increase of the SG drag force magnitude of approximately 80% is larger than the assumed systolic-diastolic pressure ratio of $\frac{130\ \mathrm{mmHg}}{80\ \mathrm{mmHg}} - 1 = 62.5\%$ which indicates nonlinear effects on the evaluation of the SG drag force. Assuming rigid SGs and rigid vessels, as done in many studies investigating the SG drag force [75, 120, 183], would lead to a 62.5% larger drag force in the systolic state than in the diastolic state as long as shear tractions are neglected in the computation of the SG drag force. This is because in case of a rigid SG and rigid vessel the integration area of the luminal graft surface does not change between diastolic and systolic pressure state. Thus, the SG drag force is only scaled by the internal pressure state p as described in Equation (3.104). Considering an elastic SG and vessel, as done in this study, a pressure increase also induces an increase of the integration area of the luminal graft surface γ_1^{G}. Hence, the SG drag force increase is larger than the assumed systolic-diastolic pressure ratio of 62.5%. Consequently, such a frequently used rigidity assumption potentially underestimates the SG drag force.

6.4. Limitations

Apart from the simplifications stated in Section 3.7, the study of this chapter is affected by the following limitations.

Although the definition of a successful EVAR intervention was defined as being complication-free for several years after the intervention, growth and remodeling of vessel tissue was not considered. However, it would be required to consider the development of the EVAR quality parameters over several years.

Furthermore, a simplified approach to investigate patient-specific uncertainties was used which did not consider intrapatient variability of vessel wall thickness and vessel wall stiffness but used spatially constant parameters. The major intention was to show the potential impact of these patient-specific uncertainties on the EVAR outcome.

To get a full understanding of the influence of the geometrical vessel and SG parameters and their potential interplay on the EVAR outcome a full factorial parameter study would be necessary. However, a full factorial analysis for the given number of parameters and number of parameter variations is computationally not achievable. Therefore, a basic vessel and SG geometry was used from which single parameters were modified while all others were kept constant. Choosing a different basic vessel and SG geometry might slightly change the outcome.

In the present study, the focus was put on quantitative evaluation of the EVAR outcome. However, a pure quantitative assessment might lead to misinterpretations in certain cases. For instance, a high value of the proximal fixation area does not necessarily mean that this is a leak-proof seal. Instead, the SG could be well attached just on one side, but an endoleak occurs on the averted side.

The parameter study of the synthetic vessel and SG revealed mean values, standard deviations and expectable ranges of the single EVAR quality parameters that can be used for comparisons. However, no statement about ranges in which the parameters are acceptable or not could be made. To determine these ranges of the EVAR quality parameters in which the EVAR outcome is acceptable, i.e., the EVAR outcome is free of complications, a large cohort of patient-specific cases has to be evaluated and statistically investigated with respect to EVAR complications. Having achieved such a clear link between EVAR complications and EVAR quality parameters with ranges of acceptable values for the EVAR quality parameters, the IFU could be formulated in terms of mechanical and geometrical EVAR quality parameters that are based on the predicted deployed SG configuration. Such IFU based on mechanical and geometrical parameters of the predicted deployed SG configuration should outline the limits of the applicability of EVAR much better than the current IFU that are based on the preinterventional vessel geometry.

6.5. Conclusions

In this chapter, a fully parameterized AAA and a fully parameterized SG model have been developed and utilized in a large parameter study of 146 different parameter realizations. The in-silico EVAR outcome was evaluated with respect to 20 mechanical and geometrical parameters that assess the quality of the in-silico EVAR outcome with respect to EVAR related complication likelihoods.

This study confirmed the hypothesis that the outcome of EVAR is strongly dependent on vessel and SG parameters. Candidates with high risk of postinterventional complications are in particular patients with a large neck angle, a large vessel diameter, a short neck length as wells as soft and thin vessel walls. It was shown that the degree of SG oversizing has a decisive role on the EVAR outcome and hence may have a big impact on the likelihood of postinterventional complications. A comparison of the EVAR outcome at the diastolic and the systolic blood pressure state showed the importance of considering both blood pressure states to assess the quality and complication likelihood of the EVAR outcome. While some parameters, such as the maximum stent stresses, are larger at the diastolic blood pressure state other parameters, such as the SG drag force, are crucial at the systolic blood pressure state.

7. Customized stent-grafts for EVAR with challenging necks: a numerical proof of concept

In clinical practice, SGs are cylindrical off-the-shelf devices. This means in the preinterventional planning, length and diameter of the SG are determined based on preinterventional CT data, but the patient-specific vessel morphology is not considered. EVAR requires a proper seal and fixation of the SG in the SG landing zones, to keep the aneurysm permanently excluded from the main blood flow. However, especially in the case of challenging aneurysm neck morphologies, i.e., challenging vessel morphologies in the region of the proximal landing zone, the morphological discrepancy between the cylindrical off-the-shelf SG and the vessel may lead to negative effects and possible secondary interventions [242, 280]. Frequent negative effects after EVAR that are directly related to the conditions in the SG landing zone are, among others, type I endoleaks and SG migration (cf. Section 1.1.2.4). Most frequently mentioned challenging neck morphologies are highly angulated and short necks [129, 233, 275]. But also conically shaped, barrel shaped, hourglass shaped or elliptic necks are frequently associated with negative effects in the SG landing zones [174, 273] since these nonuniform neck morphologies induce nonuniform SG expansion, reduced seal and reduced fixation of the SG.

Most of the existing SGs are of cylindrical shape that are unable to meet the vessel morphology of different patients. Nonuniform vessel morphologies require customized SG morphologies. This raises the need of a more personalized therapy where customized SGs [224, 242, 280] can be the next generation SGs for EVAR. By considering the vessel morphology in the region of the landing zone, the SG performance and the SG-vessel interaction should be improved leading to better long-term EVAR outcomes and a reduced number of EVAR related complications and secondary interventions. Besides reduced complication rates after EVAR in challenging necks, customized SGs could further increase the range of applicability of EVAR far beyond the IFUs of current SG manufacturers. Advanced manufacturing technologies, like additive manufacturing or electrospinning, have proved to be able to meet the demands of personalized medicine in wide ranges of medical applications [202, 223]. However, the use of these advanced manufacturing technologies in the development of highly customized SGs for EVAR is still current area of research [280] and the benefit of highly customized SGs over off-the-shelf SGs could not yet be proved. To qualitatively and quantitatively show the benefit of customized SGs compared to off-the-shelf SGs (cf. Figure 7.1), in-silico EVAR models are a valuable tool. Furthermore, numerical investigations can provide information on specific SG design aspects for advanced development of highly customized SGs.

The objective of this study is to show the added value of customized SGs, that have the same morphology as the luminal vessel surface, in a numerical proof of concept. Therefore, the in-

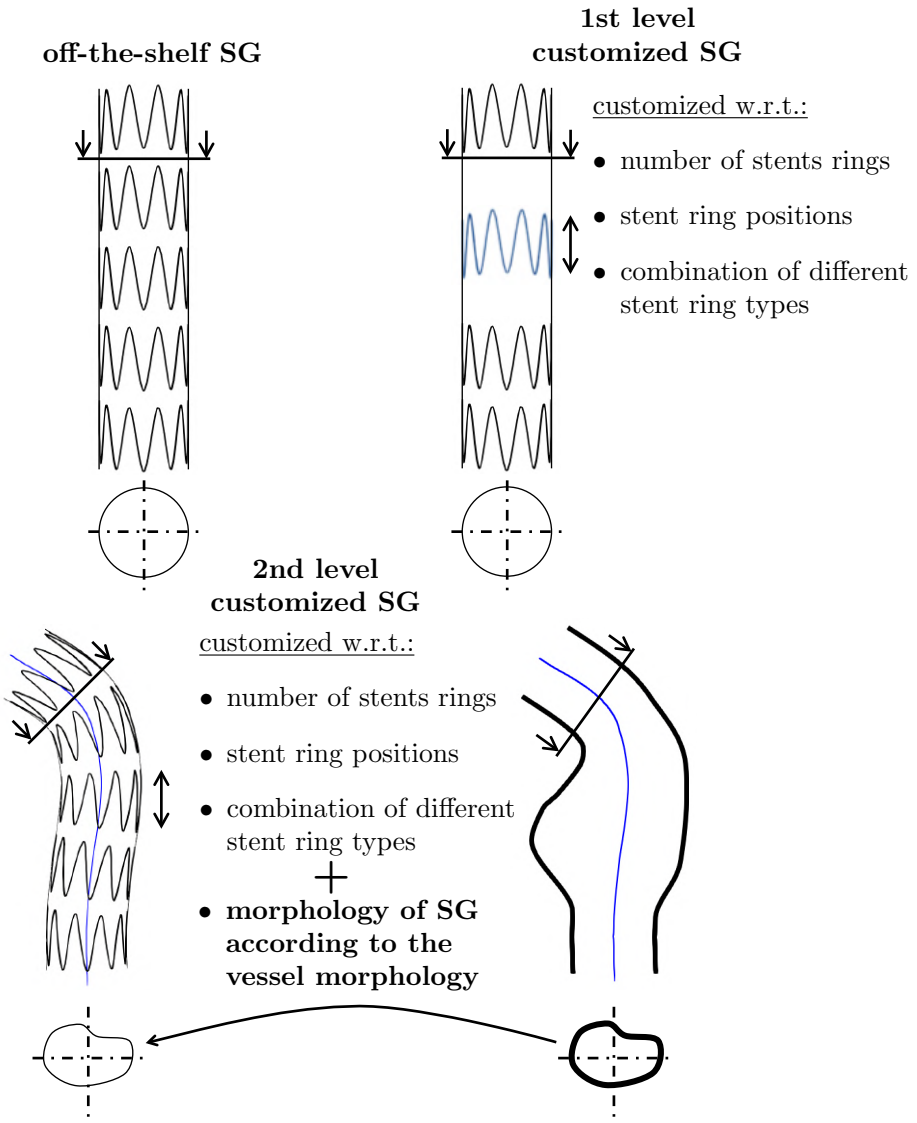

Figure 7.1 Sketch of a straight, cylindrical off-the-shelf SG as well as a first level and a second level customized SG. Reproduced with permission from [110].

silico EVAR model, which predicts the postinterventional state of SG and vessel, is used to compare customized SGs and off-the-shelf SGs. By comparison of the in-silico EVAR outcome of off-the-shelf SGs and customized SGs, the performance differences of the two SG devices is assessed in terms of mechanical and geometrical EVAR quality parameters (cf. Section 3.6.2) which indicate the potential complication likelihood after EVAR. In this chapter, the focus of these mechanical and geometrical parameters is on parameters which define the quality of the EVAR outcome in the landing zone of the SG.

In order to represent different aspects of noncylindrical geometries encountered in patient-specific anatomies, in this chapter general vessel morphologies, such as curved, conical, barrel shaped or hourglass shaped vessel morphologies are used in a numerical proof of concept. Although idealized vessels are studied, a realistic state of the deployed SG is considered which takes stent predeformation, vessel prestressing and physiological blood pressure states into ac-

count. The applied methods are shown for the abdominal region of the aorta. Nevertheless, the results are also applicable to endovascular repair of other regions of the aorta such as thoracic endovascular aortic repair.

Common medical practice is the customization of fenestrated SGs [196, 261] where the location of the fenestration is done in a patient-specific manner. Apart from this type of SG customization of advanced EVAR techniques, in this chapter, the classification of customized SGs into two different levels of customization is proposed (cf. Figure 7.1). The first level of SG customization describes an individual arrangement of stent rings on a classical graft to better meet the requirements of a patient-specific vessel. However, similar to off-the-shelf SGs the morphology of first level customized SGs is cylindrical and straight in the undeformed state. Romarowski et al. [224] numerically showed the advantage of such first level customized SGs compared to two off-the-shelf SGs.

In contrast to first level customized SGs, second level customized SGs are not cylindrical and straight, but are of the same morphology as the patient-specific luminal vessel surface and hence can even better meet the requirements of patient-specific vessels. To the best of the authors knowledge, the work by Zhang et al. [280] is the only published study on second level customized SGs. Zhang et al. [280] proposed a manufacturing technique of customized SGs which have the same morphology as the patient-specific vessel but did not investigate the advantage of this type of customized SGs compared to off-the-shelf SGs.

The outline of this chapter is as follows: in section 7.1, the morphological advantages of second level customized SGs are investigated theoretically. Afterwards, the basic concept of the manufacturing process of the presented customized SGs and the framework of the presented numerical proof of concept are presented. In section 7.2, the in-silico EVAR outcomes of customized SGs and off-the-shelf SGs are compared for several different vessel morphologies. The discussion of these results is presented in section 7.3. Subsequently, limitations and conclusions are drawn in section 7.4 and 7.5, respectively.

This chapter is a revised version of the published work by Hemmler et al. [110].

7.1. Methods

In the following, first geometrical aspects of second level customized SGs are discussed in Section 7.1.1. Afterwards, the basic manufacturing idea of second level customized SGs is provided in Section 7.1.2 and the framework of the numerical study is given in Section 7.1.3.

7.1.1. Morphology of second level customized stent-grafts

Given a noncylindrical vessel landing zone (e.g., a conical vessel landing zone), correct sizing of cylindrical off-the-shelf SGs is very challenging. Mostly, the maximum vessel diameter $D^{\mathrm{Ao}}_{\mathrm{max}}$ along the total potential vessel landing zone is chosen as recommended for instance in the IFU of Cook Zenith® SGs [44]. However, sizing of the SG according to the maximum vessel diameter $D^{\mathrm{Ao}}_{\mathrm{max}}$ results in excessive oversizing ($o = o_{\mathrm{max}}$) at narrow regions of the conical vessel (cf. Figure 7.2I) which may result in long-term negative effects such as aortic neck dilatation [257, 267]. Using the minimum vessel diameter $D^{\mathrm{Ao}}_{\mathrm{min}}$ for sizing of the cylindrical off-the-shelf SGs increases the risk of SG undersizing at wide regions of the conical vessel ($o = o_{\mathrm{min}}$) with its

negative consequences such as type I endoleaks. Using second level customized SGs that have the same morphology as the vessel, this inconsistency in SG sizing is obsolete. A constant degree of SG oversizing ($o(s) = \text{const}$) along the total arc length s of the vessel centerline can be achieved (cf. Figure 7.2I).

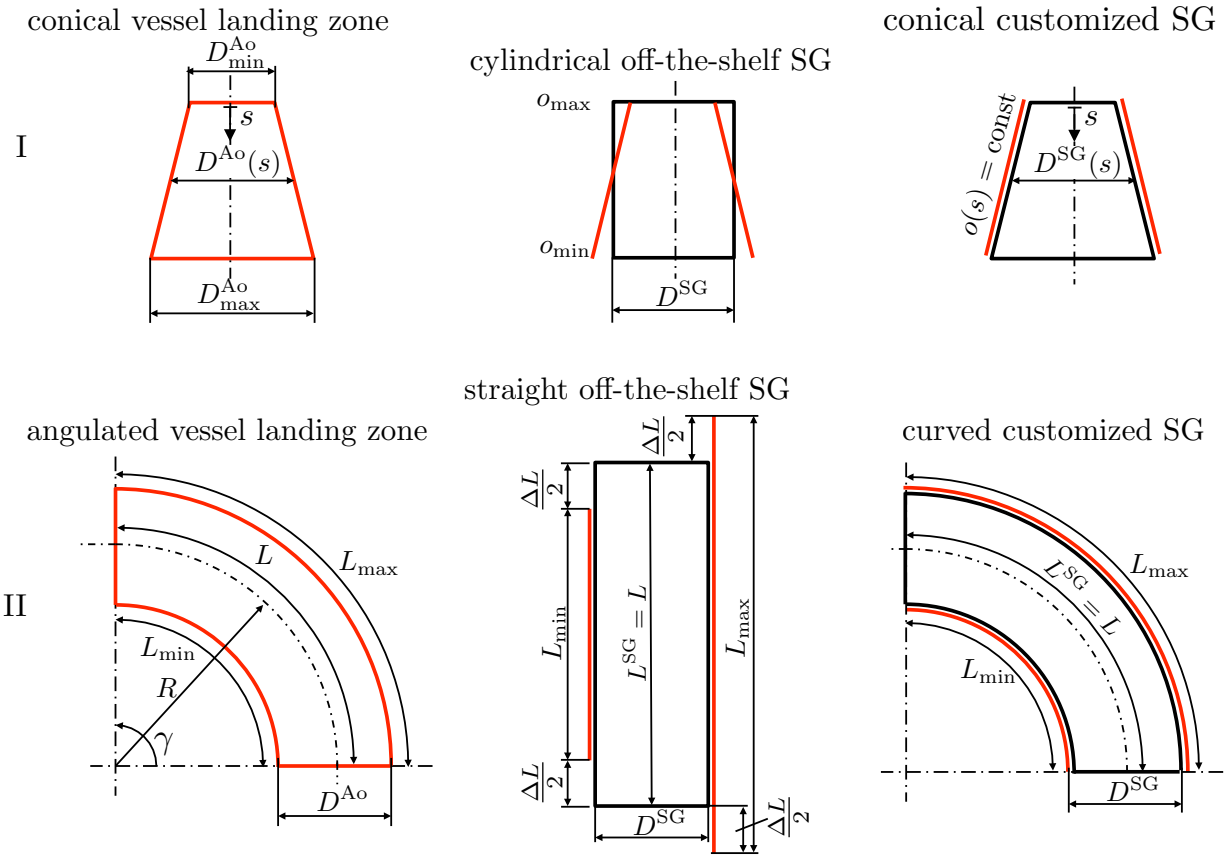

Figure 7.2 Illustration of SG sizing problems of off-the-shelf SGs in a conical vessel landing zone (I) and an angulated vessel landing zone (II) as well as improvement by second level customized SGs. Vessel landing zones are visualized in red, SGs in black. Reproduced with permission from [110].

The length of the landing zone is one of the most important parameters for positive EVAR outcomes [182, 256]. Hence, the length of the SG generally is chosen such that all of the potential length of the vessel landing zone is used, i.e., is covered by the SG. Given an angulated vessel landing zone (cf. Figure 7.2II), the effective length of the landing zone is smaller at the inner curvature of the vessel ($L_{\text{min}} = \frac{\gamma}{180}\pi(R - \frac{D^{\text{Ao}}}{2})$) than at the outer curvature of the vessel ($L_{\text{max}} = \frac{\gamma}{180}\pi(R + \frac{D^{\text{Ao}}}{2})$)[256]. Generally, the vessel centerline is used to determine the SG length. Accordingly, a straight off-the-shelf SG of length $L^{\text{SG}} = L$ is not able to use the total potential length of the vessel landing zone as it is too long at the inner curvature and too short at the outer curvature by

$$\Delta L = L - L_{\text{min}} = L_{\text{max}} - L = \frac{\gamma}{180}\pi\frac{D^{\text{Ao}}}{2}. \tag{7.1}$$

This means that a length of ΔL of the potential vessel landing zone at the outer curvature of the vessel remains unused. Excess length of the SG at the inner curvature of the vessel has to be avoided as well. This leads to longitudinal buckling of the graft at the inner curvature with its associated negative effects on the EVAR outcome such as disturbance of the blood flow. Being able to use the total potential length of the vessel landing zone $L_{\max}$ at the outer curvature of the vessel while at the same time the SG is not too long at the inner curvature of the vessel can contribute positively to the sealing and fixation of the SG. Second level customized SGs which have the same angulation as the vessel landing zone can exploit much better the restricted length of the important vessel landing zone with different effective lengths at the inner and the outer curvature (cf. Figure 7.2II).

7.1.2. Basic manufacturing idea of second level customized stent-grafts

Even though the focus of the current study is not on manufacturing of customized SGs and its technical feasibility, but rather on giving a motivation for further research and development of this kind of SGs, the basic concept of the presented customized SGs is given in this section. Discussions of specific manufacturing details are not part of this study.

In a first step using 3D printing, a mandrel according to the patient-specific vessel geometry from CT data is created. The mandrel serves as rotating collector around which the patient-specific polymeric graft is generated by application of electrospinning. Electrospinning is a manufacturing technique to form continuous nanofibers around a rotating collector using electrostatic forces. For a detailed overview of the electrospinning manufacturing technique, the interested reader is referred to the publication by Li and Xia [155]. Using electrospinning, the customized conductive mandrel is covered by continuous polymeric (polyurethane) fibers that are almost randomly distributed in plane. Continuous generation of these polymeric fibers forms a thin polymeric graft that encapsulates nitinol stent rings. No additional fixation of the metallic stent rings by sutures is required since the stent rings are placed in-between layers of polymeric fibers. After removal of the mandrel, a customized SG is obtained which in the undeformed state has the same morphology as the patient-specific luminal vessel geometry.

Manufacturing of various shapes (conical, elliptical, curved and straight) to determine the limits of electrospinning showed very promising results. Initial experiments have shown that the described manufacturing process allows to manufacture complex geometry SGs with radial expansion forces similar to commercial prostheses.

7.1.3. Framework of the study

In the study of this chapter, the focus is on the performance of customized and off-the-shelf SGs in the SG landing zones. Hence, idealized proximal neck geometries are considered whereas the aneurysm sac is not part of the model. The anisotropic, hyperelastic two-fiber model that was introduced in Section 3.3.2.1 is used to model the “healthy” vessel wall in the landing zone, whereas ILT and vessel calcifications are not considered. The SG is made up of a series of sinusoidally shaped nitinol stent rings attached to the graft. Although the material properties of marketed woven grafts and electrospun grafts are slightly different, the same material model is

applied to commercial and customized SGs to guarantee a fair comparison. Only the benefit of the customized shape of the SG is subject of the study of this chapter, independent of the slight differences in the material behavior of woven and electrospun grafts. Further, similar stent shapes with ten sinusoidally shaped periods, a stent height of $15\ \mathrm{mm}$ and a wire thickness of $0.4\ \mathrm{mm}$ as well as the same graft thickness of $0.08\ \mathrm{mm}$ are used for the model of the off-the-shelf SG and the customized SG. Stent predeformation of 15% is assumed for all stent rings. Material parameters of stent and graft are chosen as provided in Section 3.4.2, Table 3.3. The deployed configurations of the SGs are considered at a stationary blood pressure state of $130\ \mathrm{mmHg}$.

In a numerical proof of concept, general vessel morphologies (cf. Figure 7.3I), that are idealizations of realistic vessel shapes [174], are considered. The objective of this chapter is to show the advantage of second level customized SGs (cf. Figure 7.3II) that consider the morphology of the vessel compared to straight off-the-shelf SGs with a circular cross section. A mean inner vessel diameter $\bar{D}^{\mathrm{Ao}} = 25\ \mathrm{mm}$ is used for each of the consider vessel morphologies (cf. Figure 7.3I). In case of the vessel with elliptical cross section, the quadratic mean diameter

$$\bar{D}^{\mathrm{Ao}} = \sqrt{\frac{a^2 + b^2}{2}} \tag{7.2}$$

is used where $a = 20.5\ \mathrm{mm}$ is the length of the minor axis and $b = 28.8\ \mathrm{mm}$ is the length of the major axis of the ellipse (cf. Figure 7.3I).

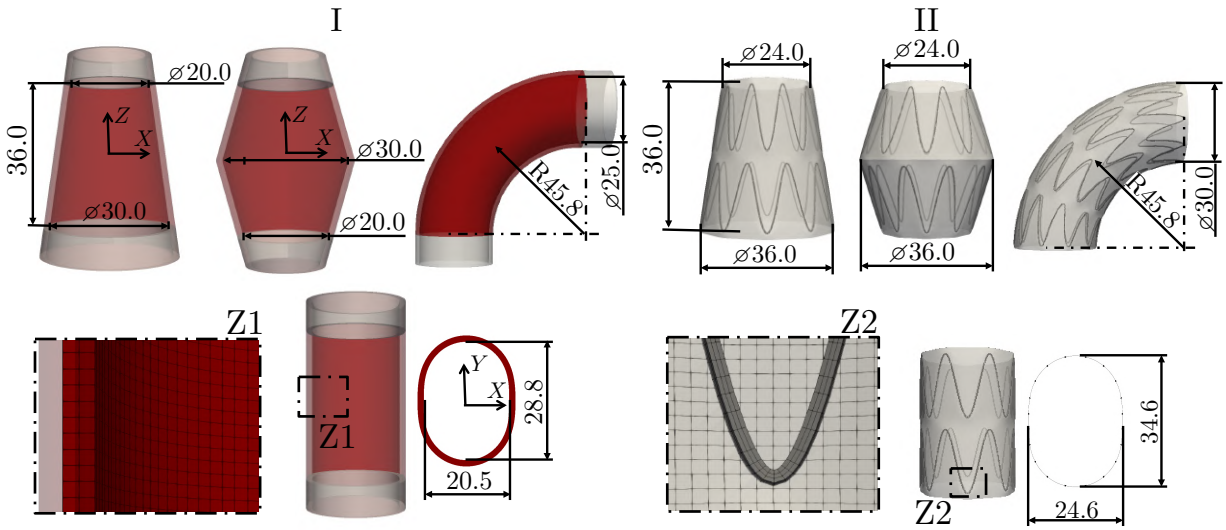

Figure 7.3 Exemplary depiction of vessel morphologies (I) and second level customized SGs(II). Discretization of the vessel (detail Z1) and SG model (detail Z2). Reproduced with permission from [110].

A meaningful comparison between the cylindrical off-the-shelf SGs and the second level customized SGs is only possible if a similar degree of SG oversizing is used for both types of SGs. The cylindrical off-the-shelf SG has a constant diameter $D^{\mathrm{SG}} = 30\ \mathrm{mm}$ which results in a variable degree of SG oversizing in the noncylindrical vessel. A mean SG oversizing $\bar{o} = 20\%$ is achieved by the constant SG diameter $D^{\mathrm{SG}} = 30\ \mathrm{mm}$ in the noncylindrical vessels with a mean inner diameter $\bar{D}^{\mathrm{Ao}} = 25\ \mathrm{mm}$ (cf. Equation (1.1)). The customized SGs, which have the same

morphology as the vessel, are sized such that they have a constant degree of SG oversizing of $o = 20\%$. Hence, the local diameter of customized SGs is

$$D^{\mathrm{SG}}(s) = 1.2 D^{\mathrm{Ao}}(s), \tag{7.3}$$

where s is the arc length of the vessel centerline and $D^{\mathrm{Ao}}(s)$ is the local inner vessel diameter in an orthogonal plane to the vessel centerline at location s. The same SG length of $36\ \mathrm{mm}$ ($72\ \mathrm{mm}$ for the curved SG) is used for the off-the-shelf and the customized SGs.

The consideration of curved vessels is of major importance as the IFU of SG manufacturers limit the application of EVAR mostly to neck angles below $60°$ since the likelihood of negative outcomes of off-the-shelf SGs is higher for larger neck angles. A vessel with an angle of $\gamma = 90°$ and a radius of curvature of $R = 45.8\ \mathrm{mm}$ is chosen for the current study (cf. Figure 7.3I). The radius of curvature of $R = 45.8\ \mathrm{mm}$ is chosen such that the arc length of the centerline of the curved vessel is $72\ \mathrm{mm}$. In keeping with the straight vessel examples, the curved vessel has a luminal diameter of $D^{\mathrm{Ao}} = 25\ \mathrm{mm}$. In contrast to the considered SGs of the straight vessels, the SGs for the curved vessel consist of four stent rings (cf. Figure 7.3II). All other SG related characteristics are equivalent to the examples of straight vessels and SGs.

In total, seven different straight vessels (cylindrical, conical, elliptical, barrel shaped, hourglass shaped and two irregularly shaped vessels) as well as one curved vessel with a cylindrical cross section are considered. For each of the eight different vessel morphologies, the in-silico EVAR outcomes of the customized SG and the off-the-shelf SG are compared qualitatively and quantitatively with respect to the following EVAR quality parameters (cf. Section 3.6): graft-vessel gap, graft-vessel sealing pattern, SG fixation force, stent stress as well as normal contact pressure between vessel and SG.

7.2. Results

In the following, the deployed states of the off-the-shelf SG and the customized SG are evaluated for all eight vessel morphologies with respect to the graft-vessel gap, the graft-vessel sealing pattern, the normal contact pressure and the stent stresses in Figure 7.4-7.8 as well as with respect to the SG fixation force in Figure 7.9. For improved visualization a projection of the results into the flat auxiliary $\breve{X}\breve{Z}$-plane is used in Figure 7.4-7.7. The auxiliary $\breve{X}\breve{Z}$-plane represents the uncoiled lateral surface of a virtual cylinder with radius $\breve{R} = 15\ \mathrm{mm}$ (cf. Appendix A.8).

7.2.1. Reference solution of a straight, cylindrical vessel

First, the in-silico EVAR outcome in a straight, cylindrical vessel is considered as a reference (cf. Figure 7.4). A straight and cylindrical vessel is considered to be the optimal vessel morphology for the deployment of a SG [233, 275]. For this setting, the off-the-shelf and the second level customized SG are identical.

A very uniform deployment and attachment of the cylindrical SG in the cylindrical vessel is obtained with moderate radial buckling of the graft (cf. Figure 7.4I) due to 20% oversizing of the SG compared to the vessel. The SG is in direct contact with the vessel only at the location of the

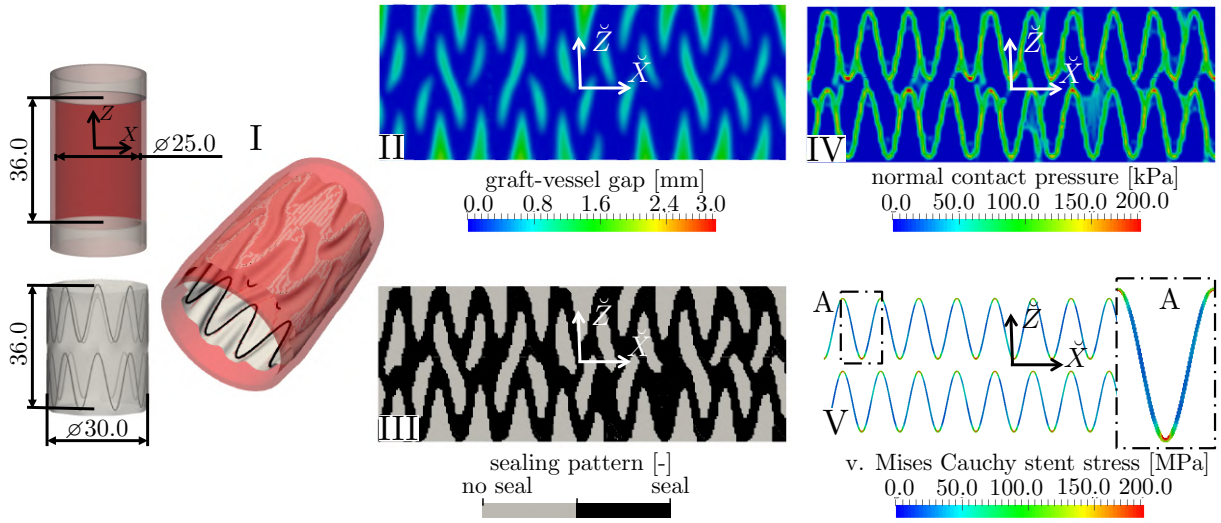

Figure 7.4 In-silico EVAR results of a straight, cylindrical SG deployed in a straight, cylindrical vessel: deployed state (I), graft-vessel gap (II), graft-vessel sealing pattern (III), normal contact pressures between SG and vessel (IV) and Cauchy von Mises stent stresses (V). Reproduced with permission from [110].

stent rings (cf. Figure 7.4III). Minor radial buckling of the graft leads to a maximum gap between SG and vessel of approximately 1.5 mm (cf. Figure 7.4II). A relatively uniform distribution of the normal contact pressure of approximately 100 kPa is found between SG and vessel at the location of the stent rings (cf. Figure 7.4IV). Maximum stent stresses of approximately 200 MPa occur in the curved parts of the stent rings (cf. Figure 7.4V). The stress distribution is identical for each stent loop.

7.2.2. Straight, conical vessel

The use of the cylindrical off-the-shelf SG with a constant diameter of 30 mm results in a degree of SG oversizing of 50% at the narrow end ($Z = 18$) of the conical vessel and a degree of SG oversizing of 0% at the wide end ($Z = -18$) of the conical vessel. In contrast to the off-the-shelf SG, the conical customized SG has a constant degree of SG oversizing of 20% along the total length of the SG (cf. Figure 7.5).

A clear difference between the in-silico EVAR outcome of the cylindrical off-the-shelf SG and the conical customized SG can be seen in Figure 7.5. A full expansion of the off-the-shelf SG at the wide end ($Z = -18$) and severe buckling of the graft at the narrow end ($Z = 18$) can be identified, which results in larger graft-vessel gaps of up to 2.5 mm at the narrow end ($Z = 18$). The off-the-shelf SG exerts high normal contact pressures at the narrow end. At the wide end ($Z = -18$) of the conical vessel, the off-the-shelf SG is not even in contact with the vessel. Unlike the off-the-shelf SG, the conical customized SG is more uniformly attached to the luminal vessel surface with a uniform distribution of normal contact pressures of approximately 100 kPa and very small gaps between SG and vessel. Due to the better and more uniform apposition of the SG to the vessel, the conical customized SG results in an approximately 1.5 times higher SG fixation force compared to the off-the-shelf SG in the same conical vessel (cf. Figure 7.9). The

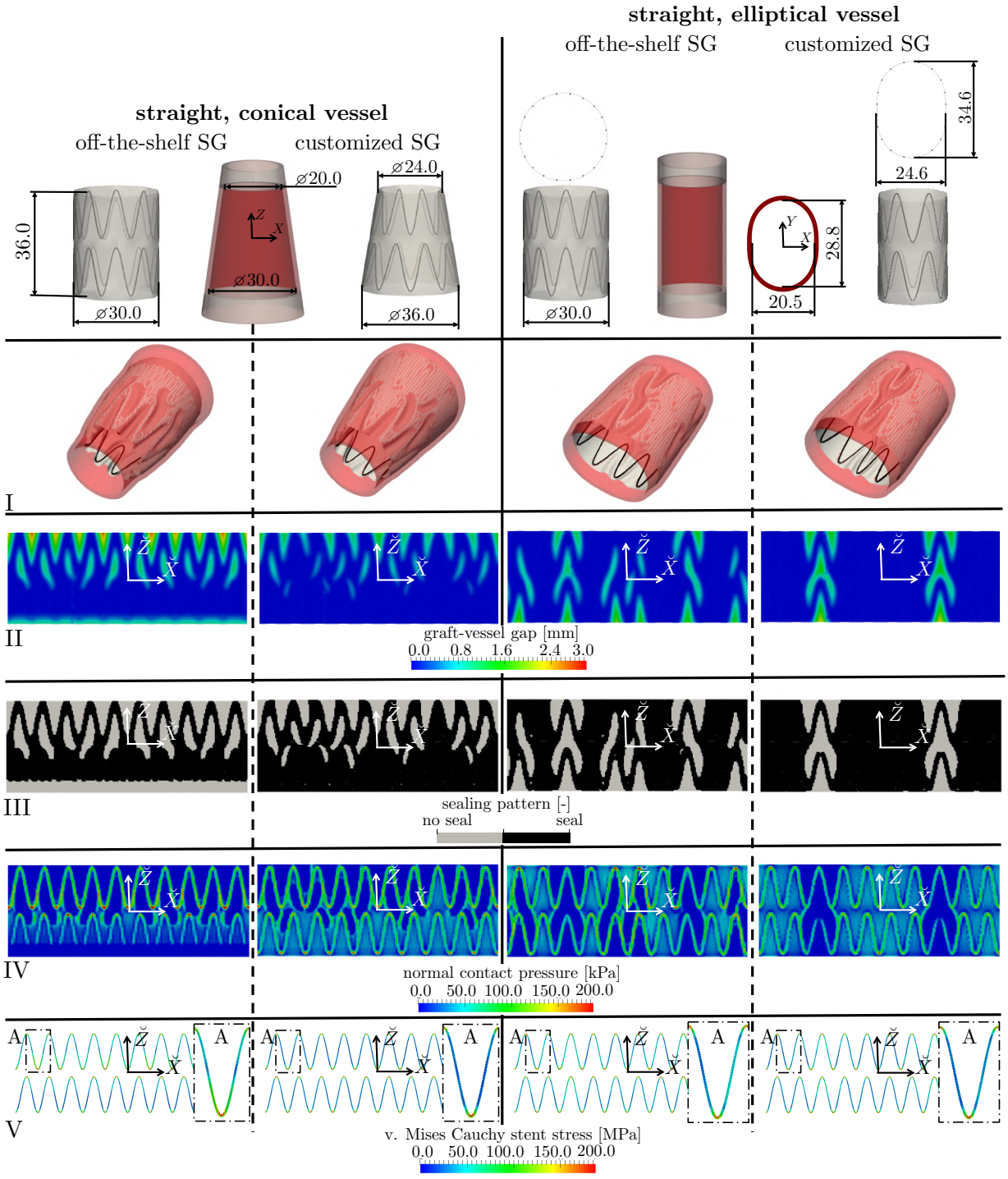

Figure 7.5 In-silico EVAR results of off-the-shelf SGs and customized SGs deployed in a straight, conical vessel as well as in a straight, elliptical vessel: deployed state (I), graft-vessel gap (II), graft-vessel sealing pattern (III), normal contact pressures between SG and vessel (IV) and Cauchy von Mises stent stresses (V). Reproduced with permission from [110].

deployed state of the customized SG in Figure 7.5I also shows that at the narrow end ($Z = -18$) more severe graft buckling is apparent than at the wide end ($Z = 18$), although constant SG oversizing of 20% is used along the total SG length. This shows that depending on the vessel diameter the same degree of SG oversizing can have a different influence on the deployed state.

7.2.3. Straight, elliptical vessel

Only very minor differences between the deployed state of the off-the-shelf SG and the customized SG can be identified for the straight, elliptical vessel (cf. Figure 7.5 and Figure 7.9). The graft-vessel sealing area is slightly larger for the customized SG since the off-the-shelf SG undergoes more graft buckling. The maximum graft-vessel gap, the distribution of stent stresses, the distribution of normal contact pressures as well as the SG fixation force of the off-the-shelf SG and the customized SG are almost identical and very similar to the results obtained for the straight, cylindrical vessel (Section 7.2.1).

7.2.4. Straight, barrel shaped vessel

The deployed off-the-shelf SG has minimal graft buckling at the wide region of the vessel ($Z = 0$) and severe buckling at the narrow regions of the barrel shaped vessel, which leads to relatively large graft-vessel gaps of up to $2.8\ \mathrm{mm}$ (cf. Figure 7.6). In contrast, the customized SG undergoes uniform graft buckling along the total SG and has a relatively uniform graft-vessel sealing pattern. The normal contact pressures between SG and vessel are slightly higher for the customized SG which results in an approximately 1.2 times higher SG fixation force (cf. Figure 7.9). No discernible differences in stent stresses can be identified between the deployed off-the-shelf SG and the deployed customized SG.

7.2.5. Straight, hourglass shaped vessel

In the hourglass shaped vessel, the cylindrical off-the-shelf SG exhibits severe buckling of the graft with graft-vessel gaps of up to $2.0\ \mathrm{mm}$ whereas the customized SG almost fully expands and exhibits only minor buckling (cf. Figure 7.6). The hourglass shaped customized SG in the hourglass shaped vessel leads to an almost complete seal between graft and vessel. The off-the-shelf SG produces high normal contact pressures between SG and vessel above $200\ \mathrm{kPa}$ at the narrow region of the vessel ($Z = 0$). Unlike the off-the-shelf SG, the distribution of normal contact pressures of the customized SG is very uniform without hotspots at the narrow region of the vessel ($Z = 0$). The stent stresses of the deployed customized SG are slightly higher than the stent stresses of the off-the-shelf SG (cf. Figure 7.6). The use of the customized SG leads to an approximately 1.5 times higher SG fixation force compared to the off-the-shelf SG (cf. Figure 7.9).

7.2.6. Straight, irregularly shaped vessels

In this section, the deployed SGs in two straight and irregularly shaped vessels are considered. The first vessel has a one-sided widening and the second vessel one-sided narrowing (cf. Figure 7.7).

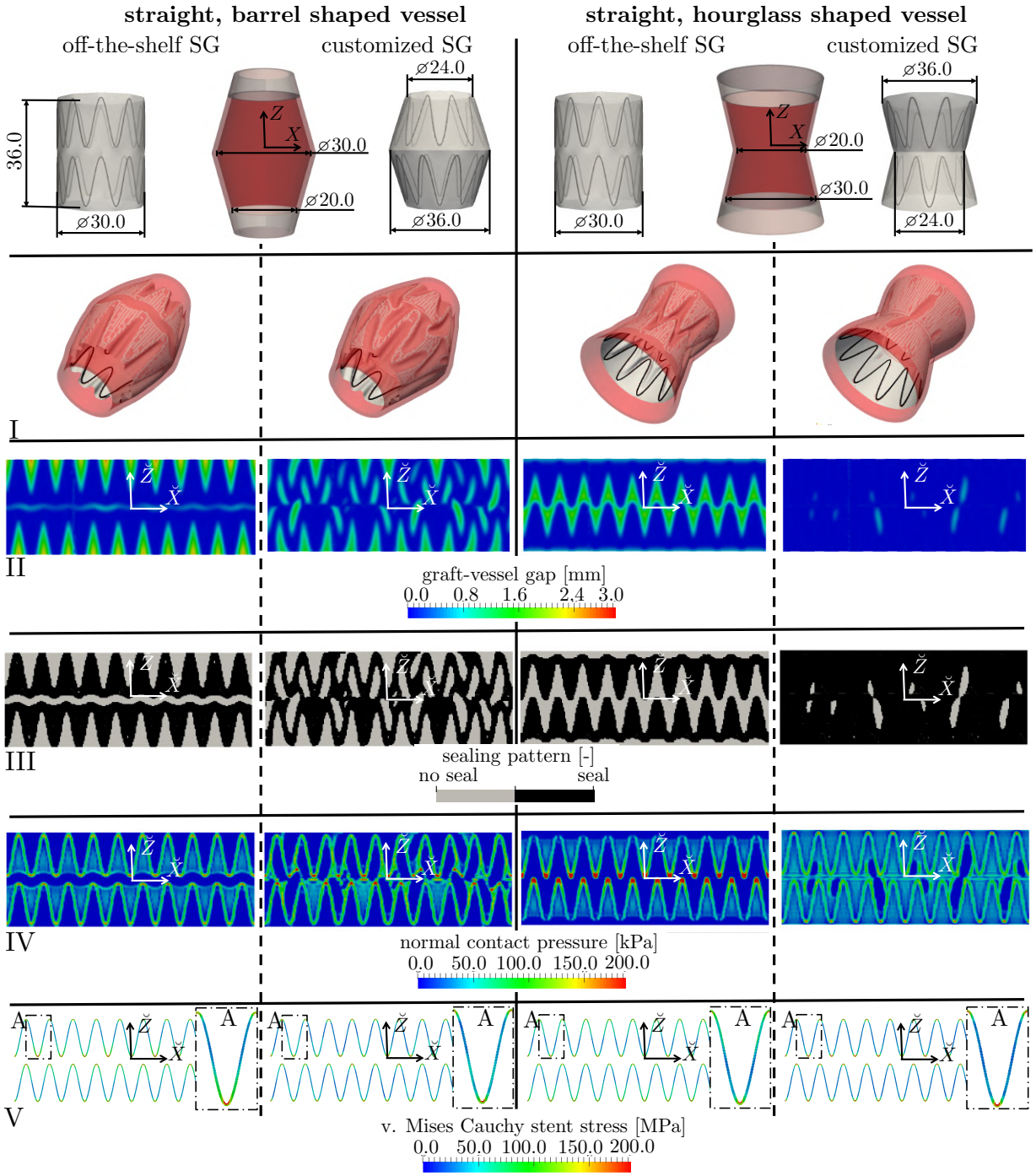

Figure 7.6 In-silico EVAR results of off-the-shelf SGs and customized SGs deployed in a straight, barrel shaped vessel as well as in a straight, hourglass shaped vessel: deployed state (I), graft-vessel gap (II), graft-vessel sealing pattern (III), normal contact pressures between SG and vessel (IV) and Cauchy von Mises stent stresses (V). Reproduced with permission from [110].

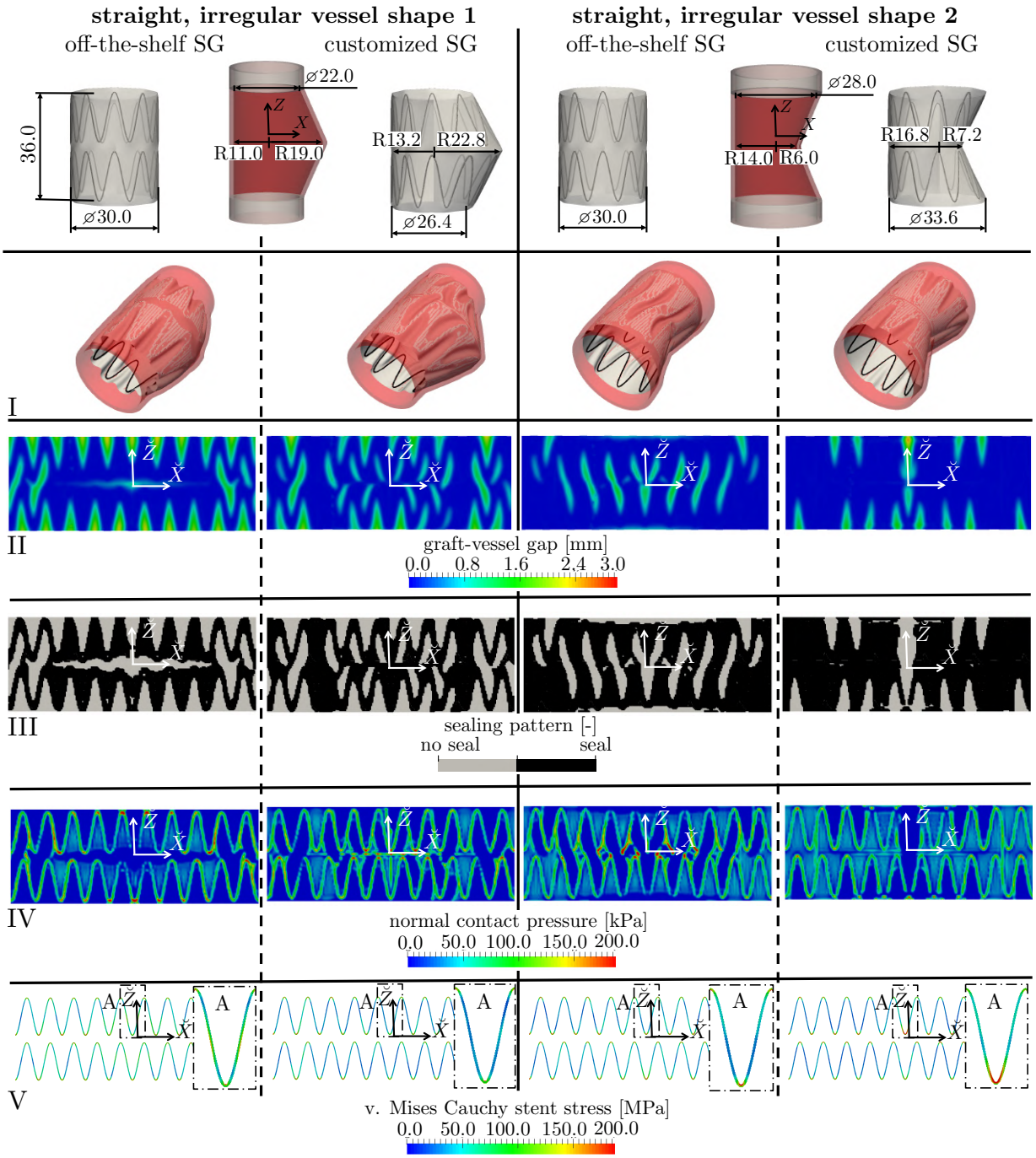

Figure 7.7 In-silico EVAR results of off-the-shelf SGs and customized SGs deployed in two different straight, irregularly shaped vessels: deployed state (I), graft-vessel gap (II), graft-vessel sealing pattern (III), normal contact pressures between SG and vessel (IV) and Cauchy von Mises stent stresses (V). Reproduced with permission from [110].

The results of the first irregular vessel are very similar to those from the straight, barrel shaped vessel (cf. Section 7.2.4) and the results of the second irregular vessel are very similar to the findings of the straight, hourglass shaped vessel (cf. Section 7.2.5). However, the difference between the off-the-shelf SG and the customized SG is less pronounced. While for the first irregular vessel model the customized SG results in slightly smaller stent stresses, for the second irregular vessel the customized SG results in slightly larger stent stresses in the highly curved parts of the stent rings.

7.2.7. Curved, cylindrical vessel

In the curved vessel (cf. Figure 7.8), the straight off-the-shelf SG of length $72\ \mathrm{mm}$ is longer than the potential vessel landing zone at the inner curvature and shorter than the potential vessel landing zone at the outer curvature of the vessel by $\Delta L = 19.6\ \mathrm{mm}$ as stated in Equation (7.1). Hence, the off-the-shelf SG is unable to adapt to the curved vessel, which results in severe longitudinal buckling of the graft at the inner curvature (cf. Figure 7.8I) where the SG is longer than the corresponding vessel attachment side. In contrast to the off-the-shelf SG, the curved customized SG can almost perfectly adapt to the curved vessel. Only minor radial graft buckling exists and no stent collapse occurs.

Strong out-of-plane asymmetry of the first and last stent ring of the straight off-the-shelf SG with an asymmetry angle α of approximately $20°$ exists (cf. Figure 7.8I). The cross section of the vessel in a plane defined by the asymmetry angle α is elliptical (cf. Figure 7.8I, slice S2). The circumference of the ellipse, i.e., the coverage length in circumferential direction, is larger than the circumference of a circular vessel cross section. Hence, asymmetric stent expansion results in a reduced degree of SG oversizing [256].

It is important to distinguish between the out-of-plane asymmetry and the in-plane asymmetry which defines an ovalization of the stent in the plane orthogonal to the postinterventional SG centerline (cf. Section 3.6.2). A purely geometric consideration of out-of-plane asymmetric stent expansion leads to the reduced degree of SG oversizing (cf. Equation (1.1))

$$
\begin{aligned}
o_{\mathrm{asym}} &= \frac{D^{\mathrm{SG}}}{\bar{D}^{\mathrm{Ao}}_{\mathrm{ellipse}}} - 1 = \frac{D^{\mathrm{SG}}}{\sqrt{\frac{(D^{\mathrm{Ao}})^2 + (D^{\mathrm{Ao}}/\cos(\alpha))^2}{2}}} - 1 = \frac{D^{\mathrm{SG}}}{D^{\mathrm{Ao}}} \sqrt{\frac{2}{1 + 1/(\cos(\alpha))^2}} - 1 \\
&= (o+1) \sqrt{\frac{2}{1 + 1/(\cos(\alpha))^2}} - 1 \leq o,
\end{aligned} \tag{7.4}
$$

where $\bar{D}^{\mathrm{Ao}}_{\mathrm{ellipse}}$ is the quadratic mean diameter of the ellipse that results from slicing the vessel in an angle of α with respect to the orthogonal plane to the vessel centerline (cf. Figure 7.8I, slice S2). Further, in (7.4), D^{SG} is the nominal SG diameter and D^{Ao} is the preinterventional vessel diameter. For the given asymmetric stent expansion of $\alpha \approx 20°$ of the off-the-shelf SG, the reduced degree of SG oversizing is $o_{\mathrm{asym}} \approx 16.2\%$ compared to the nominal degree of SG oversizing of $o = 20\%$. Unlike the off-the-shelf SG, the customized SG does not lead to asymmetric stent expansion in the angulated vessel ($\alpha \approx 0°$, Figure 7.8I), i.e., $o_{\mathrm{asym}} \approx o = 20\%$.

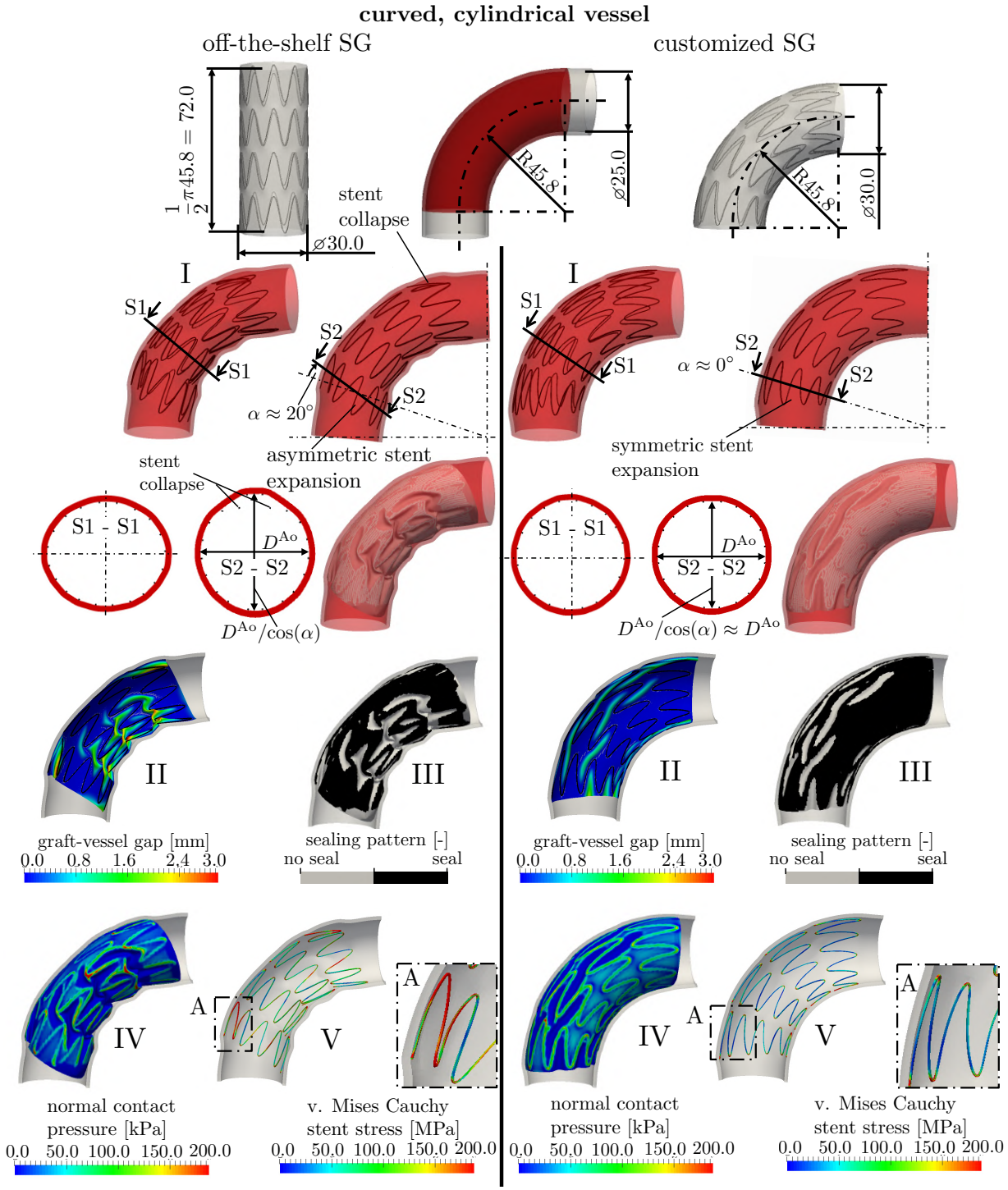

Figure 7.8 In-silico EVAR results of an off-the-shelf SG and a customized SG deployed in a curved, cylindrical vessel: deployed state (I), graft-vessel gap (II), graft-vessel sealing pattern (III), normal contact pressures between SG and vessel (IV) and Cauchy von Mises stent stresses (V). Modified figure reproduced with permission from [110].

Stent collapse at the outer curvature of the vessel at the first and last stent ring (cf. Figure 7.8I, slice S2) with poor attachment between SG and vessel are further negative consequences of the deployment of the straight off-the-shelf SG in the angulated vessel.

Large gaps between SG and vessel above $3\ \mathrm{mm}$ exist at the inner curvature of the vessel in the case of the off-the-shelf SG whereas the gaps between the customized SG and the curved vessel are below $1.5\ \mathrm{mm}$ (cf. Figure 7.8II). At the critical inner curve of the vessel, the customized SG is almost fully in contact with the vessel (cf. Figure 7.8III). Therefore, in total the graft-vessel sealing is better in the case of the customized SG.

Due to the nonuniform compression of the straight off-the-shelf SG in the curved vessel, the stent rings exhibit in-plane asymmetric deformation as defined in Equation (3.115) with $y^{\mathrm{S}} = 0.15$ (cf. Figure 7.8, slice S1). This oval shape of the stent rings in the deployed state results in higher normal contact pressures between SG and vessel at the major axis of the elliptical SG and lower normal contact pressures at the minor axis of the elliptical SG. In contrast to the straight off-the-shelf SG, the curved customized SG maintains its cylindrical shape even in the deployed state. Hence, the distribution of normal contact pressure is very uniform in the case of the customized SG (cf. Figure 7.8IV).

The perfect attachment of the customized SG in the curved vessel as well as the uniform distribution of normal contact pressure is also reflected in the around 1.5 times higher SG fixation force compared to the off-the-shelf SG (cf. Figure 7.9).

At the location of the collapsed stent parts of the off-the-shelf SG, high stent stresses of above $500\ \mathrm{MPa}$ occur. In contrast, maximum stent stresses of approximately $300\ \mathrm{MPa}$ occur only at the curved parts of the stent rings of the customized SG (cf. Figure 7.8V).

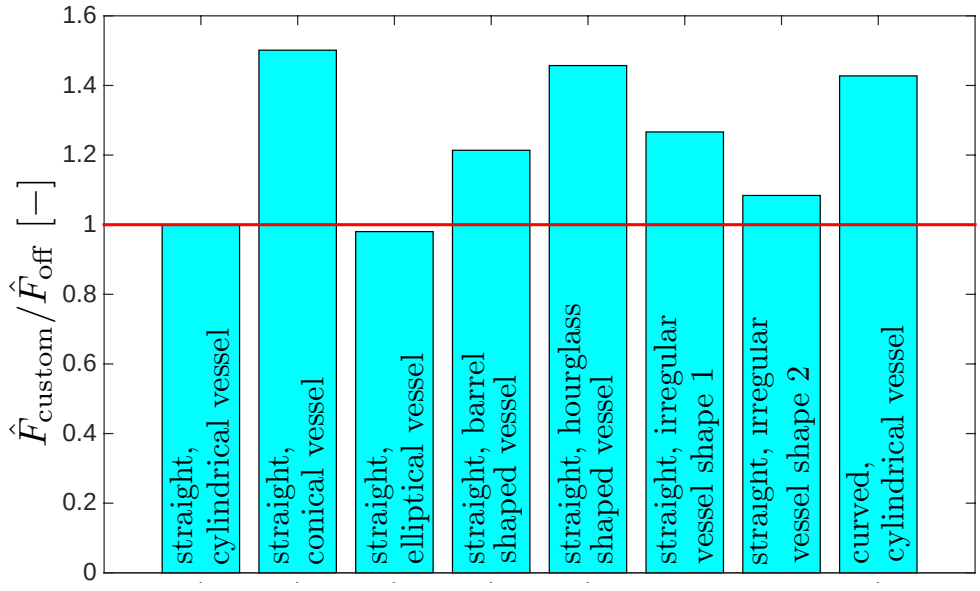

Figure 7.9 Relative difference of the SG fixation force as defined in Equation (3.105) of customized SGs $\hat{F}_{\mathrm{custom}}$ and off-the-shelf SGs $\hat{F}_{\mathrm{off}}$ in the eight considered vessel morphologies. Values of $\hat{F}_{\mathrm{custom}}/\hat{F}_{\mathrm{off}} > 1$ illustrate the improvement of customized SGs with respect to the SG fixation force. Reproduced with permission from [110].

7.3. Discussion

In the study of this chapter, second level customized SGs with a morphology equivalent to the morphology of the luminal vessel surface were investigated. The comparison of the in-silico EVAR outcome of straight, cylindrical off-the-shelf SGs and second level customized SGs has shown that using customized SGs can lead to considerably better EVAR outcomes. The numerical proof of concept of the benefit of customized SGs compared to off-the-shelf SGs was done with eight different vessel morphologies: seven straight vessels of different morphologies and one curved vessel with a circular cross section.

Noncylindrical vessel morphologies result in a variable degree of SG oversizing when cylindrical off-the-shelf SGs are used. For instance, in a conical vessel there is always the trade-off between SG undersizing (i.e., too little SG oversizing) at the wide end of the vessel and excessive SG oversizing at the narrow end of the vessel. This means there is always a trade-off between complications associated with SG undersizing [254, 257], such as SG migration and endoleaks, and complications related to excessive SG oversizing [46, 232], such as aortic neck dilatation. It was shown that by using second level customized SGs this inconsistency in choosing the degree of SG oversizing is obsolete. A constant degree of SG oversizing along the total length of the vessel landing zone can be achieved by using customized SGs that have the same morphology as the vessel.

Compared to the off-the-shelf SGs, the second level customized SGs led to reduced graft buckling and larger sealing areas. Furthermore, the maximum gaps between SG and vessel were smaller for customized SGs. In total, the improved attachment of the customized SG to the vessel is a clear indicator that second level customized SGs may be able to reduce the likelihood of type I endoleaks in challenging aortic morphologies. Furthermore, the more uniform attachment of the customized SG to the vessel led to a more uniform distribution of normal contact pressure. Whilst off-the-shelf SGs partly showed local hot spots of normal contact pressure with increased risk of vessel damage, the distribution of normal contact pressure of customized SGs mostly was very uniform even in nonuniform vessel geometries. Using the same degree of SG oversizing, the customized SGs exhibited considerably larger passive fixation forces than the off-the-shelf SGs for all investigated vessel morphologies. Therefore, the fixation of the SG in the landing zone is improved and the risk of SG migration may be reduced by application of second level customized SGs. Moreover, a smaller degree of SG oversizing could be used for customized SGs to obtain the same passive fixation force between SG and vessel and thus reduce potential negative effects of large SG oversizing [46, 232, 257].

The smallest impact of SG customization was identified for straight and elliptical vessels. It is explained by the relatively small lateral stiffness of a cylindrical SG. This means that little deformation energy is required to deform the cylindrical SG into an elliptical one. Hence, the mechanical behavior of the cylindrical off-the-shelf SG and the elliptical customized SG are almost identical.

The largest benefit of the customized SG compared to the off-the-shelf prosthesis could be observed for curved vessels as well as straight, conical vessels and straight, hourglass shaped vessels which are frequently observed vessel morphologies in clinical practice [174]. Using the customized SG in a curved vessel with an angle of $90°$ increased the passive SG fixation force by approximately 50%. This substantial difference in passive SG fixation force between the straight off-the-shelf SG and the curved customized SG can be explained by the following points:

- **The exploitation of the restricted length of the vessel landing zone is improved by second level customized SGs**, resulting in a considerably longer attachment length of the SG. A small SG attachment length is a frequently mentioned reason for insufficient SG fixation [6, 278]. The effective length of the vessel landing zone is larger at the outer curvature than at the inner curvature of a curved vessel [256]. The straight off-the-shelf SG, whose length is sized according to the length of the vessel centerline, is too short to be able to fully exploit the effective length of the vessel landing zone at the outer curvature of an angulated vessel.

- **Removal of longitudinal buckling at the inner curvature of angulated vessels by using second level customized SGs** which results in larger sealing areas and a more uniform radial force transmission between SG and vessel. The length of a straight off-the-shelf SG, which is sized according to the length of the vessel centerline, is longer than the effective length of the vessel landing zone at the inner curvature of the angulated vessel. This incompatibility between effective length of the vessel landing zone and the SG length leads to longitudinal compression of the graft at the inner curvature resulting in severe longitudinal buckling of the SG.

- **Second level customized SGs do not show out-of-plane asymmetric stent expansion** which is associated with the reduction of the degree of SG oversizing [256]. The most proximal and the most distal stent rings of the investigated off-the-shelf SG showed asymmetric stent expansion with a reduction of the degree of SG oversizing from a nominal value of 20% to 16.2%. A smaller degree of SG oversizing is commonly associated with smaller radial forces between SG and vessel (cf. Chapter 6).

- **No ovalization of second level customized SGs.** Bending of a straight off-the-shelf SG results in ovalization of the SG [58]. The SG with elliptic cross section does not fit perfectly into the vessel with circular cross section. It follows a nonuniform attachment between off-the-shelf SG and vessel with a nonuniform distribution of contact pressure.

- **Second level customized SGs lead to a reduced risk of stent collapse.** The straight off-the-shelf SG showed stent collapse located at the outer curvature of the vessel which is frequently observed for SGs in aortic necks with large angulation [6, 34, 123]. Stent collapse is associated with a loss of the SG-vessel attachment and hence a loss of radial force transmission between SG and vessel.

In addition to reduced SG-vessel attachment and a reduced fixation force, stent collapse of the off-the-shelf SG lead to locally high stent stresses within the region of the collapsed stent that may trigger SG fatigue [20, 127]. Second level customized SGs did not show any stent collapse in the angulated vessel. Thus, maximum stent stresses and the likelihood of SG fatigue is reduced.

Besides reduced complication likelihoods, these positive results of second level customized SGs in vessels with large angulation are very promising to increase the range of applicability of EVAR far beyond the IFU of current SG manufacturers, i.e., far beyond the current restrictions to vessels with a neck angle below $60°$.

7.4. Limitations

Apart from the simplifications stated in Section 3.7, the study of this chapter is affected by the use of idealizations of realistic vessel shapes. In future studies, the advantage of customized SGs in a realistic and patient-specific setting should be investigated. In the presented examples, only the aortic neck was considered, whereas the aneurysm sac was not part of the model.

Subject of this study was the investigation of the impact of the SG shape of customized SGs. Hence, the same material model was used for customized and off-the-shelf SGs. Slight differences in the material behavior of off-the-shelf SGs, that mostly use woven PET grafts, and the proposed customized electrospun grafts might have an impact on the outcome which should be investigated in further studies.

Further, the SG morphology of the considered customized SGs was equivalent to the luminal vessel morphology. In clinical practice, accurate placement of SGs is facilitated by radiopaque markers and radiographic guidance, but precise placement of the SG remains very challenging. Therefore, it is questionable if the morphology of the customized SG as an exact copy of the luminal vessel surface is the best choice taking into account the maximum SG placement accuracy. In the study of this chapter, perfect placement of the SG was assumed, i.e., the shape of the customized SG fit perfectly to the luminal vessel surface. A sensitivity study of the effect of misplacement of customized SGs on the EVAR outcome should be investigated in future studies. Furthermore, shape optimization [1, 15] could be used in a more general approach to find the optimal SG morphology of customized SGs for a specific vessel. Such a shape optimization of customized SGs should also consider the possible placement accuracy of the SG.

7.5. Conclusions

In clinical practice, the usage of EVAR is limited to relatively friendly aneurysm neck anatomies. Especially in challenging vessel morphologies, EVAR related complication likelihoods are still high. Many of these complications are associated with a mismatch between SG and vessel. Highly customized SGs can considerably improve the quality of EVAR outcomes with reduced complication likelihoods and can increase the applicability of EVAR to patients with extreme vessel morphologies.

In this chapter, models of highly customized SGs were presented which have the same morphology as the luminal vessel surface. The advantage of these highly customized SGs compared to off-the-shelf SGs was shown in a numerical proof of concept in several different vessel morphologies, where the in-silico EVAR outcome was compared with respect to several mechanical and geometrical EVAR quality parameters. Especially SG fixation forces can be improved drastically by this type of SG customization leading to a better fixation of the deployed SG and potentially reduced likelihoods of SG migration.

In summary, this numerical proof of concept showed that the presented type of customized SGs can meet the demand of personalized therapy and can improve the EVAR outcome. The study motivates further development of highly personalized SGs toward the usage of customized SGs in clinical practice.

8. Summary and outlook

In the following, the overall results and conclusions are recapitulated in Section 8.1 and an outlook on possible future work is given in Section 8.2.

8.1. Overall summary

In this thesis, a novel in-silico EVAR model has been developed, validated against real-world postinterventional measurements and extensively applied. The validated in-silico EVAR model is able to predict the postinterventional configuration of SG and vessel for patient-specific cases. The presented computational approaches go beyond available studies on in-silico EVAR with respect to the following major points:

- A geometrical and material nonlinear vessel model has been presented, which uses state of the art constitutive models of aortic wall, AAA wall, ILT and calcifications. Furthermore, the vessel model based on patient-specific preinterventional CT data considers vessel prestressing and physiological blood pressure states.

- A parameterized realistic and fully resolved SG model of bifurcated, commercial SG devices has been proposed. To this end, a novel stent predeformation methodology has been developed which is able to recover residual strains and stresses resulting from the real-world SG manufacturing process.

- A novel in-silico methodology has been presented to place and deploy SG models within patient-specific vessel models. In comparison to previously published in-silico SG P&D methodologies, the presented methodology uses a novel morphing algorithm to apply suitable deformation constraints directly to the degrees of freedom of the SG model during the in-silico SG placement. This results in a computationally more robust SG placement.

- SG parameter continuation has been established. Once the SG is deployed in the vessel, the initial SG diameter can be modified without having to repeat the in-silico SG placement and deployment. This enables efficient parameter and sensitivity studies with respect to SG oversizing.

- A novel qualitative and quantitative validation methodology of the in-silico EVAR model has been developed. It is based on the comparison of stent diameters between in-silico results and real-world postinterventional CT data pseudo-continuously along the total length of the deployed SG. Validation considering patient-specific cases revealed high accuracy of the in-silico EVAR model.

- Based on an engineering perspective, an assessment of the in-silico EVAR outcome with respect to EVAR related complication likelihoods by mechanical and geometrical parameters has been suggested. These parameters were investigated in realistic scenarios of four patient-specific cases.

- Fully parameterized models of synthetic, but realistic, SGs and vessels have been generated. Usage of these synthetic geometries in a large parameter study has revealed the dependence of the successful EVAR outcome upon vessel and SG parameters. In particular, patients with a large neck angle, a large vessel diameter and a short neck length are prone to developing SG related complications.

- A "new generation" SG for AAAs with challenging neck morphology has been presented. The advantage of these highly customized SGs, which have the same morphology as the luminal vessel surface, as compared to off-the-shelf SGs has been shown for several different idealized vessel morphologies.

Based on the results of this thesis, the developed and validated in-silico EVAR model is very promising for the use in clinical practice. This thesis has shown essential steps toward the application of such models to assist clinicians in the preinterventional planning of EVAR. The computational model allows the clinician to perform virtual parameter variations, such as the SG type and size, and assess the EVAR related complication likelihood before the actual intervention.

8.2. Outlook on future work

The outlook on future work is subdivided into the following two aspects:

Potential model improvements

The following forthcoming model improvements could be considered to further increase the accuracy and the applicability of the presented in-silico EVAR model.

First, the presented SG model assumes an isotropic graft material. However, PET grafts, as woven structures exhibit anisotropic material behavior [58, 228]. Hence, an in-plane orthotropic constitutive model, as proposed by [58], could improve the prediction of the mechanical graft behavior. Further, the SG model could be improved with respect to geometrical modeling of the most proximal stent ring that is not covered by the graft. In this thesis, the barbs of this stent ring were considered implicitly. However, the stent ring itself was not geometrically modeled.

Second, population-averaged mean values are assumed in the proposed vessel model. However, patient-specific data is associated with inter- and intrapatient variability of various parameters incorporated into the model [219]. A parameter study has shown that these uncertain parameters can have a profound impact on the EVAR outcome. Therefore, consideration of the variability of these parameters of the patient-specific vessel model could further improve the predictive quality of the in-silico EVAR model.

Third, most of the EVAR related complications are long-term complications that often arise several years after the intervention. In this time span of several years, growth and remodeling of

the vessel tissue can substantially change the postinterventional configuration of the vessel and the SG [142]. Hence, incorporation of the long-term behavior into the vessel model would allow to trace the development of EVAR related complications over time after the intervention.

Fourth, the deployed SG configuration might depend on clinician-specific factors, such as intrainterventional device rotation [61] or application of a molding angioplasty to further unfold the SG. Including clinician-specific factors into the in-silico EVAR model could further increase the predictive quality of the in-silico EVAR model for individual cases.

Fifth, besides these four model improvements, model reduction techniques [4] could be used in future to reduce computational costs of the EVAR simulation, thus enabling the application of in-silico EVAR models in clinical practice.

Large cohort validation and applications of the in-silico EVAR model

The developed in-silico EVAR model provides the basis of a wide range of potential model extensions and potential future applications. Hence, using the in-silico EVAR model and the process chain from patient-specific preinterventional medical imaging to the in-silico predicted postinterventional configurations, the following six possible future studies could be considered.

First, in this thesis, the validation of the in-silico EVAR model was based on only three patient-specific cases. Therefore, an extension to a cohort of an appropriate size should be considered in future studies. To this end, the process chain from patient-specific preinterventional medical imaging to the in-silico predicted postinterventional configuration should be further optimized toward a fully automated process chain.

Second, the ability of the proposed EVAR quality parameters to predict complication likelihoods needs to be validated. To this end, a large cohort of patient-specific cases should be investigated over several years. Correlation studies between EVAR quality parameters and related complications of these real-world cases can provide a clear link between the single EVAR quality parameters (e.g., SG drag force) and the EVAR related complication (e.g., SG migration). Further, such a correlation study could provide ranges of the EVAR quality parameters in which the parameters are acceptable and ranges in which a complication is very likely.

Third, advanced manufacturing techniques, such as 3D printing and electrospinning, enable manufacturing of highly customized SGs. Indeed, the optimal SG design depends on the patient-specific case and is difficult to estimate. Thus, as a potential step toward further personalization of the EVAR procedure, the in-silico EVAR model could be used as the basis for an optimization tool to design and build personalized SGs for challenging patient-specific cases. In Chapter 7, the benefit of customized SGs over off-the-shelf SGs was shown in a numerical proof of concept. However, the considered customized SGs were not the result of an optimization process, but for simplicity the morphology of the preinterventional luminal vessel surface was assumed as optimal SG design. Using a combination of topology and shape optimization, the performance of customized SGs could be further improved. Topology optimization could be used to develop the patient-specific optimal design of the stent rings with respect to fixation forces and uniform attachment to the vessel. Shape optimization could be a valuable tool to determine the optimal morphology of the entire SG for patient-specific cases.

Fourth, the in-silico EVAR model could be extended to advanced types of EVAR, such as FEVAR or CHEVAR. A predictive comparison of these different types of EVAR could be used

to find the optimal treatment for patient-specific cases already in the preinterventional planning phase.

Fifth, the demonstrated models and techniques could be directly transferred to related endovascular procedures, such as TEVAR or the endovascular treatment of stenosed or occluded blood vessels by deployment of self-expandable pure stents (i.e., without graft).

Sixth, stiff guidewires and other medical devices that are introduced into the vessel prior to the SG deployment can lead to substantial deformations of the vessel which can be the source of intrainterventional or postinterventional complications [87]. A preliminary study has shown that the developed framework can also be used for the prediction of guidewire induced vessel deformations. Such a predictive guidewire simulation could even be used as an extension of the proposed in-silico EVAR model, i.e., the results of the predicted deformations by the introduced guidewire could be used as starting point for the subsequent in-silico SG deployment.

A. Appendix

A.1. Summary of clinical data

Table A.1 Clinical summary of the four patients treated by EVAR that are considered in this thesis. Reproduced with permission from [107].

	Patient 1	Patient 2	Patient 3	Patient 4
Thrombus max. thickness [mm]	27.0	28.0	13.6	24.7
Calcification [-]	severe	moderate	moderate	moderate
Mean vessel diameters[a] (preinterventional) [mm]				
AAA sac	49.3	59.2	45.1	54.3
Proximal	25.5	25.6	25.1	25.4
Left iliac	14.5	19.8	14.3	12.4
Right iliac	14.0	16.6	13.1	15.2
SG manufacturer	Cook	Cook	Cook	Medtronic
SG prosthesis [-]				
Main body	TFFB-30-96-ZT	TFFB-30-96-ZT	TFFB-30-82-ZT	ETBF-32-16-C-166-E
Left iliac	ZSLE-16-90-ZT	ZSLE-24-74-ZT	ZSLE-16-74-ZT	ETLW-16-13-C-124-E
Right iliac	ZSLE-16-39-ZT	ZSLE-20-56-ZT	ZSLE-16-74-ZT	-[b]
Prosthesis oversizing [%]				
Proximal	18.6	17.2	19.5	26.0
Left iliac	10.3	21.2	11.9	4.8
Right iliac	14.3	20.5	22.1	5.3
Prosthesis overlap [mm]				
Main body - left iliac	31	35	30	30
Main body - right iliac	26	47	29	-[b]

[a] Diameter measured inner wall to inner wall

[b] In standard use, Medtronic Endurant^{TM} II SGs use only one docking leg

This section is taken from Hemmler et al. [107] with permission for reuse. Four clinical cases are considered in this thesis with patient characteristics provided in Table A.1. Patients 1-3

were treated by Cook Zenith Flex/Spiral-Z® SGs, whereas patient 4 was treated by a Medtronic Endurant™ II SG. The lengths of prosthesis overlaps between the main SG component and the iliac SG components are chosen such that the distal ends of the SG do not cover the bifurcation of the common iliac arteries to the external and internal iliac arteries. The prosthesis overlaps between the main SG component and the iliac components used in the EVAR interventions of the four patient-specific cases are provided in Table A.1. Based on the preinterventional vessel diameters D^{Ao} and the nominal diameter D^{SG} of the SG, the degree of SG oversizing (cf. Equation (1.1)) is provided in Table A.1 for the proximal and distal landing zones.

A.2. In-silico study of stent predeformation

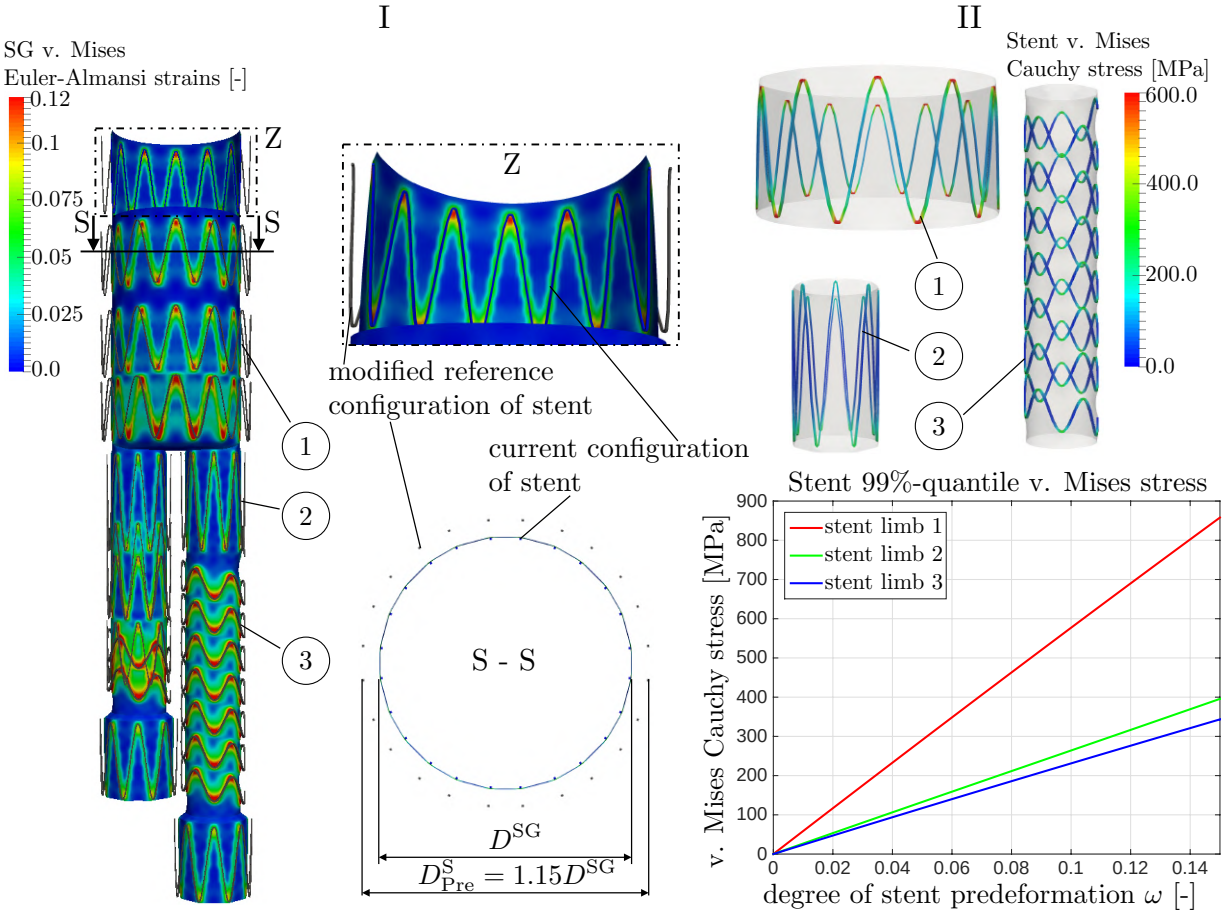

Figure A.1 Effect of stent predeformation ($\omega = 15\%$) on the stress and strain states of the CZ-SG model. Visualization of the SG von Mises Euler-Almansi strains (I) and the von Mises Cauchy stresses for three different stent limbs (II).

In Figure A.1, the effect of stent predeformation on the stress and strain states of the CZ-SG model for a spatially constant degree of stent predeformation of $\omega = 15\%$ is considered. The change in the reference configuration of the stent from $\Omega^{\mathrm{S}}_{\mathrm{I},0}$ to $\Omega^{\mathrm{S}}_{\mathrm{Pre},0}$ by application of the morphing map $\tilde{\boldsymbol{M}}^{-1}_{\mathrm{Pre}}$ according to Equations (3.62)-(3.65) in combination with the mesh tying

constraint between stent and graft results in residual strains and stresses within the predeformed SG.

In Figure A.1I, the von Mises Euler-Almansi strains of the SG after application of stent predeformation of $\omega = 15\%$ are visualized. The residual strains in the graft after the assembly of the SG with stent predeformation are very local at the regions connected to the stent. In Figure A.1II, residual stresses in three different stent limbs after the assembly of the SG with stent predeformation are investigated. The residual stresses in all three stent limbs increases approximately linearly with the degree of stent predeformation ω. Highest residual stresses occur at the curved regions of the stent limbs. The absolute value of the residual stresses also strongly depends on the shape as well as size of the stent limb and strongly varies among the three examined stent limbs.

A.3. Mesh convergence study

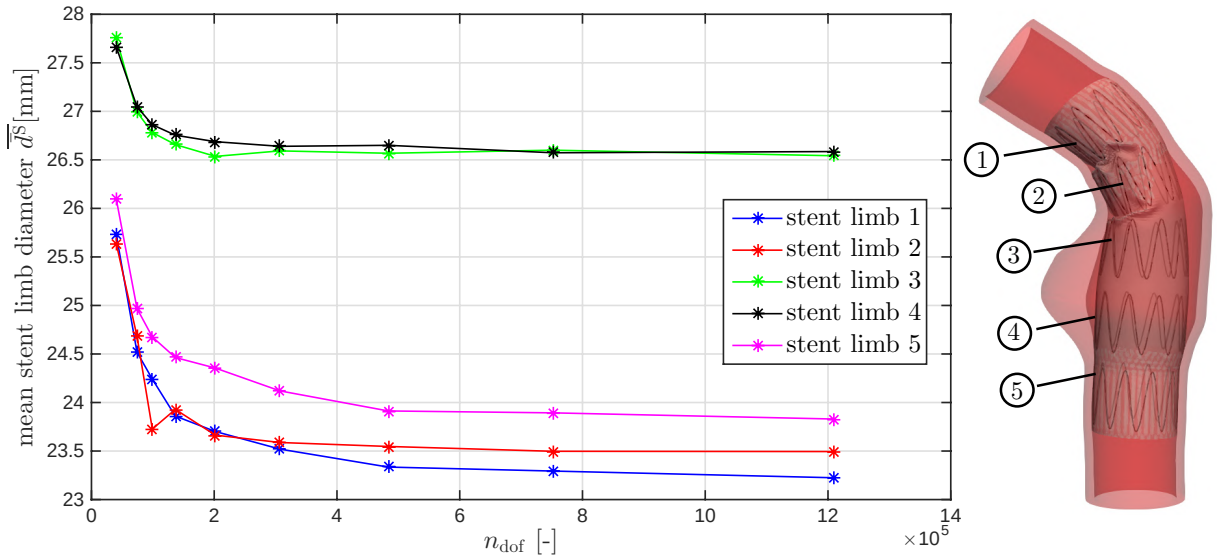

Figure A.2 Mesh convergence study: mean stent limb diameters $\overline{\overline{d^{\mathrm{S}}}}$ of the five stent limbs in the deployed state for different discretizations with the total number of degrees of freedom n_{dof}. Reproduced with permission from [109].

The following section is taken with permission from Hemmler et al. [109]. The mesh convergence is proven for the SG and vessel described by the basic parameters $\hat{g} \in \mathcal{G}$ provided in Table 6.2. In Figure A.2, the mean stent limb diameters $\overline{\overline{d^{\mathrm{S}}}}$ of the five stent limbs in the deployed state are investigated for different discretizations of vessel and SG. The mean stent limb diameter $\overline{\overline{d^{\mathrm{S}}}}$ is given by

$$\overline{\overline{d^{\mathrm{S}}}} = \frac{1}{h^{\mathrm{S}}_{\mathrm{De}}} \int_{s_0}^{s_1} \bar{d}^{\mathrm{S}}(s_{\mathrm{De}}) \mathrm{d}s_{\mathrm{De}}, \tag{A.1}$$

where $h^{\mathrm{S}}_{\mathrm{De}}$ is the stent limb height in the deployed state, s_0 describes the location of the most proximal point of the stent limb, s_1 is the location of the most distal point of the stent limb and $\bar{d}^{\mathrm{S}}(s_{\mathrm{De}})$ is the average stent diameter in an orthogonal slice at the location s_{De} as defined in Equation (3.95). Accordingly, $\overline{\bar{d}^{\mathrm{S}}}$ describes the mean diameter of one total stent limb, which is visualized for each of the five stent limbs in Figure A.2.

A.4. Study of path-dependency of the stent-graft parameter continuation approach

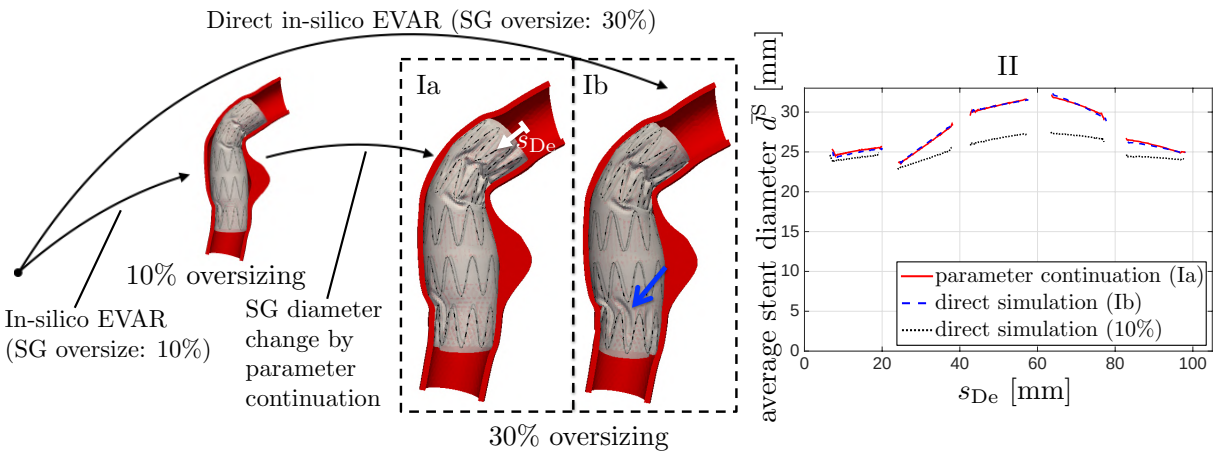

Figure A.3 Qualitative comparison of the results obtained by in-silico EVAR of a SG with 10% oversizing and subsequent SG parameter continuation to a SG oversizing of 30% (Ia) with the results obtained by in-silico EVAR of a SG with 30% oversizing; blue arrow indicates marginal differences in the graft buckling. Quantitative comparison (II) of the stent diameter of the direct simulation (Ib) and the simulation based on the SG parameter continuation approach (Ia) plotted along the arc length s_{De} of the centerline of the SG in the deployed state. Reproduced with permission from [106].

This section is reused with permission from Hemmler et al. [106]. As the given problem is nonlinear, the results might be path-dependent. Especially, the parameter continuation approach has to be validated carefully with respect to this issue. Hence, to show that the use of the parameter continuation approach for variable SG oversizing has a negligible influence on the final deployed state of the SG, the following comparison is made in Figure A.3: the results of the parameter continuation approach from 10% to 30% SG oversizing are compared to the results of the direct approach for a SG oversized by 30% and the same synthetic vessel geometry. Vessel and SG parameters of this comparison correspond to the basic parameter set described in Chapter 6.

Qualitatively only slight differences in the buckling pattern of the graft are visible (cf. Figure A.3I, blue arrow). Quantitatively, the absolute error $e = \bar{d}^{\mathrm{S}}_{\mathrm{cont}} - \bar{d}^{\mathrm{S}}_{\mathrm{dir}}$ between the resulting stent diameters of the two simulations are compared, where $\bar{d}^{\mathrm{S}}_{\mathrm{cont}}$ and $\bar{d}^{\mathrm{S}}_{\mathrm{dir}}$ are the average stent diameters in the deployed state after the parameter continuation approach and the direct approach,

respectively. This investigation shows an error with mean ± SD of $\mu_{\mathrm{e}} \pm \sigma_{\mathrm{e}} = 0.02 \pm 0.21\ \mathrm{mm}$ (cf. Figure A.3II). Hence, the path-dependency can be assumed to be small when the SG parameter continuation approach is used for the sizing of the SG diameter.

A.5. Calculation of percentiles

The following section is taken with permission from Hemmler et al. [109]. The q-percentile of a continuously given function $f(\boldsymbol{X})$ in the domain Ω_0^A with $\boldsymbol{X} \in \Omega_0^A$ is defined by

$$f_q^A : \frac{\int_{\Omega_0^A} \left(I_{(f(\boldsymbol{X}) - f_q^A) > 0} \right) \mathrm{d}V}{\int_{\Omega_0^A} \mathrm{d}V} = 1 - \frac{q}{100} \tag{A.2}$$

where $I_{(f(\boldsymbol{X}) - f_q^A) > 0}$ is the indicator function defined by

$$I_{(\bullet)>0} := \begin{cases} 1, & (\bullet) > 0, \\ 0, & (\bullet) \leq 0 \end{cases}. \tag{A.3}$$

A.6. Filtering of postinterventional CT data

This section is reused with permission from Hemmler et al. [107]. A moving average filter with a span of

$$l_{\mathrm{span}} = 2 n_{\mathrm{postIV}} \left\lceil \frac{\Delta z_{\mathrm{CT}}}{\bar{\Delta} s_{\mathrm{De}}} \right\rceil + 1 \tag{A.4}$$

is used to limit the impact of obvious artifacts in the stent diameter measurement from postinterventional CT data. In Equation (A.4), $\Delta z_{\mathrm{CT}} = 1\ \mathrm{mm}$ is the slice thickness of the postinterventional CT data, $n_{\mathrm{postIV}} = 3$ is a filtering constant that scales the length of the moving average filter. $\bar{\Delta} s_{\mathrm{De}}$ is the mean edge length of SG centerline $\mathcal{C}_{\mathrm{De}}$ in deployed state, i.e., the mean distance between the centers of gravity of the sets $\mathsf{A}_{\mathrm{I,postIV}}^{\mathrm{S},j}$ defined by Equation (3.92). The result of the filtering process is visualized for patient 3 in Figure A.4. Each asterisk denotes the measured average diameter $\bar{d}_{\mathrm{postIV}}^{\mathrm{S},(\Theta),j}$ of one distinct set $\mathsf{A}_{\mathrm{I,postIV}}^{\mathrm{S},(\Theta),j}$ of SG part $\Theta \in \{\mathrm{P}, \mathrm{L}, \mathrm{R}\}$.

A.7. Quality estimation of segmented data from postinterventional CT scans

This section is taken with permission from Hemmler et al. [107]. The quality of the postinterventional CT data is crucial for the reliability of a quantitative validation of the in-silico EVAR results, but local artifacts have a non-negligible effect on the segmentation of the stent from postinterventional CT data. To obtain an estimation of the measurement inaccuracy due to the vagueness in the segmentation process of the stent from postinterventional CT data, the relative difference between the measured average diameter $\bar{d}_{\mathrm{postIV}}^{\mathrm{S},(\Theta),j}$ and the average diameter of the

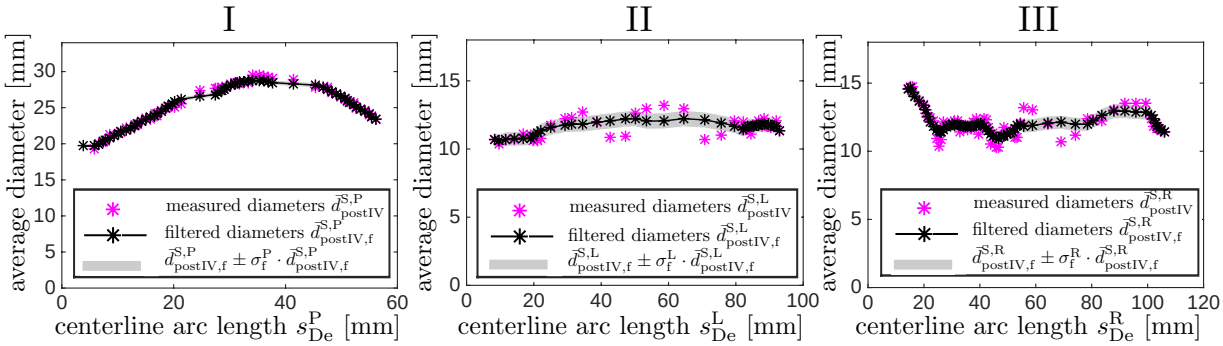

Figure A.4 Difference between measured average stent diameters $\bar{d}^{\mathrm{S},j}_{\mathrm{postIV}}$ from postinterventional CT data and filtered average stent diameters $\bar{d}^{\mathrm{S},j}_{\mathrm{postIV,f}}$ as well as visualization of the standard deviation σ_{f} (cf. Appendix A.7) for the proximal SG part (I), the left iliac SG part (II) and the right iliac SG part (III) of patient 3. Reproduced with permission from [107].

filtered data $\bar{d}^{\mathrm{S},(\Theta),j}_{\mathrm{postIV,f}}$ is defined by

$$\varepsilon_f^{(\Theta),j} = \frac{\bar{d}^{\mathrm{S},(\Theta),j}_{\mathrm{postIV}} - \bar{d}^{\mathrm{S},(\Theta),j}_{\mathrm{postIV,f}}}{\bar{d}^{\mathrm{S},(\Theta),j}_{\mathrm{postIV,f}}}, \quad \forall j = 1, 2, ..., n_{\mathrm{C}}^{(\Theta)}. \tag{A.5}$$

Further, the standard deviation

$$\sigma_f^{(\Theta)} = \sqrt{\frac{1}{n_{\mathrm{C}}^{(\Theta)}} \sum_{j=1,2,...,n_{\mathrm{C}}^{(\Theta)}} \left(\varepsilon_f^{(\Theta),j} - \mu_f^{(\Theta)}\right)^2} \tag{A.6}$$

is calculated, where

$$\mu_f^{(\Theta)} = \frac{1}{n_{\mathrm{C}}^{(\Theta)}} \sum_{j=1,2,...,n_{\mathrm{C}}^{(\Theta)}} \varepsilon_f^{(\Theta),j} \tag{A.7}$$

is the mean relative difference. $n_{\mathrm{C}}^{(\Theta)}$ is the number of points describing the piecewise linear curve $\mathcal{C}_{\mathrm{De}}^{(\Theta)}$ which is equivalent to the number of discrete sets $\mathsf{A}_{\mathrm{I,postIV}}^{(\Theta),j}$. Equations (A.5)-(A.7), can be equally applied to all three SG parts $\Theta \in \{\mathrm{P}, \mathrm{L}, \mathrm{R}\}$. In Figure A.4, the plain stent diameters from postinterventional CT data $\bar{d}^{\mathrm{S},(\Theta),j}_{\mathrm{postIV}}$, the filtered stent diameters $\bar{d}^{\mathrm{S},(\Theta),j}_{\mathrm{postIV,f}}$ and the standard deviation $\sigma_f^{(\Theta)}$ are opposed for patient 3.

A large standard deviation $\sigma_f^{(\Theta)}$ of the relative difference $\varepsilon_f^{(\Theta),j}$ is an indicator that the measurements are strongly affected by local artifacts of the segmented stent. The standard deviation $\sigma_{\mathrm{f}}^{(\Theta)}$ is small for the proximal SG parts ($\sigma_{\mathrm{f}}^{\mathrm{P}} \leq 2.0\%$) but more significant for the iliac SG parts (cf. Table A.2) due to two main reasons:

- The segmentation process of the Cook Zenith Spiral-Z® SGs from postinterventional CT data is more difficult as those stent limbs are less clearly visible.

- $\sigma_{\mathrm{f}}^{(\Theta)}$ is the standard deviation of the relative difference between the measured average diameters $\bar{d}_{\mathrm{postIV}}^{\mathrm{S},j}$ and the filtered average diameters $\bar{d}_{\mathrm{postIV,f}}^{\mathrm{S},(\Theta),j}$. Hence, local artifacts in the postinterventional CT data of equivalent size would have a larger relative impact on $\sigma_{\mathrm{f}}^{(\Theta)}$ in regions of small stent diameters such as in iliac SG parts.

Table A.2 Standard deviation $\sigma_{\mathrm{f}}^{(\Theta)}$ of the relative difference between the measured average diameter $\bar{d}_{\mathrm{postIV}}^{\mathrm{S},(\Theta),j}$ and the average diameter of the filtered data $\bar{d}_{\mathrm{postIV,f}}^{\mathrm{S},(\Theta),j}$ of the postinterventional CT data in [%] according to Equation (A.6) for patient 1-3 and the three SG parts. Reproduced with permission from [107].

σ_{f} [%]	Patient 1	Patient 2	Patient 3
Main part	0.8	2.0	1.3
Left iliac part	2.7	3.8	5.1
Right iliac part	3.8	4.8	4.2

A.8. Auxiliary plane for visualization of the results

The following section is taken with permission from Hemmler et al. [110]. For improved visualization of the results in the SG landing zones, a projection of the results into the flat auxiliary $\breve{X}\breve{Z}$-plane is used. The auxiliary $\breve{X}\breve{Z}$-plane represents the uncoiled lateral surface of a virtual cylinder with radius $\breve{R}$. The coordinates of the flat auxiliary $\breve{X}\breve{Z}$-plane ($\breve{Y} = 0$) are given by

$$\breve{X} = \begin{cases} \breve{R}\left(\arctan\left(\frac{Y}{X}\right) + \frac{\pi}{2}\right), & Y \leq 0 \\ \breve{R}\left(\arctan\left(\frac{Y}{X}\right) - \frac{\pi}{2}\right), & Y > 0 \end{cases} \tag{A.8}$$

$$\breve{Z} = Z \tag{A.9}$$

where X and Y are the reference coordinates of the SG and $\breve{R}$ is the radius of a virtual cylinder.

A.9. Detailed overview of the parameter study

This section is used with permission from Hemmler et al. [109]. In the Figures A.5-A.10, a detailed overview of the parameter study of Chapter 6 is given.

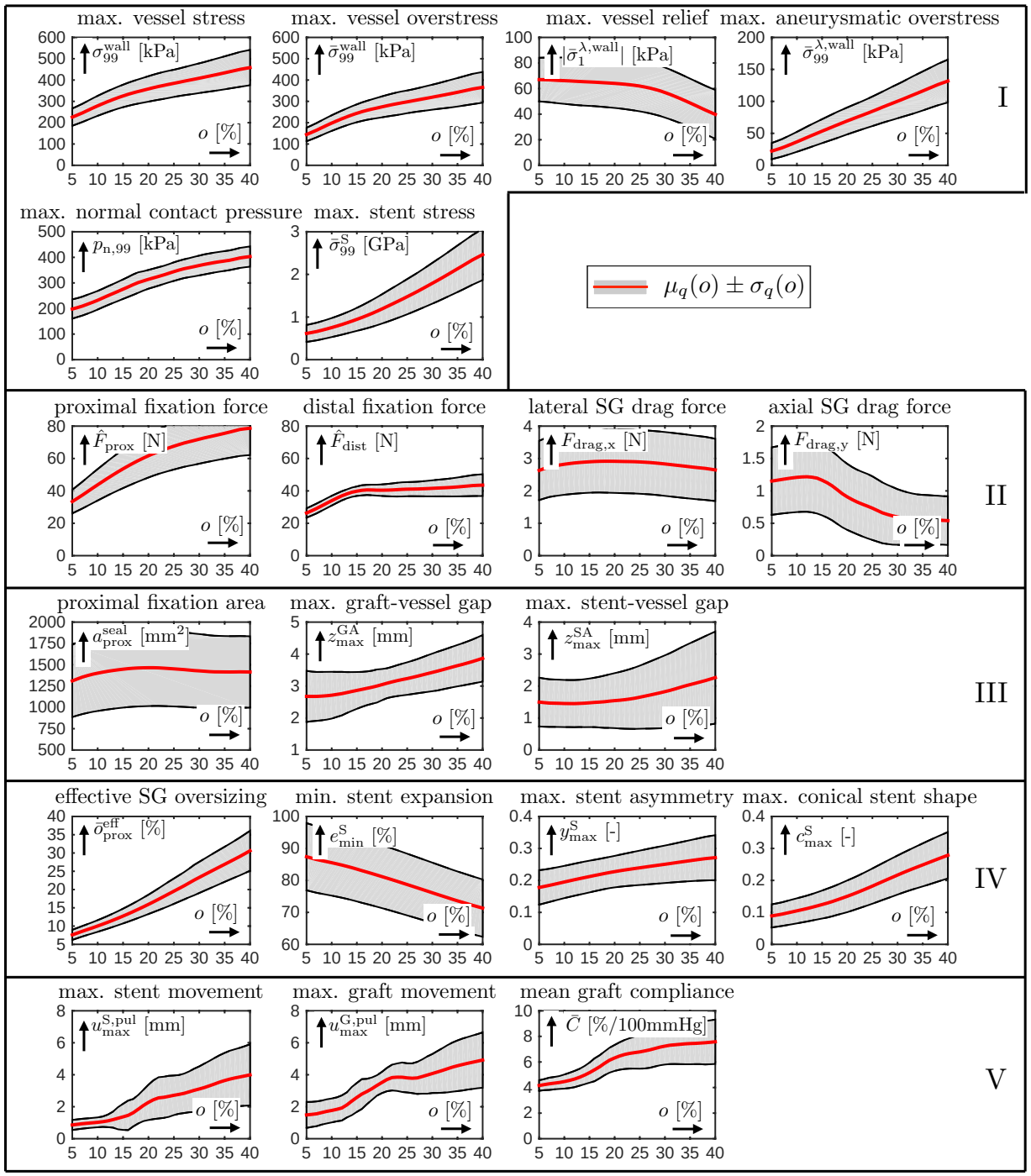

Figure A.5 Mean±std of all EVAR quality parameters $q \in \mathcal{Q}$ according to Equation (6.10) and (6.11) depending on the degree of SG oversizing o. The EVAR quality parameters $q \in \mathcal{Q}$ are sorted as they had been introduced in Section 3.6.2: vessel and SG stresses and tractions (I), drag and fixation forces(II), quality of seal (III), geometrical parameters of the deployed SG (IV) and parameters depending on the pulsatile blood pressure (V). Reproduced with permission from [109].

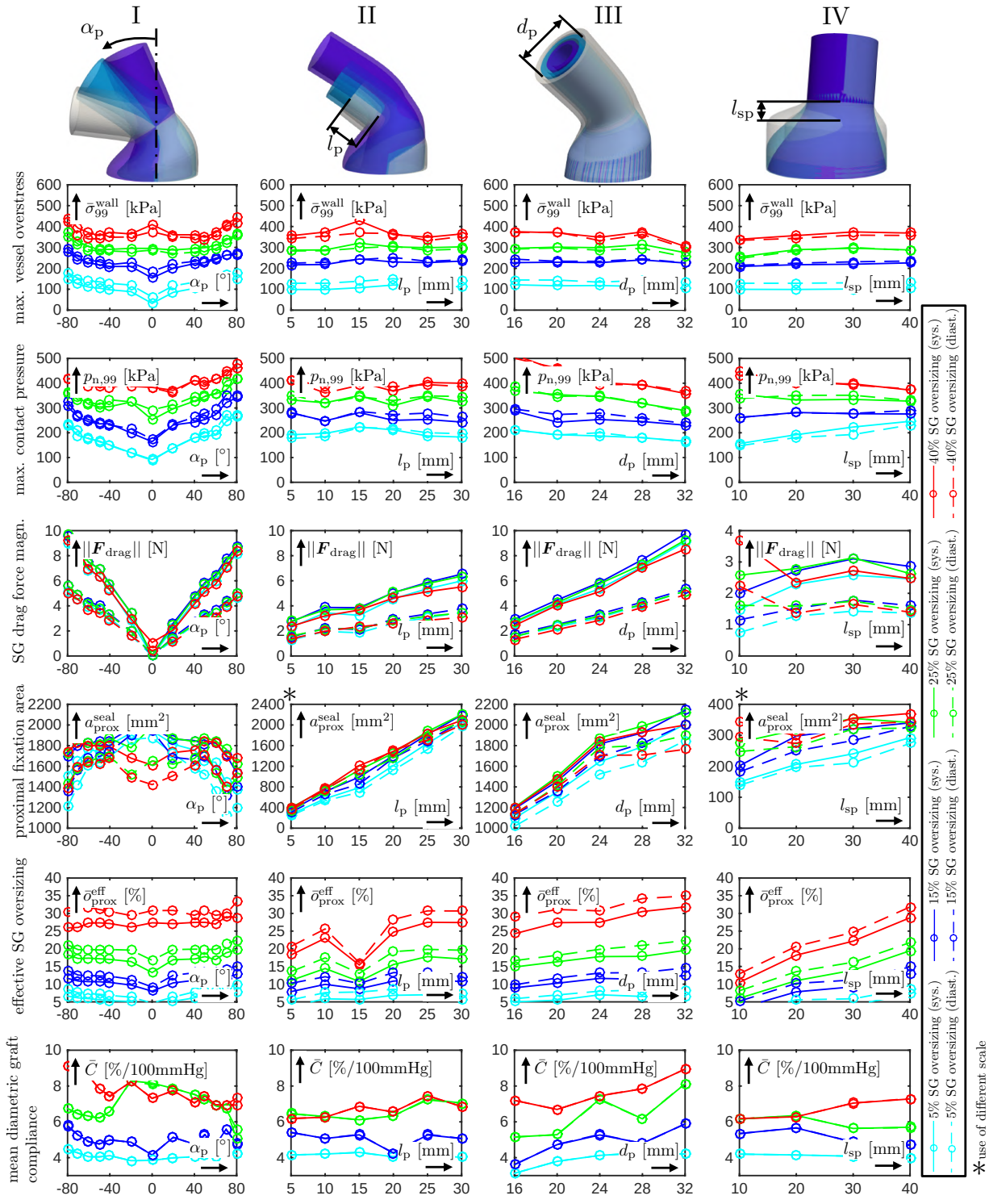

Figure A.6 Selected EVAR quality parameters plotted over variations of the proximal neck angle α_p (I), the proximal neck length l_p (II), the proximal neck diameter d_p (III) and the proximal AAA shoulder length l_{sp} (IV) for different degrees of SG oversizing o as well as different blood pressure states $p^{diast} = 80$ mmHg and $p^{sys} = 130$ mmHg. Reproduced with permission from [109].

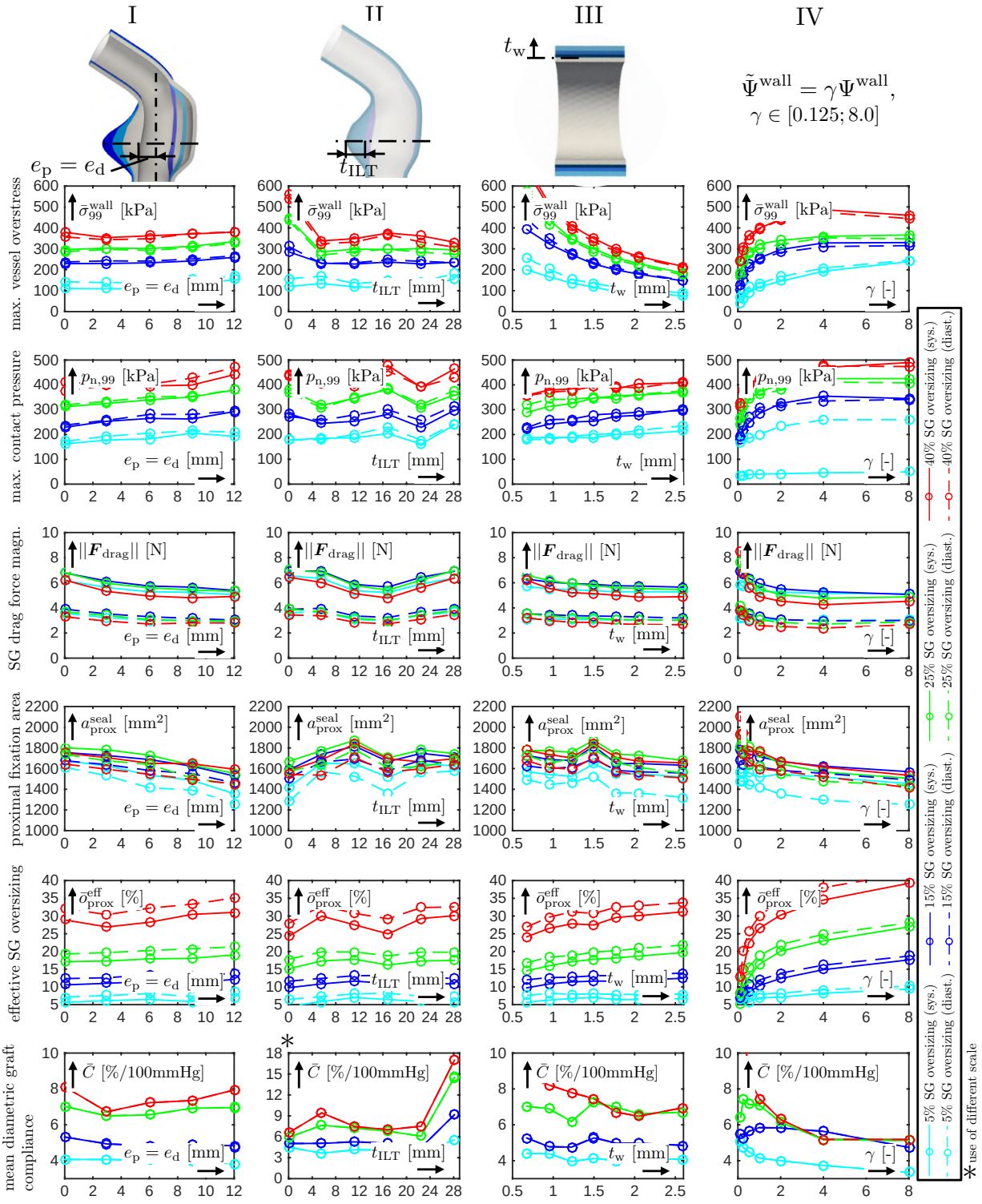

Figure A.7 Selected EVAR quality parameters plotted over variations of the aneurysm eccentricity $e_p = e_d$ (I), the ILT thickness t_{ILT} (II), the vessel wall thickness t_w (III) and the vessel wall stiffness γ (IV) for different degrees of SG oversizing o as well as different blood pressure states $p^{diast} = 80$ mmHg and $p^{sys} = 130$ mmHg. Reproduced with permission from [109].

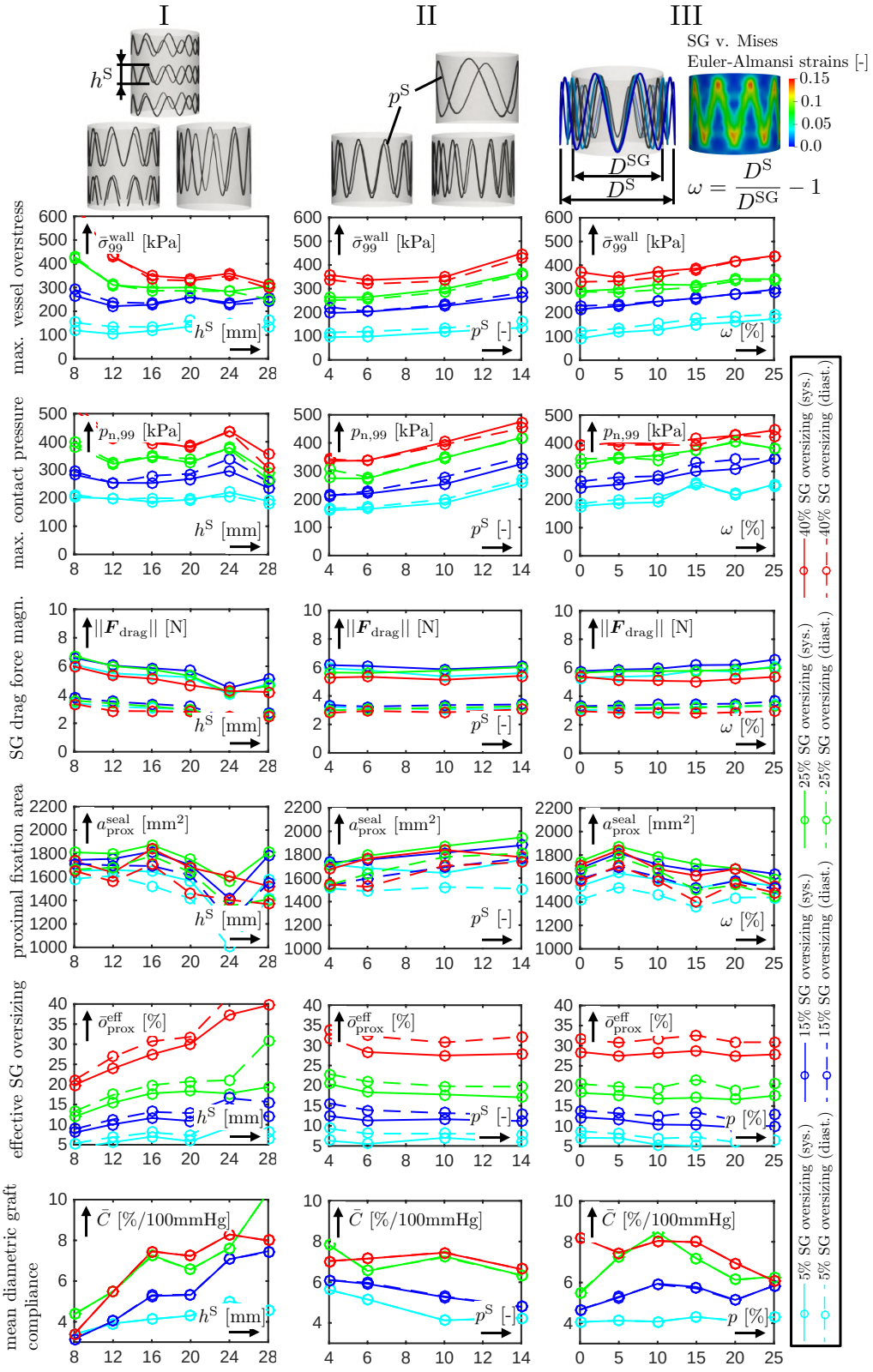

Figure A.8 Selected EVAR quality parameters plotted over variations of the stent limb height h^S(I), the number of periods per stent limb p^S (II) and the degree of stent predeformation ω (III) for different degrees of SG oversizing o as well as different blood pressure states $p^{diast} = 80$ mmHg and $p^{sys} = 130$ mmHg. Reproduced with permission from [109].

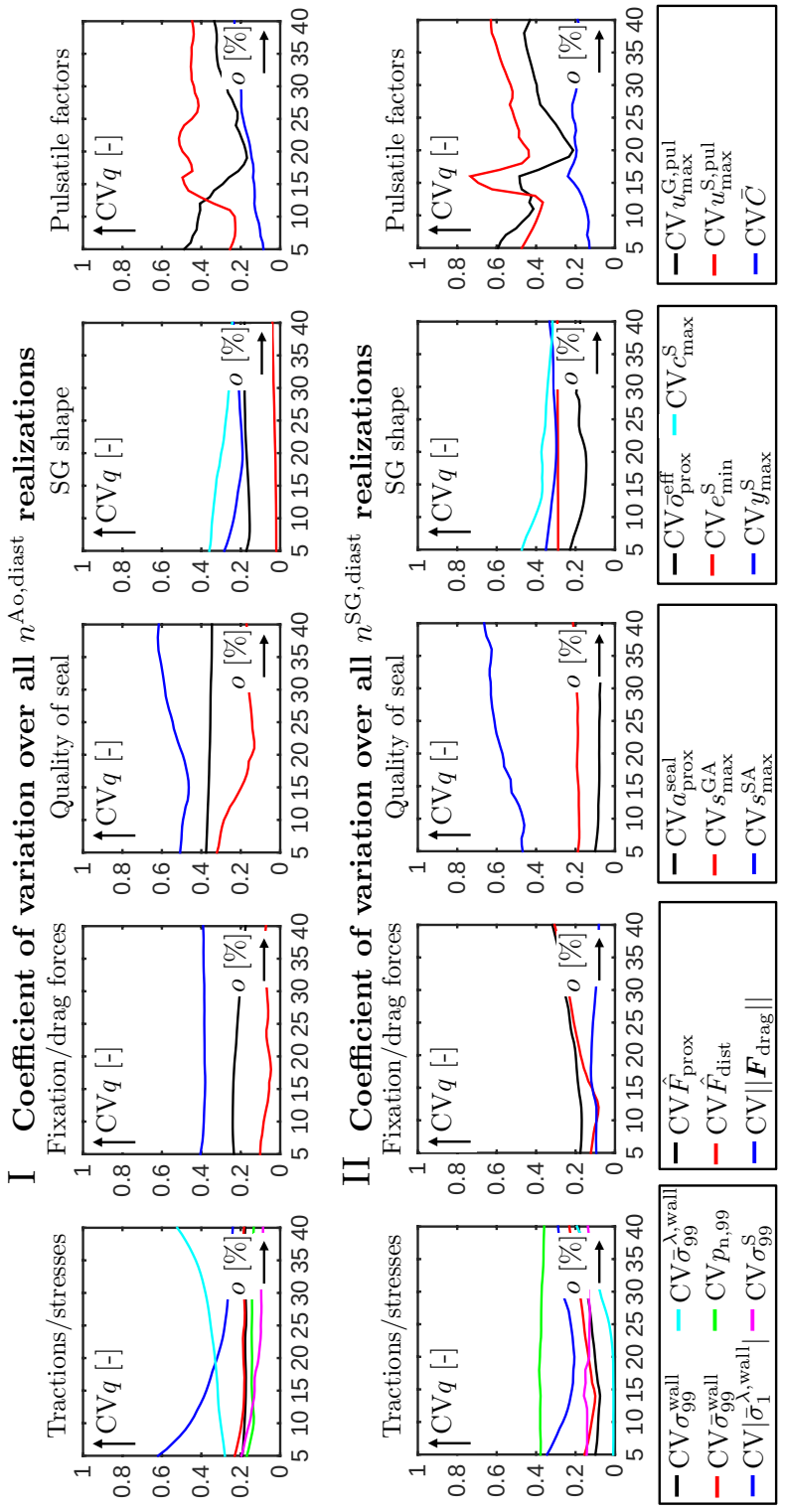

Figure A.9 Coefficient of variation CVq (cf. Equation (6.9)) over all $n^{\mathrm{Ao,diast}}$ realizations with different vessel geometries (I) as well as over all $n^{\mathrm{SG,diast}}$ realizations with different SG geometries (II) at the diastolic pressure level of $p^{\mathrm{diast}} = 80$ mmHg as a function of the degree of SG oversizing o. CVq is the coefficient of variation of EVAR quality parameter $q \in \mathcal{Q}$. For instance, CV$\sigma_{99}^{\mathrm{wall}}$ is the coefficient of variation of the maximum vessel wall stress $\sigma_{99}^{\mathrm{wall}}$. Reproduced with permission from [109].

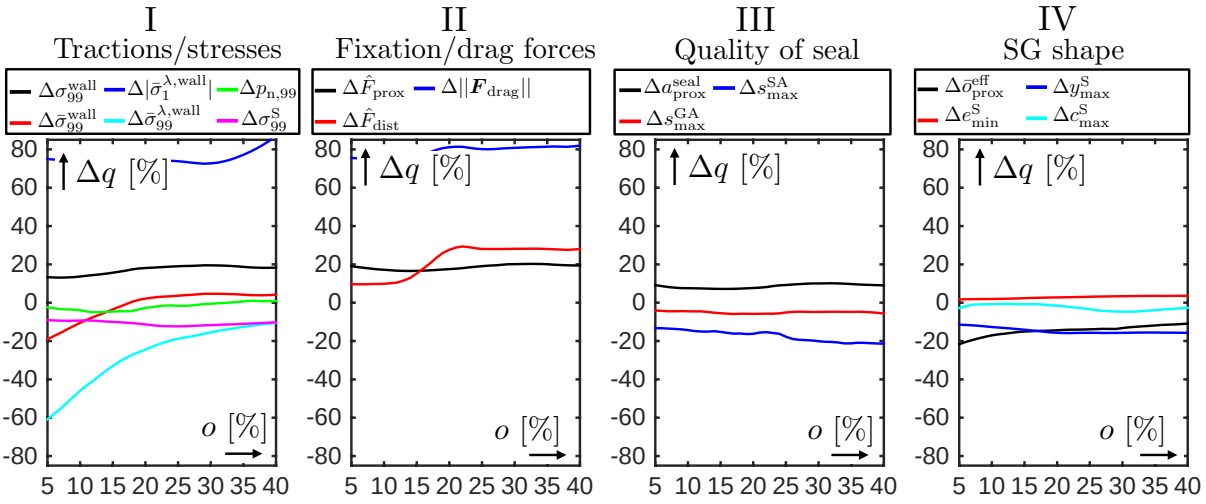

Figure A.10 Influence of the arterial blood pressure state Δq according to Equation (6.16) on EVAR quality parameters q as a function of the degree of SG oversizing o. Δq describes the relative change of the EVAR quality parameter $q \in \mathcal{Q}$ by a change of the arterial blood pressure from the diastolic state $p^{\text{diast}} = 80\ \text{mmHg}$ to the systolic state $p^{\text{sys}} = 130\ \text{mmHg}$. For instance, $\Delta\sigma_{99}^{\text{wall}}$ is the relative change of the maximum vessel wall stress $\sigma_{99}^{\text{wall}}$ induced by the blood pressure change. Reproduced with permission from [109].

Bibliography

[1] E. M. K. Abad, D. Pasini, and R. Cecere, Shape optimization of stress concentration-free lattice for self-expandable nitinol stent-grafts, *Journal of biomechanics* **45**, 1028–1035, 2012.

[2] A. F. AbuRahma, J. E. Campbell, A. Y. Mousa, S. M. Hass, P. A. Stone, A. Jain, A. Nanjundappa, L. S. Dean, T. Keiffer, and J. Habib, Clinical outcomes for hostile versus favorable aortic neck anatomy in endovascular aortic aneurysm repair using modular devices, *Journal of vascular surgery* **54**, 13–21, 2011.

[3] A. F. AbuRahma, M. Yacoub, A. Y. Mousa, S. Abu-Halimah, S. M. Hass, J. Kazil, Z. T. AbuRahma, M. Srivastava, L. S. Dean, and P. A. Stone, Aortic neck anatomic features and predictors of outcomes in endovascular repair of abdominal aortic aneurysms following vs not following instructions for use, *Journal of the American College of Surgeons* **222**, 579–589, 2016.

[4] V. A. Acosta Santamaría, G. Daniel, D. Perrin, J. N. Albertini, E. Rosset, and S. Avril, Model reduction methodology for computational simulations of endovascular repair, *Computer Methods in Biomechanics and Biomedical Engineering* **21**, 139–148, 2018.

[5] M. Alexa, D. Cohen-Or, and D. Levin, As-rigid-as-possible shape interpolation, In *Proceedings of the 27th Annual Conference on Computer Graphics and Interactive Techniques*, pages 157–164, New York, NY, USA, 2000, ACM Press/Addison-Wesley Publishing Co.

[6] H.-E. Altnji, B. Bou-Saïd, and H. Walter-Le Berre, Morphological and stent design risk factors to prevent migration phenomena for a thoracic aneurysm: a numerical analysis, *Medical engineering and physics* **37**, 23–33, 2015.

[7] H.-E. Altnji, B. Bou-Saïd, and H. Walter-Le Berre, Numerical simulation for design evaluation of thoracic stent graft to investigate the migration phenomena and type 1a endoleak of thoracic aneurysm, *J Vasc Med Surg* **3**, 1–7, 2015.

[8] G. A. Antoniou, G. S. Georgiadis, S. A. Antoniou, G. Kuhan, and D. Murray, A meta-analysis of outcomes of endovascular abdominal aortic aneurysm repair in patients with hostile and friendly neck anatomy, *Journal of vascular surgery* **57**, 527–538, 2013.

[9] F. Auricchio, M. Conti, S. Marconi, A. Reali, J. L. Tolenaar, and S. Trimarchi, Patient-specific aortic endografting simulation: From diagnosis to prediction, *Computers in Biology and Medicine* **43**, 386 – 394, 2013.

[10] F. Auricchio, A robust integration-algorithm for a finite-strain shape-memory-alloy superelastic model, *International Journal of plasticity* **17**, 971–990, 2001.

[11] F. Auricchio and R. L. Taylor, Shape-memory alloys: modelling and numerical simulations of the finite-strain superelastic behavior, *Computer methods in applied mechanics and engineering* **143**, 175–194, 1997.

[12] F. Auricchio, R. L. Taylor, and J. Lubliner, Shape-memory alloys: macromodelling and numerical simulations of the superelastic behavior, *Computer methods in applied mechanics and engineering* **146**, 281–312, 1997.

[13] F. Auricchio, M. Conti, M. De Beule, G. De Santis, and B. Verhegghe, Carotid artery stenting simulation: from patient-specific images to finite element analysis, *Medical engineering and physics* **33**, 281–289, 2011.

[14] F. Auricchio, M. Conti, R. M. Romarowski, H. W. De Beaufort, V. Grassi, and S. Trimarchi, Computational tools for thoracic endovascular aortic repair planning, *Italian Journal of Vascular and Endovascular Surgery* **26**, 51–58, 2019.

[15] M. Azaouzi, N. Lebaal, A. Makradi, and S. Belouettar, Optimization based simulation of self-expanding nitinol stent, *Materials & Design* **50**, 917–928, 2013.

[16] M. R. Barnes, Form finding and analysis of tension structures by dynamic relaxation, *International journal of space structures* **14**, 89–104, 1999.

[17] H. E. Barrett, E. M. Cunnane, H. Hidayat, J. M. O'Brien, M. A. Moloney, E. G. Kavanagh, and M. T. Walsh, On the influence of wall calcification and intraluminal thrombus on prediction of abdominal aortic aneurysm rupture, *Journal of Vascular Surgery* **67**, 1234–1246, 2018.

[18] C. Basciano, C. Kleinstreuer, S. Hyun, and E. A. Finol, A relation between near-wall particle-hemodynamics and onset of thrombus formation in abdominal aortic aneurysms, *Annals of biomedical engineering* **39**, 2010–2026, 2011.

[19] J.-P. Becquemin, J.-C. Pillet, F. Lescalie, M. Sapoval, Y. Goueffic, P. Lermusiaux, E. Steinmetz, J. Marzelle, et al., A randomized controlled trial of endovascular aneurysm repair versus open surgery for abdominal aortic aneurysms in low-to moderate-risk patients, *Journal of vascular surgery* **53**, 1167–1173, 2011.

[20] H. G. Beebe, J. L. Cronenwett, B. T. Katzen, D. C. Brewster, R. M. Green, V. E. T. Investigators, et al., Results of an aortic endograft trial: impact of device failure beyond 12 months, *Journal of vascular surgery* **33**, 55–63, 2001.

[21] T. Beier and S. Neely, Feature-based image metamorphosis, *Computer Graphics* **26**, 35–42, 1992.

[22] V. M. Belvroy, I. B. Houben, S. Trimarchi, H. J. Patel, F. L. Moll, and J. A. Van Herwaarden, Identifying and addressing the limitations of evar technology, *Expert review of medical devices* **15**, 541–554, 2018.

[23] J. Biehler, M. W. Gee, and W. A. Wall, Towards efficient uncertainty quantification in complex and large-scale biomechanical problems based on a bayesian multi-fidelity scheme, *Biomechanics and modeling in mechanobiology* **14**, 489–513, 2015.

[24] J. Bloomenthal, Calculation of reference frames along a space curve, *Graphics gems* **1**, 567–571, 1990.

[25] F. E. Boas and D. Fleischmann, CT artifacts: causes and reduction techniques, *Imaging Med* **4**, 229–240, 2012.

[26] U. M. Bracale, A. M. Giribono, G. Vitale, D. Narese, G. Santini, and L. del Guercio, Accidental coverage of both renal arteries during infrarenal aortic stent-graft implantation: cause and treatment, *Case reports in vascular medicine* **2014**, 1–4, 2014.

[27] F. A. Braeu, A. Seitz, R. C. Aydin, and C. J. Cyron, Homogenized constrained mixture models for anisotropic volumetric growth and remodeling, *Biomechanics and modeling in mechanobiology* **16**, 889–906, 2017.

[28] M. Breeuwer, S. De Putter, U. Kose, L. Speelman, K. Visser, F. Gerritsen, R. Hoogeveen, R. Krams, H. van den Bosch, J. Buth, et al., Towards patient-specific risk assessment of abdominal aortic aneurysm, *Medical & biological engineering & computing* **46**, 1085–1095, 2008.

[29] K. E. Brown, K. S. Heyer, J. S. Matsumura, and M. K. Eskandari, Late type iii endoleak and graft failure of an ancure stent-graft, *Journal of Vascular and Interventional Radiology* **19**, 1506–1508, 2008.

[30] L. Brown, J. Powell, S. Thompson, D. Epstein, M. Sculpher, and R. Greenhalgh, The uk endovascular aneurysm repair (evar) trials: randomised trials of evar versus standard therapy., In *NIHR Health Technology Assessment programme: Executive Summaries*, NIHR Journals Library, 2012.

[31] K. J. Bruen, R. J. Feezor, M. J. Daniels, A. W. Beck, and W. A. Lee, Endovascular chimney technique versus open repair of juxtarenal and suprarenal aneurysms, *Journal of vascular surgery* **53**, 895–905, 2011.

[32] S. Brugaletta, J. Gomez-Lara, R. Diletti, V. Farooq, R. Jan van Geuns, B. de Bruyne, D. Dudek, H. M. Garcia-Garcia, J. A. Ormiston, and P. W. Serruys, Comparison of in vivo eccentricity and symmetry indices between metallic stents and bioresorbable vascular scaffolds: insights from the absorb and spirit trials, *Catheterization and Cardiovascular Interventions* **79**, 219–228, 2012.

[33] J. Brunkwall, How to design the optimal stent graft—what have we learnt?, *Scandinavian Journal of Surgery* **97**, 191–194, 2008.

[34] L. Canaud, P. Alric, M. Laurent, T.-P. Baum, P. Branchereau, C. H. Marty-Ané, and J.-P. Berthet, Proximal fixation of thoracic stent-grafts as a function of oversizing and increasing aortic arch angulation in human cadaveric aortas, *Journal of Endovascular Therapy* **15**, 326–334, 2008.

[35] T. E. Carew, R. N. Vaishnav, and D. J. Patel, Compressibility of the arterial wall, *Circulation research* **23**, 61–68, 1968.

[36] E. Carmel and D. Cohen-Or, Warp-guided object-space morphing, *The Visual Computer* **13**, 465–478, 1998.

[37] M. Carmo, L. Colombo, A. Bruno, F. R. M. Corsi, L. Roncoroni, M. Cuttin, F. Radice, E. Mussini, and P. Settembrini, Alteration of elastin, collagen and their cross-links in abdominal aortic aneurysms, *European journal of vascular and endovascular surgery* **23**, 543–549, 2002.

[38] N. Chakfe, F. Dieval, G. Riepe, D. Mathieu, I. Zbali, F. Thaveau, C. Heintz, J.-G. Kretz, and B. Durand, Influence of the textile structure on the degradation of explanted aortic endoprostheses, *European Journal of Vascular and Endovascular Surgery* **27**, 33–41, 2004.

[39] D. Chamié, H. G. Bezerra, G. F. Attizzani, H. Yamamoto, T. Kanaya, G. T. Stefano, Y. Fujino, E. Mehanna, W. Wang, A. Abdul-Aziz, et al., Incidence, predictors, morphological characteristics, and clinical outcomes of stent edge dissections detected by optical coherence tomography, *JACC: Cardiovascular Interventions* **6**, 800–813, 2013.

[40] E. Choke, G. Munneke, R. Morgan, A.-M. Belli, I. Loftus, R. McFarland, T. Loosemore, and M. M. Thompson, Outcomes of endovascular abdominal aortic aneurysm repair in patients with hostile neck anatomy, *Cardiovascular and interventional radiology* **29**, 975–980, 2006.

[41] T. Chuter, K. Ivancev, M. Malina, T. Resch, J. Brunkwall, B. Lindblad, and B. Risberg, Aneurysm pressure following endovascular exclusion, *European journal of vascular and endovascular surgery* **13**, 85–87, 1997.

[42] T. A. M. Chuter, G. Wendt, B. R. Hopkinson, R. A. P. Scott, B. Risberg, E. Keiffer, D. Raithel, J. H. Van Bockel, G. White, and P. Walker, Bifurcated stent-graft for abdominal aortic aneurysm, *Cardiovascular Surgery* **5**, 388–392, 1997.

[43] F. Cochennec, J. P. Becquemin, P. Desgranges, E. Allaire, H. Kobeiter, and F. Roudot-Thoraval, Limb graft occlusion following evar: clinical pattern, outcomes and predictive factors of occurrence, *European journal of vascular and endovascular surgery* **34**, 59–65, 2007.

[44] *Endovascular Aortic Repair - Abdominal*. Cook Medical, Bloomington, Indiana, USA, 2019.

[45] T. J. Corbett, A. Callanan, and T. M. McGloughlin, In vitro measurement of the axial migration force on the proximal end of a bifurcated abdominal aortic aneurysm stent-graft model, *Proceedings of the Institution of Mechanical Engineers, Part H: Journal of Engineering in Medicine* **225**, 401–409, 2011.

[46] T. Corbett, D. Molony, E. Kavanagh, P. Grace, M. Walsh, and T. McGloughlin, Experimental analysis of endovascular treatment of aaa and predictors of long term outcomes, *Biomechanics and Mechanobiology of Aneurysms*, 247–284, 2011.

[47] T. J. Corbett, A. Callanan, L. G. Morris, B. J. Doyle, P. A. Grace, E. G. Kavanagh, and T. M. McGloughlin, A review of the in vivo and in vitro biomechanical behavior and performance of postoperative abdominal aortic aneurysms and implanted stent-grafts, *Journal of Endovascular Therapy* **15**, 468–484, 2008.

[48] S. A. Cornelissen, H. J. Verhagen, M. Prokop, F. L. Moll, and L. W. Bartels, Visualizing type iv endoleak using magnetic resonance imaging with a blood pool contrast agent, *Journal of vascular surgery* **47**, 861–864, 2008.

[49] S. De Bock, *A (Bio)Mechanical Analysis of Stent Grafts for the Treatment of Abdominal Aortic Aneurysms*, PhD thesis, Gent University, 2014.

[50] S. De Bock, F. Iannaccone, G. De Santis, M. De Beule, P. Mortier, B. Verhegghe, and P. Segers, Our capricious vessels: the influence of stent design and vessel geometry on the mechanics of intracranial aneurysm stent deployment, *Journal of biomechanics* **45**, 1353–1359, 2012.

[51] S. De Bock, F. Iannaccone, G. De Santis, M. De Beule, D. Van Loo, D. Devos, F. Vermassen, P. Segers, and B. Verhegghe, Virtual evaluation of stent graft deployment: a validated modeling and simulation study, *Journal of the mechanical behavior of biomedical materials* **13**, 129–139, 2012.

[52] S. De Bock, F. Iannaccone, M. De Beule, D. Van Loo, F. Vermassen, B. Verhegghe, and P. Segers, Filling the void: A coalescent numerical and experimental technique to determine aortic stent graft mechanics, *Journal of biomechanics* **46**, 2477–2482, 2013.

[53] S. De Bock, F. Iannaccone, M. De Beule, F. Vermassen, P. Segers, and B. Verhegghe, What if you stretch the ifu? a mechanical insight into stent graft instructions for use in angulated proximal aneurysm necks, *Medical engineering and physics* **36**, 1567–1576, 2014.

[54] J. L. De Bruin, A. F. Baas, J. Buth, M. Prinssen, E. L. Verhoeven, P. W. Cuypers, M. R. Van Sambeek, R. Balm, D. E. Grobbee, and J. D. Blankensteijn, Long-term outcome of open or endovascular repair of abdominal aortic aneurysm, *New England Journal of Medicine* **362**, 1881–1889, 2010.

[55] E. de Souza Neto, D. Perić, M. Dutko, and D. Owen, Design of simple low order finite elements for large strain analysis of nearly incompressible solids, *International Journal of Solids and Structures* **33**, 3277–3296, 1996.

[56] M. H. de Vaal, *Computational modeling, clinical comprehension and improvement of aortic manipulation*, PhD thesis, Technische Universität München, 2015.

[57] N. Demanget, *Analyses des performances mécaniques des endoprothèses aortiques par simulation numérique: application au traitement des anévrismes tortueux*, PhD thesis, Ecole des Mines de Saint Etienne, 2012.

[58] N. Demanget, S. Avril, P. Badel, L. Orgéas, C. Geindreau, J.-N. Albertini, and J.-P. Favre, Computational comparison of the bending behavior of aortic stent-grafts, *Journal of the mechanical behavior of biomedical materials* **5**, 272–282, 2012.

[59] N. Demanget, P. Latil, L. Orgéas, P. Badel, S. Avril, C. Geindreau, J.-N. Albertini, and J.-P. Favre, Severe bending of two aortic stent-grafts: an experimental and numerical mechanical analysis, *Annals of biomedical engineering* **40**, 2674–2686, 2012.

[60] N. Demanget, A. Duprey, P. Badel, L. Orgéas, S. Avril, C. Geindreau, J.-N. Albertini, and J.-P. Favre, Finite element analysis of the mechanical performances of 8 marketed aortic stent-grafts, *Journal of Endovascular Therapy* **20**, 523–535, 2013.

[61] L. Derycke, D. Perrin, F. Cochennec, J.-N. Albertini, and S. Avril, Predictive numerical simulations of double branch stent-graft deployment in an aortic arch aneurysm, *Annals of Biomedical Engineering* **47**, 1051–1062, 2019.

[62] N. Diehm, F. Dick, B. T. Katzen, J. Schmidli, C. Kalka, and I. Baumgartner, Aortic neck dilatation after endovascular abdominal aortic aneurysm repair: a word of caution, *Journal of vascular surgery* **47**, 886–892, 2008.

[63] E. D. Dillavou, S. C. Muluk, R. Y. Rhee, E. Tzeng, J. D. Woody, N. Gupta, and M. S. Makaroun, Does hostile neck anatomy preclude successful endovascular aortic aneurysm repair?, *Journal of vascular surgery* **38**, 657–663, 2003.

[64] G. Dobson, J. Flewitt, J. V. Tyberg, R. Moore, and M. Karamanoglu, Endografting of the descending thoracic aorta increases ascending aortic input impedance and attenuates pressure transmission in dogs, *European journal of vascular and endovascular surgery* **32**, 129–135, 2006.

[65] S. Doll and K. Schweizerhof, On the development of volumetric strain energy functions, *Journal of applied mechanics* **67**, 17–21, 2000.

[66] A. Dumenil, A. Kaladji, M. Castro, S. Esneault, A. Lucas, M. Rochette, C. Göksu, and P. Haigron, Finite-element-based matching of pre-and intraoperative data for image-guided endovascular aneurysm repair, *IEEE Transactions on Biomedical Engineering* **60**, 1353–1362, 2013.

[67] S. Duvnjak, Endovascular treatment of aortoiliac aneurysms: From intentional occlusion of the internal iliac artery to branch iliac stent graft, *World journal of radiology* **8**, 275–280, 2016.

[68] K. Eckroth-Bernard, R. Garvin, and E. Ryer, Current status of endovascular devices to treat abdominal aortic aneurysms, *Biomedical Engineering and Computational Biology* **5**, 25–32, 2013.

[69] H.-H. Eckstein, D. Böckler, I. Flessenkämper, T. Schmitz-Rixen, S. Debus, and W. Lang, Ultrasonographic screening for the detection of abdominal aortic aneurysms, *Deutsches Ärzteblatt International* **106**, 657–663, 2009.

[70] S. H. Ellozy, A. Carroccio, R. A. Lookstein, T. S. Jacobs, M. D. Addis, V. J. Teodorescu, and M. L. Marin, Abdominal aortic aneurysm sac shrinkage after endovascular aneurysm repair: correlation with chronic sac pressure measurement, *Journal of vascular surgery* **43**, 2–7, 2006.

[71] R. Erbel, V. Aboyans, C. Boileau, E. Bossone, R. D. Bartolomeo, H. Eggebrecht, A. Evangelista, V. Falk, H. Frank, et al., 2014 esc guidelines on the diagnosis and treatment of aortic diseases: Document covering acute and chronic aortic diseases of the thoracic and abdominal aorta of the adult the task force for the diagnosis and treatment of aortic diseases of the european society of cardiology (esc), *European heart journal* **35**, 2873–2926, 2014.

[72] P. W. Farah, *Mortar Methods for Computational Contact Mechanics Including Wear and General Volume Coupled Problems*, PhD thesis, Technische Universität München, 2017.

[73] R. T. Farouki, Exact rotation-minimizing frames for spatial pythagorean-hodograph curves, *Graphical Models* **64**, 382–395, 2002.

[74] J. Ferruzzi, D. A. Vorp, and J. D. Humphrey, On constitutive descriptors of the biaxial mechanical behaviour of human abdominal aorta and aneurysms, *Journal of the Royal Society Interface* **8**, 435–450, 2010.

[75] C. A. Figueroa, C. A. Taylor, V. Yeh, A. J. Chiou, and C. K. Zarins, Effect of curvature on displacement forces acting on aortic endografts: a 3-dimensional computational analysis, *Journal of Endovascular Therapy* **16**, 284–294, 2009.

[76] M. F. Fillinger, S. P. Marra, M. L. Raghavan, and F. E. Kennedy, Prediction of rupture risk in abdominal aortic aneurysm during observation: wall stress versus diameter, *Journal of vascular surgery* **37**, 724–732, 2003.

[77] M. F. Fillinger, J. Racusin, R. K. Baker, J. L. Cronenwett, A. Teutelink, M. L. Schermerhorn, R. M. Zwolak, R. J. Powell, D. B. Walsh, and E. M. Rzucidlo, Anatomic characteristics of ruptured abdominal aortic aneurysm on conventional ct scans: implications for rupture risk, *Journal of vascular surgery* **39**, 1243–1252, 2004.

[78] T. L. Forbes, G. DeRose, S. W. Kribs, and K. A. Harris, Cumulative sum failure analysis of the learning curve with endovascular abdominal aortic aneurysm repair, *Journal of vascular surgery* **39**, 102–108, 2004.

[79] T. Frauenfelder, M. Lotfey, T. Boehm, and S. Wildermuth, Computational fluid dynamics: hemodynamic changes in abdominal aortic aneurysm after stent-graft implantation, *Cardiovascular and interventional radiology* **29**, 613–623, 2006.

[80] T. C. Gasser, R. W. Ogden, and G. A. Holzapfel, Hyperelastic modelling of arterial layers with distributed collagen fibre orientations, *Journal of the royal society interface* **3**, 15–35, 2006.

[81] T. C. Gasser, G. Görgülü, M. Folkesson, and J. Swedenborg, Failure properties of intraluminal thrombus in abdominal aortic aneurysm under static and pulsating mechanical loads, *Journal of vascular surgery* **48**, 179–188, 2008.

[82] A. Gebert de Uhlenbrock, *Designanalyse von endovaskulären Aortenprothesen*, PhD thesis, Technische Universität Hamburg, 2009.

[83] M. W. Gee, C. Reeps, H. H. Eckstein, and W. A. Wall, Prestressing in finite deformation abdominal aortic aneurysm simulation, *Journal of biomechanics* **42**, 1732–1739, 2009.

[84] M. W. Gee, C. Förster, and W. A. Wall, A computational strategy for prestressing patient-specific biomechanical problems under finite deformation, *International Journal for Numerical Methods in Biomedical Engineering* **26**, 52–72, 2010.

[85] M. W. Gee, C. M. Siefert, J. J. Hu, R. S. Tuminaro, and M. G. Sala, Ml 5.0 smoothed aggregation user's guide, Technical report, Technical Report SAND2006-2649, Sandia National Laboratories, 2006.

[86] M. W. Gee, C. T. Kelley, and R. Lehoucq, Pseudo-transient continuation for nonlinear transient elasticity, *International journal for numerical methods in engineering* **78**, 1209–1219, 2009.

[87] J. Gindre, A. Bel-Brunon, A. Kaladji, A. Duménil, M. Rochette, A. Lucas, P. Haigron, and A. Combescure, Finite element simulation of the insertion of guidewires during an evar procedure: example of a complex patient case, a first step toward patient-specific parameterized models, *International journal for numerical methods in biomedical engineering* **31**, e02716, 2015.

[88] J. Gindre, A. Bel-Brunon, M. Rochette, A. Lucas, A. Kaladji, P. Haigron, and A. Combescure, Patient-specific finite-element simulation of the insertion of guidewire during an evar procedure: Guidewire position prediction validation on 28 cases, *IEEE Transactions on Biomedical Engineering* **64**, 1057–1066, 2017.

[89] M. Gitterle, *A dual mortar formulation for finite deformation frictional contact problems including wear and thermal coupling*, PhD thesis, Technische Universität München, 2012.

[90] M. Gitterle, A. Popp, M. W. Gee, and W. A. Wall, Finite deformation frictional mortar contact using a semi-smooth newton method with consistent linearization, *International Journal for Numerical Methods in Engineering* **84**, 543–571, 2010.

[91] E. Goldstein and C. Gotsman, Polygon morphing using a multiresolution representation, In *Graphics Interface*, pages 247–247. Canadian Information Processing Society, 1995.

[92] J. Golledge and P. E. Norman, Atherosclerosis and abdominal aortic aneurysm: cause, response, or common risk factors?, *Arteriosclerosis, Thrombosis, and Vascular Biology* **30**, 1075–1077, 2010.

[93] J. Golzarian, E. B. Maes, and S. Sun, Endoleak: treatment options, *Techniques in vascular and interventional radiology* **8**, 41–49, 2005.

[94] L. Grassi, N. Hraiech, E. Schileo, M. Ansaloni, M. Rochette, and M. Viceconti, Evaluation of the generality and accuracy of a new mesh morphing procedure for the human femur, *Medical engineering & physics* **33**, 112–120, 2011.

[95] R. M. Greenhalgh, Comparison of endovascular aneurysm repair with open repair in patients with abdominal aortic aneurysm (evar trial 1), 30-day operative mortality results: randomised controlled trial, *The Lancet* **364**, 843 – 848, 2004.

[96] R. M. Greenhalgh and C. C. Campus, Endovascular aneurysm repair versus open repair in patients with abdominal aortic aneurysm (evar trial 1): randomised controlled trial, *The Lancet* **365**, 2179–2186, 2005.

[97] R. M. Greenhalgh and J. T. Powell, Endovascular repair of abdominal aortic aneurysm, *New England Journal of Medicine* **358**, 494–501, 2008.

[98] R. M. Greenhalgh, L. C. Brown, and J. T. Powell, Endovascular versus open repair of abdominal aortic aneurysm, *New England Journal of Medicine* **362**, 1863–1871, 2010.

[99] H. Guggenheimer, Computing frames along a trajectory, *Computer Aided Geometric Design* **6**, 77–78, 1989.

[100] G. J. Hall and E. P. Kasper, Comparison of element technologies for modeling stent expansion, *Journal of Biomechanical Engineering* **128**, 751–756, 2006.

[101] K. A. Hance, J. Hsu, T. Eskew, and A. S. Hermreck, Secondary aortoesophageal fistula after endoluminal exclusion because of thoracic aortic transection, *Journal of vascular surgery* **37**, 886–888, 2003.

[102] D. Haskett, G. Johnson, A. Zhou, U. Utzinger, and J. V. Geest, Microstructural and biomechanical alterations of the human aorta as a function of age and location, *Biomechanics and modeling in mechanobiology* **9**, 725–736, 2010.

[103] C. M. He and M. R. Roach, The composition and mechanical properties of abdominal aortic aneurysms, *Journal of vascular surgery* **20**, 6–13, 1994.

[104] N. Hedayati, P. H. Lin, A. B. Lumsden, and W. Zhou, Prolonged renal artery occlusion after endovascular aneurysm repair: endovascular rescue and renal function salvage, *Journal of vascular surgery* **47**, 446–449, 2008.

[105] P. Heider, O. Wolf, C. Reeps, M. Hanke, A. Zimmermann, H. Berger, and H. Eckstein, Aneurysmen und dissektionen der thorakalen und abdominellen aorta, *Der Chirurg* **78**, 600–610, 2007.

[106] A. Hemmler, B. Lutz, C. Reeps, G. Kalender, and M. W. Gee, A methodology for in silico endovascular repair of abdominal aortic aneurysms, *Biomechanics and Modeling in Mechanobiology* **17**, 1139–1164, 2018.

[107] A. Hemmler, B. Lutz, G. Kalender, C. Reeps, and M. W. Gee, Patient-specific in silico endovascular repair of abdominal aortic aneurysms: application and validation, *Biomechanics and Modeling in Mechanobiology* **18**, 983–1004, 2019.

[108] A. Hemmler, B. Lutz, C. Reeps, and M. W. Gee, Der digitale Zwilling in der endovaskulären Versorgung, *Gefäßchirurgie* **24**, 548–556, 2019.

[109] A. Hemmler, B. Lutz, C. Reeps, and M. W. Gee, In silico study of vessel and stent-graft parameters on the potential success of endovascular aneurysm repair, *International Journal for Numerical Methods in Biomedical Engineering* **35**, e3237, 2019.

[110] A. Hemmler, A. Lin, N. Thierfelder, T. Franz, M. Gee, and D. Bezuidenhout, Customized stent-grafts for endovascular aneurysm repair with challenging necks: a numerical proof of concept, *International Journal for Numerical Methods in Biomedical Engineering* **36**, e3316, 2020.

[111] J. W. Hinnen, O. H. J. Koning, J. H. Van Bockel, and J. F. Hamming, Aneurysm sac pressure after evar: the role of endoleak, *European Journal of Vascular and Endovascular Surgery* **34**, 432–441, 2007.

[112] J.-W. Hinnen, O. H. J. Koning, M. J. T. Visser, and H. J. Van Bockel, Effect of intraluminal thrombus on pressure transmission in the abdominal aortic aneurysm, *Journal of vascular surgery* **42**, 1176–1182, 2005.

[113] M. Hirschvogel, *Computational modeling of patient-specific cardiac mechanics with model reduction-based parameter estimation and applications to novel heart assist technologies*, PhD thesis, Technische Universität München, 2018.

[114] G. A. Holzapfel, *Nonlinear Solid Mechanics - A Continuum Approach for Engineering*, Wiley Press Chichester, 2000.

[115] G. A. Holzapfel and T. C. Gasser, A viscoelastic model for fiber-reinforced composites at finite strains: Continuum basis, computational aspects and applications, *Computer methods in applied mechanics and engineering* **190**, 4379–4403, 2001.

[116] G. A. Holzapfel, T. C. Gasser, and R. W. Ogden, A new constitutive framework for arterial wall mechanics and a comparative study of material models, *Journal of elasticity and the physical science of solids* **61**, 1–48, 2000.

[117] G. A. Holzapfel, M. Stadler, and T. C. Gasser, Changes in the mechanical environment of stenotic arteries during interaction with stents: computational assessment of parametric stent designs, *Journal of biomechanical engineering* **127**, 166–180, 2005.

[118] G. A. Holzapfel, J. A. Niestrawska, R. W. Ogden, A. J. Reinisch, and A. J. Schriefl, Modelling non-symmetric collagen fibre dispersion in arterial walls, *Journal of The Royal Society Interface* **12**, 20150188, 2015.

[119] G. A. Holzapfel, R. W. Ogden, and S. Sherifova, On fibre dispersion modelling of soft biological tissues: a review, *Proceedings of the Royal Society A* **475**, 20180736, 2019.

[120] B. A. Howell, T. Kim, A. Cheer, H. Dwyer, D. Saloner, and T. A. Chuter, Computational fluid dynamics within bifurcated abdominal aortic stent-grafts, *Journal of Endovascular Therapy* **14**, 138–143, 2007.

[121] F. Iannaccone, *Computer Simulations in Stroke Prevention: Design Tools and Strategies towards Virtual Procedure Planning*, PhD thesis, Gent University, 2014.

[122] F. Iannaccone, M. De Beule, S. De Bock, I. M. Van der Bom, M. J. Gounis, A. K. Wakhloo, M. Boone, B. Verhegghe, and P. Segers, A finite element method to predict adverse events in intracranial stenting using microstents: In vitro verification and patient specific case study, *Annals of biomedical engineering* **44**, 442–452, 2016.

[123] M. M. Idu, J. A. Reekers, R. Balm, K.-J. Ponsen, B. A. de Mol, and D. A. Legemate, Collapse of a stent-graft following treatment of a traumatic thoracic aortic rupture, *Journal of Endovascular Therapy* **12**, 503–507, 2005.

[124] K. Igari, T. Kudo, T. Toyofuku, M. Jibiki, and Y. Inoue, Outcomes following endovascular abdominal aortic aneurysm repair both within and outside of the instructions for use, *Annals of Thoracic and Cardiovascular Surgery* **20**, 61–66, 2014.

[125] U. K. E. T. Investigators, Endovascular repair of aortic aneurysm in patients physically ineligible for open repair, *New England Journal of Medicine* **362**, 1872–1880, 2010.

[126] F. Inzoli, F. Boschetti, M. Zappa, T. Longo, and R. Fumero, Biomechanical factors in abdominal aortic aneurysm rupture, *European journal of vascular surgery* **7**, 667–674, 1993.

[127] T. S. Jacobs, J. Won, E. C. Gravereaux, P. L. Faries, N. Morrissey, V. J. Teodorescu, L. H. Hollier, and M. L. Marin, Mechanical failure of prosthetic human implants: a 10-year experience with aortic stent graft devices, *Journal of vascular surgery* **37**, 16–26, 2003.

[128] R. Jayendiran, B. Nour, and A. Ruimi, Fluid-structure interaction (fsi) analysis of stent-graft for aortic endovascular aneurysm repair (evar): Material and structural considerations, *Journal of the mechanical behavior of biomedical materials* **87**, 95–110, 2018.

[129] W. D. Jordan, K. Ouriel, M. Mehta, D. Varnagy, W. M. Moore, F. R. Arko, J. Joye, J.-P. P. de Vries, J. P. de Vries, H. Eckstein, et al., Outcome-based anatomic criteria for defining the hostile aortic neck, *Journal of vascular surgery* **61**, 1383–1390, 2015.

[130] N. P. Kadoglou, K. G. Moulakakis, I. Papadakis, I. Ikonomidis, M. Alepaki, J. Lekakis, and C. D. Liapis, Changes in aortic pulse wave velocity of patients undergoing endovascular repair of abdominal aortic aneurysms, *Journal of Endovascular Therapy* **19**, 661–666, 2012.

[131] A. Kaladji, A. Dumenil, M. Castro, A. Cardon, J.-P. Becquemin, B. Bou-Saïd, A. Lucas, and P. Haigron, Prediction of deformations during endovascular aortic aneurysm repair using finite element simulation, *Computerized medical imaging and graphics* **37**, 142–149, 2013.

[132] T. Kanai, H. Suzuki, and F. Kimura, 3d geometric metamorphosis based on harmonic map, In *Computer Graphics and Applications, 1997. Proceedings., The Fifth Pacific Conference on*, pages 97–104, 1997.

[133] H. Kandail, M. Hamady, and X. Y. Xu, Comparison of blood flow in branched and fenestrated stent-grafts for endovascular repair of abdominal aortic aneurysms, *Journal of Endovascular Therapy* **22**, 578–590, 2015.

[134] K. Kansagra, J. Kang, M.-C. Taon, S. Ganguli, R. Gandhi, G. Vatakencherry, and C. Lam, Advanced endografting techniques: snorkels, chimneys, periscopes, fenestrations, and branched endografts, *Cardiovascular diagnosis and therapy* **8**, 175–183, 2018.

[135] K. Kasirajan, M. D. Dake, A. Lumsden, J. Bavaria, and M. S. Makaroun, Incidence and outcomes after infolding or collapse of thoracic stent grafts, *Journal of vascular surgery* **55**, 652–658, 2012.

[136] A. Katsargyris, D. Spinelli, K. Oikonomou, H. Mufty, and E. L. Verhoeven, Incomplete expansion of chimney stent graft during chimney-thoracic endovascular aneurysm repair, *Annals of vascular surgery* **39**, 293–e1, 2017.

[137] M. Kimura, K. Hoshina, K. Miyahara, J. Nitta, M. Kobayashi, S. Yamamoto, and M. Ohshima, Geometric analysis of ruptured and nonruptured abdominal aortic aneurysms, *Journal of vascular surgery* **69**, 86–91, 2019.

[138] D. E. Kiousis, T. C. Gasser, and G. A. Holzapfel, A numerical model to study the interaction of vascular stents with human atherosclerotic lesions, *Annals of biomedical engineering* **35**, 1857–1869, 2007.

[139] C. Kleinstreuer, Z. Li, C. Basciano, S. Seelecke, and M. Farber, Computational mechanics of nitinol stent grafts, *Journal of biomechanics* **41**, 2370–2378, 2008.

[140] F. Klok, Two moving coordinate frames for sweeping along a 3d trajectory, *Computer Aided Geometric Design* **3**, 217–229, 1986.

[141] F. Koschnick, *Geometrische Locking-Effekte bei Finiten Elementen und ein allgemeines Konzept zu ihrer Vermeidung*, PhD thesis, Technische Universität München, 2004.

[142] G. N. Kouvelos, K. Oikonomou, G. A. Antoniou, E. L. Verhoeven, and A. Katsargyris, A systematic review of proximal neck dilatation after endovascular repair for abdominal aortic aneurysm, *Journal of Endovascular Therapy* **24**, 59–67, 2017.

[143] J. A. Kratzberg, J. Golzarian, and M. L. Raghavan, Role of graft oversizing in the fixation strength of barbed endovascular grafts, *Journal of vascular surgery* **49**, 1543–1553, 2009.

[144] A. Kühnl, A. Erk, M. Trenner, M. Salvermoser, V. Schmid, and H.-H. Eckstein, Incidence, treatment and mortality in patients with abdominal aortic aneurysms: An analysis of hospital discharge data from 2005–2014, *Deutsches Ärzteblatt International* **114**, 391–398, 2017.

[145] S. T. Kwon, J. E. Rectenwald, and S. Baek, Intrasac pressure changes and vascular remodeling after endovascular repair of abdominal aortic aneurysms: review and biomechanical model simulation, *Journal of biomechanical engineering* **133**, 011011, 2011.

[146] D. C. Lagoudas, *Shape Memory Alloys - Modeling and Engineering Applications*, Springer Science+Business Media, LLC, 2008.

[147] T. Länne, B. Sonesson, D. Bergqvist, H. Bengtsson, and D. Gustafsson, Diameter and compliance in the male human abdominal aorta: influence of age and aortic aneurysm, *European journal of vascular surgery* **6**, 178–184, 1992.

[148] R. Layman, S. Missoum, and J. Vande Geest, Simulation and probabilistic failure prediction of grafts for aortic aneurysm, *Engineering Computations* **27**, 84–105, 2010.

[149] F. Lazarus, S. Coquillart, and P. Jancene, Axial deformations: an intuitive deformation technique, *Computer-Aided Design* **26**, 607–613, 1994.

[150] F. A. Lederle, J. A. Freischlag, T. C. Kyriakides, F. T. Padberg, J. S. Matsumura, T. R. Kohler, P. H. Lin, J. M. Jean-Claude, D. F. Cikrit, K. M. Swanson, et al., Outcomes following endovascular vs open repair of abdominal aortic aneurysm: a randomized trial, *Jama* **302**, 1535–1542, 2009.

[151] F. A. Lederle, J. A. Freischlag, T. C. Kyriakides, J. S. Matsumura, F. T. Padberg Jr, T. R. Kohler, P. Kougias, J. M. Jean-Claude, D. F. Cikrit, and K. M. Swanson, Long-term comparison of endovascular and open repair of abdominal aortic aneurysm, *New England Journal of Medicine* **367**, 1988–1997, 2012.

[152] J. T. Lee, B. W. Ullery, C. K. Zarins, C. Olcott, E. J. Harris, and R. L. Dalman, Evar deployment in anatomically challenging necks outside the ifu, *European Journal of Vascular and Endovascular Surgery* **46**, 65–73, 2013.

[153] A. Lerios, C. D. Garfinkle, and M. Levoy, Feature-based volume metamorphosis, In *Proceedings of the 22nd annual conference on Computer graphics and interactive techniques*, pages 449–456. ACM, 1995.

[154] J. H. Leung, A. R. Wright, N. Cheshire, J. Crane, S. A. Thom, A. D. Hughes, and Y. Xu, Fluid structure interaction of patient specific abdominal aortic aneurysms: a comparison with solid stress models, *Biomedical engineering online* **5**, 1–15, 2006.

[155] D. Li and Y. Xia, Electrospinning of nanofibers: reinventing the wheel?, *Advanced materials* **16**, 1151–1170, 2004.

[156] Z. Li, C. Kleinstreuer, and M. Farber, Computational analysis of biomechanical contributors to possible endovascular graft failure, *Biomechanics and Modeling in Mechanobiology* **4**, 221–234, 2005.

[157] Z. Li and C. Kleinstreuer, Analysis of biomechanical factors affecting stent-graft migration in an abdominal aortic aneurysm model, *Journal of biomechanics* **39**, 2264–2273, 2006.

[158] K. Liffman, M. M. Lawrence-Brown, J. B. Semmens, A. Bui, M. Rudman, and D. E. Hartley, Analytical modeling and numerical simulation of forces in an endoluminal graft, *Journal of Endovascular Therapy* **8**, 358–371, 2001.

[159] K. K. Lin, J. A. Kratzberg, and M. L. Raghavan, Role of aortic stent graft oversizing and barb characteristics on folding, *Journal of vascular surgery* **55**, 1401–1409, 2012.

[160] J. Lu, X. Zhou, and M. L. Raghavan, Inverse method of stress analysis for cerebral aneurysms, *Biomechanics and modeling in mechanobiology* **7**, 477–486, 2008.

[161] A. H. Mahnken, CT imaging of coronary stents: past, present, and future, *ISRN cardiology* **2012**, 1–12, 2012.

[162] A. Maier, M. W. Gee, C. Reeps, H.-H. Eckstein, and W. A. Wall, Impact of calcifications on patient-specific wall stress analysis of abdominal aortic aneurysms, *Biomechanics and modeling in mechanobiology* **9**, 511–521, 2010.

[163] A. Maier, M. W. Gee, C. Reeps, J. Pongratz, H.-H. Eckstein, and W. A. Wall, A comparison of diameter, wall stress, and rupture potential index for abdominal aortic aneurysm rupture risk prediction, *Annals of biomedical engineering* **38**, 3124–3134, 2010.

[164] A. Maier, *Computational Modeling of Rupture Risk in Abdominal Aortic Aneurysms*, PhD thesis, TU München, 2012.

[165] A. Maier, M. Essler, M. W. Gee, H.-H. Eckstein, W. A. Wall, and C. Reeps, Correlation of biomechanics to tissue reaction in aortic aneurysms assessed by finite elements and [18f]–fluorodeoxyglucose–pet/ct, *International journal for numerical methods in biomedical engineering* **28**, 456–471, 2012.

[166] R. Makar, J. Reid, A. Pherwani, L. Johnston, R. Hannon, B. Lee, and C. Soong, Aorto-enteric fistula following endovascular repair of abdominal aortic aneurysm, *European Journal of Vascular and Endovascular Surgery* **20**, 588–590, 2000.

[167] G. Maleux, M. Koolen, S. Heye, and A. Nevelsteen, Limb occlusion after endovascular repair of abdominal aortic aneurysms with supported endografts, *Journal of vascular and interventional radiology* **19**, 1409–1412, 2008.

[168] G. Maleux, M. Koolen, and S. Heye, Complications after endovascular aneurysm repair, *Seminars in interventional radiology* **26**, 3–9, 2009.

[169] G. Maleux, L. Poorteman, A. Laenen, B. Saint-Lèbes, S. Houthoofd, I. Fourneau, and H. Rousseau, Incidence, etiology, and management of type iii endoleak after endovascular aortic repair, *Journal of vascular surgery* **66**, 1056–1064, 2017.

[170] J. M. Manunga and G. S. Oderich, Endovascular training and learning curve for complex endovascular procedures, In *Endovascular Aortic Repair*, pages 245–257, Springer, 2017.

[171] A. Marchiori, A. v. Ristow, M. Guimaraes, C. Schönholz, and R. Uflacker, Predictive factors for the development of type ii endoleaks, *Journal of Endovascular Therapy* **18**, 299–305, 2011.

[172] S. P. Marra, C. P. Daghlian, M. F. Fillinger, and F. E. Kennedy, Elemental composition, morphology and mechanical properties of calcified deposits obtained from abdominal aortic aneurysms, *Acta biomaterialia* **2**, 515–520, 2006.

[173] T. Matsumoto, Y. Matsubara, Y. Aoyagi, D. Matsuda, J. Okadome, K. Morisaki, K. Inoue, S. Tanaka, T. Ohkusa, and Y. Maehara, Radial force measurement of endovascular stents: Influence of stent design and diameter, *Vascular* **24**, 171–176, 2016.

[174] C. O. McDonnell, M. Halak, A. Bartlett, and S. R. Baker, Abdominal aortic aneurysm neck morphology: proposed classification system, *Irish journal of medical science* **175**, 4–8, 2006.

[175] D. J. McGrath, B. O'Brien, M. Bruzzi, N. Kelly, J. Clauser, U. Steinseifer, and P. E. McHugh, Evaluation of cover effects on bare stent mechanical response, *Journal of the mechanical behavior of biomedical materials* **61**, 567–580, 2016.

[176] *Endurant*$^{\text{TM}}$ *II - Stent Graft System*. Medtronic Cardiovascular, Santa Rosa, California, USA, 2019.

[177] N. Melas, A. Saratzis, N. Saratzis, J. Lazaridis, D. Psaroulis, K. Trygonis, and D. Kiskinis, Aortic and iliac fixation of seven endografts for abdominal-aortic aneurysm repair in an experimental model using human cadaveric aortas, *European Journal of Vascular and Endovascular Surgery* **40**, 429–435, 2010.

[178] L. E. Miller, M. K. Razavi, and B. K. Lal, Suprarenal versus infrarenal stent graft fixation on renal complications after endovascular aneurysm repair, *Journal of vascular surgery* **61**, 1340–1349, 2015.

[179] T. A. Mirza, A. Karthikesalingam, D. Jackson, S. R. Walsh, P. J. Holt, P. D. Hayes, and J. R. Boyle, Duplex ultrasound and contrast-enhanced ultrasound versus computed tomography for the detection of endoleak after evar: systematic review and bivariate meta-analysis, *European Journal of Vascular and Endovascular Surgery* **39**, 418–428, 2010.

[180] A. Moglia, G. Di Franco, and L. Morelli, Use of 3d models for planning, simulation, and training in vascular surgery, *Updates in surgery* **71**, 185–186, 2019.

[181] H. Mohammadi, S. Lessard, E. Therasse, R. Mongrain, and G. Soulez, A numerical pre-operative planning model to predict arterial deformations in endovascular aortic aneurysm repair, *Annals of biomedical engineering* **46**, 2148–2161, 2018.

[182] I. V. Mohan, R. J. F. Laheij, and P. L. Harris, Risk factors for endoleak and the evidence for stent-graft oversizing in patients undergoing endovascular aneurysm repair, *European Journal of Vascular and Endovascular Surgery* **21**, 344–349, 2001.

[183] I. V. Mohan, P. L. Harris, C. J. van Marrewijk, R. J. Laheij, and T. V. How, Factors and forces influencing stent-graft migration after endovascular aortic aneurysm repair, *Journal of Endovascular Therapy* **9**, 748–755, 2002.

[184] P. Moireau, N. Xiao, M. Astorino, C. A. Figueroa, D. Chapelle, C. A. Taylor, and J.-F. Gerbeau, External tissue support and fluid–structure simulation in blood flows, *Biomechanics and modeling in mechanobiology* **11**, 1–18, 2012.

[185] F. L. Moll, J. Powell, G. Fraedrich, F. Verzini, S. Haulon, M. Waltham, J. Van Herwaarden, P. Holt, J. Van Keulen, B. Rantner, et al., Management of abdominal aortic aneurysms clinical practice guidelines of the european society for vascular surgery, *European Journal of Vascular and Endovascular Surgery* **41**, S1–S58, 2011.

[186] D. S. Molony, E. G. Kavanagh, P. Madhavan, M. T. Walsh, and T. M. McGloughlin, A computational study of the magnitude and direction of migration forces in patient-specific abdominal aortic aneurysm stent-grafts, *European journal of vascular and endovascular surgery* **40**, 332–339, 2010.

[187] D. S. Molony, A. Callanan, E. G. Kavanagh, M. T. Walsh, and T. M. McGloughlin, Fluid-structure interaction of a patient-specific abdominal aortic aneurysm treated with an endovascular stent-graft, *Biomedical engineering online* **8**, 1–12, 2009.

[188] S. Morlacchi, S. G. Colleoni, R. Cárdenes, C. Chiastra, J. L. Diez, I. Larrabide, and F. Migliavacca, Patient-specific simulations of stenting procedures in coronary bifurcations: two clinical cases, *Medical engineering & physics* **35**, 1272–1281, 2013.

[189] L. Morris, P. Delassus, M. Walsh, and T. McGloughlin, A mathematical model to predict the in vivo pulsatile drag forces acting on bifurcated stent grafts used in endovascular treatment of abdominal aortic aneurysms (aaa), *Journal of biomechanics* **37**, 1087–1095, 2004.

[190] L. Morris, F. Stefanov, and T. McGloughlin, Stent graft performance in the treatment of abdominal aortic aneurysms: the influence of compliance and geometry, *Journal of biomechanics* **46**, 383–395, 2013.

[191] P. Mortier, G. A. Holzapfel, M. De Beule, D. Van Loo, Y. Taeymans, P. Segers, P. Verdonck, and B. Verhegghe, A novel simulation strategy for stent insertion and deployment in curved coronary bifurcations: comparison of three drug-eluting stents, *Annals of biomedical engineering* **38**, 88–99, 2010.

[192] J. A. Niestrawska, C. Viertler, P. Regitnig, T. U. Cohnert, G. Sommer, and G. A. Holzapfel, Microstructure and mechanics of healthy and aneurysmatic abdominal aortas: experimental analysis and modelling, *Journal of The Royal Society Interface* **13**, 20160620, 2016.

[193] D. R. Oakley and N. F. Knight, Adaptive dynamic relaxation algorithm for non-linear hyperelastic structures part i. formulation, *Computer methods in applied mechanics and engineering* **126**, 67–89, 1995.

[194] T. F. O'Donnell, M. R. Corey, S. E. Deery, G. Tsougranis, R. Maruthi, W. D. Clouse, R. P. Cambria, and M. F. Conrad, Select early type ia endoleaks after endovascular aneurysm repair will resolve without secondary intervention, *Journal of vascular surgery* **67**, 119–125, 2018.

[195] R. W. Ogden, Large deformation isotropic elasticity-on the correlation of theory and experiment for incompressible rubberlike solids, *Proceedings of the Royal Society of London A: Mathematical, Physical and Engineering Sciences (The Royal Society)* **326**, 565–584, 1972.

[196] K. Oikonomou, R. Kopp, A. Katsargyris, K. Pfister, E. L. Verhoeven, and P. Kasprzak, Outcomes of fenestrated/branched endografting in post-dissection thoracoabdominal aortic aneurysms, *European Journal of Vascular and Endovascular Surgery* **48**, 641–648, 2014.

[197] D. Palombo, D. Valenti, M. Ferri, A. Gaggiano, R. Mazzei, M. Vola, and S. Tettoni, Changes in the proximal neck of abdominal aortic aneurysms early after endovascular treatment, *Annals of vascular surgery* **17**, 408–410, 2003.

[198] J. C. Parodi, J. C. Palmaz, and H. D. Barone, Transfemoral intraluminal graft implantation for abdominal aortic aneurysms, *Annals of vascular surgery* **5**, 491–499, 1991.

[199] A. Patel, R. Edwards, and S. Chandramohan, Surveillance of patients post-endovascular abdominal aortic aneurysm repair (evar). a web-based survey of practice in the uk, *Clinical radiology* **68**, 580–587, 2013.

[200] R. Patel, M. J. Sweeting, J. T. Powell, R. M. Greenhalgh, E. T. Investigators, et al., Endovascular versus open repair of abdominal aortic aneurysm in 15-years' follow-up of the uk endovascular aneurysm repair trial 1 (evar trial 1): a randomised controlled trial, *The Lancet* **388**, 2366–2374, 2016.

[201] R. Patel, J. T. Powell, M. J. Sweeting, D. M. Epstein, J. K. Barrett, and R. M. Greenhalgh, Individual patient data meta-analysis of evar trial 1, the dutch randomised endovascular aneurysm management trial, the open versus endovascular repair trial and anévrysme de l'aorte abdominale, chirurgie versus endoprothése trial, In *The UK EndoVascular Aneurysm Repair (EVAR) randomised controlled trials: long-term follow-up and cost-effectiveness analysis*, NIHR Journals Library, 2018.

[202] S. W. Pattinson, M. E. Huber, S. Kim, J. Lee, S. Grunsfeld, R. Roberts, G. Dreifus, C. Meier, L. Liu, N. Hogan, et al., Additive manufacturing of biomechanically tailored meshes for compliant wearable and implantable devices, *Advanced Functional Materials* **online ahead of print**, doi.org/10.1002/adfm.201901815, 2019.

[203] J. Peidro, M. Boufi, A. D. Loundou, O. Hartung, B. Dona, F. Vernet, D. Bensoussan, and Y. S. Alimi, Aortic anatomy and complications of the proximal sealing zone after endovascular treatment of the thoracic aorta, *Annals of vascular surgery* **48**, 141–150, 2018.

[204] D. Perrin, *Vers un outil d'aide à la décision pour le traitement des anévrismes par endochirurgie*, PhD thesis, Ecole des Mines de Saint Etienne, 2015.

[205] D. Perrin, P. Badel, L. Orgéas, C. Geindreau, A. Dumenil, J.-N. Albertini, and S. Avril, Patient-specific numerical simulation of stent-graft deployment: Validation on three clinical cases, *Journal of Biomechanics* **48**, 1868 – 1875, 2015.

[206] D. Perrin, N. Demanget, P. Badel, S. Avril, L. Orgéas, C. Geindreau, and J.-N. Albertini, Deployment of stent grafts in curved aneurysmal arteries: toward a predictive numerical tool, *International journal for numerical methods in biomedical engineering* **31**, e02698, 2015.

[207] D. Perrin, P. Badel, L. Orgeas, C. Geindreau, S. rolland du Roscoat, J.-N. Albertini, and S. Avril, Patient-specific simulation of endovascular repair surgery with tortuous aneurysms requiring flexible stent-grafts, *Journal of the Mechanical Behavior of Biomedical Materials* **63**, 86–99, 2016.

[208] S. Polzer and T. C. Gasser, Biomechanical rupture risk assessment of abdominal aortic aneurysms based on a novel probabilistic rupture risk index, *Journal of The Royal Society Interface* **12**, 20150852, 2015.

[209] A. Popp, *Mortar Methods for Computational Contact Mechanics and General Interface Problems*, PhD thesis, Technische Universität München, 2012.

[210] A. Popp, M. W. Gee, and W. A. Wall, A finite deformation mortar contact formulation using a primal–dual active set strategy, *International Journal for Numerical Methods in Engineering* **79**, 1354–1391, 2009.

[211] A. Popp, M. Gitterle, M. W. Gee, and W. A. Wall, A dual mortar approach for 3d finite deformation contact with consistent linearization, *International Journal for Numerical Methods in Engineering* **83**, 1428–1465, 2010.

[212] A. Prasad, N. Xiao, X.-Y. Gong, C. K. Zarins, and C. A. Figueroa, A computational framework for investigating the positional stability of aortic endografts, *Biomechanics and modeling in mechanobiology* **12**, 869–887, 2012.

[213] M. Prinssen, E. Buskens, and J. D. Blankensteijn, The dutch randomised endovascular aneurysm management (dream) trial. background, design and methods, *Journal of Cardiovascular Surgery* **43**, 379–384, 2002.

[214] F. Pugliese, F. Cademartiri, C. van Mieghem, W. B. Meijboom, P. Malagutti, N. R. Mollet, C. Martinoli, P. J. de Feyter, and G. P. Krestin, Multidetector ct for visualization of coronary stents, *Radiographics* **26**, 887–904, 2006.

[215] B. Y. Rafii, O. J. Abilez, P. Benharash, and C. K. Zarins, Lateral movement of endografts within the aneurysm sac is an indicator of stent-graft instability, *Journal of Endovascular Therapy* **15**, 335–343, 2008.

[216] M. L. Raghavan, J. A. Kratzberg, and J. Golzarian, Introduction to biomechanics related to endovascular repair of abdominal aortic aneurysm, *Techniques in Vascular & Interventional Radiology* **8**, 50–55, 2005.

[217] M. Raghavan and D. A. Vorp, Toward a biomechanical tool to evaluate rupture potential of abdominal aortic aneurysm: identification of a finite strain constitutive model and evaluation of its applicability, *Journal of Biomechanics* **33**, 475 – 482, 2000.

[218] H. S. Rayt, A. J. Sutton, N. J. M. London, R. D. Sayers, and M. J. Bown, A systematic review and meta-analysis of endovascular repair (evar) for ruptured abdominal aortic aneurysm, *European Journal of Vascular and Endovascular Surgery* **36**, 536–544, 2008.

[219] C. Reeps, A. Maier, J. Pelisek, F. Härtl, V. Grabher-Meier, W. A. Wall, M. Essler, H.-H. Eckstein, and M. W. Gee, Measuring and modeling patient-specific distributions of material properties in abdominal aortic aneurysm wall, *Biomechanics and modeling in mechanobiology* **12**, 717–733, 2013.

[220] C. Reeps, M. Gee, A. Maier, M. Gurdan, H.-H. Eckstein, and W. A. Wall, The impact of model assumptions on results of computational mechanics in abdominal aortic aneurysm, *Journal of Vascular Surgery* **51**, 679–688, 2010.

[221] F. Riveros, G. Martufi, T. C. Gasser, and J. F. Rodriguez-Matas, On the impact of intraluminal thrombus mechanical behavior in aaa passive mechanics, *Annals of biomedical engineering* **43**, 2253–2264, 2015.

[222] S. Roccabianca, C. A. Figueroa, G. Tellides, and J. D. Humphrey, Quantification of regional differences in aortic stiffness in the aging human, *Journal of the mechanical behavior of biomedical materials* **29**, 618–634, 2014.

[223] K. A. Rocco, M. W. Maxfield, C. A. Best, E. W. Dean, and C. K. Breuer, In vivo applications of electrospun tissue-engineered vascular grafts: a review, *Tissue Engineering Part B: Reviews* **20**, 628–640, 2014.

[224] R. M. Romarowski, M. Conti, S. Morganti, V. Grassi, M. Marrocco-Trischitta, S. Trimarchi, and F. Auricchio, Computational simulation of tevar in the ascending aorta for optimal endograft selection: A patient-specific case study, *Computers in biology and medicine* **103**, 140–147, 2018.

[225] R. M. Romarowski, E. Faggiano, M. Conti, A. Reali, S. Morganti, and F. Auricchio, A novel computational framework to predict patient-specific hemodynamics after tevar: integration of structural and fluid-dynamics analysis by image elaboration, *Computers and Fluids* **179**, 806–819, 2019.

[226] H. Roos, M. Tokarev, V. Chernoray, M. Ghaffari, M. Falkenberg, A. Jeppsson, and H. Nilsson, Displacement forces in stent grafts: Influence of diameter variation and curvature asymmetry, *European Journal of Vascular and Endovascular Surgery* **52**, 150–156, 2016.

[227] D. Roy, C. Kauffmann, S. Delorme, S. Lerouge, G. Cloutier, and G. Soulez, A literature review of the numerical analysis of abdominal aortic aneurysms treated with endovascular stent grafts, *Computational and Mathematical Methods in Medicine* **2012**, 1–16, 2012.

[228] D. Roy, S. Lerouge, K. Inaekyan, C. Kauffmann, R. Mongrain, and G. Soulez, Experimental validation of more realistic computer models for stent-graft repair of abdominal aortic aneurysms, including pre-load assessment, *International journal for numerical methods in biomedical engineering* **32**, e02769, 2016.

[229] Y. Saad and M. H. Schultz, Gmres: A generalized minimal residual algorithm for solving nonsymmetric linear systems, *SIAM Journal on scientific and statistical computing* **7**, 856–869, 1986.

[230] N. Sakalihasan, R. Limet, and O. D. Defawe, Abdominal aortic aneurysm, *The Lancet* **365**, 1577–1589, 2005.

[231] S. M. Sampaio, J. M. Panneton, G. I. Mozes, J. C. Andrews, T. C. Bower, M. Karla, A. A. Noel, K. J. Cherry, T. Sullivan, and P. Gloviczki, Proximal type i endoleak after endovascular abdominal aortic aneurysm repair: predictive factors, *Annals of vascular surgery* **18**, 621–628, 2004.

[232] S. M. Sampaio, J. M. Panneton, G. Mozes, J. C. Andrews, A. A. Noel, M. Kalra, T. C. Bower, K. J. Cherry, T. M. Sullivan, and P. Gloviczki, Aortic neck dilation after endovascular abdominal aortic aneurysm repair: should oversizing be blamed?, *Annals of vascular surgery* **20**, 338–345, 2006.

[233] A. Schanzer, R. K. Greenberg, N. Hevelone, W. P. Robinson, M. H. Eslami, R. J. Goldberg, and L. Messina, Predictors of abdominal aortic aneurysm sac enlargement after endovascular repair, *Circulation* **123**, 2848–2855, 2011.

[234] C. Schlensak, T. Doenst, M. Hauer, J. Bitu-Moreno, P. Uhrmeister, G. Spillner, and F. Beyersdorf, Serious complications that require surgical interventions after endoluminal stent-graft placement for the treatment of infrarenal aortic aneurysms, *Journal of vascular surgery* **34**, 198–203, 2001.

[235] G. Schurink, J. Van Baalen, M. Visser, and J. Van Bockel, Thrombus within an aortic aneurysm does not reduce pressure on the aneurysmal wall, *Journal of Vascular Surgery* **31**, 501–506, 2000.

[236] R. C. Schuurmann, S. P. Overeem, K. van Noort, B. A. de Vries, C. H. Slump, and J.-P. P. de Vries, Validation of a new methodology to determine 3-dimensional endograft apposition, position, and expansion in the aortic neck after endovascular aneurysm repair, *Journal of Endovascular Therapy* **25**, 358–365, 2018.

[237] B. Senf, S. von Sachsen, R. Neugebauer, W.-G. Drossel, H.-J. Florek, F. W. Mohr, and C. D. Etz, The effect of stent graft oversizing on radial forces considering nitinol wire behavior and vessel characteristics, *Medical engineering & physics* **36**, 1480–1486, 2014.

[238] T. Shiraev, N. Agostinho, and S. Dubenec, Sizing considerations for gore excluder in angulated aortic aneurysm necks, *Annals of vascular surgery* **49**, 152–157, 2018.

[239] D. A. Sidloff, P. W. Stather, E. Choke, M. J. Bown, and R. D. Sayers, Type ii endoleak after endovascular aneurysm repair, *British Journal of Surgery* **100**, 1262–1270, 2013.

[240] N. Simon-Kupilik, H. Schima, L. Huber, R. Moidl, G. Wipplinger, U. Losert, E. Wolner, and P. Simon, Prosthetic replacement of the aorta is a risk factor for aortic root aneurysm development, *The Annals of thoracic surgery* **73**, 455–459, 2002.

[241] I. R. Sincos, E. S. da Silva, S. Q. Belczak, A. P. W. B. Sincos, M. de Lourdes Higuchi, V. Gornati, J. P. Otoch, and R. Aun, Histologic analysis of stent graft oversizing in the thoracic aorta, *Journal of vascular surgery* **58**, 1644–1651, 2013.

[242] C. Singh, X. Wang, Y. Morsi, and C. S. Wong, Importance of stent-graft design for aortic arch aneurysm repair, *AIMS Bioengineering* **4**, 133, 2017.

[243] B. Sonesson, N. Dias, M. Malina, P. Olofsson, D. Griffin, B. Lindblad, and K. Ivancev, Intra-aneurysm pressure measurements in successfully excluded abdominal aortic aneurysm after endovascular repair, *Journal of vascular surgery* **37**, 733–738, 2003.

[244] L. Speelman, E. M. H. Bosboom, G. W. H. Schurink, F. A. M. V. I. Hellenthal, J. Buth, M. Breeuwer, M. J. Jacobs, and F. N. van de Vosse, Patient-specific aaa wall stress analysis: 99-percentile versus peak stress, *European Journal of Vascular and Endovascular Surgery* **36**, 668–676, 2008.

[245] W. C. Sternbergh, S. R. Money, R. K. Greenberg, T. A. Chuter, Z. Investigators, et al., Influence of endograft oversizing on device migration, endoleak, aneurysm shrinkage, and aortic neck dilation: results from the zenith multicenter trial, *Journal of vascular surgery* **39**, 20–26, 2004.

[246] J. Steuer, M. Lachat, F. J. Veith, and A. Wanhainen, Endovascular grafts for abdominal aortic aneurysm, *European heart journal* **37**, 145–151, 2015.

[247] D. Y. Sze, R. S. Mitchell, D. C. Miller, D. Fleischmann, J. K. Frisoli, S. T. Kee, A. Verma, M. P. Sheehan, and M. D. Dake, Infolding and collapse of thoracic endoprostheses: manifestations and treatment options, *The Journal of thoracic and cardiovascular surgery* **138**, 324–333, 2009.

[248] Y. Takeda, Y. Sakata, T. Ohtani, S. Tamaki, Y. Omori, Y. Tsukamoto, Y. Aizawa, K. Shimamura, Y. Shirakawa, T. Kuratani, et al., Endovascular aortic repair increases vascular stiffness and alters cardiac structure and function, *Circulation Journal* **78**, 322–328, 2013.

[249] G. Taubin, Curve and surface smoothing without shrinkage, In *Computer Vision, 1995. Proceedings., Fifth International Conference on*, pages 852–857. IEEE, 1995.

[250] M. P. Thon, A. Hemmler, A. Glinzer, M. Mayr, M. Wildgruber, A. Zernecke-Madsen, and M. W. Gee, A multiphysics approach for modeling early atherosclerosis, *Biomechanics and Modeling in Mechanobiology* **17**, 617–644, 2018.

[251] B. H. Tonnessen, W. C. Sternbergh, and S. R. Money, Mid-and long-term device migration after endovascular abdominal aortic aneurysm repair: a comparison of aneurx and zenith endografts, *Journal of vascular surgery* **42**, 392–401, 2005.

[252] M. Trenner, A. Kuehnl, M. Salvermoser, B. Reutersberg, S. Geisbuesch, V. Schmid, et al., High annual hospital volume is associated with decreased in hospital mortality and complication rates following treatment of abdominal aortic aneurysms: secondary data analysis of the nationwide german drg statistics from 2005 to 2013, *Journal of Vascular Surgery* **67**, 989–990, 2018.

[253] S. Vad, A. Eskinazi, T. Corbett, T. McGloughlin, and J. P. V. Geest, Determination of coefficient of friction for self-expanding stent-grafts, *Journal of biomechanical engineering* **132**, 121007, 2010.

[254] T. J. van der Steenhoven, J. M. Heyligers, I. F. Tielliu, and C. J. Zeebregts, The upside down gore excluder contralateral leg without extracorporeal predeployment for aortic or iliac aneurysm exclusion, *Journal of vascular surgery* **53**, 1738–1741, 2011.

[255] J. A. van Herwaarden, B. E. Muhs, K. L. Vincken, J. Van Prehn, A. Teutelink, L. W. Bartels, F. L. Moll, and H. J. Verhagen, Aortic compliance following evar and the influence of different endografts: determination using dynamic mra, *Journal of Endovascular Therapy* **13**, 406–414, 2006.

[256] J. W. van Keulen, F. L. Moll, and J. A. van Herwaarden, Tips and techniques for optimal stent graft placement in angulated aneurysm necks, *Journal of vascular surgery* **52**, 1081–1086, 2010.

[257] J. van Prehn, F. J. V. Schlösser, B. E. Muhs, H. J. M. Verhagen, F. L. Moll, and J. A. van Herwaarden, Oversizing of aortic stent grafts for abdominal aneurysm repair: a systematic review of the benefits and risks, *European Journal of Vascular and Endovascular Surgery* **38**, 42–53, 2009.

[258] J. P. Vande Geest, M. S. Sacks, and D. A. Vorp, A planar biaxial constitutive relation for the luminal layer of intra-luminal thrombus in abdominal aortic aneurysms, *Journal of biomechanics* **39**, 2347–2354, 2006.

[259] C. Våpenstad and S. N. Buzink, Procedural virtual reality simulation in minimally invasive surgery, *Surgical endoscopy* **27**, 364–377, 2013.

[260] V. Vento, L. Cercenelli, C. Mascoli, E. Gallitto, S. Ancetti, G. Faggioli, A. Freyrie, E. Marcelli, M. Gargiulo, and A. Stella, The role of simulation in boosting the learning curve in evar procedures, *Journal of surgical education* **75**, 534–540, 2018.

[261] E. L. G. Verhoeven, G. Vourliotakis, W. T. G. J. Bos, I. F. J. Tielliu, C. J. Zeebregts, T. R. Prins, U. M. Bracale, and J. J. A. M. van den Dungen, Fenestrated stent grafting for short-necked and juxtarenal abdominal aortic aneurysm: an 8-year single-centre experience, *European Journal of Vascular and Endovascular Surgery* **39**, 529–536, 2010.

[262] F. Verzini, G. Isernia, P. De Rango, G. Simonte, G. Parlani, D. Loschi, and P. Cao, Abdominal aortic endografting beyond the trials: a 15-year single-center experience comparing newer to older generation stent-grafts, *Journal of Endovascular Therapy* **21**, 439–447, 2014.

[263] J. Vollmer, R. Mencl, and H. Mueller, Improved laplacian smoothing of noisy surface meshes, In *Computer graphics forum*, Volume 18, pages 131–138. Wiley Online Library, 1999.

[264] S. von Sachsen, B. Senf, O. Burgert, J. Meixensberger, H.-J. Florek, F. W. Mohr, and C. D. Etz, Stent graft visualization and planning tool for endovascular surgery using finite element analysis, *international journal of computer assisted radiology and surgery* **9**, 617–633, 2014.

[265] D. A. Vorp, W. A. Mandarino, M. W. Webster, and J. Gorcsan III, Potential influence of intraluminal thrombus on abdominal aortic aneurysm as assessed by a new non-invasive method, *Cardiovascular Surgery* **4**, 732–739, 1996.

[266] L. Vu-Quoc and X. G. Tan, Optimal solid shells for non-linear analyses of multilayer composites. i. statics, *Computer methods in applied mechanics and engineering* **192**, 975–1016, 2003.

[267] E. Vukovic, M. Czerny, F. Beyersdorf, M. Wolkewitz, M. Berezowski, M. Siepe, P. Blanke, and B. Rylski, Abdominal aortic aneurysm neck remodeling after anaconda stent graft implantation, *Journal of vascular surgery* **68**, 1354–1359, 2018.

[268] J. Walker, L.-Y. Tucker, P. Goodney, L. Candell, H. Hua, S. Okuhn, B. Hill, and R. W. Chang, Adherence to endovascular aortic aneurysm repair device instructions for use guidelines has no impact on outcomes, *Journal of vascular surgery* **61**, 1151–1159, 2015.

[269] J. Walker, L.-Y. Tucker, P. Goodney, L. Candell, H. Hua, S. Okuhn, B. Hill, and R. W. Chang, Type ii endoleak with or without intervention after endovascular aortic aneurysm repair does not change aneurysm-related outcomes despite sac growth, *Journal of vascular surgery* **62**, 551–561, 2015.

[270] D. H. Wang, M. Makaroun, M. W. Webster, and D. A. Vorp, Mechanical properties and microstructure of intraluminal thrombus from abdominal aortic aneurysm, *Journal of Biomechanical Engineering* **123**, 536–539, 2001.

[271] W. Wang, B. Jüttler, D. Zheng, and Y. Liu, Computation of rotation minimizing frames, *ACM Transactions on Graphics (TOG)* **27**, 2:1–2:18, 2008.

[272] M. Wilderman and L. A. Sanchez, Fenestrated grafts or debranching procedures for complex abdominal aortic aneurysms, *Perspectives in vascular surgery and endovascular therapy* **21**, 13–18, 2009.

[273] Y. G. Wolf, B. B. Hill, W. A. Lee, C. M. Corcoran, T. J. Fogarty, and C. K. Zarins, Eccentric stent graft compression: an indicator of insecure proximal fixation of aortic stent graft, *Journal of vascular surgery* **33**, 481–487, 2001.

[274] P. Wriggers, *Computational Contact Mechanics*, Springer-Verlag Berlin Heidelberg, 2006.

[275] T. R. Wyss, F. Dick, L. C. Brown, and R. M. Greenhalgh, The influence of thrombus, calcification, angulation, and tortuosity of attachment sites on the time to the first graft-related complication after endovascular aneurysm repair, *Journal of vascular surgery* **54**, 965–971, 2011.

[276] M. S. Yeoman, B. D. Reddy, H. C. Bowles, P. Zilla, D. Bezuidenhout, and T. Franz, The use of finite element methods and genetic algorithms in search of an optimal fabric reinforced porous graft system, *Annals of biomedical engineering* **37**, 2266–2287, 2009.

[277] C. K. Zarins, Stent-graft migration: how do we know when we have it and what is its significance?, *Journal of Endovascular Therapy* **11**, 364–365, 2004.

[278] C. K. Zarins, D. A. Bloch, T. Crabtree, A. H. Matsumoto, R. A. White, and T. J. Fogarty, Stent graft migration after endovascular aneurysm repair: importance of proximal fixation, *Journal of vascular surgery* **38**, 1264–1272, 2003.

[279] S. Zeinali-Davarani, A. Sheidaei, and S. Baek, A finite element model of stress-mediated vascular adaptation: application to abdominal aortic aneurysms, *Computer methods in biomechanics and biomedical engineering* **14**, 803–817, 2011.

[280] L. Zhang, X. Chen, and M. Liu, Research of customized aortic stent graft manufacture, In *IOP Conference Series: Materials Science and Engineering*, Volume 187, pages 1–9. IOP Publishing, 2017.

[281] O. C. Zienkiewicz, R. L. Taylor, and D. D. Fox, *The finite element method for solid and structural mechanics*, Elsevier Butterworth-Heinemann, 2014.